NASA Contractor Report 182257

High Speed Turboprop Aeroacoustic Study (Single Rotation)

Volume I: Model Development

Final Report

Prepared by

C.E. Whitfield
P.R. Gliebe
R. Mani
P. Mungur

GE Aircraft Engines
Advanced Engineering Technologies Department
Cincinnati, Ohio 45215

May 1989

Prepared for

National Aeronautics and Space Administration
Lewis Research Center

Contract NAS3-23721

NASA
National Aeronautics and Space Administration

1. Report No.	2. Government Accession No.	3. Recipient's Catalog No.
CR182257		

4. Title and Subtitle	5. Report Date
High Speed Turboprop Aeroacoustic Study - Single Rotation Volume I: Model Development	May 1989 6. Performing Organization Code
7. Author(s) C.E. Whitfield, P.R. Gliebe, R. Mani, and P. Mungur	8. Performing Organization Report No. 10. Work Unit No. 535-03-01
9. Performing Organization Name and Address GE Aircraft Engines 1 Neumann Way P.O. Box 156301 Cincinnati, OH 45215-6301	11. Contract or Grant No. NAS3-23721
12. Sponsoring Agency Name and Address National Aeronautics and Space Administration Lewis Research Center, Cleveland OH 44135	13. Type of Report and Period Covered Final Report 14. Sponsoring Agency Code

15. Supplementary Notes

Project Manager, James Dittmar, Propulsion Systems Division, Lewis Research Center.

16. Abstract

A frequency-domain noncompact-source theory for the steady loading and volume-displacement (thickness) noise of high speed propellers has been developed and programmed. Both near field and far field effects have been considered. The code utilizes blade surface pressure distributions obtained from three-dimensional nonlinear areodynamic flow field analysis programs as input for evaluating the steady loading noise.

Simplified mathematical models of the velocity fields induced at the propeller disk by nearby wing and fuselage surfaces and by angle-of-attack operation have been developed to provide estimates of the unsteady loading imposed on the propeller by these potential field type interactions. These unsteady blade loadings have been coupled to a chordwise compact propeller unsteady loading noise model to provide predictions of unsteady loading noise caused by these installation effects.

Finally, an analysis to estimate the corrections to be applied to the free-field noise predictions in order to arrive at the measurable fuselage sound pressure levels has been formulated and programmed. This analysis considers the effects of fuselage surface reflection and diffraction together with surface boundary layer refraction.

The steady loading and thickness model and the unsteady loading model have been verified using NASA-supplied data for the SR-2 and SR-3 model propfans. In addition, the steady loading and thickness model has been compared with data from the SR-6 model propfan. These theoretical models have been employed in the evaluation of the SR-7 powered Gulfstream aircraft in terms of noise characteristics at representative takeoff, cruise, and approach operating conditions.

In all cases, agreement between theory and experiment is encouraging.

17. Key Words (Suggested by Author(s))	18. Distribution Statement
Propeller noise, steady loading and thickness noise, installation effects on propeller noise, fuselage effects on propeller noise, aircraft control integration	Publicly Available

19. Security Classif. (of this report)	20. Security Classif. (of this page)	21. No. of Pages	22. Price
Unclassified	Unclassified	175	

TABLE OF CONTENTS

Table of Contents (Continued)

Table of Contents (Concluded)

LIST OF ILLUSTRATIONS

List of Illustrations (Continued)

List of Illustrations (Continued)

List of Illustrations(Continued)

List of Illustrations (Continued)

List of Illustrations (Continued)

List of Illustrations (Continued)

List of Illustrations (Concluded)

LIST OF TABLES

SUMMARY

A frequency-domain, noncompact-source theory for both the steady-loading and volume-displacement (thickness) noise of high speed propellers has been developed and programmed. Both near-field and far-field effects have been considered. This code utilizes blade surface pressure distributions obtained from a 3D (three-dimensional) nonlinear aerodynamic flow field analysis program as input for evaluating the steady-loading noise.

In order to investigate the effects of the aircraft installation on the sound field generated by the propeller, simplified mathematical models of the velocity fields induced at the propeller disk by nearby wing and fuselage surfaces and by angle-of-attack operation have been developed to provide estimates of the unsteady loading imposed on the propeller by these potential field type interactions. These unsteady blade loadings have been coupled to a chordwise compact propeller unsteady-loading noise model to provide predictions of unsteady-loading noise caused by these installation effects.

Both the steady loading and thickness model and the unsteady loading model described above have been checked against NASA-supplied data for the SR-2 and SR-3 model propfans. In addition, the steady loading and thickness model has been compared with data from the SR-6 model propfan. These theoretical models have been employed in the evaluation of the SR-7-powered Gulfstream aircraft in terms of noise characteristics at representative takeoff, cruise, and approach operating conditions.

Finally, an analysis to estimate the corrections to be applied to the free-field noise predictions in order to arrive at the measurable fuselage sound pressure levels has been formulated and programmed. This analysis considers the effects of fuselage surface reflection and diffraction, together with surface boundary layer refraction.

In all cases, agreement between theory and experiment is encouraging.

ACKNOWLEDGMENTS

This work was supported by the National Aeronautics and Space Administration through Contract NAS3-23721, with Dr. James H. Dittmar of NASA Lewis Research Center as the Program Manager. The authors would like to express their thanks to Dr. Dittmar for his help over the course of this program.

The authors would also like to express their thanks to Larry Bober and Hung Huynh of NASA Lewis for their assistance with the NASPROP-E Euler Solver and its grid generator, and to Dick Caney of GEAE (GE Aircraft Engines) for his help with the flow solutions from both the NASPROP-E and GE codes.

Thanks are also due to E.A. Krejsa and R.M. Nallasamy of NASA Lewis Research Center for their invaluable help in gathering together the input required to perform the calculations described in Section 3.0 of this report.

In addition, the authors would like to express their thanks to P.J.W. Block of NASA Langley for supplying tabulated data obtained in the course of testing the SR-2 Propfan. Several helpful conversations concerning this data are also acknowledged.

Finally, the authors would like to express their thanks to Ron Coffin of GE for his work in producing readable and documented computer codes.

NOMENCLATURE (Section 2.1)

a_o	Speed of sound
B	Number of blades
B_D	Chord: diameter ratio
C_L	Blade section lift coefficient
C_p	Power coefficient
C_u	Absolute tangential velocity (swirl)
c	Blade chord
c_o	Speed of sound
D, D_T	Diameter
FA	Face alignment (defined in Figure 1)
f	Force
f_L	Normalized chordwise blade loading function (defined in Equation 2.1.4)
H	Normalized chordwise blade thickness distribution (defined in Equation 2.1.4)
i	$\sqrt{-1}$
J	Advance ratio of propeller
J( )	Bessel function
K	Arbitrary constant
k_x/k_y	Dimensionless chordwise wave numbers (defined in Equation 2.1.3)
L'	Blade section lift
M_{HT}	Helical tip Mach number
M_r	Relative Mach number
M_T	Rotational tip Mach number
M_o, M_x	Axial Mach number
MCA	Midchord alignment (defined in Figure 1)
m	Blade passing frequency harmonic number
n	Rotational speed in rps (radians per second)
P	Power
P_{LM}	Steady loading (lift force) source

P_{V_M}	Volume displacement (thickness) source
p	Pressure
R/r	Blade radius or observer distance (defined in text)
r_o	Observer distance
T′	Torque per unit span
t_b	Maximum thickness: chord ratio
u/v/w	Velocities
W	Power
X	Nondimensional chordwise coordinate, equals x/c
x	Chordwise or axial coordinate
y	Sideline distance
z	Radius ratio (r/r_{tip})
β_P	Blade pitch angle (defined in Figure 1)
γ	Ratio of specific heats
Δ	Differential
θ	Emission angle
θ_L	Defined in Sketch 2.1
Θ	Swirl coefficient ($C_w/r\Omega$)
ρ_o	Density
ϕ	Phase shift (defined in Equation 2.1.5)
ψ	Blade thickness and loading distributions in the frequency domain (defined in Equation 2.1.4)
Ω	Rotational speed in radians per second

NOMENCLATURE (Section 2.2)

B	Number of propeller blades
c	Ambient speed of sound
f_{zo}	Steady (thrust) force per unit spanwise length exerted by each blade in the z direction (Figure 37); f_{zo} is a function of radius "r"
$f_{\phi o}$	Steady (tangential) force per unit spanwise length exerted by each blade in the "ϕ" direction (Figure 33); note that $f_{\phi o}$ is a function of radius and also that, in view of Figure 33, if the sense of rotor rotation is clockwise (forward looking aft), $f_{\phi o}$ will be negative
h	Representative airfoil thickness as a function of radius
j	$\sqrt{-1}$
J	Bessel function of the first kind
l	Airfoil chord as a function of radius
M_F	Flight Mach number
n	Harmonic of blade passing frequency of interest ($n \geq 1$)
p_o	Far field acoustic pressure due to steady loading and thickness
r	Radius of interest
R	Distance of observer from center of retarded propeller disk location (reference is made to Figure 38)
R_c	Distance of observer from center of current propeller disk location (Figure 38)
t	Time
ϕ	Azimuthal angle as defined in Figure 33 (note that $\phi = 0, 180$ represent the horizontal direction)
$\bar{k}$	Wave number, $nB\,\Omega/c$
ρ_o	Ambient air density
θ	"Emission" angle for propeller noise
θ_c	"Observer" angle for propeller noise
Ω	Angular velocity of propeller in radians per second

1.0 INTRODUCTION

1.1 Background

Recent studies have shown that the high speed turboprop offers an attractive alternative to turbofan propulsion for certain future commercial aircraft applications because of its substantially higher propulsive efficiency potential. However, one of the major obstacles to the use of high speed turboprops is the high near-field noise level generated by the propeller, which may cause a potentially serious cabin noise problem. In response to this potential problem, there has been substantial activity in both theoretical and experimental investigations of the noise characteristics of high speed propellers by NASA and private industry.

The currently envisioned high speed turboprop systems call for cruise flight speed Mach numbers of 0.7 to 0.8 and propeller tip speed Mach numbers of 0.7 to 0.9, which results in propeller blade operation in the transonic and supersonic regimes. Recent theoretical models of propeller noise have been produced to account for forward flight effects, source noncompactness, and supersonic motion of the blade-fixed sources relative to the observer position. These effects are all present to some degree for propellers operating at transonic and supersonic relative Mach numbers. The concept of the propfan, a low aspect ratio, high blade number propeller with swept blades, has features which promise significantly lower noise than conventional propellers. These features include very thin blade sections with large sweep angles near the tip to produce subsonic relative Mach number components normal to the leading edge of the blade, thus reducing losses and flow field discontinuities associated with the formation of shock waves.

Experimental measurements of several propfan configurations under NASA (and NASA-sponsored) programs have shown that propellers operating at transonic tip relative Mach numbers in actual (and simulated) forward flight exhibit noise characteristics considerably different from those predicted by earlier propeller noise theories. These differences include the trends in level with increasing tip relative or helical Mach number, as well as the harmonic spectrum shape. Since the newer theories predict the measured trends quite well in the subsonic regime, there is reason to suspect the failure in the theories to be related to the changes in character of the flow in the transonic regime being not adequately simulated by the theories as they now stand.

The substantial improvements in aircraft fuel efficiency projected for turboprop systems over turbofan systems gives strong incentive to resolve the discrepancy between predicted and measured noise trends in the transonic/supersonic operating range. If an accurate prediction model which contains the essential physics of the noise production processes involved can be established with confidence, then the procedure can be exploited to understand the noise production mechanisms and their controlling parameters. From this understanding, a design optimization procedure can be developed which yields the best combination of high efficiency and low noise. An accurate prediction of the noise characteristics of a propeller, especially its near-field spectral and directivity characteristics, will also permit a better chance to design the

most effective cabin structural and airborne noise attenuation features and, hence, minimize cabin interior discomfort with the smallest possible impact on the weight of the aircraft.

Although the issue has not been resolved, several reasons and/or explanations for the apparent failure of current theories of propeller noise in the transonic/supersonic regime have been put forth. One possible explanation (which we believe to be the correct one) is that the aerodynamic input to the acoustic theory has thus far been inadequate. Current practice has been to input blade surface pressure distributions using a polynomial distribution matched to an overall lift force at each spanwise location along the blade, or to utilize linearized two-dimensional strip theory analysis to calculate the input pressure distributions. Current noise theories utilize this input pressure distribution to compute the contribution to the noise field due to blade loading. The blade geometry, blade cross section shape, or thickness distribution, is used to compute the blade volume-displacement or thickness contribution to the noise field. Both loading and thickness noise produce tones at multiples of blade-passing frequency. The thickness noise component is a function of the spatial/time variation of the component of blade surface velocity normal to the surface itself. This is a function only of blade shape and blade motion relative to the observer, and so is independent of the aerodynamic flow field around the blades. Hence, if the thickness noise component of the theory is in error, it is due to an inadequacy of the acoustic theory itself, and not due to an inadequate aerodynamic input.

The loading noise component of the theory, however, could possibly be in error as a result of shortcomings in the aerodynamic input. The inadequacy can be associated with at least two major effects:

1. Three-dimensional nature of the flow in the tip region of the blade, characterized by spanwise flow migration and blade tip "relief" effects
2. Nonlinearity of the flow in the transonic regime, including the effects of shock formations and supersonic "patches" on the blades.

The first of these effects is present even in subsonic flow, where the current acoustic theories seem to work well enough. The second effect is unique to the flow regime of interest, and it is strongly suggested as a necessary effect which must be properly modeled in order to predict the noise characteristics of propellers in the transonic regime properly. Although the three-dimensional effects may alter the nonlinear and shock-related features of the blade flow field, it is strongly felt that it is the nonlinear effect which may resolve the data/theory discrepancies in the transonic regime. Although three-dimensionality is certainly present, its effect by itself is probably not important since the two-dimensional aerodynamic input provides reasonable results in the subsonic regime.

It can be argued that future turboprop propellers will be of the propfan type, with swept blades of thin cross section, and hence will be "designed" for minimal transonic nonlinearity effects and shock-free flow. However, even if this situation could be achieved at "design" conditions, the aircraft propulsion system is required to operate at off-design conditions during takeoff, climb, descent and landing approach modes, and thin blade sections operating even slightly off-design will exhibit nonlinear flow distributions with shock formations. These

off-design conditions may well constitute a major fraction of the flight duration for the typical 500-mile missions (or less) envisioned for high speed turboprop application.

There are other possible causes of the disparity between current theories of propeller noise and recent measurements. These include:

- Nonlinear propagation effects due to the impulsive nature of the blade-generated wave forms in the transonic regime
- Other sources such as nonuniform loading noise due to installation-imposed distortions on the propeller
- Fuselage boundary layer refraction of the incident sound
- Shielding of the incident sound by nearby wing surfaces.

Some of these may not apply to all the recent experimental observations acquired by NASA but, nonetheless, are effects which need to be considered in evaluating a given turboprop aircraft installation.

1.2 Objectives

The primary objective of this program has been to provide an improved, unified theoretical model for predicting the noise of high speed propellers which can satisfactorily explain observed experimental trends in the transonic helical Mach number regime (as discussed in Section 1.1). A second objective of this program was to provide preliminary theoretical models for predicting the installation effects on propeller noise. These effects include additional unsteady loading noise due to angle-of-attack, wing and pylon/nacelle interference effects; and aircraft surface reflection, refraction, and shielding. The primary objective focused on an improved understanding of the basic propeller noise generation due to steady loading and volume-displacement (thickness), while the secondary objective focused on additional, installation-induced noise sources and modification of the basic noise source characteristics by the installation (aircraft) environment.

2.0 ANALYSIS AND RESULTS

2.1 Steady Loading Theoretical Model

2.1.1 Introduction

2.1.1.1 Acoustic

The starting point of the acoustic analysis is described by the so-called "Ffowcs Williams-Hawkings Equation" (Reference 2.1.1):

$$4\pi p\ (x,t) = \frac{\partial}{\partial t}\int\left[\frac{\rho U_n}{r|1-M_r|}\right] dS - \frac{\partial}{\partial x_j}\int\left[\frac{p_{ij}\ n_i}{r|1-M_r|}\right] dS \qquad (2.1.1)$$

where the square brackets imply evaluation of their contents at the "source" or "retarded" time τ, given by

$$\tau = t - \frac{r}{c_o}$$

when t = "observer" time. It should be noted that Equation 2.1.1 is quoted omitting the aerodynamic stress or quadrupole terms.

It can be seen that if Equation 2.1.1 is evaluated as is, namely in the time domain; singularities will occur when M_r, the Mach number of the source in the direction of the observer, becomes unity. For this reason, many workers (for example, References 2.1.2 through 2.1.5) have taken the step of Fourier Transforming Equation 2.1.1 into the frequency domain in order to make use of this formulation in the prediction of the sound generated by an open rotor.

Hawkings and Lowson (References 2.1.2 and 2.1.5) employed Equation 2.1.1 in the calculation of sound from open rotors operating at supersonic tip speeds. They assumed that the blades were thin and that the surface integrals could be replaced by integrating over the mean planform area. The thin blade assumption also led to the dropping of the quadrupole term from the original equation.

Hawkings and Lowson compared their predictions with data measured by Hubbard and Lassiter (Reference 2.1.6) and Kurbjun (Reference 2.1.7) and concluded that discrepancies in the comparisons were the result of nonlinear propagation of the acoustic signal. They employed the weak shock theory of Whitham (Reference 2.1.8) to account for this nonlinearity and were, by this means, able to improve the agreement between the reported data and the predicted results by a considerable degree. It is, perhaps, worth noting here that the data were

taken in the plane of rotation of a two- and a three-bladed propeller at distance-to-diameter ratios of 7.66 and 10.00, respectively. In addition, the information available concerning blade section geometry and loading was sparse. Several points made by Hawkings and Lowson do, however, bear repetition here. They observed that at supersonic source speeds it is possible for the source to emit signals from numerous locations which may arrive at the observer simultaneously. They also noted that changes in the lift or thickness distributions across the blade chord have direct and predictable effects upon the acoustic harmonics and that this suggests the possibility of altering the blade profile and aerodynamics to produce an acceptable acoustic spectrum.

Hawkings and Lowson used a cylindrical polar coordinate system in their derivation. They also neglected the effects of forward flight - a reasonable simplification since both sets of data used for their comparisons came from propellers on test stands. In their later paper (Reference 2.1.5) they do perform the extension to forward hub motion, observing that, acoustically, the effect of the hub velocity is equivalent to increasing the rotational speed by the Doppler factor $(1 - M_o \cos \theta)^{-1}$ while simultaneously reducing the observation distance to $r (1 - M_o \cos \theta)$.

The above-discussed approach of Hawkings and Lowson can be traced back to the Lighthill theory of aerodynamic sound (Reference 2.1.9) by means of the work of Ffowcs Williams and Hawkings (Reference 2.1.1).

Taking the same starting point, but following Goldstein (Reference 2.1.10) in the use of generalized Green's Function solutions, Hanson (Reference 2.1.11) defined a space-fixed, locally orthogonal coordinate system, tied to the helicoidal surface swept by the blade pitch change axis as the blade rotates and advances. The advantage of this coordinate system lies in the ease with which conventional airfoil coordinates can be input into the computational scheme.

At the start of this work it was decided to develop and program a linearized, distributed-source, far field, frequency-domain model for steady loading and thickness noise only (following the arguments of Hawkings and Lowson), in which the helicoidal surface coordinate system of Hanson would be employed. It was decided that, following comparisons with data taken in the acoustic near field, extensions to the theory would be formulated to account for near field effects.

2.1.1.2 Aerodynamic

Use of a distributed-source prediction procedure requires knowledge of both spanwise and chordwise distributions of blade loading and thickness. The propfan designs under consideration for application on high speed commercial transport aircraft consist of rotors containing many highly-swept blades, in stark contrast to the two- and four-bladed propellers that can be seen on today's general aviation aircraft. In addition, the aspect ratio (span/chord) of the propfan blade is small by comparison with a conventional propeller. These features combine to produce high values of solidity (chord/spacing) for the blading, especially in the lower portions of the span. In these regions, blade-to-blade interference effects cannot be neglected, and in

effect, the flow field in this region bears closer resemblance to that in a turbomachine than to that experienced by a conventional propeller.

Advances in computational fluid dynamics and in high speed computers in general have led to the development of sophisticated computer codes for solving the nonviscous Euler equations of fluid flow in three dimensions. The first of these to gain general acceptance in the turbomachinery world was written by Denton (Reference 2.1.12). Since the appearance of the original Denton code, many other solvers have appeared (for example, References 2.1.13 and 2.1.14), each offering subtle differences in the assumptions made, the grid employed, and the computational scheme involved. Since viscosity is the only flow phenomenon neglected in these codes, nonlinearities in the flow (such as shock waves) are present in the solution. It was felt, at the start of the work described here, that the combination of a linear acoustic theory with blade loads obtained from a nonlinear aerodynamic solution would provide an excellent basis for prediction of the sound generated by a high speed propfan of the type under consideration for high speed transport applications.

In addition, it was considered that results from a 3D (three-dimensional) flow solution could be used to obtain the fluctuating pressure on a cylindrical surface surrounding the rotor. This pressure could then be Fourier Transformed to provide near field noise levels. The main disadvantage to using this technique was believed to be the amount of detail required to define the flow field adequately. Fine detail requires a large number of grid points, with a corresponding increase in computation time.

2.1.2 Model Development

2.1.2.1 Far Field Acoustic Model

Following the arguments outlined above, it was decided that the helicoidal coordinate system developed by Hanson (Reference 2.1.11) would allow the easier input of blade geometry in standard coordinates. Consequently, the following equation was taken as the starting point for the program development (Reference 2.1.11, Equation 36).

$$\left.\begin{matrix} P_{V_m} \\ P_{L_m} \end{matrix}\right\} = \frac{\rho_o \, c_o^{\,2} \, B \sin\theta \, \exp\left\{ imB \left(\frac{\Omega_D r}{c_o} - \frac{\pi}{2} \right) \right.}{8\pi \left(\frac{V}{D} \right) \left(1 - M_x \cos\theta \right)} \int_0^1 M_r^{\,2} \, e^{\,i \, (\phi_o + \phi_s)}$$

$$* J_{mB} \left(\frac{mBz \, M_T \sin\theta}{1 - M_x \cos\theta} \right) \left\{ \begin{matrix} - k_x^{\,2} \, t_b \, \psi_V \left(k_x \right) \\ \\ i \, k_y \left(\frac{C_L}{2} \right) \psi_L \left(k_x \right) \end{matrix} \right\} dz \qquad (2.1.2)$$

In this equation:

P_{Vm} = volume displacement or thickness source,

P_{Lm} = steady loading (lift force) source,

θ = emission angle

Ω_D = $\Omega/(1 - M_x \cos\theta)$ where Ω = rotational frequency in radians per second

r = observation distance

k_x and k_y are dimensionless chordwise wave numbers given by:

$$\left.\begin{aligned} k_x &= \frac{2mB\ B_D\ M_T}{M_r\ (1 - \cos\theta)} \\ \text{and} \\ k_y &= \frac{2mB\ B_D}{z\ M_r} \left(\frac{M_r^2 \cos\theta - M_x}{1 - M_x \cos\theta} \right) \end{aligned}\right\} \qquad (2.1.3)$$

B_D = chord/diameter ratio.

The parameters ψ_V (k_x) and ψ_L (k_x) define the chordwise thickness and loading distributions in the frequency domain. They are given by:

$$\left.\begin{aligned} \psi_V\ (k_x) &= \int_{-\frac{1}{2}}^{+\frac{1}{2}} H\ (X)\ e^{ik_x X}\ dX \\ \text{and} \\ \psi_L\ (k_x) &= \int_{-\frac{1}{2}}^{+\frac{1}{2}} f_L\ (X)\ e^{ik_x X}\ dX \end{aligned}\right\} \qquad (2.1.4)$$

and are Fourier Transforms of the chordwise normalized thickness and loading distributions, respectively.

The phase shifts, ϕ_S and ϕ_O, resulting from sweep and offset respectively, are given by:

$$\left.\begin{aligned} \phi_s &= \frac{2m\ B\ M_T}{M_r\ (1 - M_x \cos\theta)}\ \frac{MCA}{D} \\ \text{and} \\ \phi_o &= \frac{2mB}{zM_r}\left(\frac{M_r^2 \cos\theta - M_x}{1 - M_x \cos\theta}\right)\frac{FA}{D} \end{aligned}\right\} \qquad (2.1.5)$$

MCA and FA, or midchord alignment and face alignment, are defined in Figure 1. They describe the deviation of the blade section midchord from the helicoid swept out by the pitch change axis.

It may be worth observing here that Hanson's observation; namely, that the Hawkings and Lowson theory can be recovered exactly from Equation 2.1.2 by setting the flight Mach number, M_x, to zero; should be treated with caution. The factor k_y above is used to split the lift on the blade into the thrust and drag components employed by Hawkings and Lowson and, essentially, uses the helicoidal vector diagram (Figure 1) to define the sine and cosine of the angle β_L. This relation should be preserved, and thus, the decomposition of the lift force into its components should be carried out before M_x is set to zero.

An alternative method of establishing the relationship between the Hawkings and Lowson theory and Equation 2.1.2 is to follow the approach suggested by Hawkings and Lowson in a later paper (Reference 2.1.5). They observed that the effect of forward flight on the acoustics of an open rotor is equivalent to deriving the equation for a stationary source, then increasing the rotational speed by the factor $(1 - M_x \cos\theta)^{-1}$ while simultaneously reducing the observation distance (r) to $r\ (1 - M_x \cos\theta)$. It should be noted that the reduction in observation distance is applied to the amplitude terms only.

In the computer code delivered under this Contract, an alternative form for the chordwise wave number k_y has been included as an option. In this formulation:

$$k_y = \frac{2mB\ B_D\ M_T}{(1 - M_X \cos\theta)}\left(\cos\beta_p \cos\theta - \frac{(1 - M_X \cos\theta)}{zM_T}\right)$$

where β_P is the blade pitch angle and is defined in Figure 1.

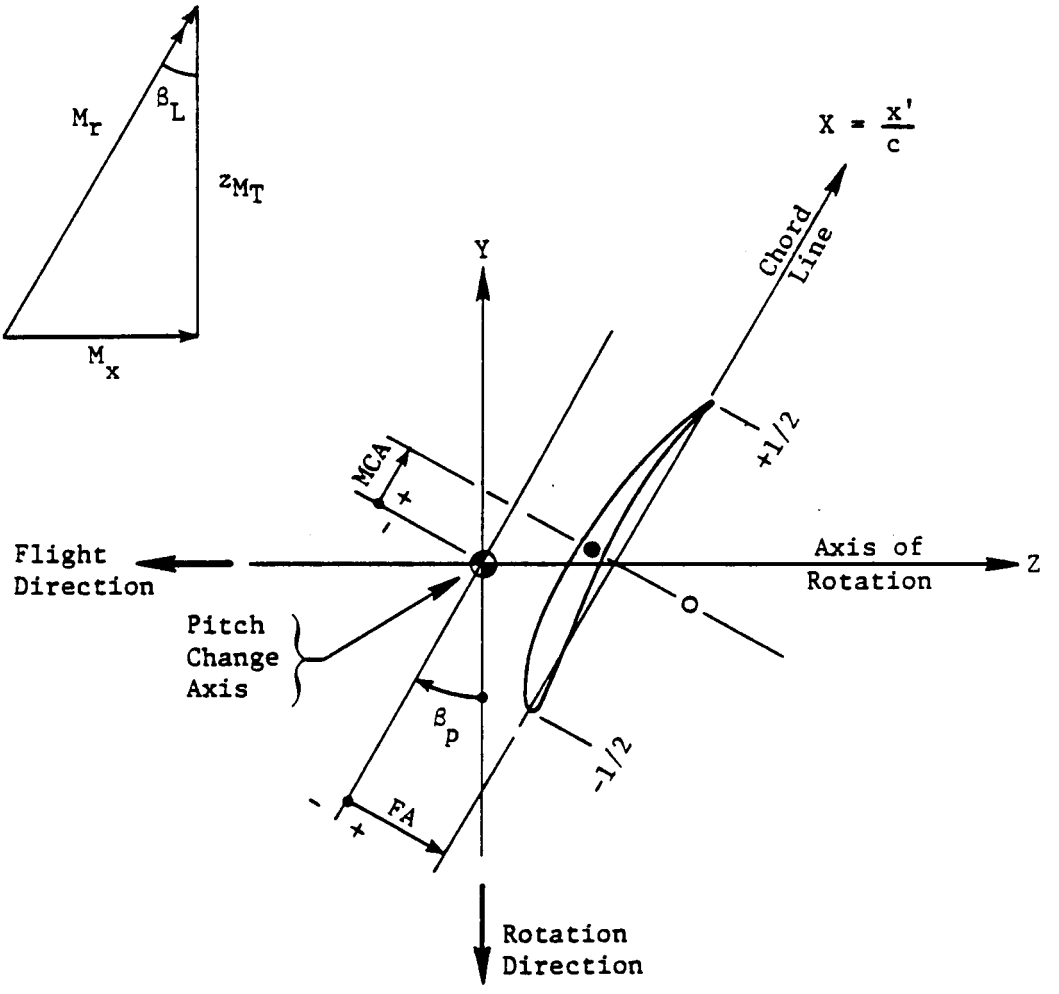

FA = Face Alignment (Offset or Dihedral)
MCA = Midchord Alignment (Sweep)

Suction (Camber Side) Surface and Pressure (Face Side) Surface Coordinates (y'/c)ss and (y'/c)ps Specified as a Function of X = x'/c from X = -0.5 to X = +0.5

Figure 1. Definition of MCA and FA.

This expression uses the blade angle, β_P, rather than the helicoidal angle, β_L, to resolve the lift on the blade section into its thrust and drag components and, generally, has been found to give better agreement between prediction and data than is shown by the use of Equation 2.1.3.

2.1.2.2 Aerodynamic Model

In order to use Equation 2.1.2 to predict the tone noise generated by an open rotor, it is necessary to define both the thickness distribution of the blading and also the lift on the blades in both the chordwise and spanwise directions.

At the outset of this work, it was decided that, in view of the fact that high speed propfan blading will experience relative Mach numbers in excess of unity leading to nonlinearities such as shock waves in the flow, loading distributions generated by a 3D Euler equation flow solver should be used.

The Euler equation (the Navier-Stokes equations, minus the viscous terms) can be written as:

$$\rho \frac{Du_i}{Dt} \equiv \rho \frac{\partial u_i}{\partial t} + \rho u_k \frac{\partial u_i}{\partial x_k} = - \frac{\partial p}{\partial x_i} + f_i \qquad (2.1.6)$$

The general approach for solving these equations in turbomachinery applications has been to follow the time-marching technique of Denton. Since Denton's original work, many alternative computational schemes have been devised, but they are all designed for the basic problem of axial turbomachinery; the flow is confined within an annular duct. In order to extend these schemes to the case of highly swept propfan blading, two options are available. First, an existing code may be adapted by removal of the casing boundary to a radius much larger than that of the blade tip, to simulate an open rotor. Alternatively, the propfan analysis may be considered as a problem in its own right, and the calculation procedure and computational grid developed to deal exclusively with open rotor geometries.

For the purposes of this study, one example of each type of code was available. The first, developed at GE-CRD (GE Corporate Research and Development) is based on a code used extensively within GE for turbomachinery applications. It employs a Jameson computational algorithm (Reference 2.1.14) and is described in Reference 2.1.15. The second code, designated NASPROP-E, was developed under contract from NASA Lewis Research Center and is described in detail in References 2.1.16 and 2.1.17. An early version (circa 1983) of this code was made available to GE at the start of this project; and it, together with the code developed by GE-CRD was installed on a GEAE (GE Aircraft Engines) minicomputer. As illustrated in Figures 2 and 3, the computational grids employed by the two codes are radically different - it was felt that the results of exercising the two codes for the same propfan case would be of interest.

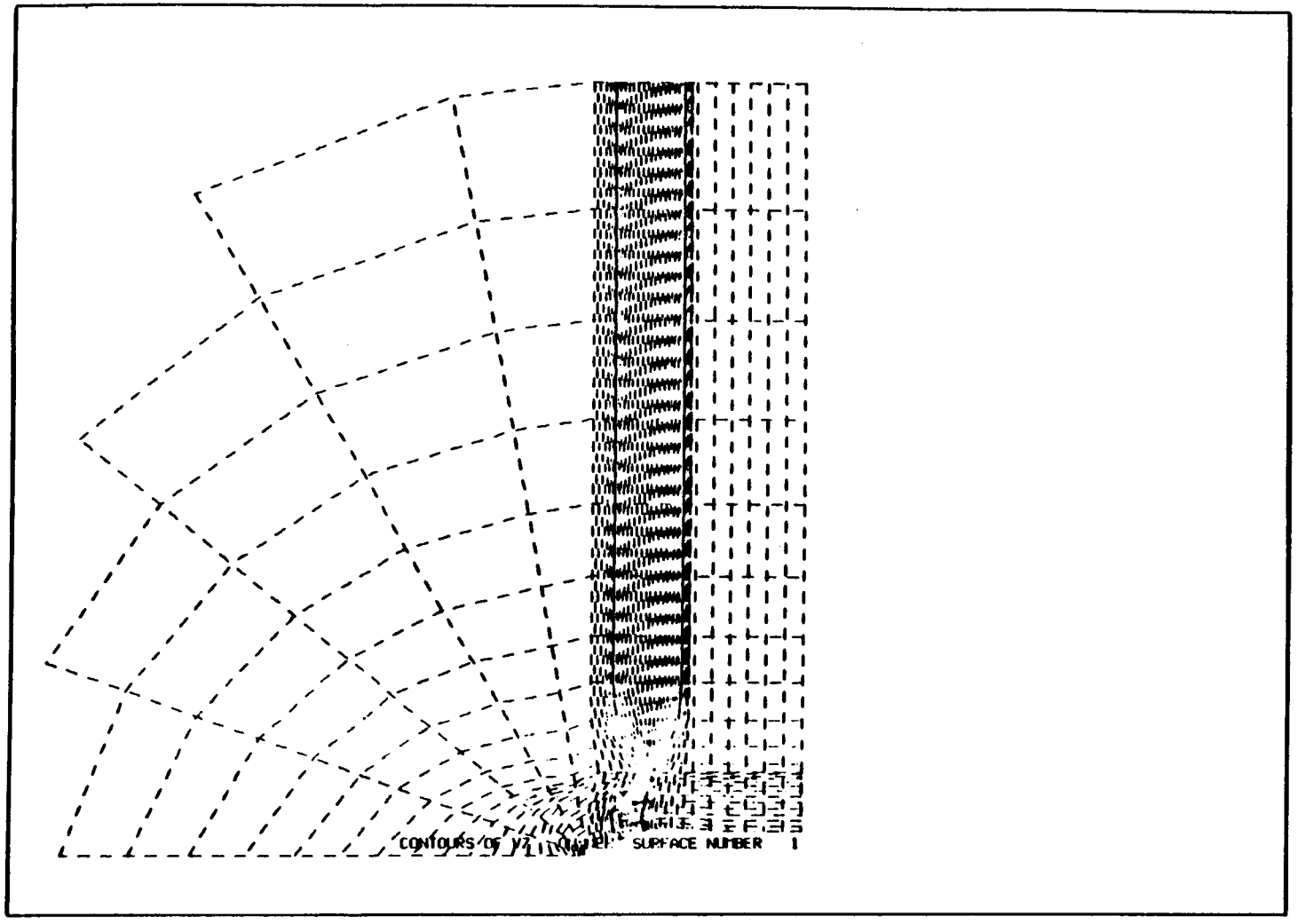

GRID USED FOR NASPROP-E CALCULATION OF SR-3

M_∞=0.8, J=3.06, $\Lambda_{3/4}$ =61.3^0

24750 Nodes, 66 "Axial" (JLE=18, JTE=48)

25 "Radial", 15 "Tangential"

Figure 2. Computational Grid - NASPROP-E.

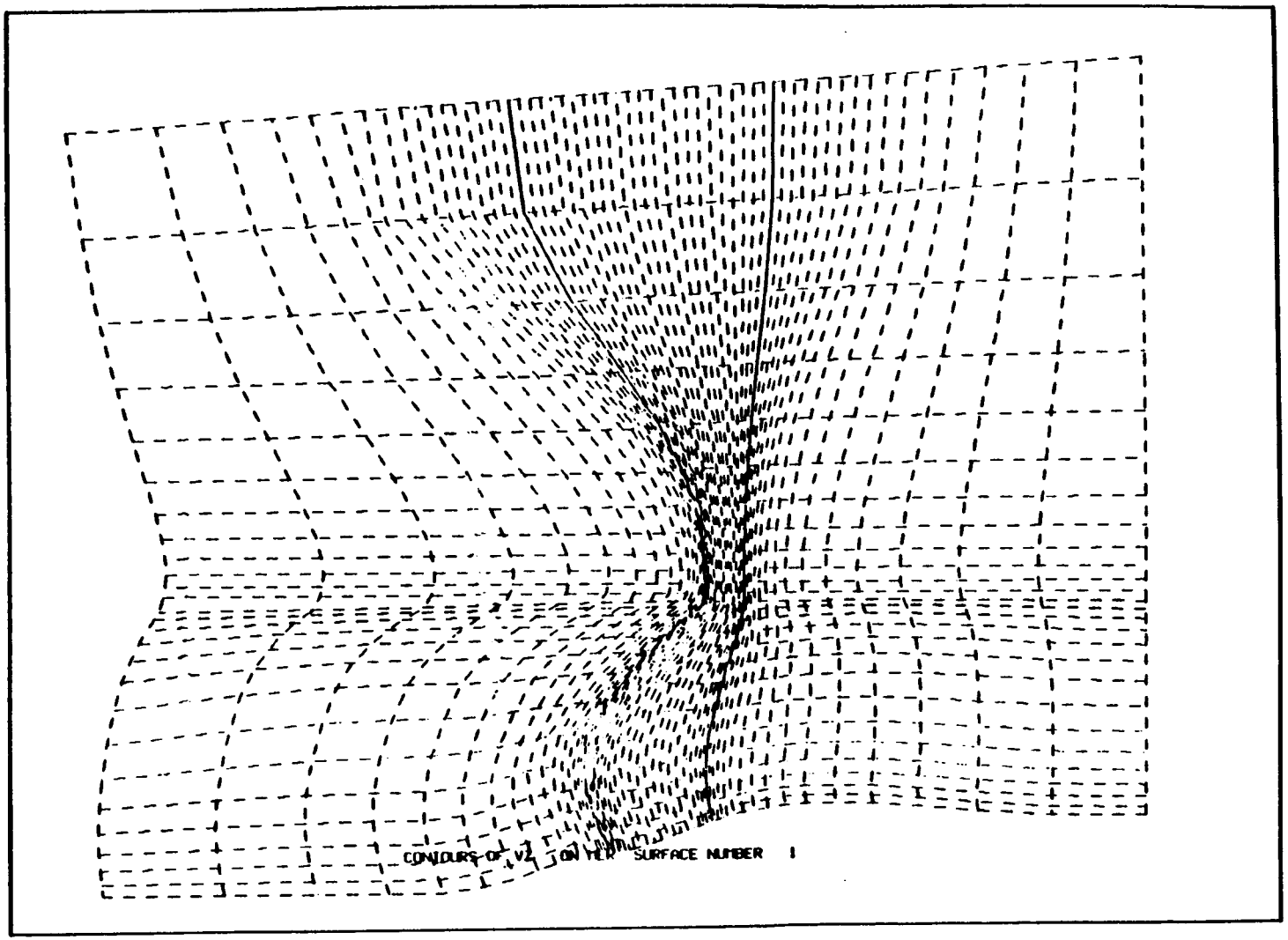

GRID USED FOR GE-CRD CALCULATION OF SR3

M_∞=0.8, J=3.06, $\beta_{3/4}$=61.3°

27081 Nodes, 59 "Axial" (JLE=19, JTE=43)

27 "Radial", 17 "Tangential"

Figure 3. Computational Grid - GE-CRD.

2.1.2.3 Blade-Loading Parameters

Blade chordwise loading is input as a normalized function $f_L(X)$, (Equation 2.1.4). This is defined as:

$$\left.\begin{aligned} \psi_L(k_x) &= \int_{-\frac{1}{2}}^{+\frac{1}{2}} f_L(X)\, e^{ik_x X}\, dX \\ \text{Also,} \quad \psi_L(o) &= \int_{-\frac{1}{2}}^{+\frac{1}{2}} f_L(X)\, dX = 1.0 \end{aligned}\right\} \qquad (2.1.7)$$

Now; from the three-dimensional aerodynamic flow solver we can obtain a chordwise distribution of pressure differential $\Delta p = p_{ps} - p_{ss}$ as a function of x.

We thus have:

$$L' = \int_{x_{le}}^{x_{te}} \Delta p\,(x)\, dx \qquad (2.1.8)$$

Write the lift coefficient as

$$C_L = \frac{L'}{\frac{1}{2}\rho_o V_r^2\, c}$$

where:

$V_r = a_o M_r$

c = blade chord.

Then

$$L' = \frac{1}{2} \rho_o V_r^2 \, c \, C_L = \int_{x_{le}}^{x_{te}} \Delta p \, (x) \, dx$$

or

$$1 = \int_{-\frac{1}{2}}^{+\frac{1}{2}} \frac{\Delta p \, (X)}{\frac{1}{2} \rho_o V_r^2 \, C_L} dX \qquad (2.1.9)$$

Hence,

$$f_L \, (X) = \frac{\Delta p \, (X)}{\frac{1}{2} \rho_o V_r^2 C_L} \qquad (2.1.10)$$

The power absorbed by the rotor can be evaluated from the above as follows:

At each radial section,

$$L' = \frac{1}{2} \rho_o V_r^2 \, c \, C_L$$

$$= \frac{\gamma}{2} p_o M_r^2 \, c \, C_L$$

The lift direction relative to the direction of rotation is given by θ_L (per sketch below).

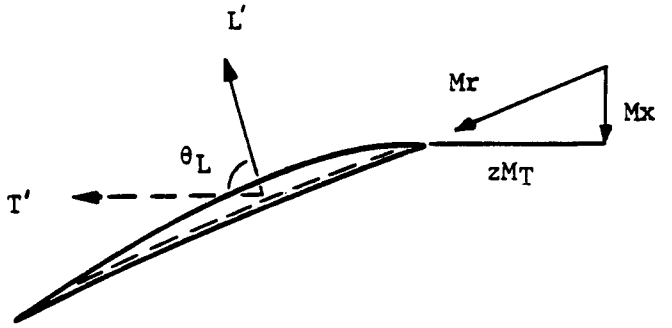

Sketch 2.1 (See Also Figure 1)

The torque per unit span is thus:

$$T' = Br\, L' \cos\theta_L$$

where,

B = number of blades

r = radius of section of interest.

The power is then given by:

$$W = \Omega \int_{hub}^{tip} Br\ L'\ \cos\theta_L\ dr$$

$$= \Omega \int_{hub}^{tip} Br\ M_r^2\ \frac{\gamma}{2}\ c\ C_L\ \cos\theta_L\ dr$$

If we write $\cos\theta_L = \frac{M_x}{M_r}$, $z = \frac{r}{r_{tip}}$, this becomes

$$W = \frac{\Omega}{8} \gamma p_o B D_T^3 \int_{hub}^{tip} \left(M_r M_x C_L \frac{c}{D_T} \right) z \, dz$$

If it is assumed that M_x is a constant, and writing

$$M_T = \frac{\Omega D_T}{2a_o}$$

this becomes:

$$W = \frac{\gamma}{4} p_o a_o D_T^2 M_x M_T B \int_{hub}^{tip} M_r C_L \frac{c}{D_T} z \, dz \qquad (2.1.11)$$

From the above, it can be seen that the results of the three-dimensional Euler computer code can be employed in both the spanwise and chordwise directions, and this is the approach followed in the code developed under this contract. However, it is also possible that, bearing in mind the long term objective of the development of simplified analytical models for the chordwise loading parameters, a hybrid approach could be adopted in which the normalized chordwise loading distribution would be obtained from the aerodynamic flow solution as described above, while the loading distribution in the spanwise direction would be input separately.

Turbomachinery designers tend to describe blade loading in terms of "swirl"; the component of tangential velocity in the absolute frame of reference. It is a measure of the work put into the fluid. Propfan references, on the other hand, use "elemental power coefficient" in this context. These two are related as follows.

Power Coefficient:

$$C_p = \frac{P}{\rho_o \, n^3 \, D_T^5}$$

where

P = power

n = rps

D_T = diameter

ρ = density

Consider an element of fluid passing through the rotor. The work added to the element is:

$$dP = d(\Omega Q) = \Omega\Delta(rC_u)d\dot{m}$$

where

C_u = Swirl

and

$$d\dot{m} = \rho_o V_o(2\pi r dr)$$

Assume that, for a propeller, $(rC_u)_{in} = 0$.

Then,

$$\frac{dP}{dr} = \rho_o V_o 2\pi\Omega r^2 C_u$$

The elemental power coefficient,

$$\frac{dC_P}{dz} = \frac{r_T}{\rho_o \, n^3 \, D_T^5} \rho_o \, V_o \, 2\pi\Omega r^2 \, C_u$$

Writing

$$U_T = \pi n D_T, \text{ and } \theta = \frac{C_u}{U} = \frac{C_u}{zU_T},$$

it can be shown that this equation reduces to:

$$\theta = \frac{2\ M_T}{\pi^4 z^3\ M_x} \frac{dC_p}{dz}$$

$$= \frac{2}{\pi^3 z^3 J} \frac{dC_p}{dz}$$

where J is the advance ratio.

θ is referred to as a swirl coefficient; or, alternatively, a work coefficient. It is input to the noise prediction code and used to calculate section lift coefficients as follows.

Given

$$L' = \int_{x_{le}}^{x_{te}} \Delta p\ dx = K\left(\Delta r C_u\right) \qquad (2.1.15)$$

and

$$\Omega\Delta\left(rC_u\right) = \Delta\left(a_o z M_T C_u\right);$$

writing

$$\theta = \frac{C_u}{a_o\ z\ M_T}$$

and assuming zero inlet swirl as before, gives:

$$\Omega\Delta\,(rC_u) = a_o^2 z^2 M_T^2 \theta\,;$$

and

$$\frac{L'}{c} = \int_0^1 \Delta p \; d\left(\frac{x}{c}\right) = \frac{a_o^2 \; z^2 \; M_T^2 \quad \theta}{\Omega c}$$

Now:

$$K = \frac{2\pi \; r\rho_o V_x \; \Omega}{\Omega r \; B \; \cos\theta_L}$$

from the above, hence

$$\frac{L'}{c} = \frac{2\pi r \; \rho_o V_x}{c \; \Omega r \; B \; \cos\theta_L} \quad z^2 \; M_T^2 \; a_o^2 \quad \theta$$

which yields, after some rearrangement,

$$\frac{L'}{cp_o} = \frac{\gamma \; z \; M_T \; M_r \quad \theta}{\sigma}\,;$$

where "σ," the solidity, is given by:

$$\sigma = \frac{cB}{2\pi r}\,.$$

Thus,

$$\int_0^1 \frac{\Delta p}{p_o} \, d\left(\frac{x}{c}\right) = \frac{L'}{cp_o} = \frac{\gamma \, z \, M_T \, M_r \, \theta}{\sigma} \qquad (2.1.16)$$

and the lift coefficient,

$$C_L = \frac{\frac{L'}{c}}{\frac{1}{2} \rho_o V_r^2} \qquad (2.1.17)$$

$$= \frac{2z \, M_T \, \theta}{\sigma \, M_r} .$$

The lift coefficients used in the noise code in the evaluation of Equation 2.1.2 are obtained as described above.

2.1.2.4 Near Field Acoustic Model

In the theoretical development leading to the formulation of Equation 2.1.2, the standard far field approximation for R (the source-to-observer distance) was employed. This has the effect of locating the sound source, for radiation purposes, at the center of the propeller disk and is eminently reasonable when the observer is in the acoustic far field.

In the acoustic near field, however, this compact source assumption is less reasonable; individual points on the blades can be considered as acoustic radiators in their own right. The inclusion of exact source-to-distance terms in the theoretical derivation greatly increases the complexity of the analysis, as can be seen in the fuselage diffraction/refraction formulation of Section 2.3 hereof.

At the outset of this program, it was felt that the "stationary phase" approach of Hawkings and Lowson (Reference 2.1.2) could be employed in this regime. This result is an approximation for large values of mB and is valid irrespective of the location of the observer. It is thus applicable in the acoustic near field. The result shows that the main contribution to the integrals over the blade surface comes from the vicinity of a so-called stationary point. In this instance, this is given by:

$$r_s = \frac{R_o a_o}{\Omega y}, \quad \theta = \frac{3\pi}{2}$$

where r_s is the stationary radial location, θ is the azimuthal location of the source point, and R_o is the distance from the center of rotation to the observer.

In addition, as an alternative approach, it was proposed that, since the aerodynamic Euler code calculations essentially evaluate the pressure distribution on a cylindrical surface surrounding the rotor, it should be possible to estimate the near field noise directly from the flow solution. The main disadvantage to this approach is the necessity of obtaining a solution with a sufficiently fine resolution in terms of grid density in the blade-to-blade direction. It was felt, however, that with advances in supercomputers, obtaining these solutions in a reasonable amount of computing time was not totally infeasible.

As a preliminary exercise, data/theory comparisons were made using the far field radiation model already in the computer code. Results were encouraging, leading to the belief that development of a sophisticated near field model was, perhaps, not as imperative a task as had at first been envisaged.

It was, thus, decided to adopt the semiempirical approach used by Sulc, et al. (Reference 2.1.18) for conventional propellers; and to apply such modifications as seemed appropriate with regard to current experience.

Sulc, et al. found that the near field noise of a conventional propeller can be predicted reasonably well utilizing a far field formulation (such as, Gutin's equation) if the source-to-observer distance is replaced by the distance between the observer and an equivalent near field source.

In the far field, the range is given by the distance from the observer to the center of rotation of the propeller, R_o. The equivalent near field range is given in Reference 2.1.18 as:

$$R_e = R_o - 0.7\, r_T$$

where

r_T = tip radius.

Effectively, this is assuming that the propeller noise sources lie on the surface of a sphere, centered at the center of the propeller, and having a radius of $0.7\, r_T$.

However, it may be speculated that the effective source radius will be some function of the source frequency (or wavelength) with the effective radius becoming smaller as the frequency increases.

With this in mind, let us write:

$$R_e = R_o - K\left(\frac{\lambda}{r_T}\right) r_T$$

where

λ = wavelength of the sound source (propeller);

K = a constant whose value is to be determined.

Now:

$$\frac{\lambda}{r_T} = \frac{2\pi\ c_o}{\Omega m B r_T} = \frac{2\pi}{mBM_T}$$

where

M_T = tip Mach number.

If we follow Reference 2.1.18 and state that for a conventional four-bladed propeller with a tip Mach number, M_T, of 0.8,

$$\frac{K\lambda}{r_T} \cong 0.7$$

we have

$$K \cong \frac{0.7\ mBM_T}{2\pi} = \frac{0.7 \times 4 \times 0.8}{2\pi}$$

$$K \cong \frac{0.7}{2}$$

Further, assuming that this "constant" is general,

$$R_e \cong R_o - \frac{0.7\ \pi}{mBM_T}\ r_T$$

This shows that as the frequency (represented by the number of blades and the harmonic number m) increases, the effective source radius becomes smaller and the effective range approaches the far field limit.

The effects of forward flight can be included by adopting the procedure described in Reference 2.1.2. The frequency is multiplied by a factor

$$\frac{1}{C_v},$$

where

$$C_v = 1 - M_o \cos \theta_e$$

and

M_o is the flight Mach number

θ_e is the emission angle.

In addition, the source-to-observer distance, R_e, is reduced by a factor C_v, resulting in

$$R_e \cong C_v R_o \left[1 - \frac{0.7 \pi C_v}{mB M_T}\left(\frac{r_T}{C_v R_o}\right)\right]. \qquad (2.1.19)$$

On simplification, this shows that the "near field effect" can be expressed as:

$$\Delta dB_{nf} \cong - 20 \log_{10}\left(\frac{R_e}{C_v R_o}\right). \qquad (2.1.20)$$

For an 8-bladed rotor operating at a tip Mach number equal to the flight Mach number of 0.8, the near field corrections (calculated at a tip clearance of 0.8 times the diameter), range from 1.23 dB at the first BPF (Blade Passing Frequency) harmonic to 0.23 dB at the fifth harmonic.

It is felt that this approach is reasonable but that further study is required to determine the "constant" K with a higher degree of confidence.

2.1.3 Data/Theory Comparisons (Steady Loading and Thickness Model)

2.1.3.1 Aerodynamic

In the absence of detailed measurements of the aerodynamic flow field around a high speed propfan, direct comparisons between the flows calculated by the three-dimensional Euler codes and that achieved in real life are not feasible. An indirect comparison, showing the spanwise variation of the elemental power coefficient, can be seen in Figure 4 which compares data from Reference 2.1.19 with values obtained from the results of 3D Euler calculations of the flow field of the SR-3 propfan at its design point. Before hasty conclusions are drawn from the comparison, it should be emphasized that at the time when these calculations were made, both flow codes were at a relatively early stage in their development. Certain anomalies which may be apparent in results presented here have since been corrected.

Examination of Figure 4 shows the two aerodynamic codes to have considerably higher values of elemental power coefficient (especially toward the tip of the blade), than do the measured data. An explanation for this is provided in Figure 5, wherein the same spanwise information is plotted in the form of swirl coefficient. Both aerodynamic codes show finite values of swirl at a z-value of unity, implying that the tip of the blade is carrying some load. The conversion from swirl coefficient to elemental power coefficient is (from Section 2.1.2.3, Equation 2.1.14)

$$\theta = \left(\frac{2}{\pi^3 z^3 J}\right)\frac{dC_p}{dz}$$

or, by rearrangement,

$$\frac{dC_p}{dz} = \frac{\pi^3 z^3 J}{2}\ \theta .$$

From this it can be seen that small differences in swirl coefficient toward the tip of the blade will produce (through the Factor z^3) much larger discrepancies in dC_p/dz than would be observed for the same swirl coefficient differential located toward the hub region.

It was noted during this investigation that calculations of absorbed power by means of the equations sketched out in Section 2.1.2.3 using the swirl coefficients obtained from the aerodynamic flow codes did not necessarily produce results in agreement with measurements. It was decided to assume that the predicted distribution represented the physics with regard to shape, but the levels should be adjusted by a constant factor of $SHP_{measured}/SHP_{predicted}$ for each case under consideration. The values of lift coefficient used to calculate the steady-loading noise harmonics reflect this adjustment.

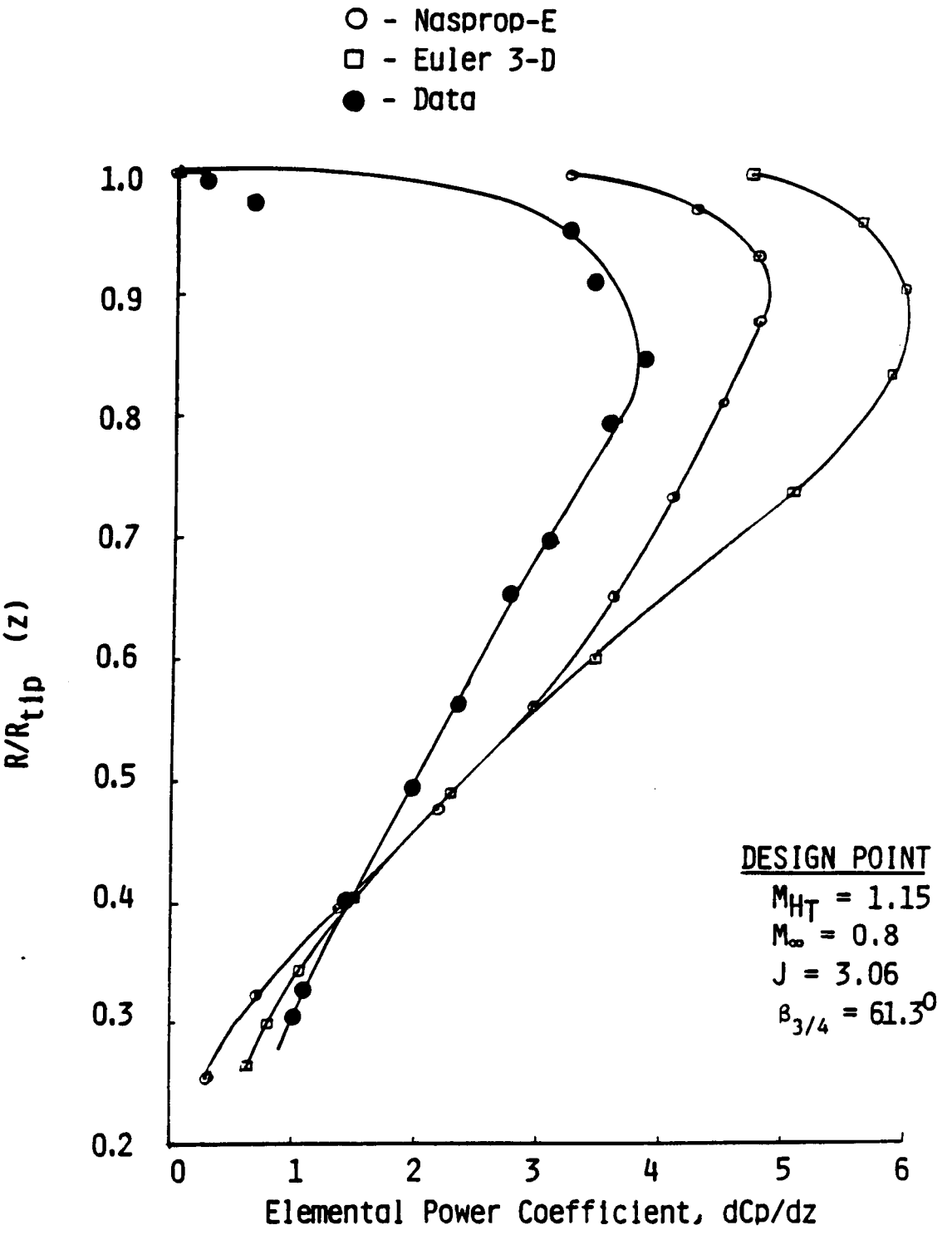

Figure 4. Comparison of dCp/dz.

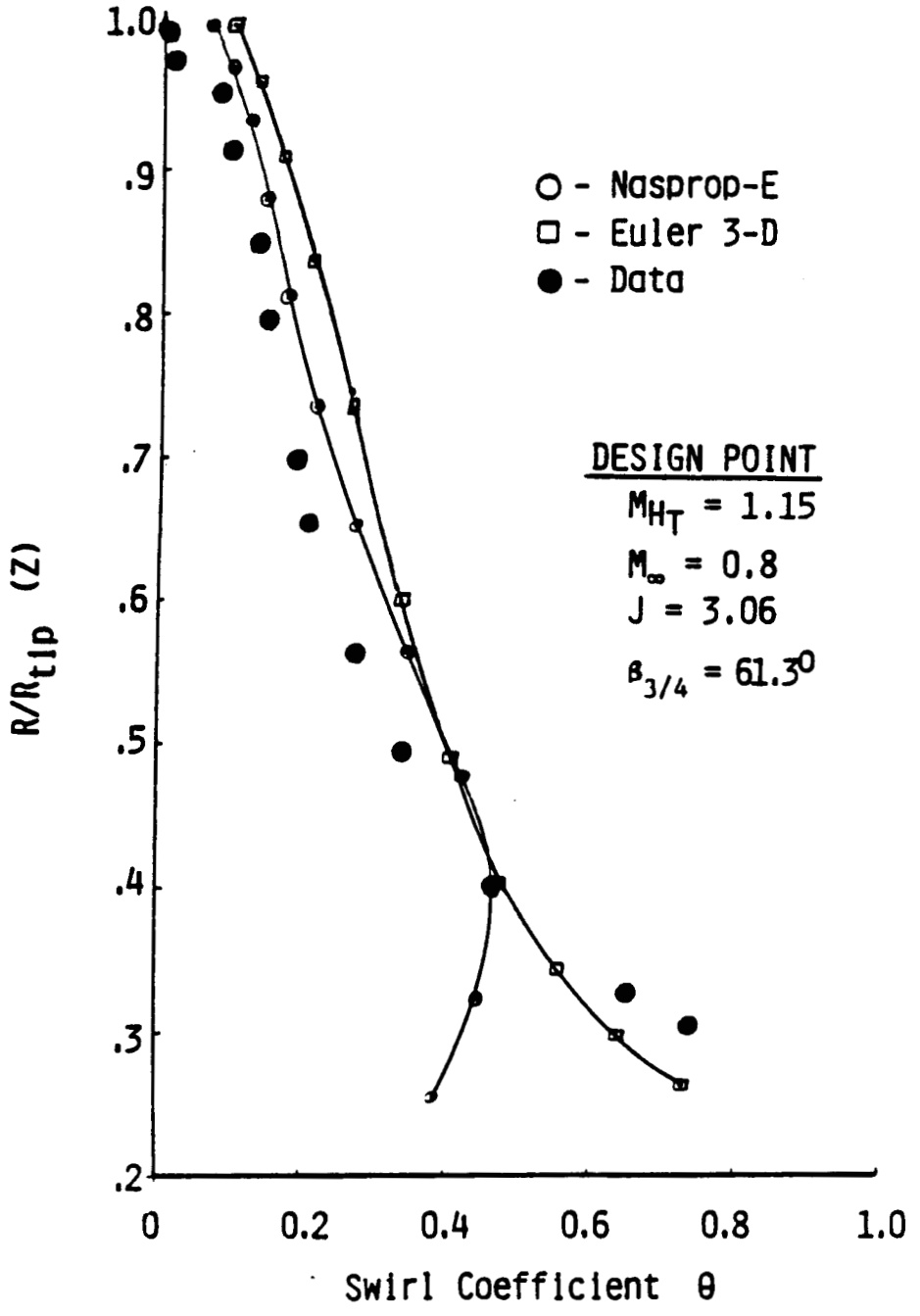

Figure 5. Propfan Exit Swirl Coefficient Distribution Comparison.

The second input required from the aerodynamic solution is the normalized chordwise load function $f_L(X)$, defined in Equation 2.1.10 as:

$$f_L(X) = \frac{\Delta p(X)}{\frac{1}{2}\rho_o V_r^2 C_L}.$$

Figures 6 through 8 show examples of this function, which were calculated for the design point of the SR-3 propfan by the two 3D Euler solvers available. The presence of two NASPROP-E solutions reflects the utilization of a better estimate of blade geometry in the solution used to generate Figure 7. It will be noted that, whereas, all three solutions give chordwise distributions in the tip region that can be described as rectangular; toward the hub there is a divergence from this pattern. This divergence is most pronounced in Figure 8, generated from the GE in-house solution. Comparisons with later figures indicate that the location and magnitude of the peaks in the loading distribution correspond to the location and strength of the shock pattern computed on the blades by the two computer codes. In terms of the blading acoustics, it would be anticipated that the rectangular distribution at the tip would have greater significance than the distorted distribution at the hub.

Figures 9 through 12 show contours of relative Mach number on the surface of the SR-3 blade at its design point, as calculated by the two codes. These, together with Figures 13 and 14 (which demonstrate the contours in the hub blade-to-blade passage), go some way toward explaining the differences in Figures 7 and 8. For example, the supersonic relative flow calculated by NASPROP-E in the hub passage is confined to two isolated "bubbles," whereas in the GE calculation, there is a region of supersonic flow extending across the blade passage. It is the presence of these large regions of supersonic relative flow in the GE prediction that gives rise to the distorted character of the normalized chordwise load distribution.

One further question concerning the available flow solutions surfaced during this investigation. Because of the large amounts of computer time required to obtain a converged solution from scratch, the standard operating procedure that was employed was to obtain a converged solution at the design point of the propfan, and use this solution as the starting point for the various "off-design" cases required. Figure 15 portrays the radial variation of the circumferential average of static pressure along the grid lines corresponding to the leading and trailing edges of the blading, and extending out into the region beyond the tip of the blades. This solution is from the NASPROP-E program calculation of the SR-3 at its design point and is regarded as a converged result. It will be noted that the limiting value is unity; this is a function of the normalization system used in the code. The tip of the blades is denoted by the R = 0.5 grid line. Figures 16 through 18 show equivalent plots for different values of helical tip Mach number, all of which took the solution of Figure 15 as the starting point. These solutions were all obtained for constant advance ratio J = 3.06, thus the change in helical tip Mach number implies changes in axial and rotational Mach numbers to maintain the value of J. It can be seen that, in the region outside the blades, the static pressure "gradient" from blade tip

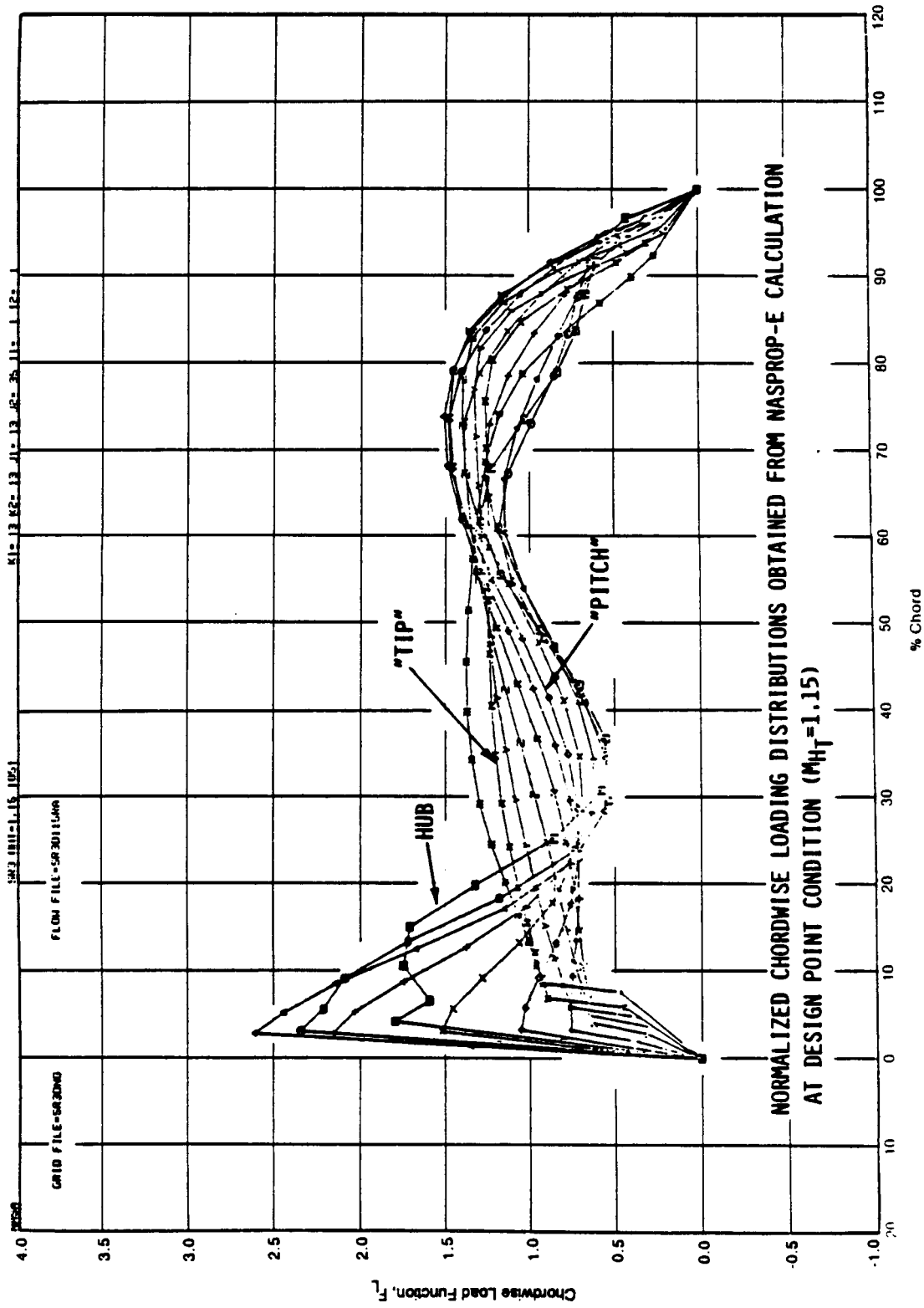

Figure 6. Chordwise Loading - NASPROP-E (1).

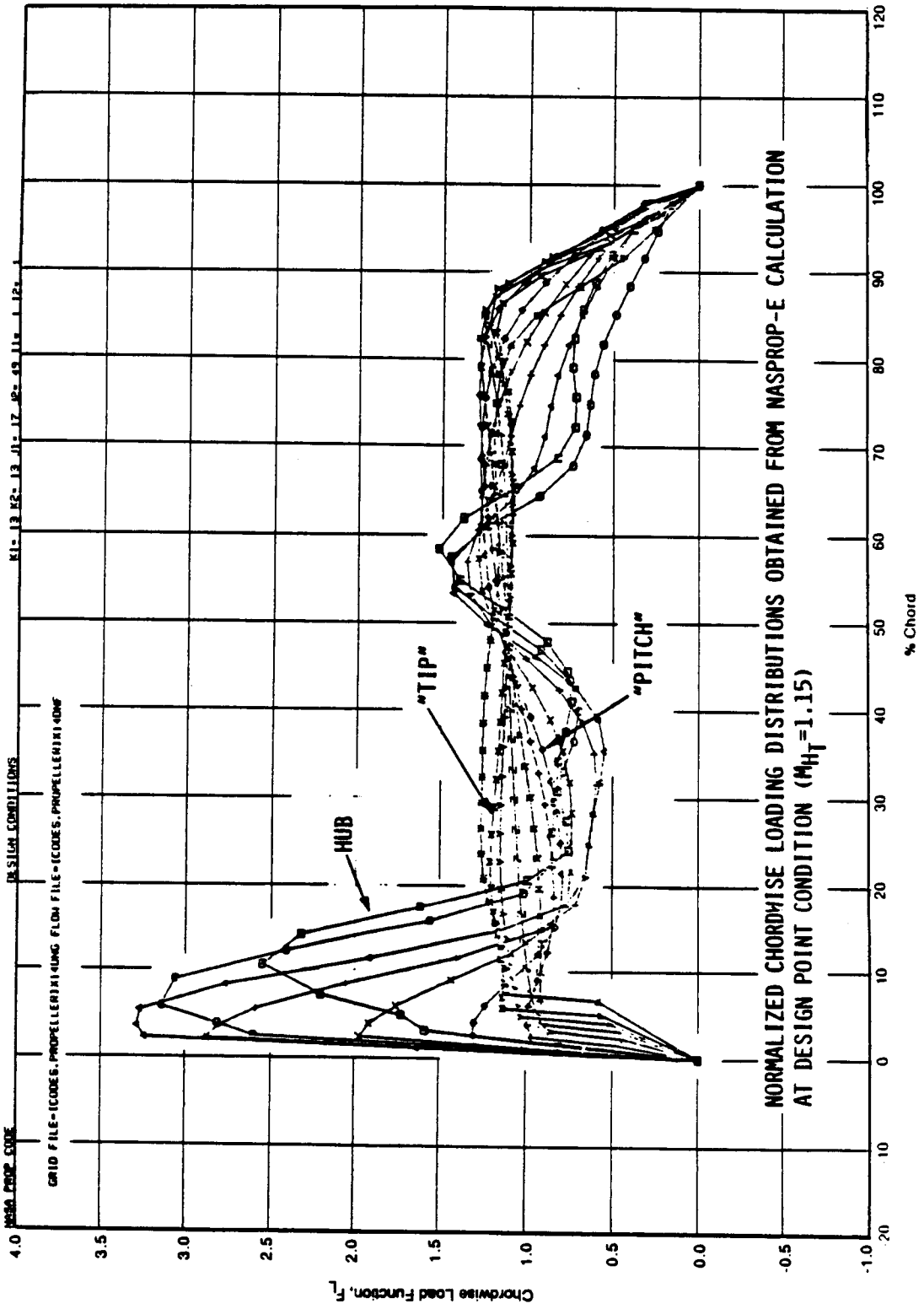

Figure 7. Chordwise Loading - NASPROP-E (2).

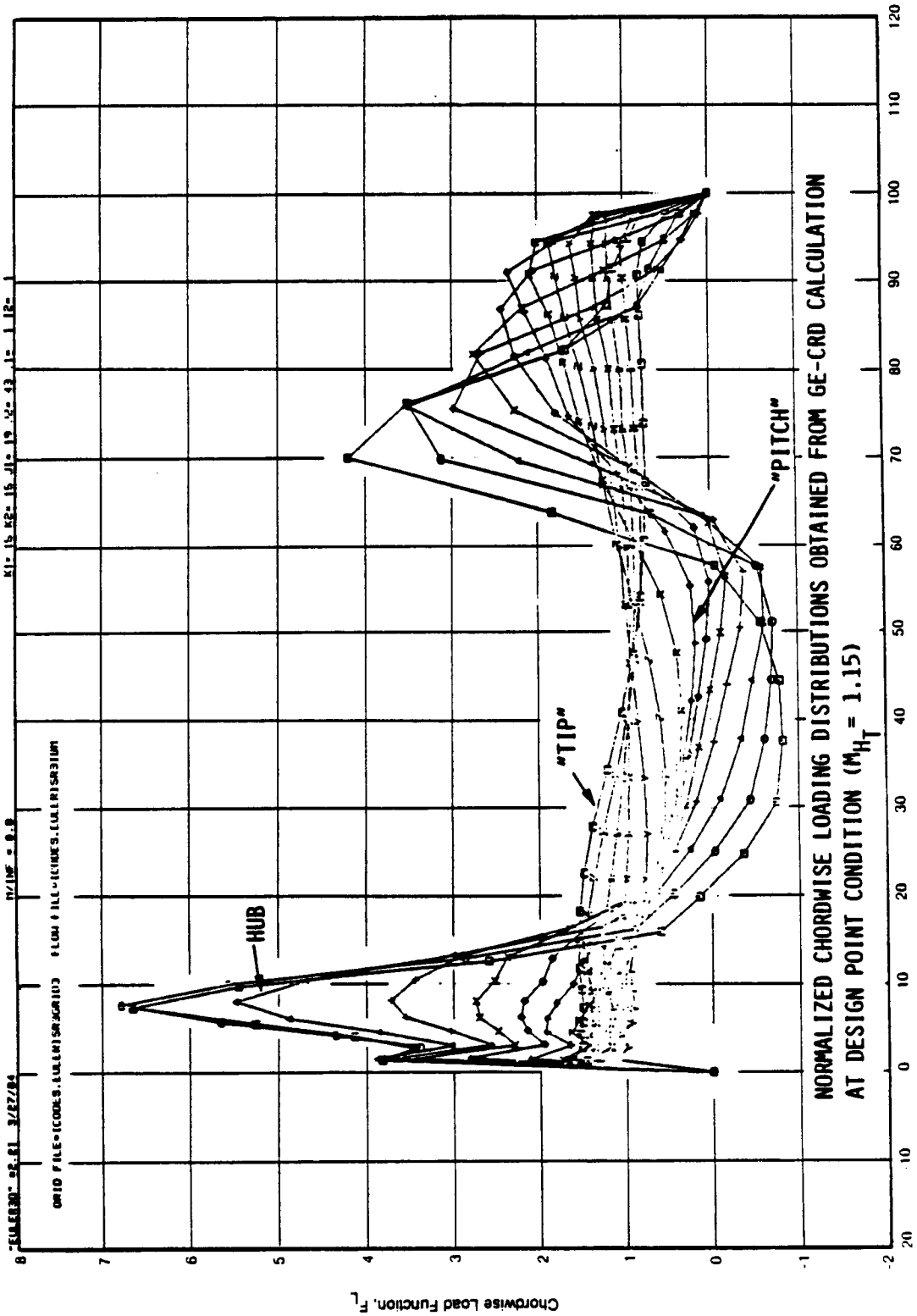

Figure 8. Chordwise Loading - GE-CRD.

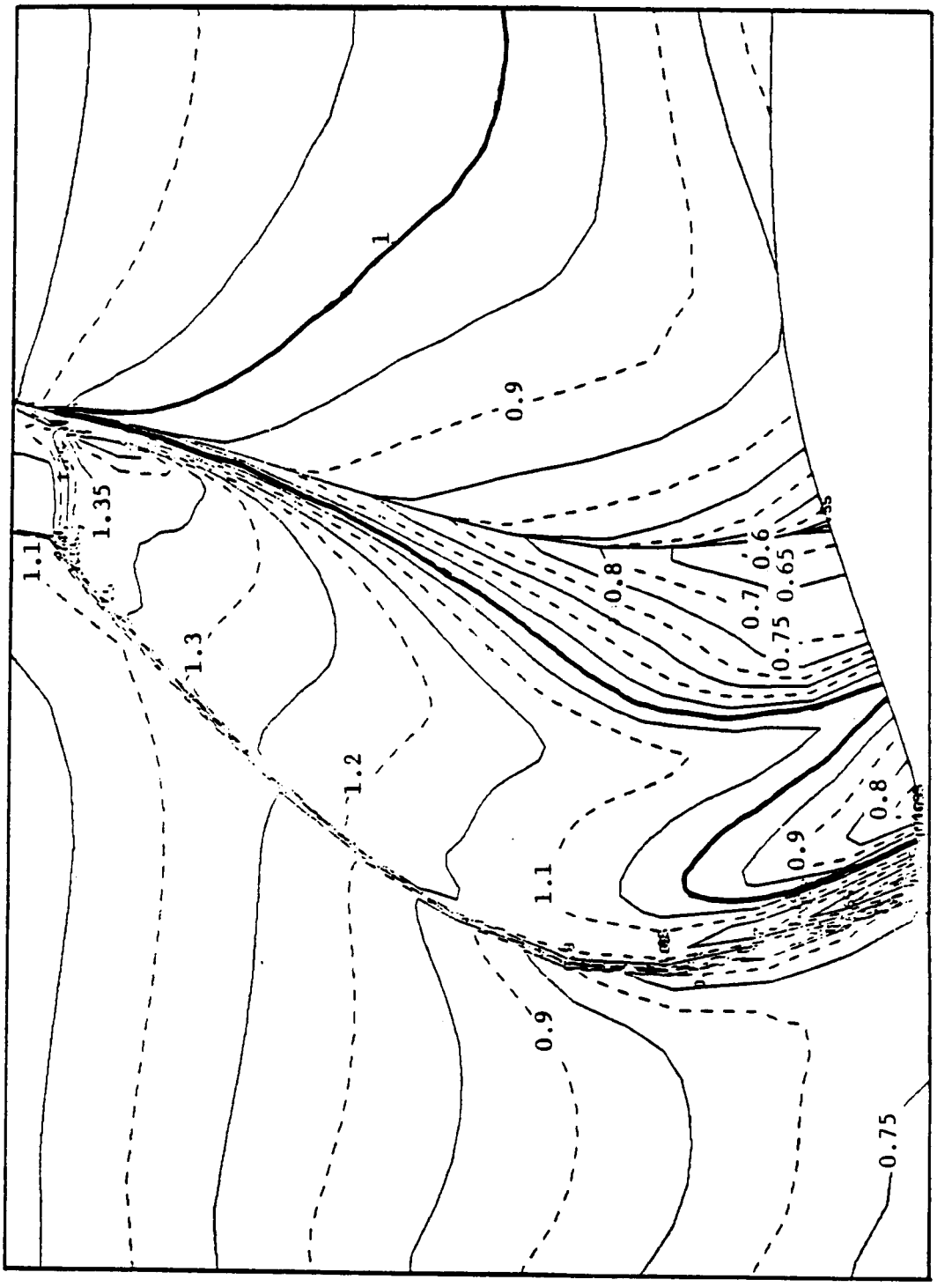

Figure 9. Contours of M_{rel} on the Blade Suction Surface - NASPROP-E.

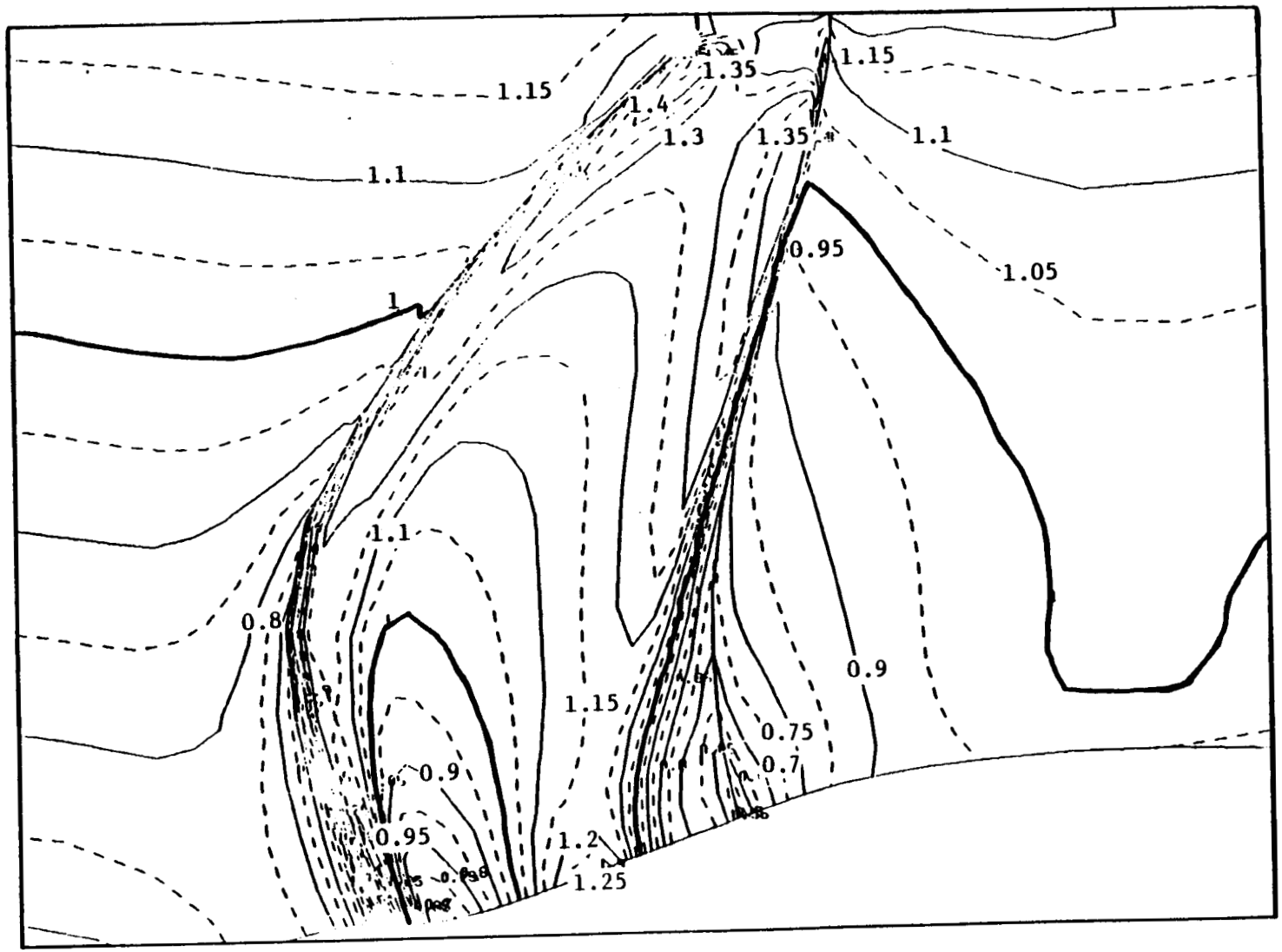

Figure 10. Contours of M_{rel} on the Blade Suction Surface - GE-CRD.

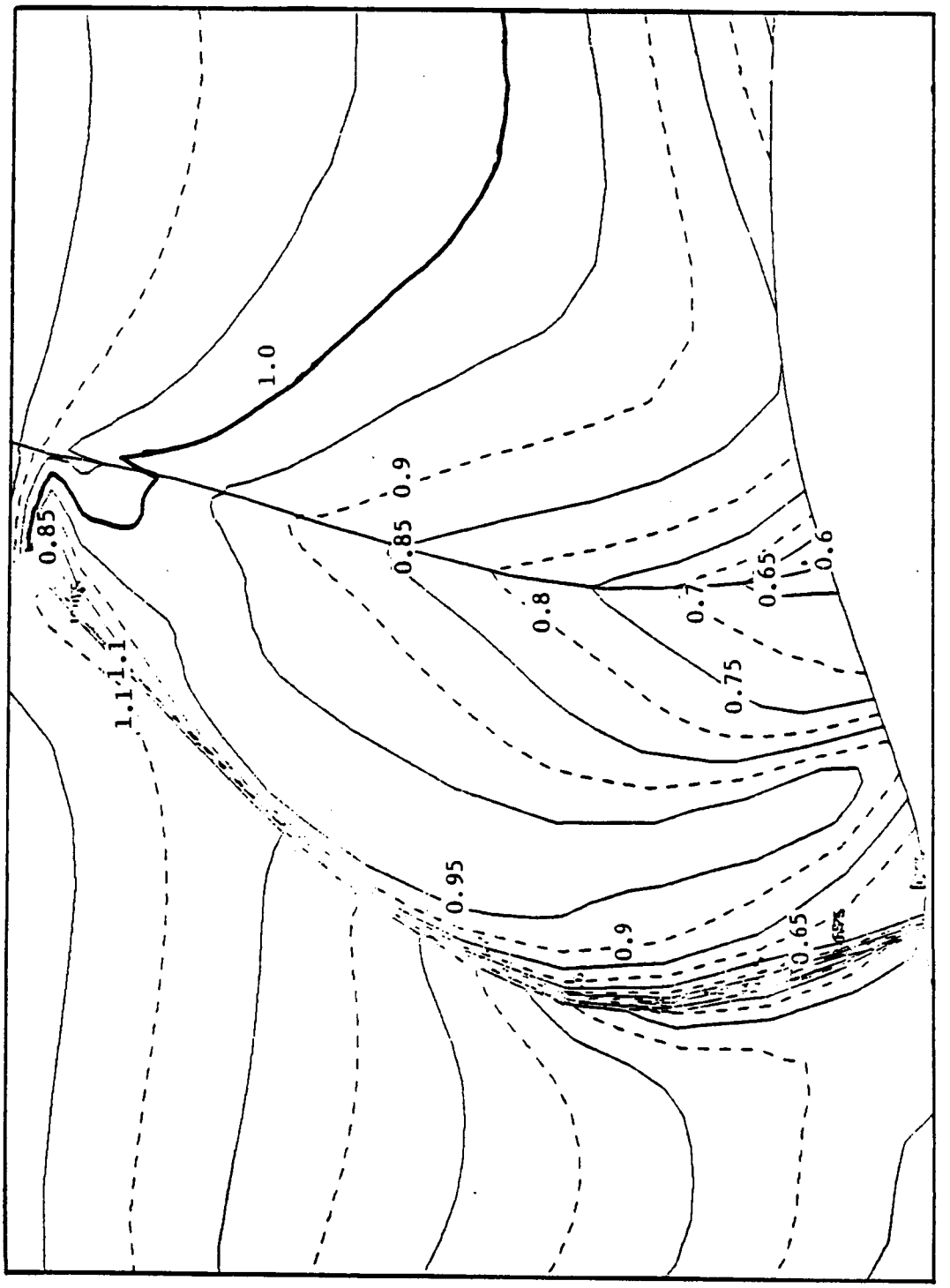

Figure 11. Contours of M_{rel} on the Blade Pressure Surface - NASPROP-E.

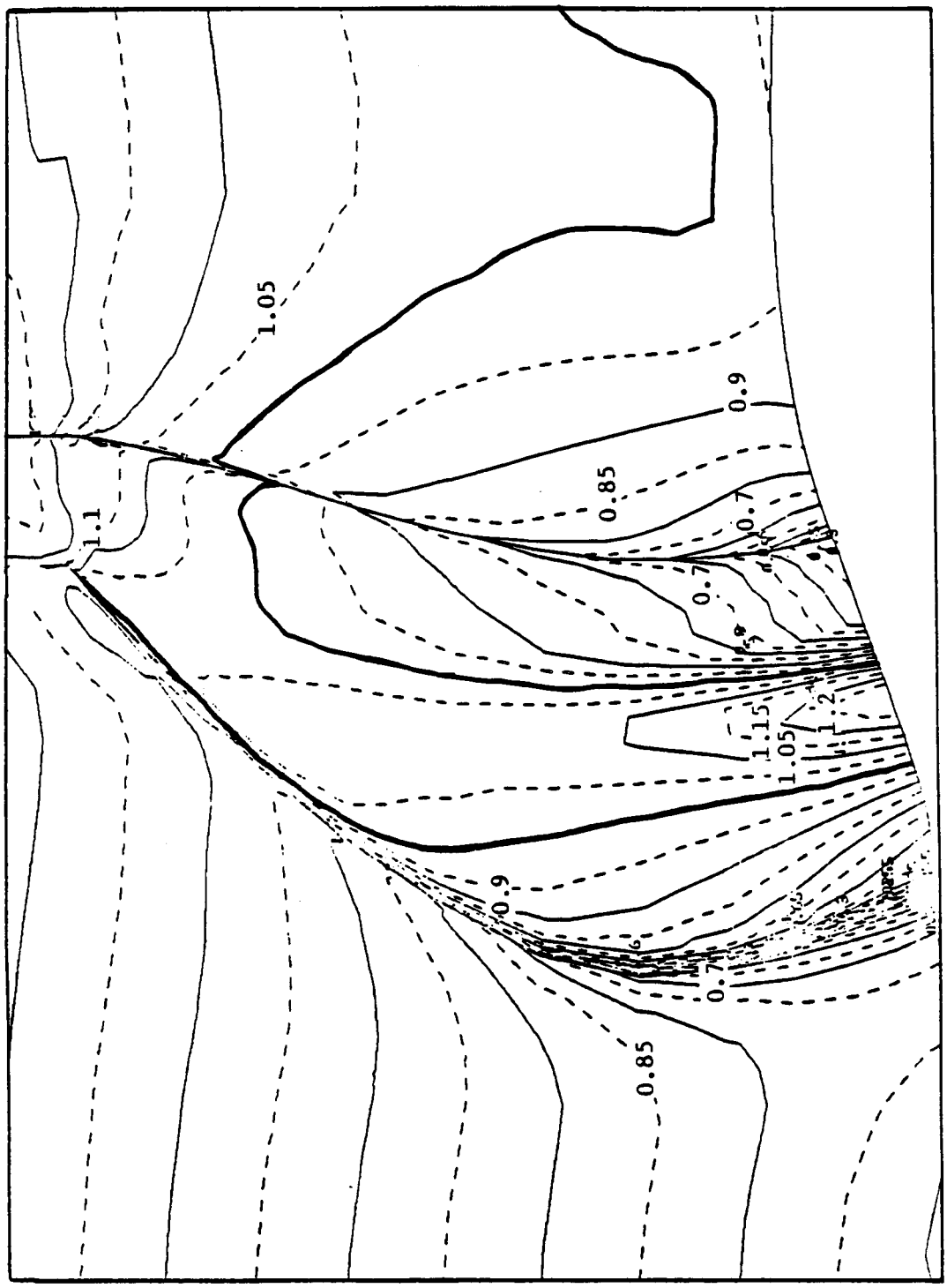

Figure 12. Contours of M_{rel} on the Blade Pressure Surface - GE-CRD.

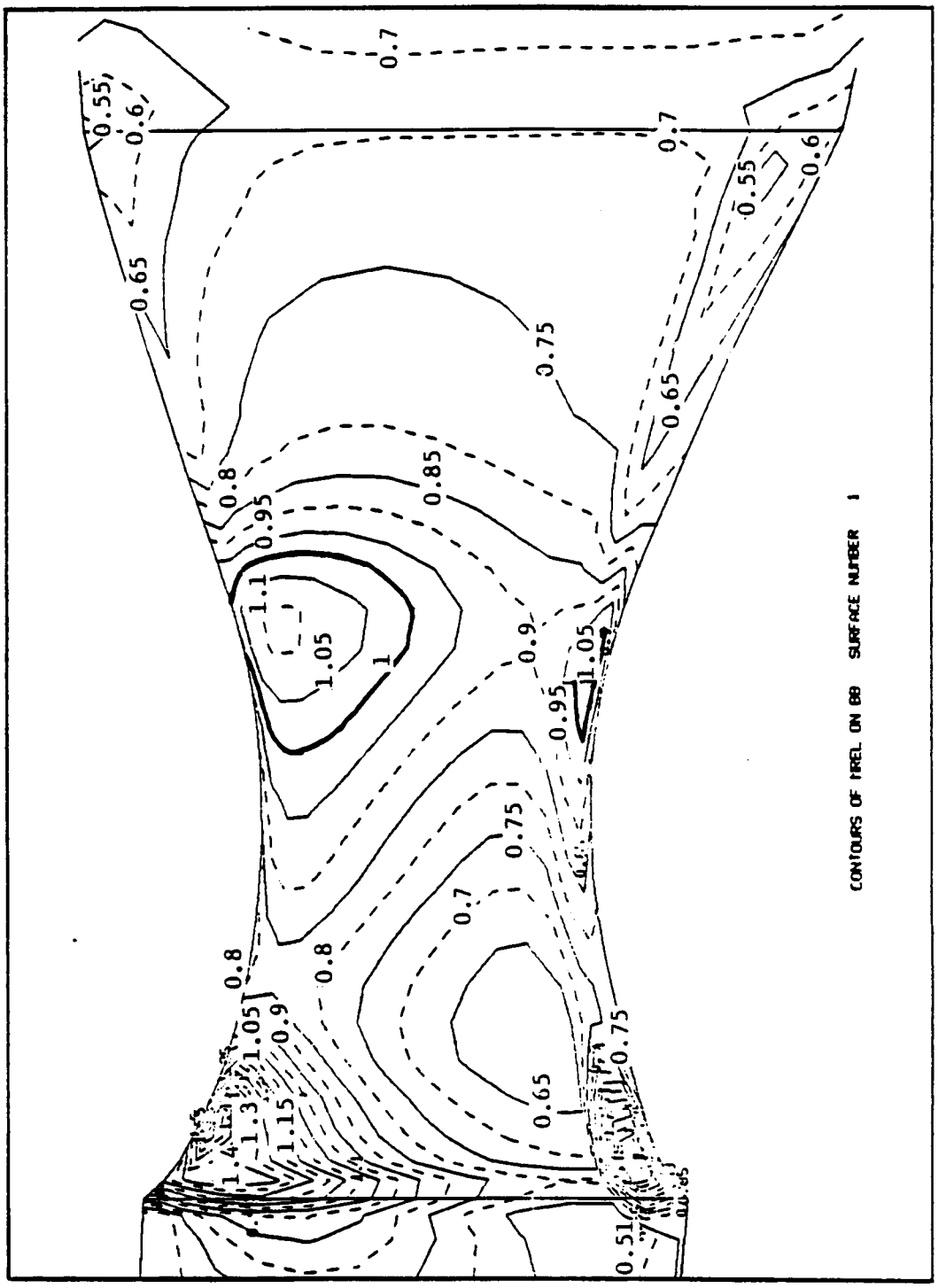

Figure 13. Contours of M_{rel} on the Hub Blade-to-Blade Surface - NASPROP-E.

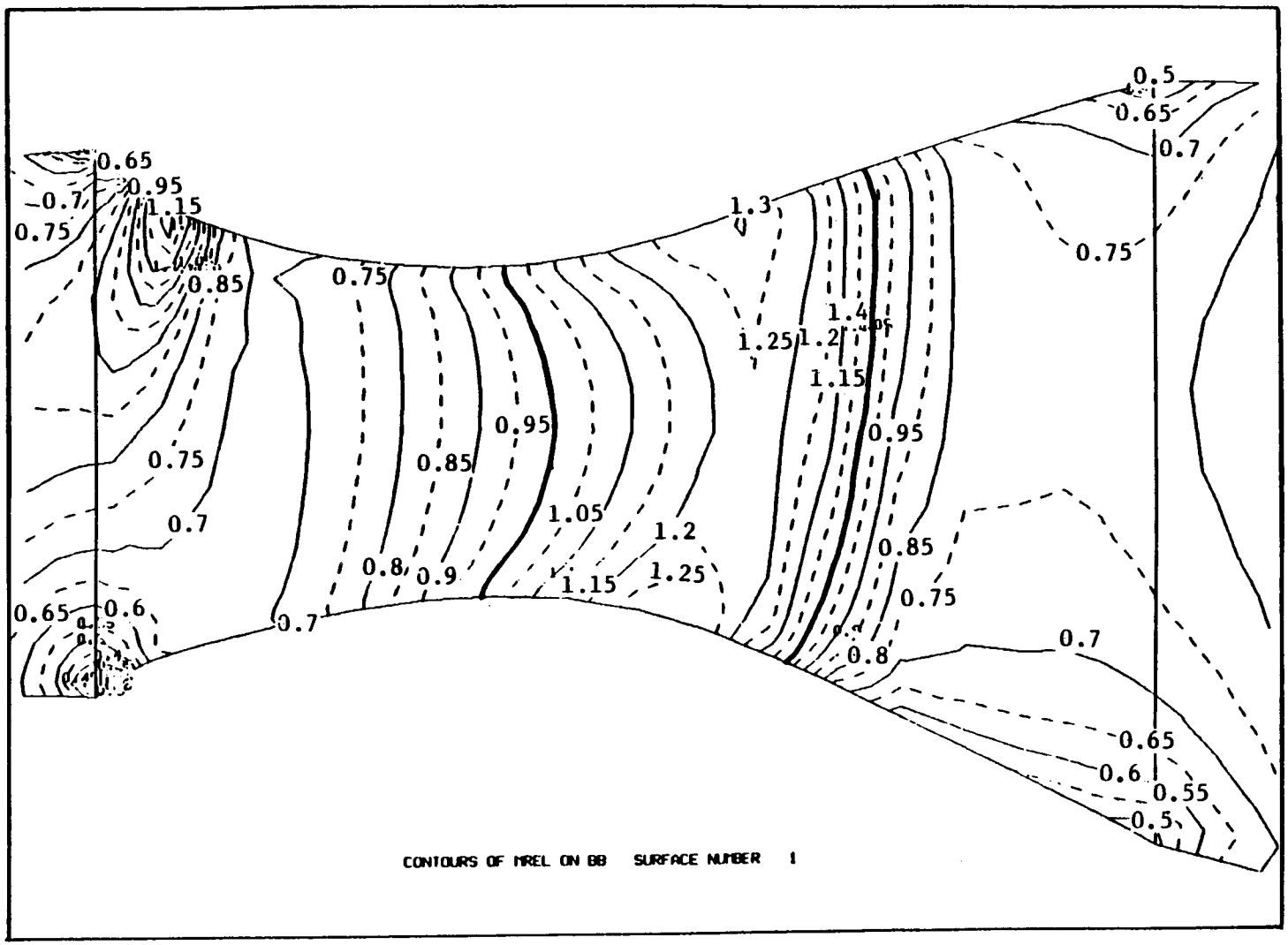

Figure 14. Contours of M_{rel} on the Hub Blade-to-Blade Surface - GE-CRD.

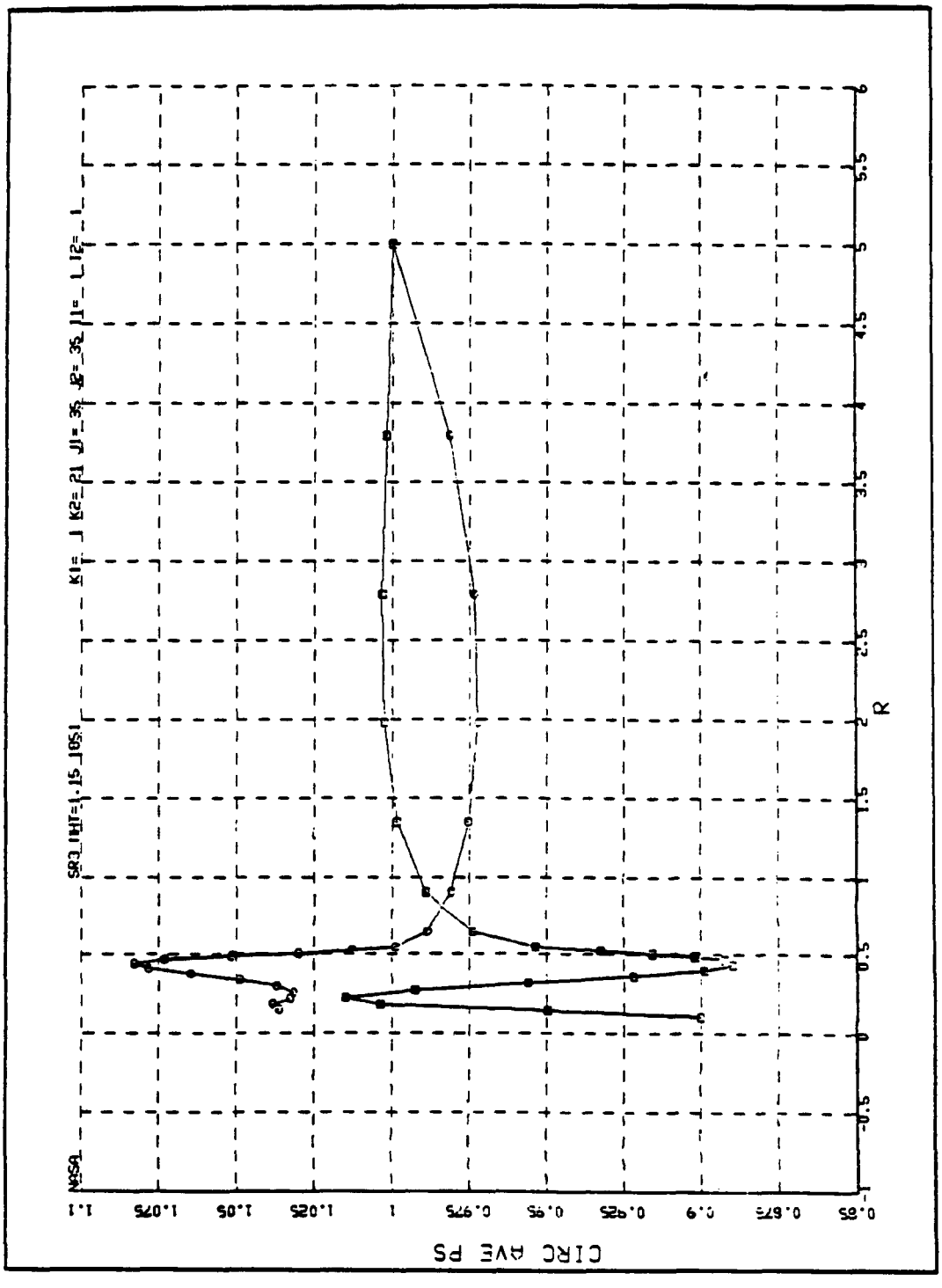

Figure 15. Radial Variation of the Circumferential Average of Static Pressure at Blade Leading and Trailing Edges - $M_{1_T} = 1.15$, $M_\infty = 0.8$, No Starting Solution.

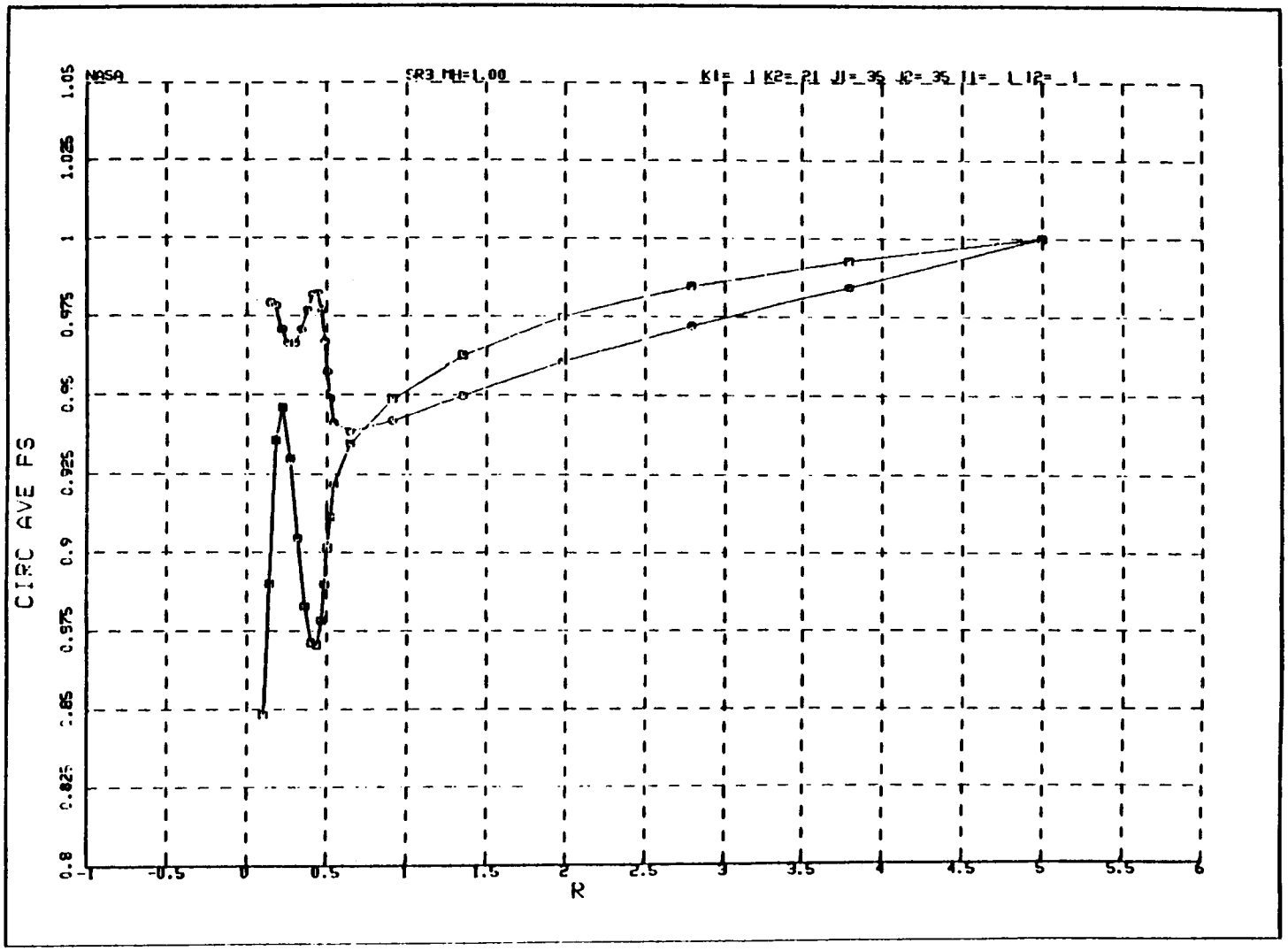

Figure 16. Radial Variation of the Circumferential Average of Static Pressure at Blade Leading and Trailing Edges - $M_{IIT} = 1.00$, $M_\infty = 0.7$, Solution of Figure 15 Used as Starting Solution.

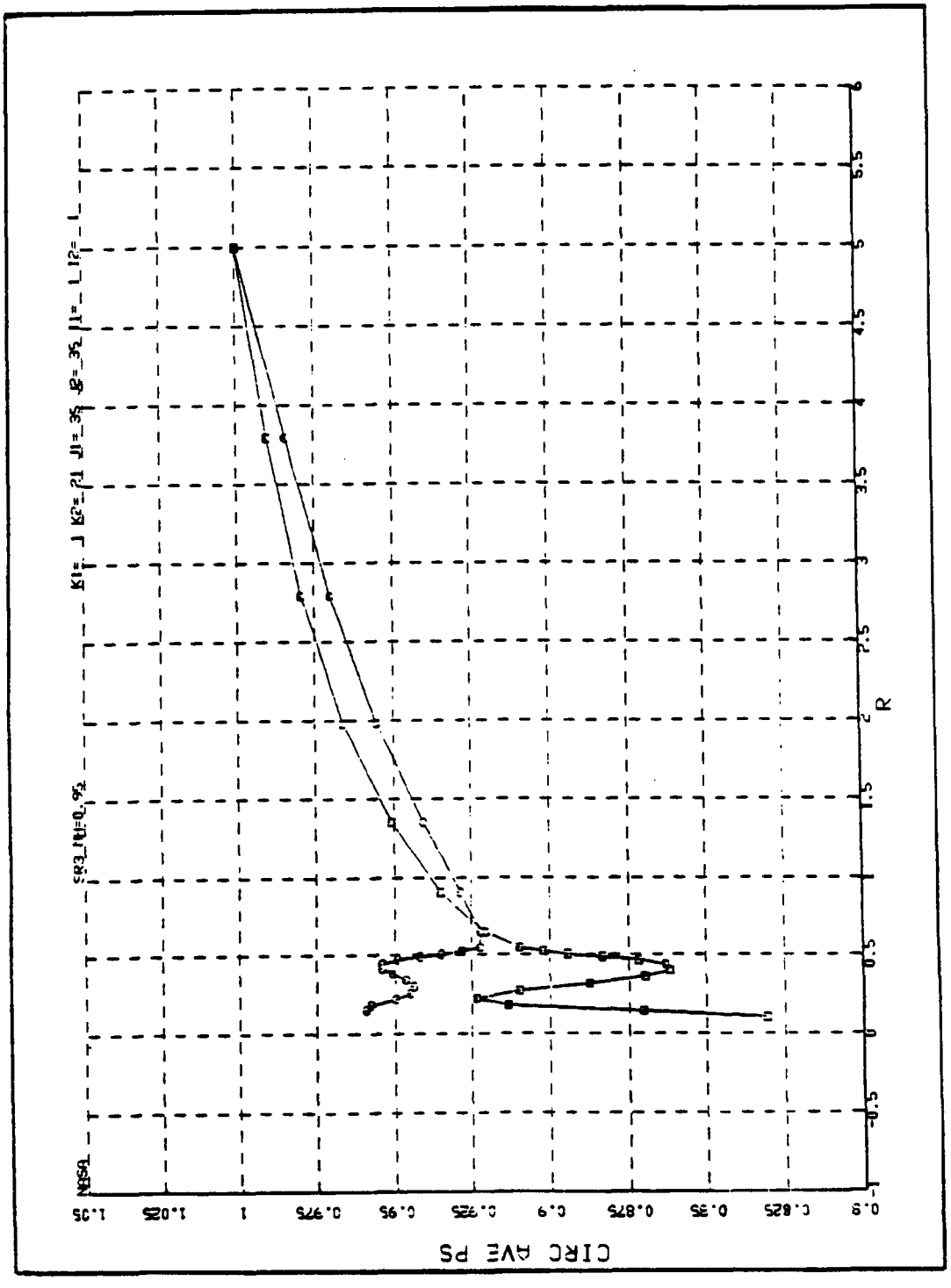

Figure 17. Radial Variation of the Circumferential Average of Static Pressure at Blade Leading and Trailing Edges - M_{1_T} = 0.95, M_∞ = 0.66, Solution of Figure 15 Used as Starting Solution.

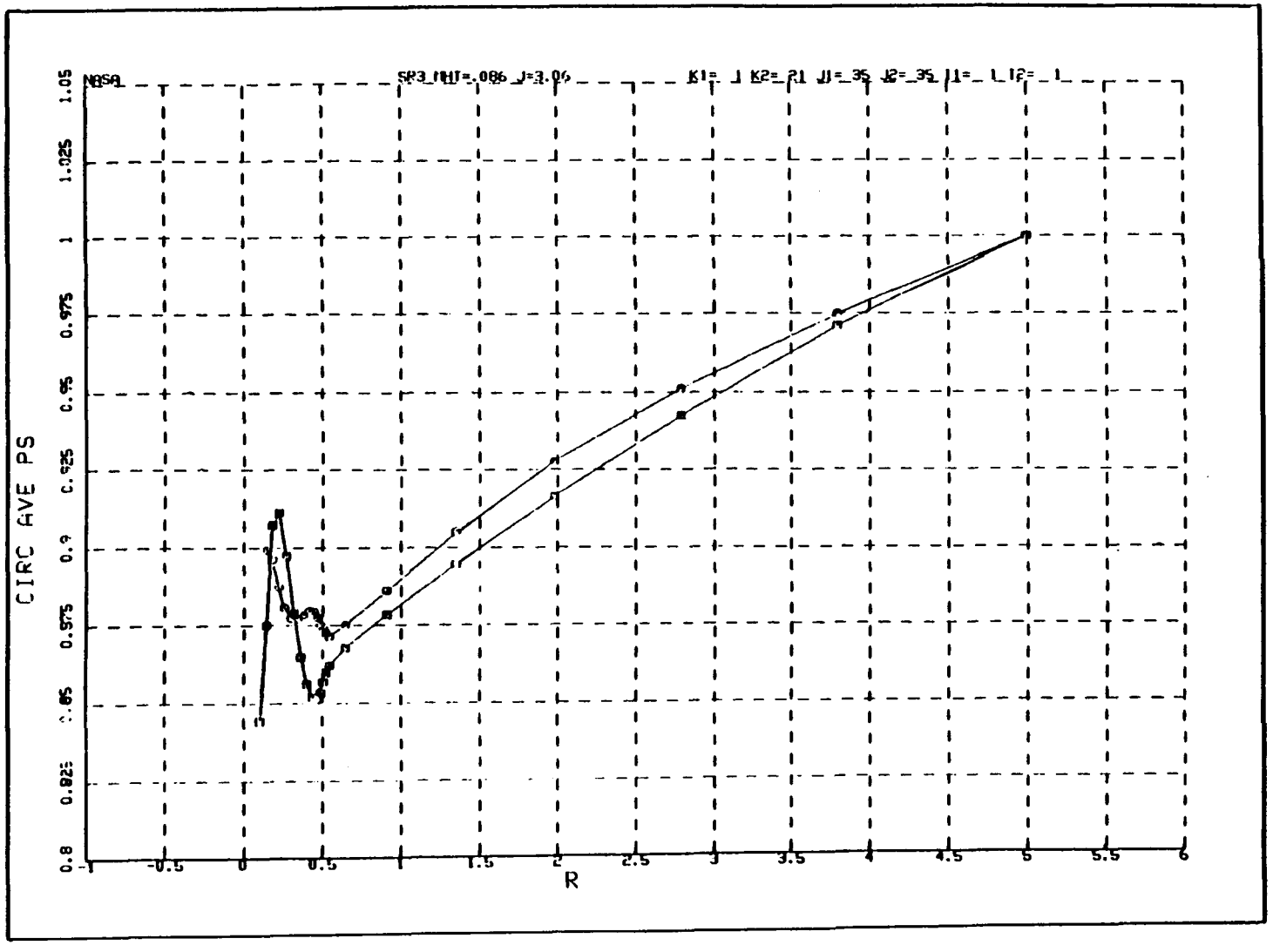

Figure 18. Radial Variation of the Circumferential Average of Static Pressure at Blade Leading and Trailing Edges - $M_{1rT} = 0.86$, $M_\infty = 0.6$, Solution of Figure 15 Used as Starting Solution.

to the boundary becomes more and more pronounced as the helical tip Mach number is reduced. In contrast, the solution used to produce Figure 19 was run from scratch. Here, the region outside the blades appears as uniform as that of Figure 15.

As a result of these figures, some doubts surfaced as to the validity of the utilization of these solutions in the prediction of the noise generated by high speed turboprops. However, it was determined that, since the region of acoustic interest was confined to the vicinity of the propeller disk, and since all the quantities required were normalized by other parameters from the same solution, the use of these results was justified.

It should be emphasized here that it is not the purpose of this report to criticize or to express dissatisfaction with the flow solutions available at the time this work was performed. These examples are provided as an illustration of the uncertainties involved in the acoustic predictions used in the data/theory comparisons which follow.

2.1.3.2 Acoustic

Comparisons between measured and predicted tone results have been made for three model propfans identified as SR-2, SR-3, and SR-6, respectively. These are illustrated in Figure 20, which is taken from Reference 2.1.20. Further theoretical predictions have been made for the SR-7L propfan as it performed on the Gulfstream airplane. These are described in Section 3.0 of this report. As shown in Figure 20, SR-2 and SR-3 each have 8 blades; SR-6 has 10 blades. SR-2 resembles a conventional propeller in having an unswept planform; SR-3 has high sweep and SR-6 falls somewhere between the other two.

Acoustic and performance data for these propfans were available from References 2.1.20, 2.1.21, 2.1.23 and 2.1.24. All three model propfans were tested in the NASA Lewis Research Center 8- by 6-foot transonic wind tunnel; in addition, data measured from the flights of the SR-2 and SR-3 models on the Jetstar airplane were available from Reference 2.1.21. The available data points are presented in Table 1.

Data/theory comparisons are presented in different formats in Figures 21 through 31. Figures 21 through 24 compare prediction with data for the first six harmonics of BPF at various observer angles; while in Figures 25 through 27, the variation of peak BPF tone SPL (sound pressure level) with helical tip Mach number at approximately constant C_p (power coefficient) and J (advance ratio) are shown. These comparisons are discussed in detail below, together with possible causes of any discrepancy between predicted and measured levels.

Figure 21 compares measured and predicted levels for the SR-2 model propfan mounted on the Jetstar aircraft. These data (from Reference 2.1.21) were obtained with both boom-mounted and fuselage-mounted transducers. Both sets of data (boom and fuselage) were taken at the same sideline distance. However, as a result of the different transducer installation geometries (namely, the difference in radius of the boom and fuselage), the levels measured at equivalent angular locations on the boom and fuselage differed. Consequently, the decision

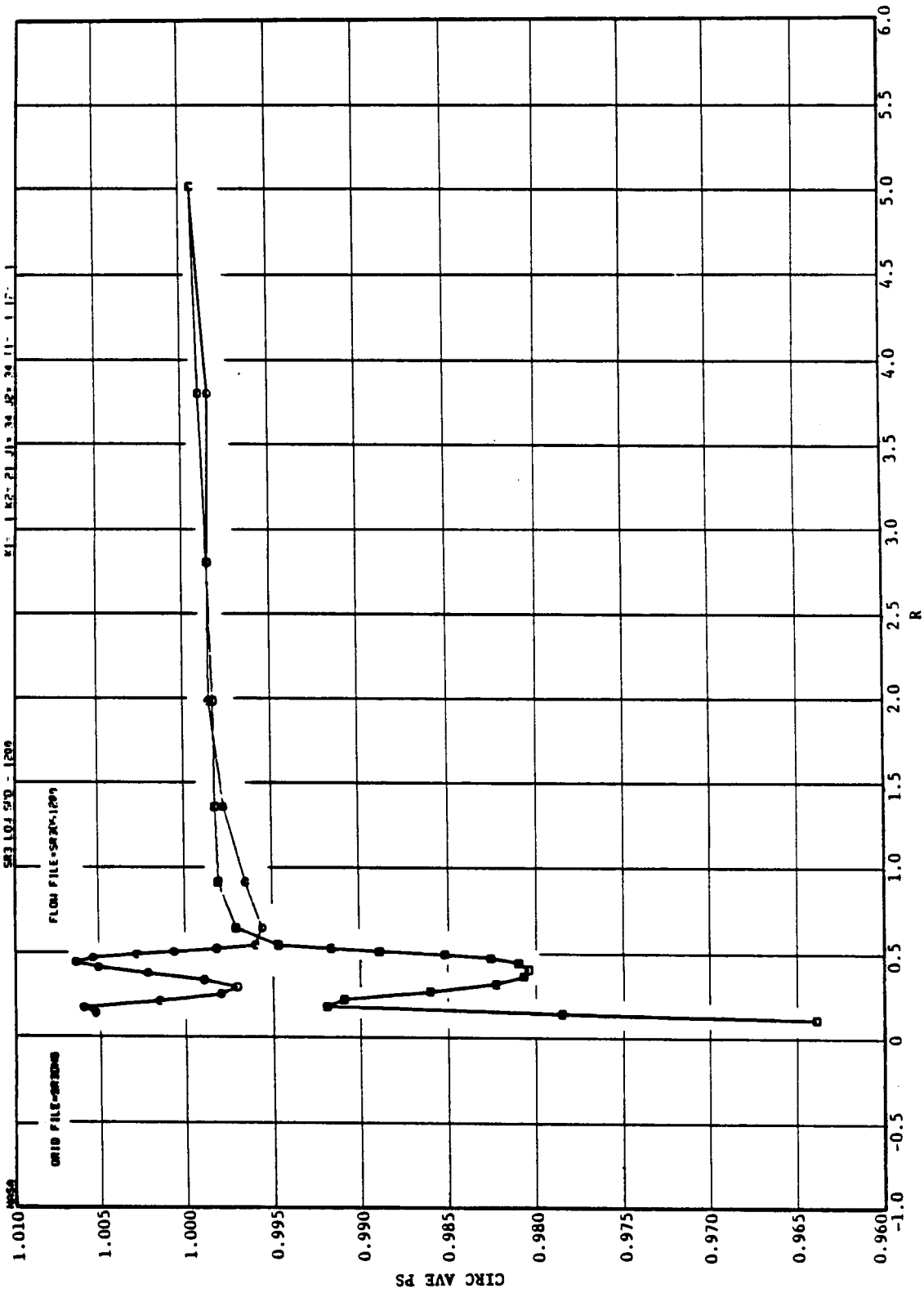

Figure 19. Radial Variation of the Circumferential Average of Static Pressure at Blade Leading and Trailing Edges - M_{ITT} = 0.72, M_∞ = 0.5, No Starting Solution.

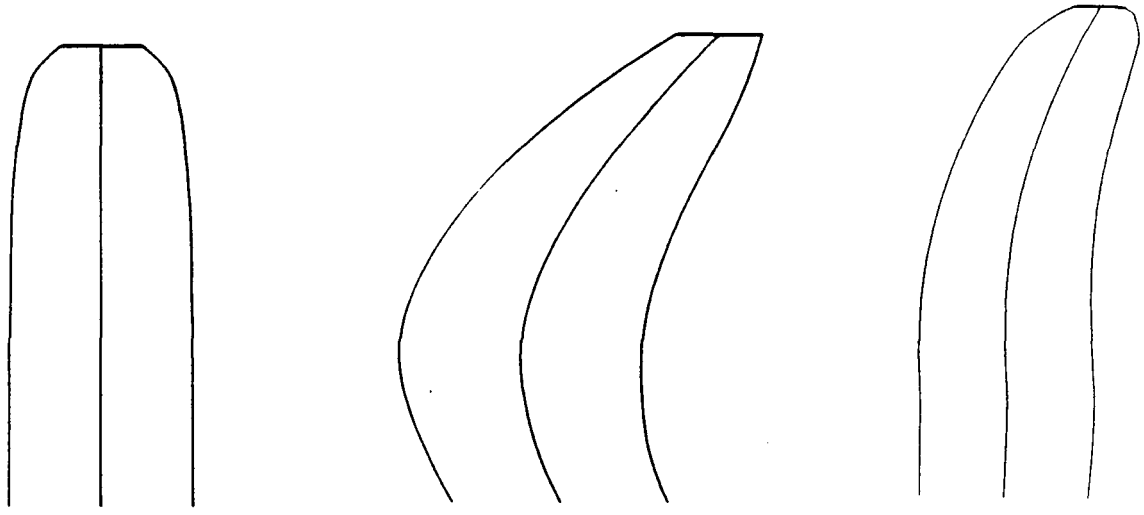

	SR-2	SR-3	SR-6
TIP SWEEP ANGLE, deg	0	45	40
PREDICTED DESIGN EFF, %	76.6	81.1	81.9
DIAMETER IN (cm)	24.5 (62.2)	→	27.4 (69.6)
TIP SPEED, ft/sec (m/sec)	800 (244)	→	700 (213)
POWER LOADING, P/D^2, hp/ft^2 (kW/m^2)	37.5 (301)	→	30.0 (241)
NO. OF BLADES	8	→	10

Design characteristics and planforms of high speed propeller models.

(From Reference 2.1.20)

Figure 20. Design Characteristics and Planforms of Various High Speed Propeller Models.

was made to make the comparisons under free field conditions; and thus, following Reference 2.1.22, 6 dB were subtracted from the fuselage levels and 4 dB from the boom levels to simulate the free field theoretical results.

Table 1. Data Used for Comparison with Theory.

Propfan	Reference	M_{HT}	M_0	C_p	J
SR-3	2.1.23	1.21	0.85	1.5	3.07
		1.14	0.80	1.78	3.07
		1.07	0.75	1.79	3.05
		1.00	0.70	1.84	3.06
		0.863	0.60	1.89	3.05
SR-3	2.1.24	1.21	0.85	1.53	3.05
		1.14	0.80	1.71	3.06
		1.08	0.75	1.79	3.06
		1.00	0.70	1.89	3.06
		0.93	0.65	1.91	3.06
		0.86	0.60	1.91	3.06
SR-3	2.1.21	1.124	0.787	1.998	3.083
SR-2	2.1.23	1.21	0.85	1.89	3.07
SR-2	2.1.21	1.105	0.787	2.094	3.186
SR-6	2.1.20	1.222	0.85	1.02	3.06

Two sets of theoretical predictions are compared in Figure 21. This is a result of selections made when the 3D Euler computer codes were being exercised. It was decided at that time to exercise the code at a constant advance ratio (J), with varying values of helical tip Mach number. In addition, the solutions were obtained for a single value of $\beta_{3/4}$, the blade pitch angle, for each blade design. This enabled the different flow solutions for each blade to be obtained from a single computational grid. For the SR-2 propfan case (Figure 21), flow solutions were obtained using the NASPROP-E code for a constant advance ratio of 3.06, with helical tip Mach numbers of 0.86, 0.95, 1.00, 1.07, 1.15, and 1.20; and the blade pitch angle, $\beta_{3/4}$ of 58°.

The particular data set plotted in Figure 21 came from a run where the advance ratio was 3.186, and the helical Mach number (M_{HT}) was 1.105. It was decided to predict this case twice using results from the M_{HT} = 1.15 solution (Theory 1), and from the M_{HT} = 1.07 solution (Theory 2). Fuselage data were available for six angular locations, with data from the boom

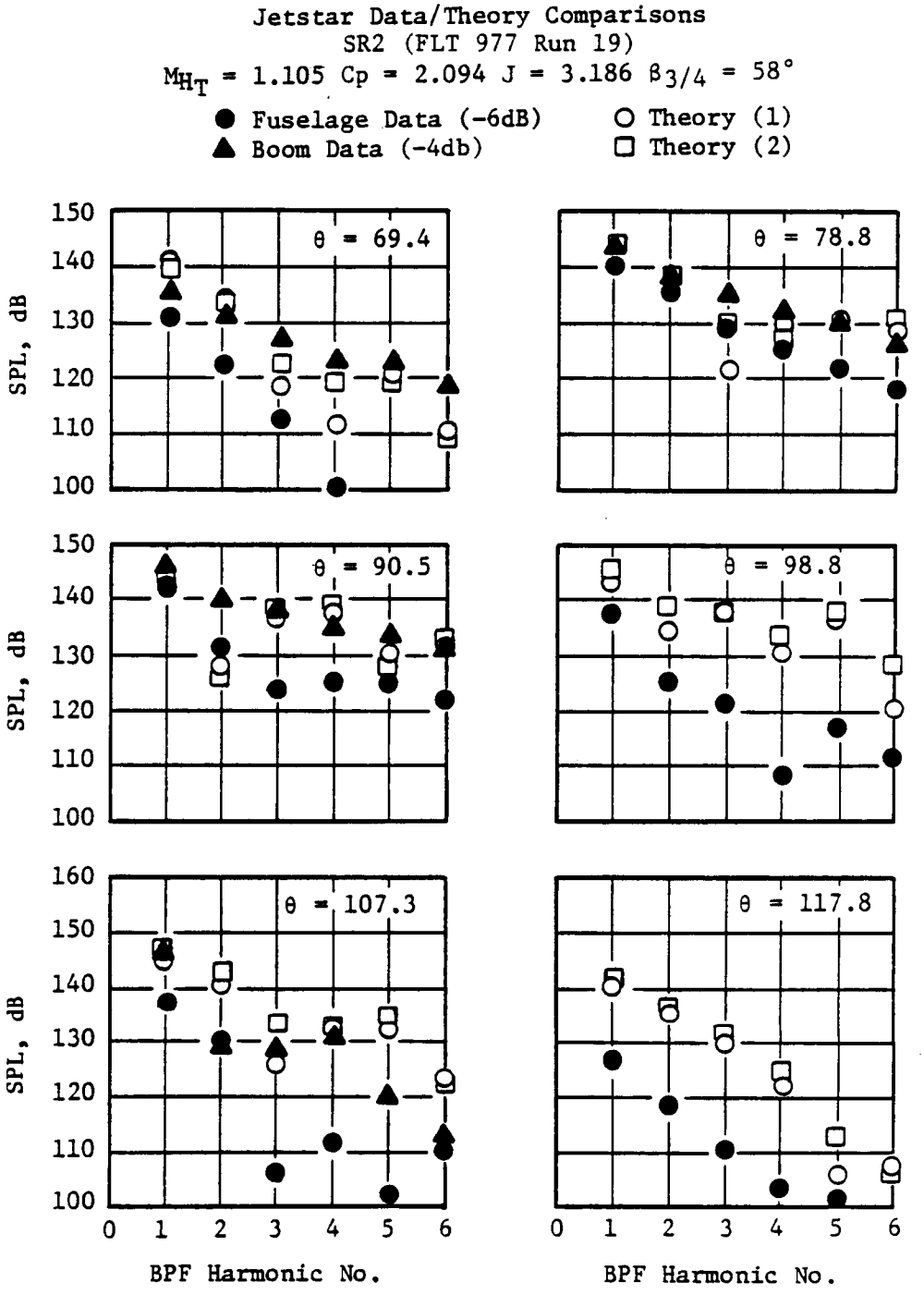

Figure 21. SR2 Jetstar Spectra Under Free Field Conditions.

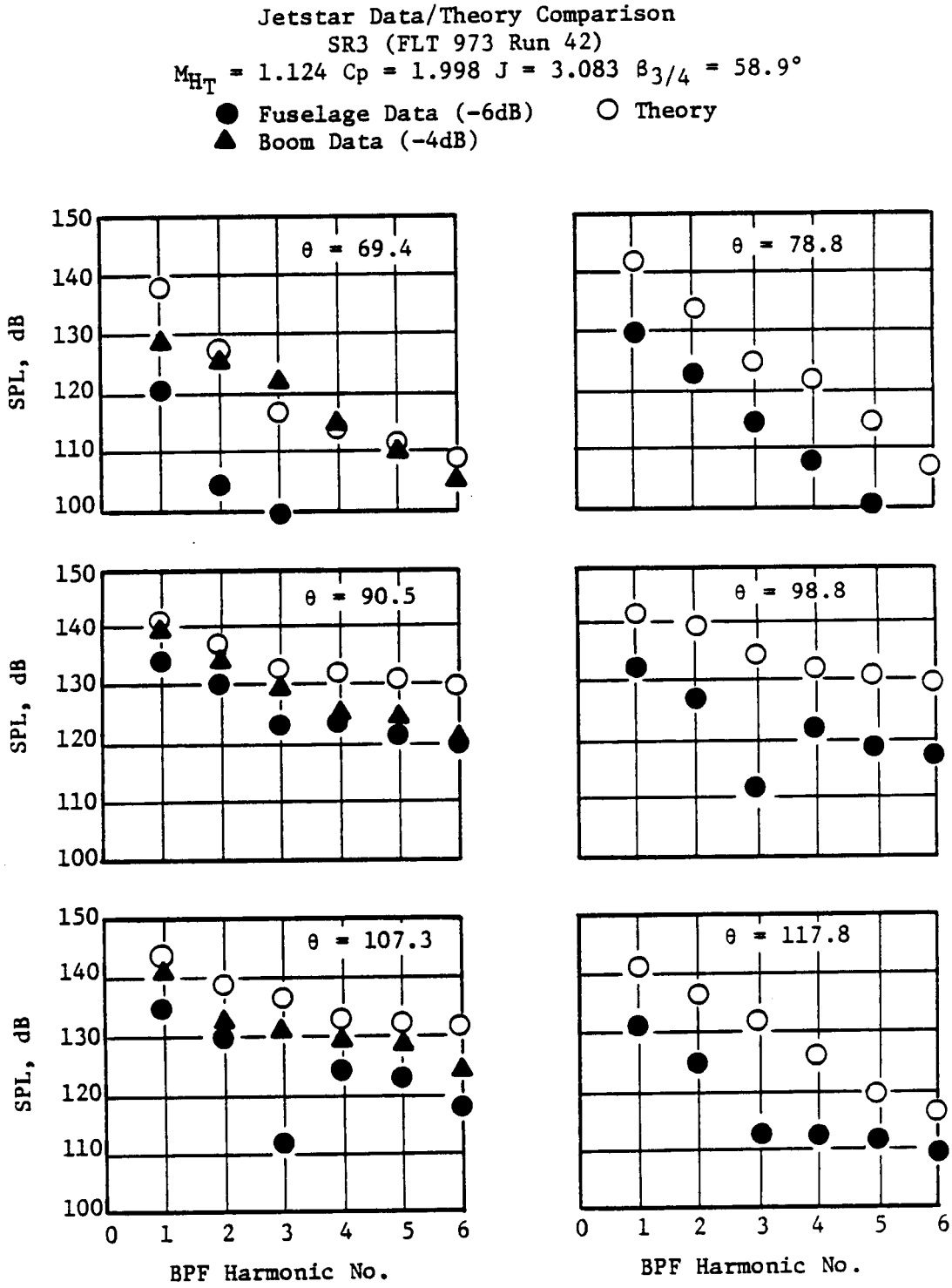

Figure 22. SR3 Jetstar Spectra Under Free Field Conditions.

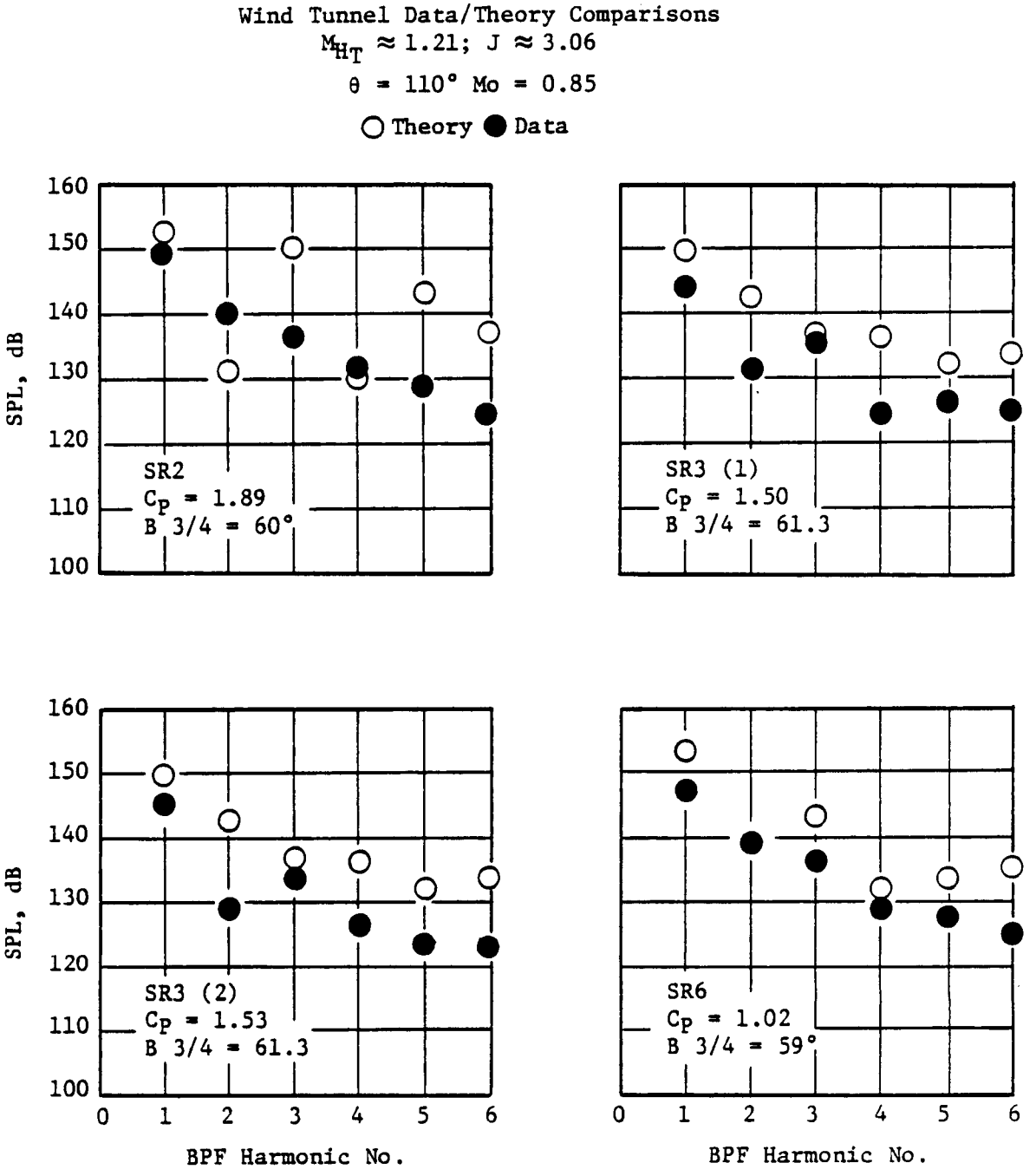

Figure 23. SR2→SR6 Wind Tunnel Spectra (110°) Under Free Field Conditions.

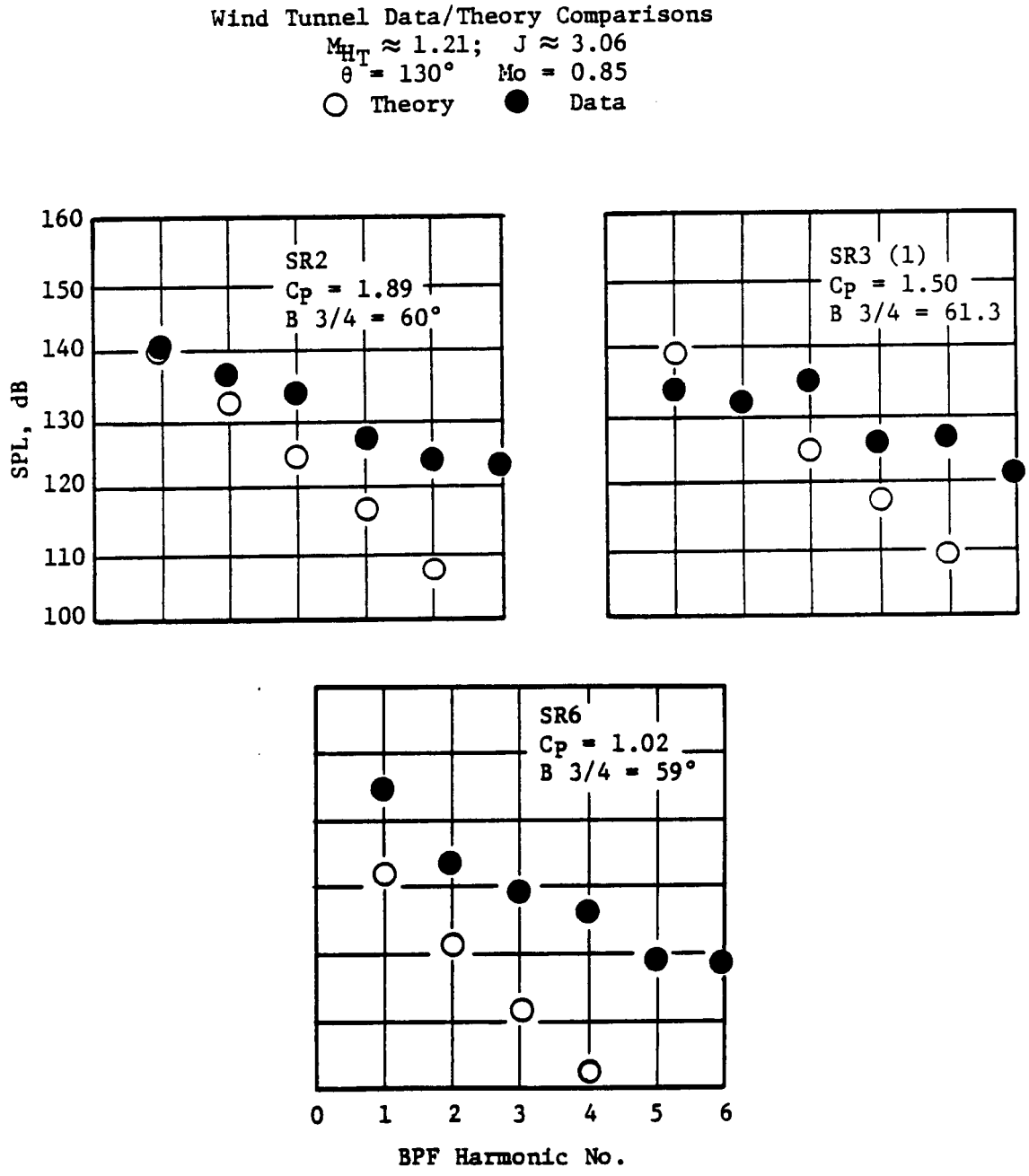

Figure 24. SR2→SR6 Wind Tunnel Spectra (130°) Under Free Field Conditions.

Variation of Peak BPF Tone SPL with Helical Tip Mach No. for the SR-3 Model Propfan in the NASA Lewis Research Center 8ft x 6ft Wind Tunnel. Note: WT1 = Ref 2.1.23; WT2 = Ref 2.1.24.

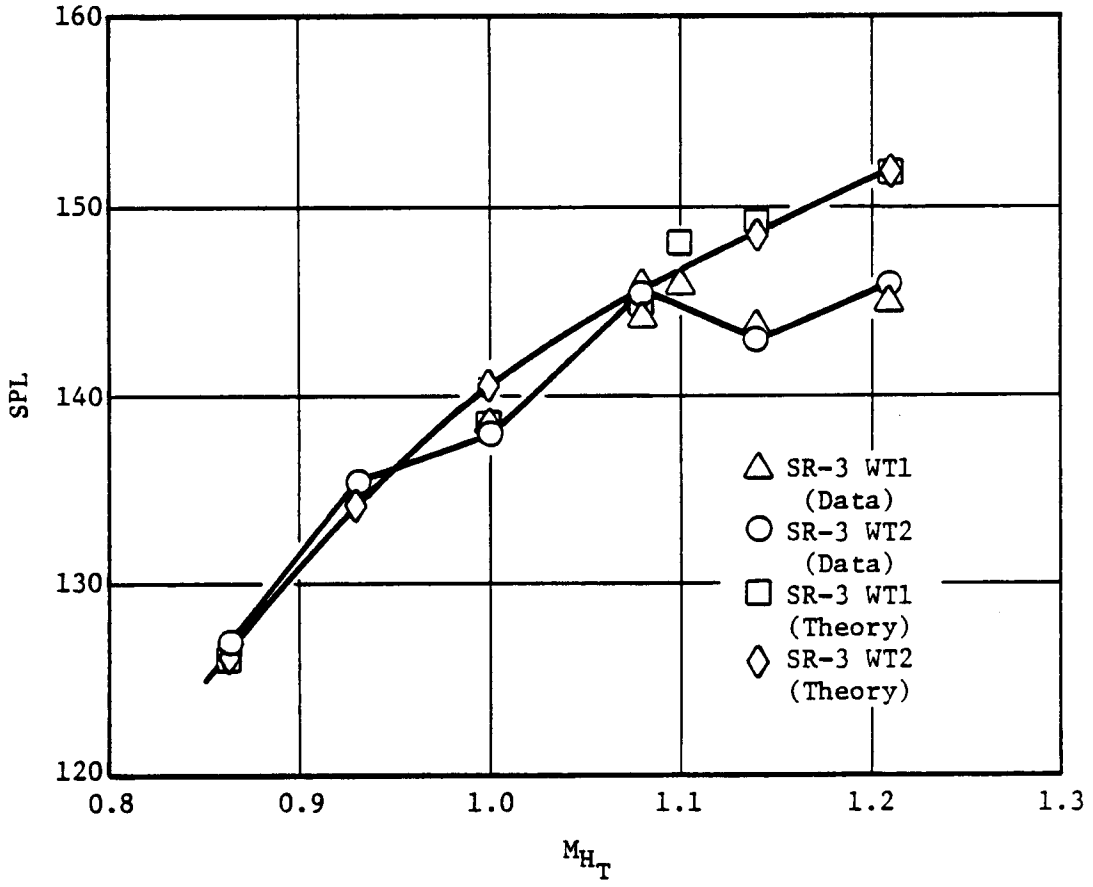

Figure 25. Peak BPF Tone SPL Versus M_{H_T}, Data and Theory (SR-3) Under Free Field Conditions.

Variation of Peak BPF Tone SPL with Helical Tip Mach No.
for the SR-3 Model Propfan on the Jetstar Airplane

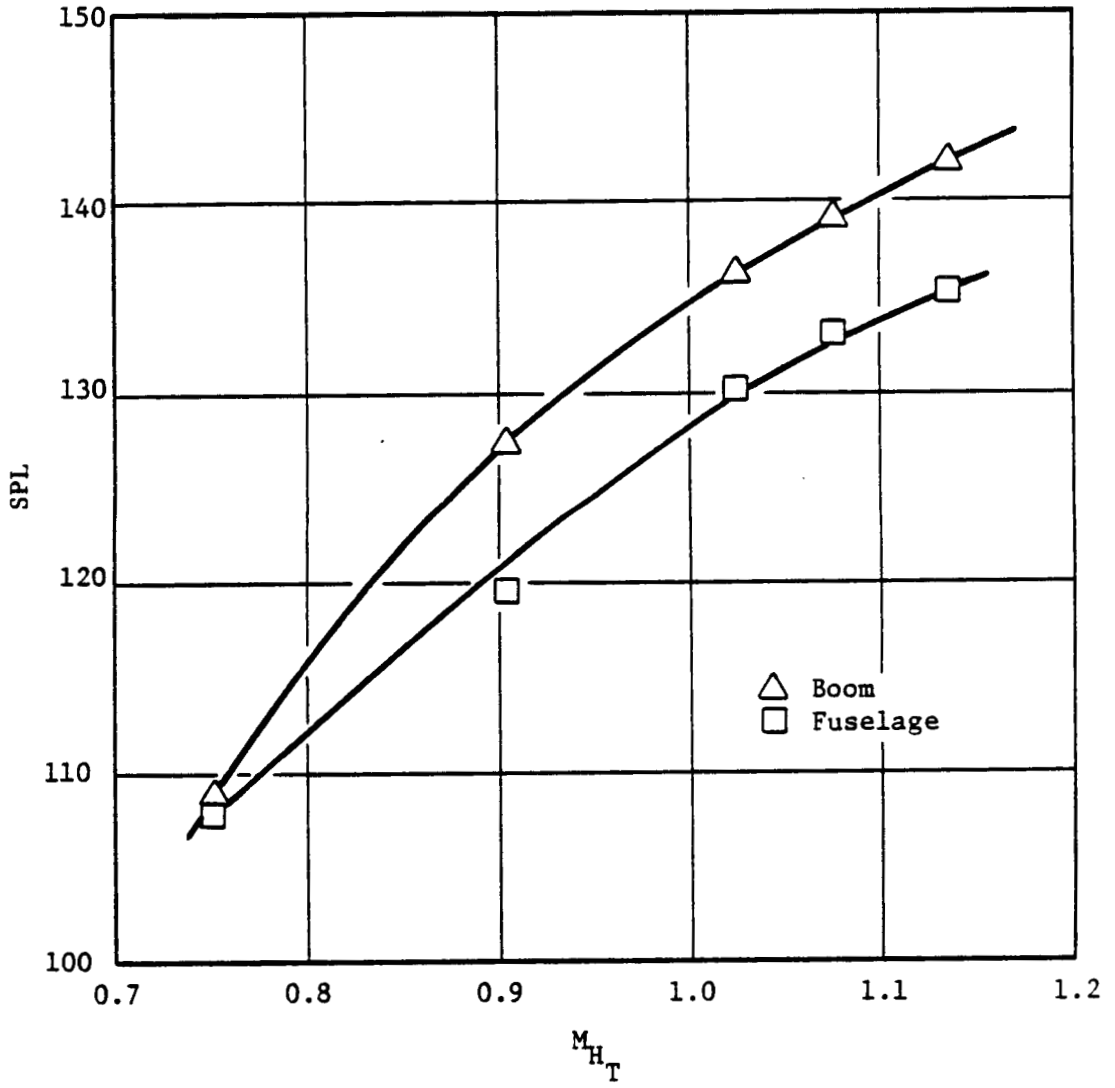

Figure 26. Jetstar Peak BPF Tone SPL Versus M_{H_T} (SR-3) Free Field Conditions, 30,000-feet Altitude.

Variation of Peak BPF Tone SPL with Helical Tip Mach No. for the SR-3 Model Propfan on the Jetstar and in the Wind Tunnel

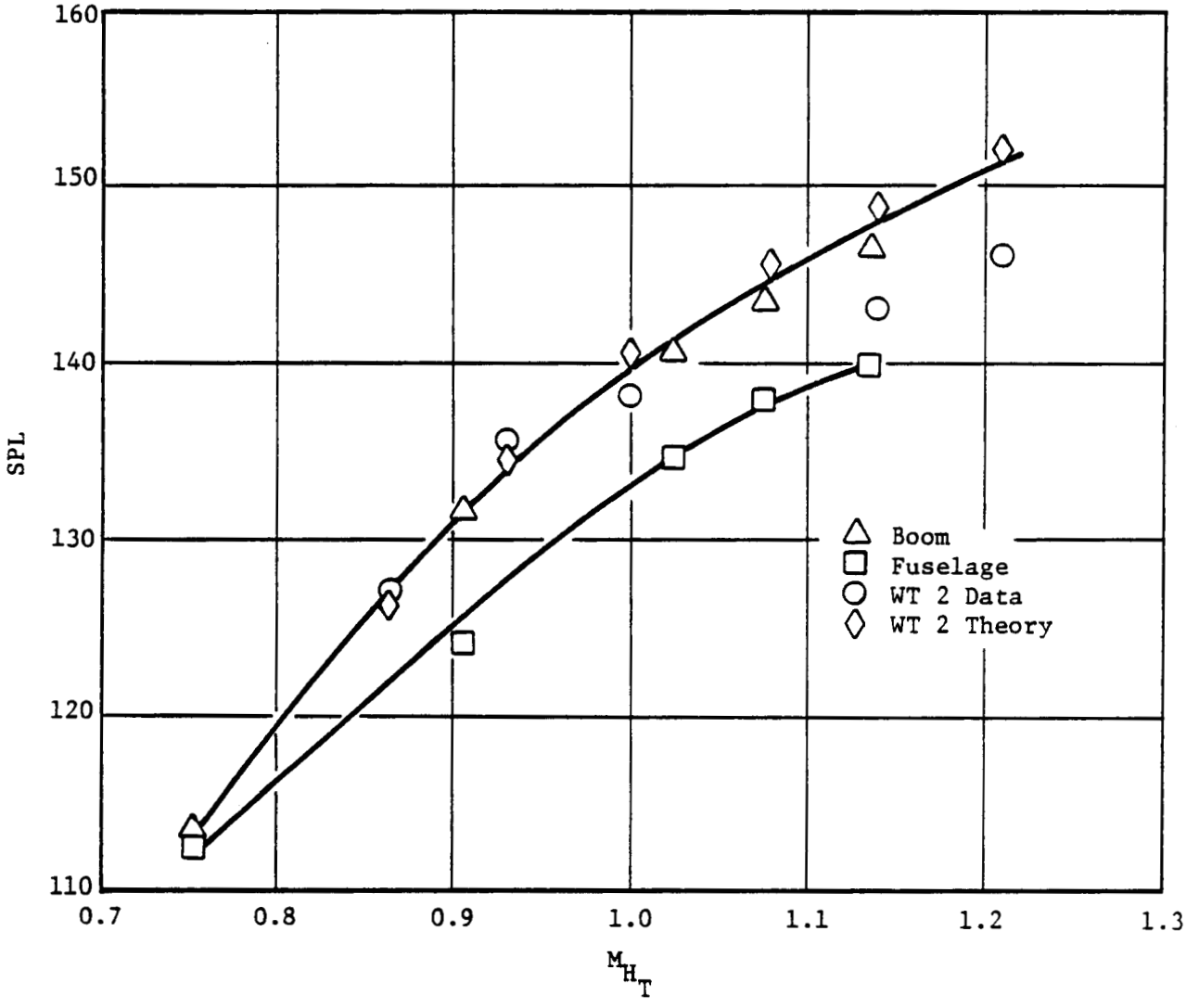

Figure 27. Wind Tunnel and Jetstar Peak BPF Tone SPL Versus M_{H_T} (SR-3) Wind Tunnel Conditions, Free Field.

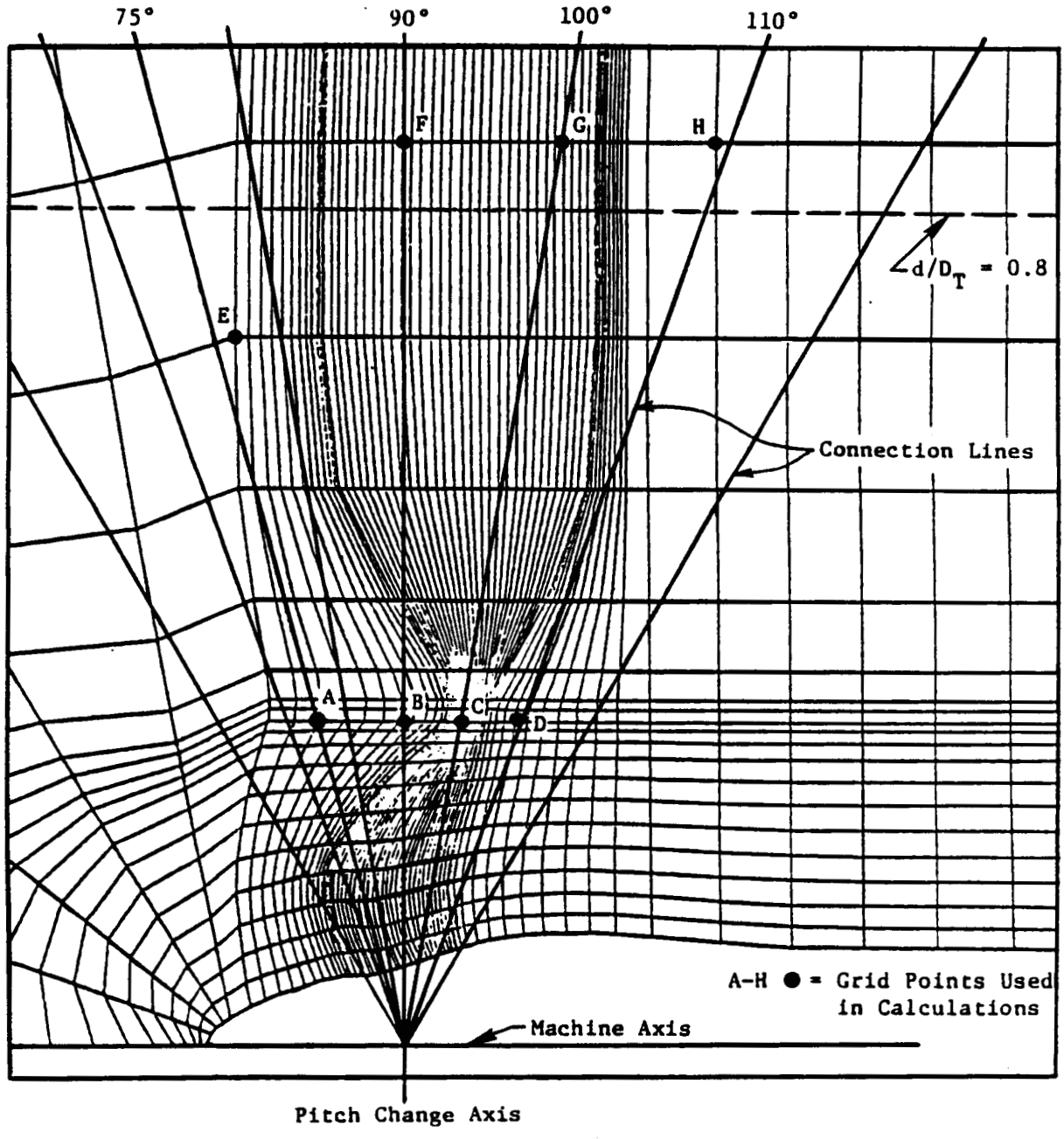

Figure 28. Near Field Calculation Grid, NASPROP-E.

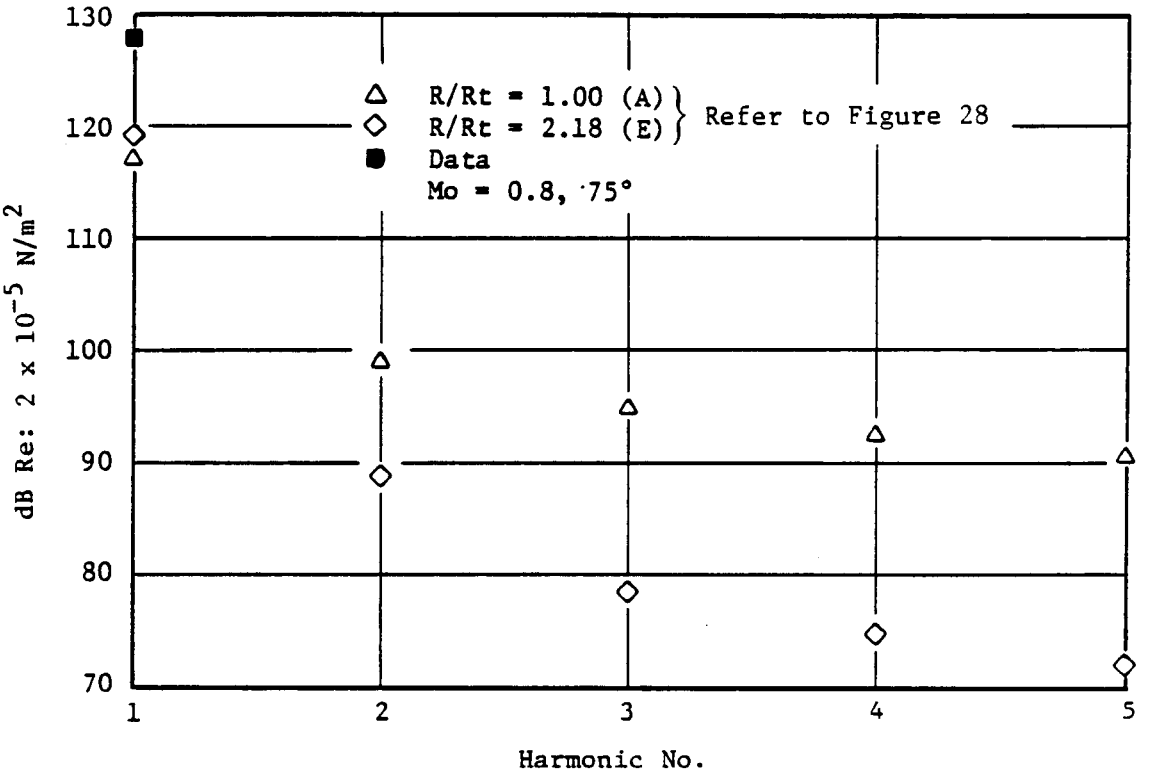

Figure 29. Near Field Data/Theory Comparison Using NASPROP-E Flow Solution at θ_o = 75°.

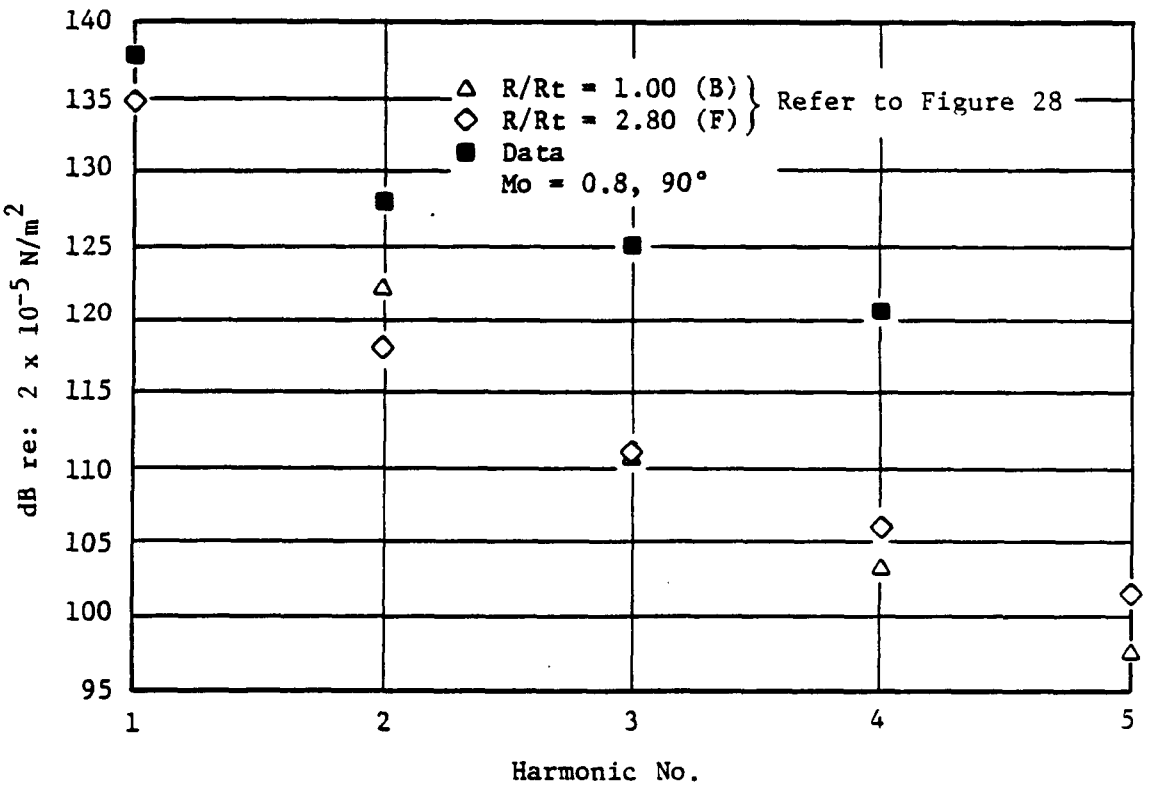

Figure 30. Near Field Data/Theory Comparison Using NASPROP-E Flow Solution at $\theta_o = 90°$.

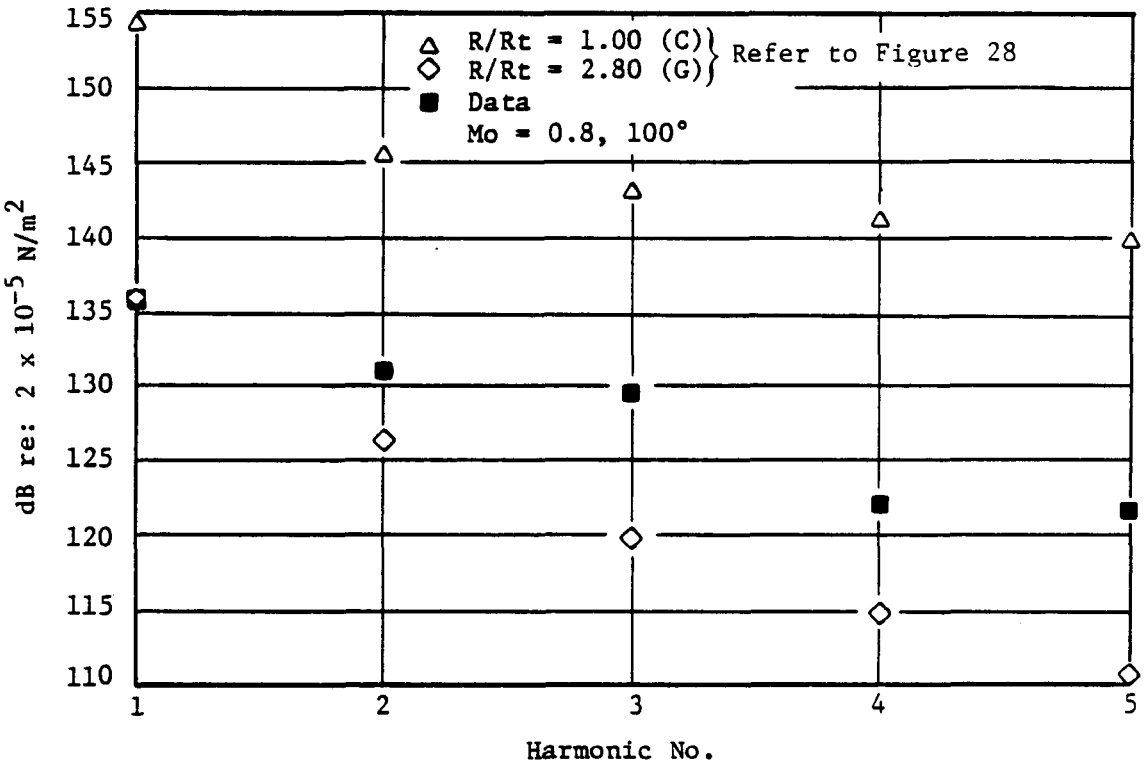

Figure 31. Near Field Data/Theory Comparison Using NASPROP-E Flow Solution at θ_o = 100°.

above the propfan available for four of these. In general, the predictions agree better with the boom data than with that from the fuselage. It is considered probable that, owing to the presence of the boundary layer on the fuselage, the assumption of "flat plate" pressure doubling (that is, 6 dB) may be in error.

Agreement between the boom microphone data and both predictions is generally seen as very good; in that, in most instances the two predictions are very close. At certain places, however, such as at the third harmonic at $\theta = 78.8$, the predictions given by the two codes are of the order of 10dB apart. Because in each case the thickness distribution is identical, this disparity must come from differences in the calculated spanwise and chordwise loading distributions and their interaction with the thickness distribution.

Figure 22 shows a similar plot for the SR-3 model propfan in flight on the Jetstar aircraft. For the SR-3, the same matrix of flow solutions was available with, in this instance, a blade pitch angle of 61.3°. The Jetstar flight was made with a $\beta_{3/4}$ of 58.9° and M_{HT} of 1.124. For this prediction, the flow solution obtained at $M_{HT} = 1.15$ was used. Again, the measured data were adjusted by subtracting 6 dB from the fuselage microphone values, and 4 dB from the boom microphones (where available). Once again, the prediction agrees better with the boom data than with the fuselage data, with a major difference being in the fundamental of BPF at an observer angle of 69.4°. Here, the prediction is approximately 10 dB higher than the actual measurement.

It is surprising that a discrepancy of this nature should be observed in the fundamental BPF tone, especially when the other harmonics are in such good agreement. More reasonable is the gradual "drift" between data and theory observed at $\theta = 90.5°$ with increasing harmonic number. It has been noted that the thickness component of the noise prediction tends to hold the levels up with increasing harmonic number, especially near the plane-of-rotation.

In summary then, Figures 21 and 22 demonstrate good agreement with the boom microphone data; while data from the fuselage-mounted microphones is consistently lower than that measured on the boom, and also lower than the predicted values. This has been ascribed to the effect of the boundary layer on the fuselage.

Figures 23 and 24 compare results obtained in the NASA Lewis Research Center transonic wind tunnel with predictions for the SR-2, SR-3, and SR-6 model propfans. These data are taken from References 2.1.20, 2.1.23, and 2.1.24. The prediction program requires, as input, local ambient conditions of temperature and pressure (in a wind tunnel environment, this amounts to static temperature and pressure), and SHP. For these predictions, tunnel static pressure was obtained from Reference 2.1.25, and the temperature and SHP were deduced from the information in References 2.1.20, 2.1.23, and 2.1.24.

No flow solutions were available for the SR-6 propfan, owing to problems with the NASPROP-E code. Approximations to the spanwise and chordwise loading distributions for this propfan were made using data from Reference 2.1.26 for the spanwise variation and a simple rectangle for the chordwise distribution. It is recognized that these approximations are

less than ideal and will probably account for at least some discrepancies between measured and predicted results. The data used for these comparisons were obtained with pressure transducers mounted in bleed holes in the ceiling of a perforated-wall wind tunnel working section. Where necessary, they have been adjusted to account for a 6 dB error discovered at a later date and reported in Reference 2.1.27. Again, the comparisons are made under free field conditions.

Figures 23 and 24 compare measured and predicted spectra at observer angles of 110° and 130°, respectively, at a wind tunnel Mach number of 0.85, giving a helical tip Mach number of 1.21, at different power coefficients for the three propfan models. The agreement for SR-2 and SR-3, while not as good as that obtained with the boom microphones on the Jetstar, is reasonable. Possibly for the reasons stated above, it is less good for the SR-6 comparison.

A frequently employed form of presentation (for example, References 2.1.20 through 2.1.24) is to plot the variation in peak Blade Passing Frequency SPL as a function of the blade helical tip Mach number, M_{HT}, at constant advance ratio, J. Figures 25 through 27 demonstrate this variation for the SR-3 propfan as tested in the NASA Lewis Research Center 8- by 6-foot transonic wind tunnel and on the Jetstar airplane. In all cases, the theoretical predictions presented in these figures were made under the measurement conditions (but free field), and such adjustments as were made (with the exception of conversion to free field) were applied to both sets of information.

A major difference between the data gathered in the wind tunnel and that obtained on the Jetstar is found in the ambient pressure at which the measurements were made. Jetstar data were primarily taken at 30,000-feet altitude, with constant ambient pressure. In the wind tunnel, a change in tunnel Mach number is accompanied by a corresponding change in static (acoustic ambient) pressure; consequently, the tone levels shown in Figure 25 have been adjusted using

$$SPL(plot) = SPL - 20*\log_{10}(P_{amb}/P_{ref})$$

where P_{ref} = 11.11 psi, the tunnel static pressure at M_O = 0.8.

Likewise, in Figure 26, with the exception of the points at M_{HT} = 0.751, all the data were taken at constant altitude (30,000 feet) and, hence, constant pressure. The values measured at M_{HT} = 0.751 were adjusted to reflect the change from 20,000 to 30,000 feet. Additionally, the boom data were adjusted to free field by subtracting 4 dB, as before; while 6 dB were subtracted from the fuselage readings. Finally, Figure 27 combines Jetstar and wind tunnel data and predictions (for this figure, the wind tunnel conditions of Figure 25 were taken as standard). Two adjustments were applied to the Jetstar data of Figure 26; namely:

1. From 4.364 ---> 11.111 psi .... + 8.12 dB (ambient pressure)
2. From 2.65 ---> 4.01 feet ..... - 3.60 dB (measurement distance)

   Total adjustment = + 4.52 dB.

Examination of these figures shows that the measured and predicted values of Figure 25 are in good agreement, up to a tip helical Mach number of about 1.1. Beyond this point, the predicted levels continue to increase with increasing tip helical Mach number, but the measured data appear to level off. This flattening of the curve is not seen in the Jetstar data (Figures 26 and 27), wherein the boom data can be seen to be in good agreement with the (wind tunnel) predictions, but the fuselage microphones show a consistently lower level.

In Reference 2.1.28, Dittmar reexamined the SR-2 and SR-3 data from the wind tunnel and Jetstar. He concluded that whereas both exhibited a tendency for the peak SPL in the blade passing frequency tone to remain constant at high helical tip Mach numbers; the flattening out occurred earlier with the SR-2 than with the SR-3. The SR-3 propfan was used for the present study because of the availability of a greater number of flow solutions. However, the agreement between data and theory as illustrated in Figures 21, 23, and 24 for the SR-2 propfan is such as to suggest that the theoretical prediction would exhibit the same trend as the data for this unswept planform.

In conclusion, these results show that the approach of combining nonlinear aerodynamics with linear acoustics has led to good agreement with data acquired with the boom microphones on the Jetstar for both the SR-2 and SR-3 model propfans. Of the three measurement "environments" available, the boom microphones most closely model the free field assumed in the theory. Data from the Jetstar fuselage is thought to be affected by the fuselage boundary layer (Reference 2.1.22), and the different trends with increasing helical tip Mach number observed on the Jetstar and in the wind tunnel are confusing. The SR-6 results shown suggest that the assumptions made as to spanwise and chordwise loading distributions, although reasonable, were not as good a representation of the flow field on the blading as that obtained from the Euler solutions for SR-3 and SR-2. The agreement for the SR-3 and SR-2 propfans suggests that the worries expressed over the degree of convergence of the flow solution outside the blading were unfounded, and also that flow solutions obtained at operating conditions that are not identical to those under which acoustic data were taken can still provide useful and valid input to an acoustic calculation.

The predicted results used in the above-described data/theory comparisons were obtained from a far field, frequency-domain, acoustic model with a semiempirical adjustment to take near field effects into consideration. A second approach to this problem is discussed briefly in Reference 2.1.28 and in Section 2.1.1.2 of this report, and is given here in more detail. The basic premise is that, since the three-dimensional flow solution describes the blade-to-blade pressure field in a frame-of-reference (locked to the rotor), by allowing this field to rotate, the time-varying pressure perceived by an observer is obtained. This can then be Fourier analyzed to obtain the acoustic near field.

A NASPROP-E solution of the design point case (M_o = 0.8, M_{HT} = 1.15) of the SR-3 propfan with 24,750 grid points (21 in the blade-to-blade direction) was utilized to investigate the feasibility of the use of 3D Euler flow solutions in the prediction of the acoustic near field of a high speed propfan.

A projection of the first meridional surface was used to establish the radial and axial locations at which the calculation should be performed. These were selected to coincide with the angular positions of the microphones in the NASA 8- by 6-foot wind tunnel test (Reference 2.1.23). The selected positions are identified in Figure 28.

For the current investigation, a Fourier analysis of the rotating pressure field was conducted at two values of (R/R_{tip}) for each angular position under consideration (75°, 90°, 100°, and 110°); namely R/R_{tip} = 1.0, in all cases, and R/R_{tip} = 2.7965, except at 75°, where the second calculation was performed at R/R_{tip} = 2.18. At each location, the computed pressure distribution in the blade-to-blade direction was interpolated to 101 points and Fourier analyzed to extract the harmonic content. Adjustments were made to these results to account for differences in static pressure between the wind tunnel and computational conditions, and differences between the computed and measured power coefficients under which the propfan was operating. The computed results were then extrapolated out to the sideline distance at which the measurements were made, using a simple $1/r^2$ law.

Figures 29 through 32 compare these data with the results obtained as described above. The data used for comparison were obtained from Reference 2.1.23 and have been adjusted to free field conditions (-6 dB), and corrected for an error (+ 6 dB) discovered after the original report was published (Reference 2.1.27). These corrected results are best examined in light of Figure 28, which gives some indication of how the computational grid used may influence the calculation.

At 75°, there is only one data point for comparison (Figure 29). The fundamentals of BPF calculated at the two radii are in close agreement, but are approximately 10 dB below the measured value. Higher harmonics fall off more rapidly at the greater radius. Consideration of Figure 28 shows that at R/R_{tip} = 1, the 75° ray is in a region where the axial grid is in transition from the coarse spacing used over the leading edge of the nacelle, to the much finer spacing used on the blade. At R/R_{tip} = 2.18, the grid is considerably coarser. It appears that the pressure field in both locations is affected by the grid, with the greater refinement of the points nearest the blade contributing to the slower falloff with increasing harmonic number.

Similar arguments can be applied at 90° (Figure 30). An apparently very good agreement of the fundamental BPF measured with that calculated at the tip radius is evident. The falloff of the calculated harmonics suggests that greater resolution is required in the blade-to-blade direction.

At 100°, the story appears somewhat different (Figure 31). Here the values calculated using the nearer radius are actually higher than the measured data, while the fundamental BPF calculated from the further radius is in very good agreement with measurement. This is believed to be due to the fact that at R/R_{tip} = 1.0, the calculation is performed at the physical tip of the blade. It is believed that there is a genuine near-field effect in this calculation, whose rapid decay rate is not accounted for by the simple distance rule applied to the calculated values.

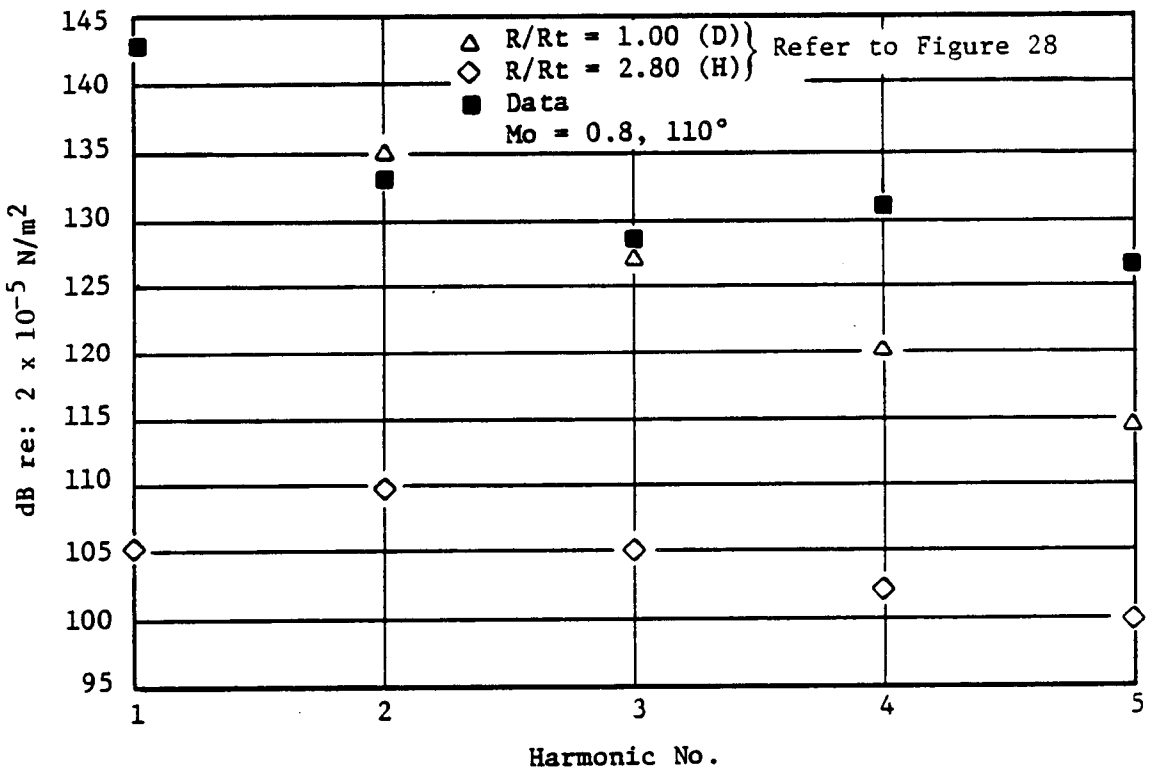

Figure 32. Near Field Data/Theory Comparison Using NASPROP-E Flow Solution at θ_o = 110°.

At 110° (Figure 32), the grid at the outer radius is extremely coarse. This is believed to be the reason for the very low values calculated. At the inner radius, on the other hand, agreement with data is obtained for the first three harmonics of BPF. This is also the angle at which the highest levels of noise were measured, so agreement between data and theory here is encouraging. Again, the degree of agreement in the higher harmonics is thought to be grid-dependent.

In view of the difficulties involved in interpreting these predictions without the benefit of measured data, and bearing in mind the added computational time and cost of obtaining solutions with a sufficient number of grid points in the blade-to-blade direction to guarantee adequate resolution for the acoustic calculation, this approach was abandoned until such time as available computers are found to have decreased in cost and increased in speed; each by an order of magnitude.

2.1.4 Conclusions

The following conclusions were drawn:

- A far field, frequency domain, noncompact source, linear acoustic model has been developed and programmed to predict the steady loading and thickness components of the noise generated by a high speed single rotation propfan.
- This model has been combined with loading distributions obtained from three-dimensional nonlinear aerodynamic Euler code flow solutions to predict the noise generated by two different model propfans, both in flight and in the wind tunnel; simplified loading distributions have been used to predict the noise from a third propfan.
- Comparisons between measured and predicted data show, on the whole, good agreement; differences between data and theory are of the same order as differences between data sets.
- The results show that nonconvergence of the flow solution in the region outside the blading does not necessarily compromise the acoustic calculation.
- The use of flow solutions directly in the calculation of near-field noise requires greater grid resolution than is practical at this point in time.

2.2 Installation Effects on Single Rotation Propeller Noise

2.2.1 Introduction

The objective of this study was to develop an approximate, analytical model to compute the additional noise produced by a single rotation propeller as a result of installation effects. The three installation effects considered herein are: the angle-of-attack (defined as the angle between the freestream and the propeller axis), the effect of wing-induced flow, and the effect

of flow induced by an axisymmetric body of revolution representing the fuselage. The calculation procedure is as follows.

First, the steady loading and thickness noise of the propeller is calculated. Next, the nonuniform axial and tangential flow fields induced at the propeller plane are developed for the three installation effects to be evaluated. Quasi-steady propeller aerodynamic theory is used to compute the induced unsteady axial and tangential forces on the propeller due to these nonuniform flow fields. In order to better account for unsteady effects, a phase lag deduced from linearized, two-dimensional, compressible, flat plate gust response theory is used in conjunction with the quasi-steady analysis to estimate the unsteady forces, which are then utilized in conjunction with an acoustic analysis to derive the far field noise.

The noise field due to installation effects has been found experimentally to be distinctly nonaxially symmetric (with respect to the propeller axis), and hence, the phase between the noise field due to steady loading (and thickness) and that due to unsteady loading must be accounted for.

The following material is discussed in four categories:

- Calculation of nonuniform flow fields due to angle-of-attack, wing loading, and an axisymmetric body of revolution representing the fuselage
- Unsteady force calculation
- Acoustic calculation linking the far field noise due to unsteady loading, steady loading, and thickness
- Data/theory comparisons.

2.2.2 Calculation of Nonuniform Flow Fields

2.2.2.1 Angle-of-Attack

This source of nonuniformity is obviously explicitly calculable and yields the simple result that, with the coordinate system shown in Figure 33, for small angles-of-attack (α) such that $\cos\alpha \sim 1$, the angle-of-attack induces a tangential velocity perturbation (v):

$$v = U\sin\alpha\cos\phi$$

where U, α, and ϕ are defined in Figure 33.

2.2.2.2 Wing Loading

The flow field due to wing loading is calculated according to a model discussed in Article 12.4 of Reference 2.2.1. In this model, the flow field is associated with an airfoil of span 2s' (with 2s denoting the true wing span) with constant circulation K and the associated trailing vortex system (the reader is referred to Figure 93 of Reference 2.2.1).

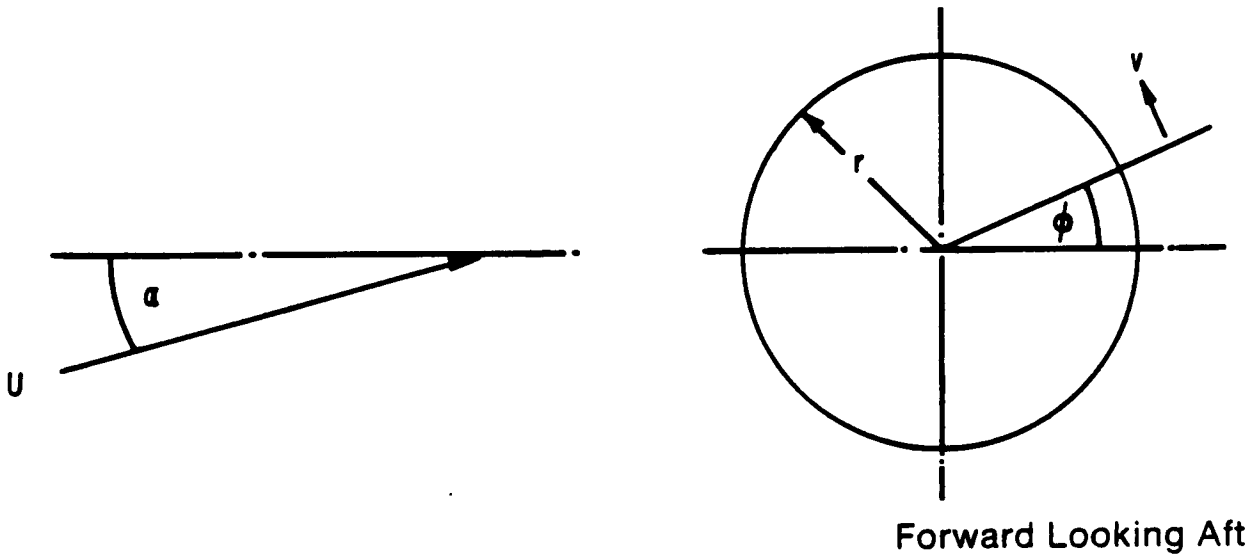

Figure 33. Definition Sketch of Angle-of-Attack and r-ϕ Coordinate System.

For an airfoil with elliptic loading, (s'/s) can be shown to be (π/4), and, given the lift coefficient and aspect ratio of the wing (C_L, AR), we can calculate K by:

$$\bar{K} = C_L \frac{4}{\pi} s \frac{U}{AR} \qquad (2.2.2)$$

Knowing K and s', the full expression for the three-dimensional flow field due to the above horseshoe vortex system is given on Pages 158 and 159 of Reference 2.2.1. These expressions are used to calculate the induced axial and tangential velocities in terms of radial location, r, and azimuthal angle, ϕ. Apart from C_L, and s, an input to such a calculation (in addition to r, and ϕ) is the location of the center of the propeller disk relative to the wing.

2.2.2.3 Flow Field Due to an Axisymmetric Body of Revolution

The axisymmetric body of revolution chosen is a Rankine solid (Reference 2.2.2). This is the closed streamline shape generated by superposition of a uniform flow (U), a point source and sink (of strength "m") separated by a distance "2a" in the direction of the stream. If the total length of the body is "2l," and its maximum radius "h", then m and a are determined by the solution of:

$$4alm = U(l^2-a^2)^2 \qquad (2.2.3)$$

$$4ma = Uh^2 \sqrt{h^2-a^2} \qquad (2.2.4)$$

Thus, knowing the total length of the body and a slenderness ratio parameter (such as "h/l"), its flow field can be computed. Finally, the chosen body of revolution must be located

relative to the wing. This can be accomplished, for example, by specifying the location of the forward stagnation point of the body relative to the wing.

2.2.2.4 Total Flow Field

Given the above analytical expressions for the three sources of nonuniform flow, the resultant flow field is computed at several fixed radii as a function of azimuthal angle, ϕ, in the propeller disk plane (Figure 34). At each fixed radius, the axial and tangential nonuniform velocity components are developed in a Fourier series in ϕ of the form:

$$\sum_{k=1}^{N} a_k \cos\left(k(\phi-\phi_k)\right)$$

"N" is chosen typically as 7 or 8. This Fourier decomposition is carried out numerically using an FFT (Fast Fourier Transform) algorithm.

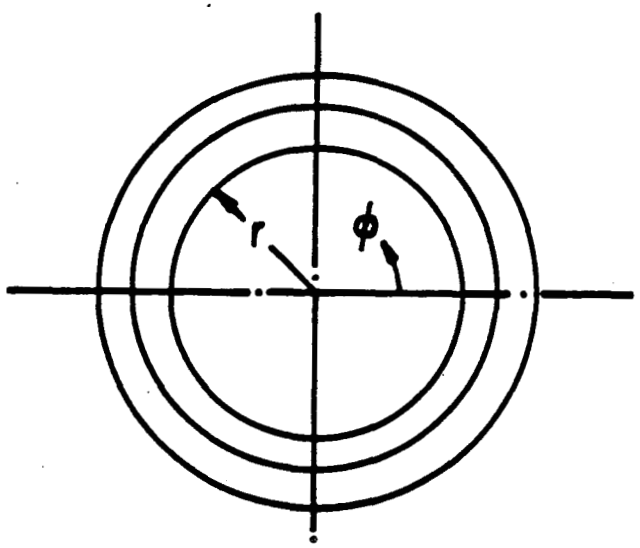

Figure 34. Circles Around Which Fourier Analysis of u, v Distortions is Carried Out.

2.2.3 Unsteady Force Calculation

2.2.3.1 Quasi-Steady Formulation

Let $u(r, \pi)$, $v(r, \phi)$ denote externally contributed nonuniform axial and tangential velocities incident on the plane of the propeller disk. "u" is taken positive in the downstream direction and "v" is taken positive in the direction of propeller rotation.

If "R" denotes the tip radius of the propeller disk and "R_h" the hub radius, u and v are defined for $R_h \leq r \geq R$, and $0 \leq \phi \geq 2\pi$.

At any radius, the quasi-steady forces (thrust and tangential force) are obtained in the functional form:

$$F = \Omega^2 f(\lambda)$$

where "Ω" denotes the propeller rotational velocity in radians per second, and "λ" the speed ratio "$U/\Omega R$," where U is the advance velocity of the propeller.

The change in the force, F, due to u and v can be obtained as follows.

In the quasi-steady approximation, changes in Ω and λ due to u and v, will be:

$$\delta \Omega = - \frac{v}{r}$$

$$\delta \lambda = \lambda \left(\frac{u}{U} + \frac{v}{\Omega r} \right)$$

The resulting change in F can be written:

$$\delta F = 2\Omega f(\lambda)\delta\Omega + \Omega^2 \left(\frac{\partial f}{\partial \lambda} \right) \delta\lambda$$

$$= \left[-2F + \lambda \left(\frac{\partial F}{\partial \lambda} \right) \right] \frac{v}{\Omega r} + \left(\frac{\partial F}{\partial \lambda} \right) \frac{u}{\Omega R}$$

Thus, if u, v are nondimensionalized by introducing:

$$u' = \frac{u}{\Omega R} \quad \text{and} \quad v' = \frac{v}{\Omega R}$$

we have:

$$\delta F = \left(-2F + \lambda \frac{\partial F}{\partial \lambda} \right) \frac{R}{r} v' + \frac{\partial F}{\partial \lambda} u'$$

The quasi-steady theory is needed to obtain F and $\partial F/\partial \lambda$.

Now, $\partial F/\partial \lambda$ can be approximated by a central difference formula:

$$\frac{\partial F}{\partial \lambda} \sim \frac{F(\lambda+\varepsilon) - F(\lambda-\varepsilon)}{2\varepsilon}$$

where "ε" is a small increment.

It can be seen that the theory is thus only required to obtain the force F for arbitrary λ since $\partial F/\partial \lambda$ can be approximated by numerical differentiation as outlined above.

The theory needed to compute both axial and tangential forces is based on that of Glauert as presented in Reference 2.2.3. The formulation is based on incompressible flow theory and the inputs needed are: relative radius (r/R) of interest, solidity (chord/transverse spacing) at this radius of interest, number of blades, specification of the section lift and drag coefficients as functions of angle-of-attack (including the orientation of the reference line with reference to which the angle-of-attack is specified), and the speed ratio, $\lambda = U/\Omega R$. The version used for the work described herein incorporates the Prandtl tip loss factor. (There is a misprint in the development in Reference 2.2.3 - Equations 5.5 and 5.6 of Chapter VII - accounting for the tip loss factor. This misprint is also pointed out by E.E. Larrabee in SAE Paper 790585.) The essence of the analysis is the solution of two simultaneous nonlinear algebraic equations (for the so-called axial and tangential interference factors.)

2.2.3.2 Phase Lag Effects

The quasi-steady theory discussed above is felt to be the most appropriate for the large-scale low-frequency distortions resulting from the installation geometries addressed in Section 2.2.2. It is accepted that, in a quasi-steady theory, phase lag or lead effects are not accounted for. On the other hand, features of the problem related to the fact that a propeller (possibly with a large number of blades) is involved are recognized. To improve the accounting for unsteady aerodynamic effects, phase lag (or lead) effects have been included in the development, based on a two-dimensional, linearized, compressible flow gust response theory. The expressions used are those of Goldstein (Reference 2.2.4). At any given radius, if the rotor angular velocity is Ω, the relative velocity V_r is taken as:

$$\sqrt{U^2 + \Omega^2 r^2},$$

and the relative Mach number, M_r, is just the same quantity divided by the ambient speed of sound. The reduced frequency, σ_k, is a function of the Fourier component of the relevant non-uniform velocity and can be written: $\sigma_k = k\Omega c/2V_r$ where "c" is the propeller blade chord at radius "r." Defining a parameter, p, as $\sigma_k M_r/(1-M_r)^2$, Goldstein's Equation 3.71 of Reference 2.2.4 is used if p is less than unity, and $M_r < 1$. Otherwise Equation 3.70 of the same reference is used. It should be emphasized that, in the present study, only the phase lag (that is, the argument of the complex numbers in Equations 3.70 or 3.71 of Reference 2.2.4) is deduced from the linearized, two-dimensional gust response theory. The amplitude employed is computed from quasi-steady theory. The data/theory comparisons of Section 2.2.5 show the effects of including phase lag in the calculations.

2.2.4 Acoustic Calculation

In the work described herein, the acoustic source distributions are assumed to be acoustically compact in the chordwise direction. In other words, a line source model is employed. At time "t = 0," let the location of this line source be as shown in Figure 35, and let the sweep be as shown in Figure 36. Thus, "$\alpha_1(r)$" and "$\Delta x(r)$" define the radial lean and axial sweep of the blades. The following results were derived for the purposes of this work by the use of axial Fourier transforms and the method of stationary phase, but they are in agreement with results

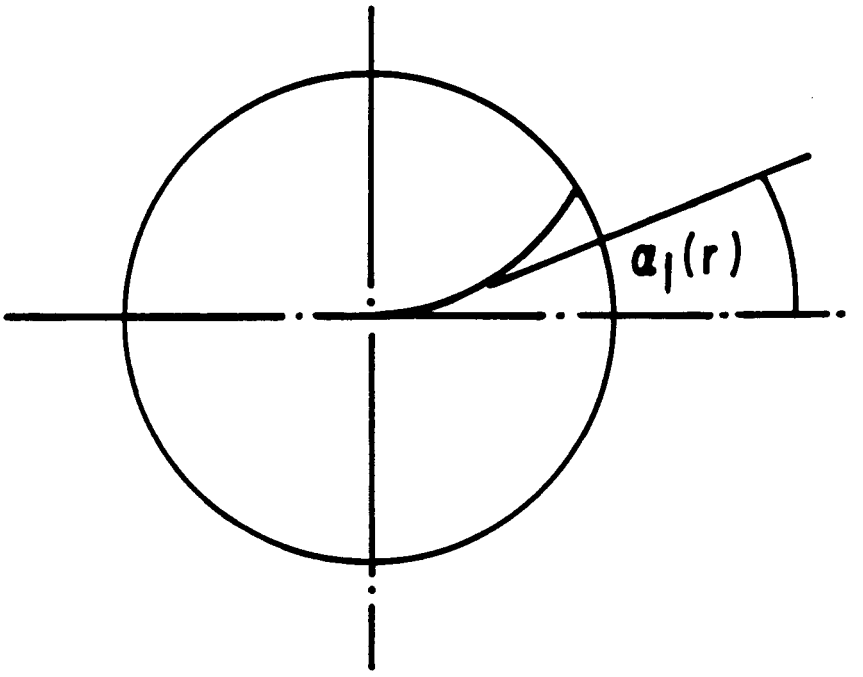

Figure 35. Definition Sketch for Radial Lean.

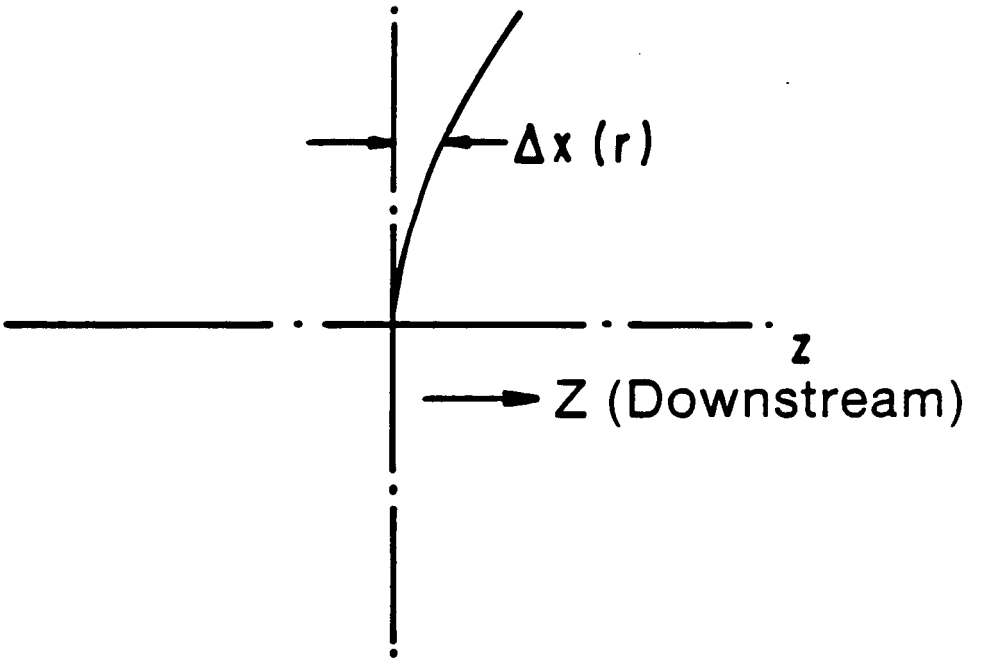

Figure 36. Definition Sketch for Axial Sweep.

given by Hawkings and Lowson (Reference 2.2.5) and Hanson (Reference 2.2.6), and hence, only the final result of the analysis is shown.

The contribution to "p_o" from the blade element lying between "r" and "r + dr" is given by:

$$\frac{dp_o}{dr} = \frac{jnB^2\Omega}{2\pi Rc\,(1-M_F\cos\theta)}\; J_{\pm nB}\left[\frac{nB\Omega r\,\sin\theta}{c\,(1-M_F\cos\theta)}\right]$$

$$\exp\left[j\left[\frac{k(R+\Delta x\cos\theta)}{(1-M_F\cos\theta)} \pm nB\,(\phi-\tfrac{\pi}{2}) \mp nB\alpha_1(r) - \frac{nB\Omega t}{(1-M_F\cos\theta)}\right]\right]$$

$$\left[\frac{f_{zo}\cos\theta}{(1-M_F\cos\theta)} \mp \frac{cf_{\phi o}}{\Omega r} + \frac{jnB\rho_o c\Omega h1}{(1-M_F\cos\theta)^2}\right] \qquad (2.2.5)$$

In Equation 2.2.5, the far field noise is expressed in terms of R, θ (the coordinates of the observer relative to the "retarded" propeller disk location.) The relationship between these coordinates and R_c, θ_c (the coordinates of the observer relative to the current propeller disk location) is shown in Figures 37 and 38. In Equation 2.2.5, wherever two signs appear, the upper sign refers to counterclockwise rotor rotation, and the lower sign to clockwise rotation (forward looking aft).

Now consider the noise due to unsteady loading. Let the unsteady loading per blade per unit spanwise length in a frame of reference fixed with a rotating blade be expressed in the form:

$$\text{Unsteady z component} = \sum_{k=1}^{\infty} f_{zk}\cos(k\Omega t) \qquad (2.2.6)$$

and

$$\text{Unsteady } \phi \text{ component} = \sum_{k=1}^{\infty} f_{\phi k}\cos(k\Omega t) \qquad (2.2.7)$$

Both f_{zk} and $f_{\phi k}$ are positive functions of "r." Also, let $\beta_{zk}(r)$ and $\beta_{\phi k}(r)$ denote the azimuthal angles in the coordinate system of Figure 33 where these unsteady components achieve their maximum positive values. Then, unsteady loading noise from blade elements lying between "r" and "r + dr" contributes to the far field pressure a quantity dp_k/dr, given by the sum of:

$$\left(\frac{dp_k}{dr}\right)_+ \text{ and } \left(\frac{dp_k}{dr}\right)_-$$

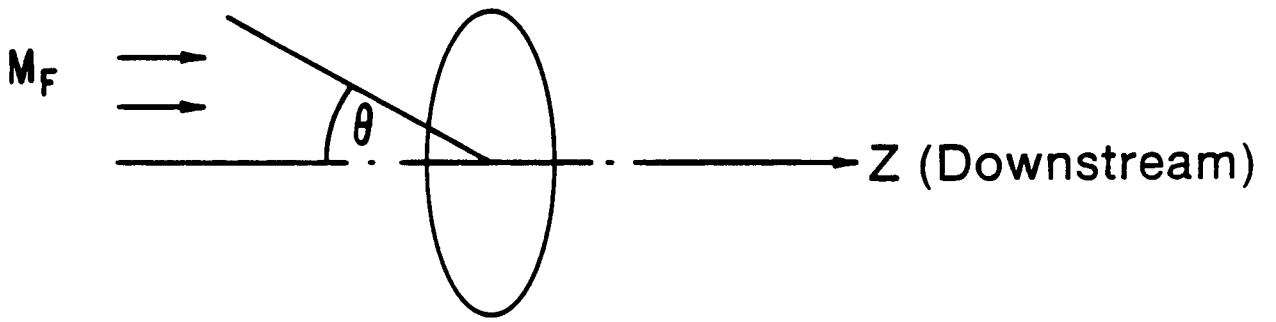

Figure 37. Definition Sketch for θ.

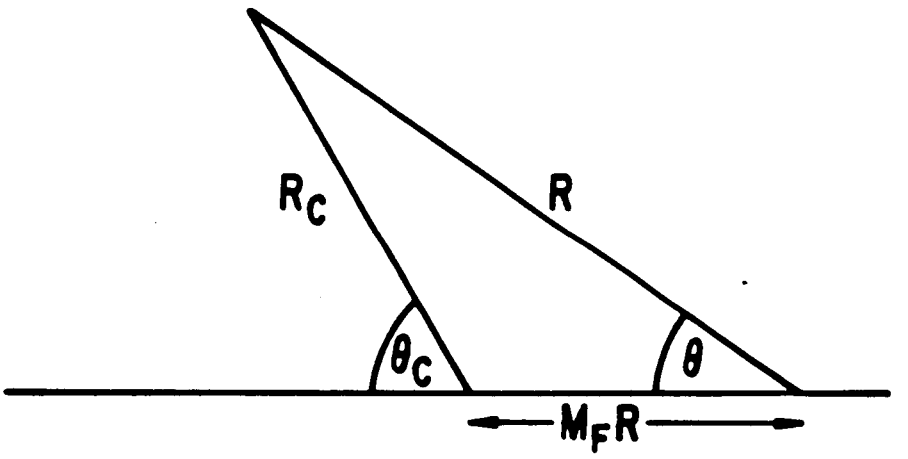

Figure 38. Current and Retarded Coordinates.

where

$$\left(\frac{dp_k}{dr}\right)_+ = \frac{jnB^2\Omega}{4\pi Rc(1-M_F\cos\theta)} \cdot J_{(\pm nB+k)}\left[\frac{nB\Omega r\sin\theta}{c(1-M_F\cos\theta)}\right]$$

$$\exp\left[j\left[\frac{\bar{k}(R+\Delta x\cos\theta)}{(1-M_F\cos\theta)} + (\pm nB+k)\left(\phi-\frac{\pi}{2}\right) \mp nB\alpha_1(r) - \frac{nB\Omega t}{(1-M_F\cos\theta)}\right]\right]$$

$$\left[\frac{\exp(-jk\beta_{zk})\, f_{zk}\cos\theta}{(1-M_F\cos\theta)} \mp \frac{c\exp(-jk\beta_{\phi k}) f_{\phi k}(nB\pm k)}{nB\Omega r}\right] \qquad (2.2.8)$$

and

$$\left(\frac{dp_k}{dr}\right)_- = \frac{jnB^2\Omega}{4\pi Rc(1-M_F\cos\theta)} \cdot J_{(\pm nB-k)}\left[\frac{nB\Omega r\sin\theta}{c(1-M_F\cos\theta)}\right]$$

$$\exp\left[j\left[\frac{\bar{k}(R+\Delta x\cos\theta)}{(1-M_F\cos\theta)} + (\pm nB-k)\left(\phi-\frac{\pi}{2}\right) \mp nB\alpha_1(r) - \frac{nB\Omega t}{(1-M_F\cos\theta)}\right]\right]$$

$$\left[\frac{\exp(jk\beta_{zk})\, f_{zk}\cos\theta}{(1-M_F\cos\theta)} \mp \frac{c\exp(jk\beta_{\phi k}) f_{\phi k}}{nB\,\Omega r}(nB \mp k)\right] \qquad (2.2.9)$$

The total far field acoustic pressure can now be computed as:

$$p = \int_{r_h}^{r_t}\left[\frac{dp_o}{dr} + \sum_{k=1}^{\infty}\left(\frac{dp_k}{dr}\right)_+ + \sum_{k=1}^{\infty}\left(\frac{dp_k}{dr}\right)_-\right]dr \qquad (2.2.10)$$

where r_h and r_t denote the inner and outer radii of the propeller disk, respectively, and where "p" is a complex number whose amplitude gives the amplitude of the far field pressure in the nth harmonic of blade passing frequency.

The above formulation could, perhaps, be expressed more concisely with more extensive use of complex notation. However, it was felt that it was preferable to restrict consideration to positive n and k and, also, to consider both clockwise and counterclockwise rotating propellers. These interests, and the desire to be accurate concerning phase relations, have led to the above formulations. One minor addition has been made to the above equation.

The existence of unsteady thickness noise has been recognized for the following reason. The thickness noise arises from a source term related to the product of the relative velocity

incident on a blade section and its thickness. Since this relative velocity varies in magnitude around the propeller disk, unsteady thickness noise can arise. Consequently, this source has been taken into account in the computer program associated with this work.

2.2.5 Comparisons Between Data and Predictions

Data/theory comparisons have principally been carried out using data from Reference 2.2.7. Only angle-of-attack effects have been examined in this case. Predictions have also been made for the SR-3 propeller data of Reference 2.2.8. Assumptions made in order to perform the comparisons are noted below:

- Blade section lift and drag coefficients (versus angle-of-attack) were calculated from performance maps given for the SR-2 model propeller in Reference 2.2.9, and for the SR-3 model propeller in Reference 2.2.10. Model propeller blade geometry information was also obtained from these sources.

- The SR-2 noise data of Reference 2.2.7 were obtained at both an 8° and 10° angle-of-attack. The theoretical calculations were performed at an angle-of-attack of 9°. In addition, the SR-2 tested acoustically and described in Reference 2.2.7 differs from that utilized for the performance evaluation of Reference 2.2.9; in that, due to power limitations, a four-bladed configuration was used for the acoustic data acquisition, rather than the eight-bladed configuration of Reference 2.2.9. It was assumed that this change did not affect the behavior of the lift and drag versus angle-of-attack characteristics.

- The representative airfoil thickness was taken as one-fourth the maximum thickness at a given radial location.

- The measurement angles quoted in the acoustic data are taken to observe angles as shown in Figure 38. This neglects shear layer corrections in the data of Reference 2.2.7 (which should be small in view of the low axial velocities of the freejet).

- Because the phase lag formulae discussed earlier apply only to convected two-dimensional gusts, their use in the present context could be challenged. Therefore, results are presented both with and without the use of such phase lag.

Comparisons for the SR-2 low tip speed case are contained in Figures 39 through 47. These comparisons are rather encouraging (especially in the case of Figures 46 and 47), with regard to the data scatter. The SR-2 high tip speed comparisons are also encouraging (Figures 48 through 56), although clearly both the measured and predicted effects of angle-of-attack are small and hence the comparisons are somewhat inconclusive.

Some theoretical calculations relevant to the data reported in Reference 2.2.8 are shown in Figures 57 through 59. Figure 59 is interesting in that it shows that, if the phase lag in the force response is neglected, the theoretical predictions are in accord with the comments in

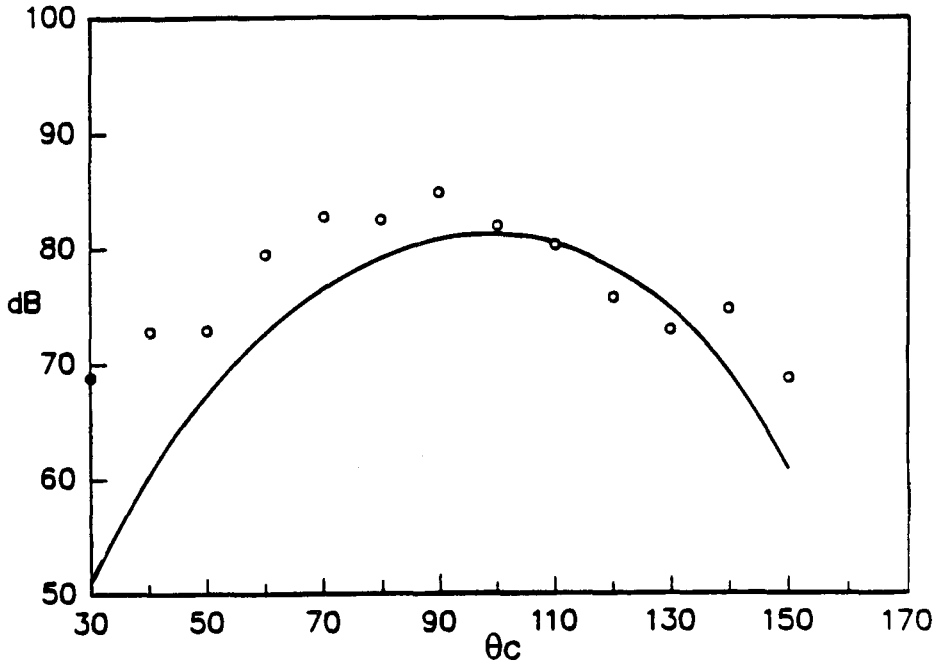

Figure 39. Four-Bladed SR-2, 443-fps Tip Speed, 100-fps Forward Flight Speed, Fundamental Blade Passing Frequency Noise. Acoustic Data Source is Reference 2.2.7, Symbols are Measured Data, and Full Line is Theoretical Prediction. Noise at Zero Angle-of-Attack Versus θ at 35-inch Radius from Center of Propeller.

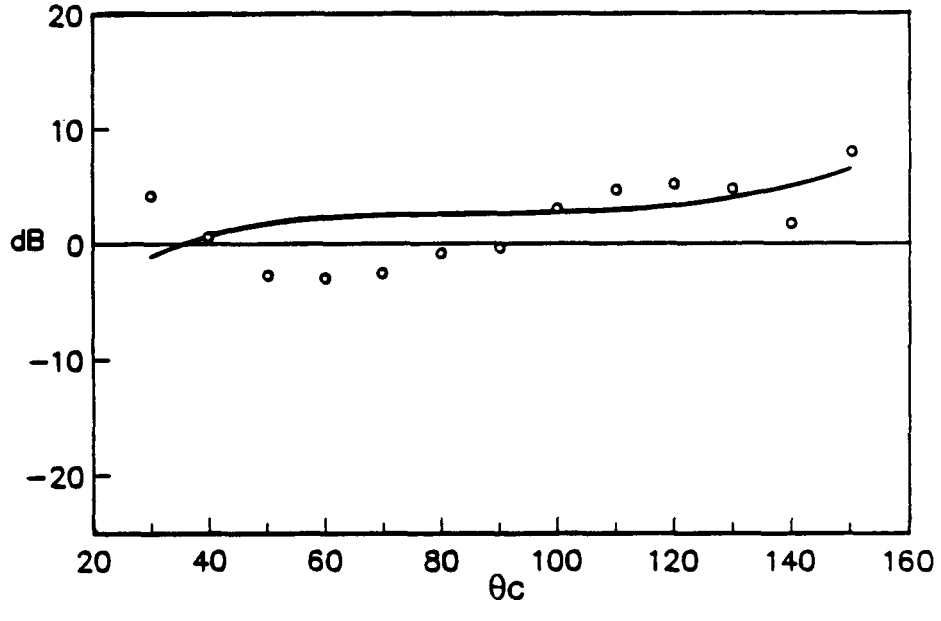

Figure 40. Four-Bladed SR-2, 443-fps Tip Speed, 100-fps Forward Flight Speed, Fundamental Blade Passing Frequency Noise. Acoustic Data Source is Reference 2.2.7, Symbols are Measured Data, and Full Line is Theoretical Prediction. Increase/Decrease of Noise Due to 9° Angle-of-Attack (Relative to Zero Angle-of-Attack) Versus θ. ϕ = 0°, Phase Lag in Force Response Neglected in Theoretical Prediction.

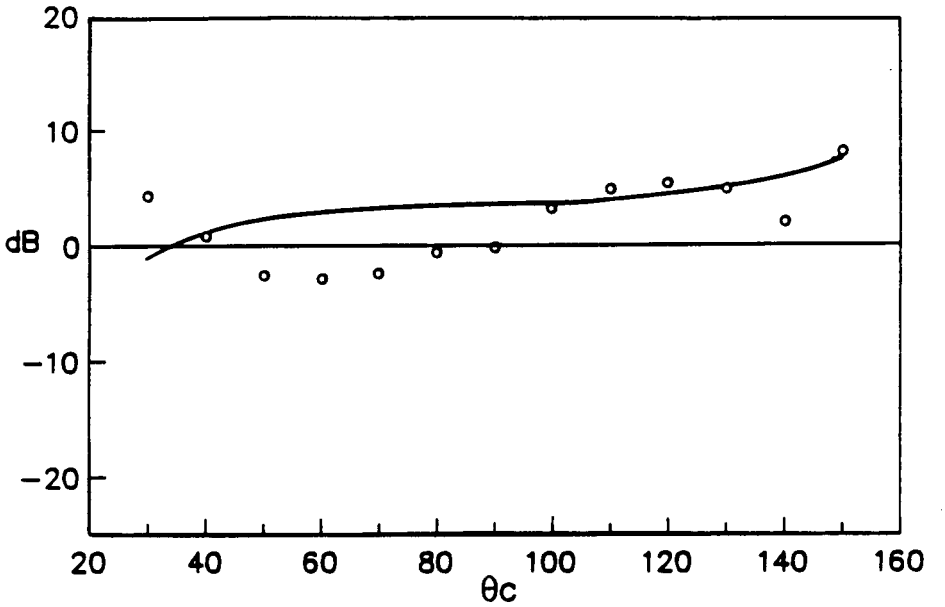

Figure 41. Four-Bladed SR-2, 443-fps Tip Speed, 100-fps Forward Flight Speed, Fundamental Blade Passing Frequency Noise. Acoustic Data Source is Reference 2.2.7, Symbols are Measured Data, and Full Line is Theoretical Prediction. Increase/Decrease of Noise Due to 9° Angle-of-Attack (Relative to Zero Angle-of-Attack) Versus θ. ϕ = 0°, Phase Lag in Force Response Included in Theoretical Prediction.

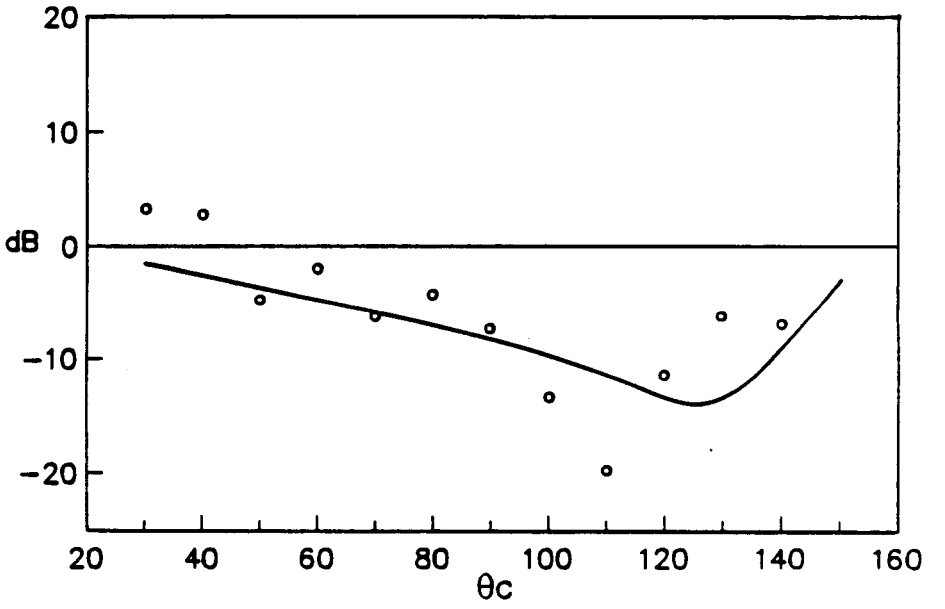

Figure 42. Four-Bladed SR-2, 443-fps Tip Speed, 100-fps Forward Flight Speed, Fundamental Blade Passing Frequency Noise. Acoustic Data Source is Reference 2.2.7, Symbols are Measured Data, and Full Line is Theoretical Prediction. Increase/Decrease of Noise Due to 9° Angle-of-Attack (Relative to Zero Angle-of-Attack) Versus θ. ϕ = 90°, Phase Lag in Force Response Neglected in Theoretical Prediction.

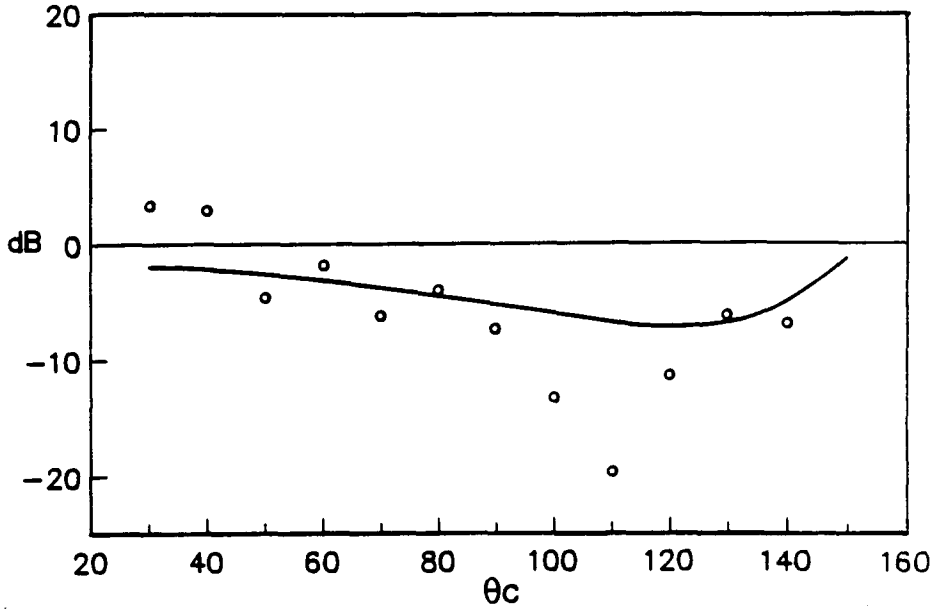

Figure 43. Four-Bladed SR-2, 443-fps Tip Speed, 100-fps Forward Flight Speed, Fundamental Blade Passing Frequency Noise. Acoustic Data Source is Reference 2.2.7, Symbols are Measured Data, and Full Line is Theoretical Prediction. Increase/Decrease of Noise Due to 9° Angle-of-Attack (Relative to Zero Angle-of-Attack) Versus θ. ϕ = 90°, Phase Lag in Force Response Included in Theoretical Prediction.

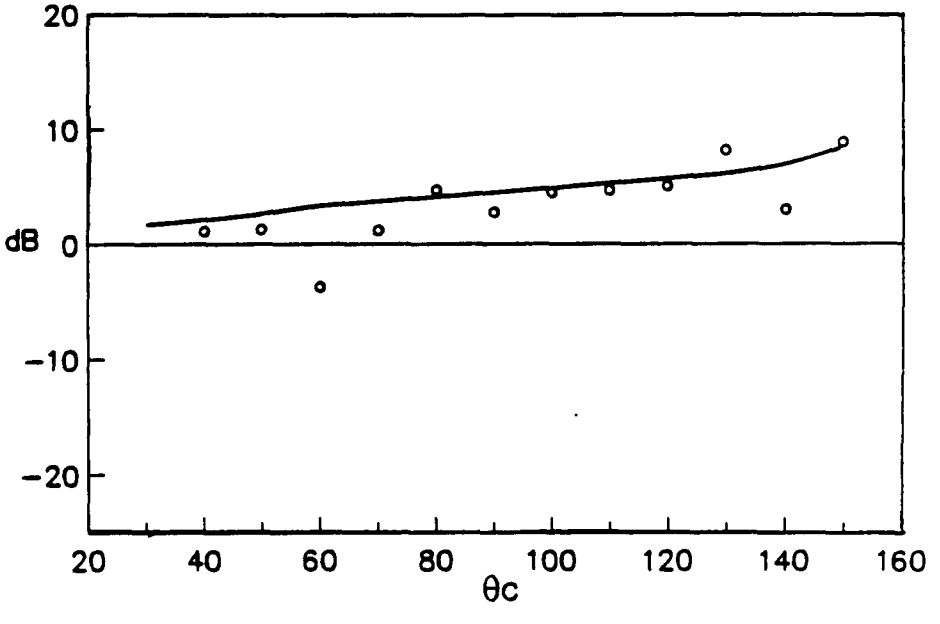

Figure 44. Four-Bladed SR-2, 443-fps Tip Speed, 100-fps Forward Flight Speed, Fundamental Blade Passing Frequency Noise. Acoustic Data Source is Reference 2.2.7, Symbols are Measured Data, and Full Line is Theoretical Prediction. Increase/Decrease of Noise Due to 9° Angle-of-Attack (Relative to Zero Angle-of-Attack) Versus θ. ϕ = 270°, Phase Lag in Force Response Neglected in Theoretical Prediction.

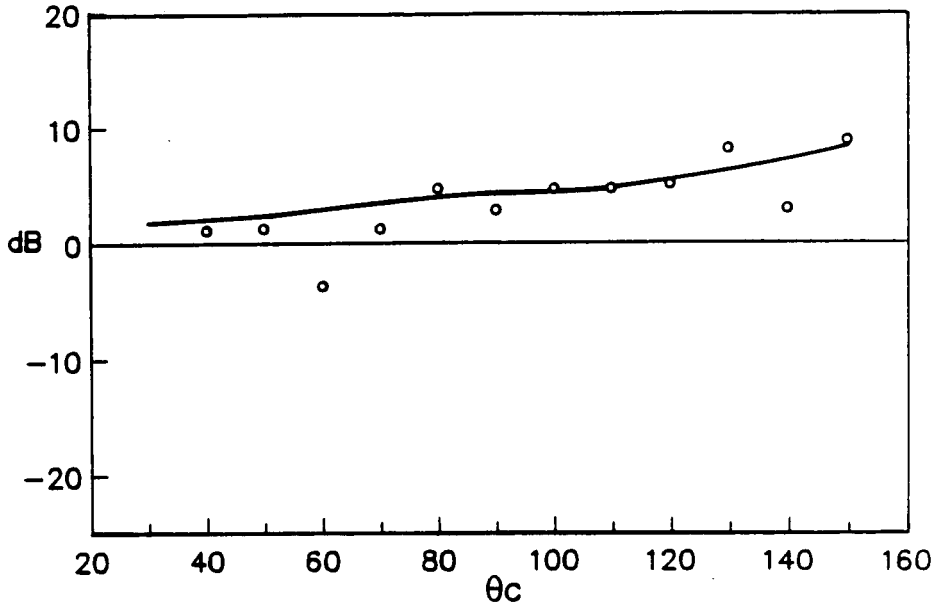

Figure 45. Four-Bladed SR-2, 443-fps Tip Speed, 100-fps Forward Flight Speed, Fundamental Blade Passing Frequency Noise. Acoustic Data Source is Reference 2.2.7, Symbols are Measured Data, and Full Line is Theoretical Prediction. Increase/Decrease of Noise Due to 9° Angle-of-Attack (Relative to Zero Angle-of-Attack) Versus θ. ϕ = 270°, Phase Lag in Force Response Included in Theoretical Prediction.

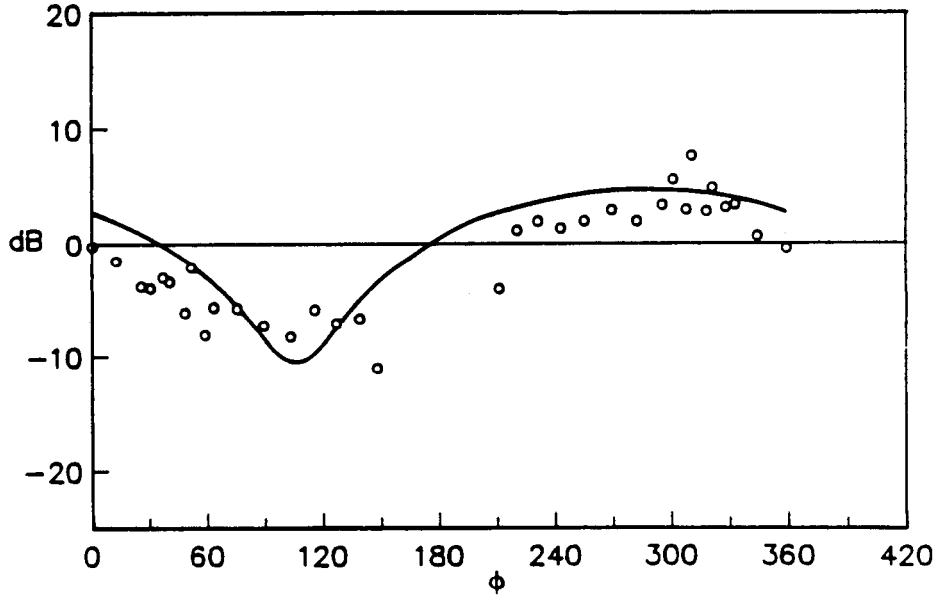

Figure 46. Four-Bladed SR-2, 443-fps Tip Speed, 100-fps Forward Flight Speed, Fundamental Blade Passing Frequency Noise. Acoustic Data Source is Reference 2.2.7, Symbols are Measured Data, and Full Line is Theoretical Prediction. Increase/Decrease of Noise Due to 9° Angle-of-Attack (Relative to Zero Angle-of-Attack) Versus ϕ, θ = 90°, Phase Lag in Force Response Neglected in Theoretical Prediction.

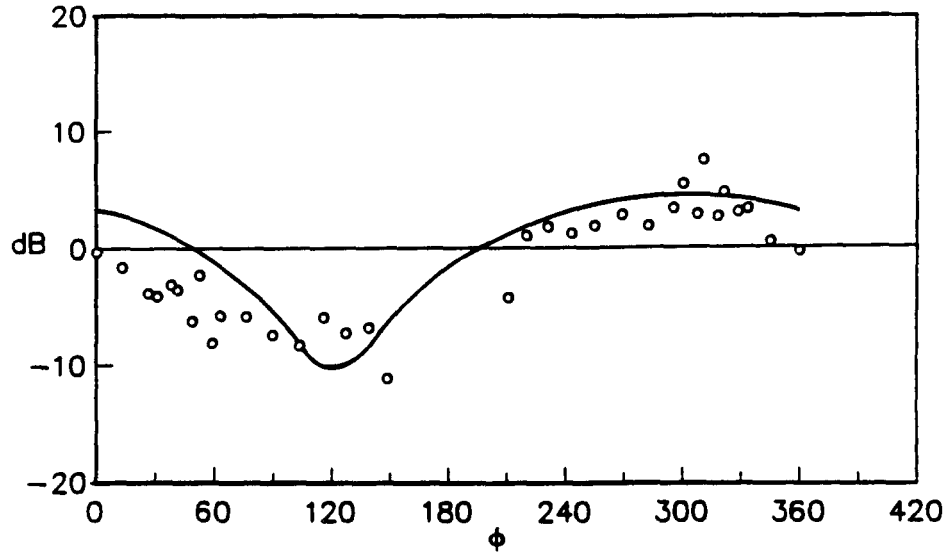

Figure 47. Four-Bladed SR-2, 443-fps Tip Speed, 100-fps Forward Flight Speed, Fundamental Blade Passing Frequency Noise. Acoustic Data Source is Reference 2.2.7, Symbols are Measured Data, and Full Line is Theoretical Prediction. Increase/Decrease of Noise Due to 9° Angle-of-Attack (Relative to Zero Angle-of-Attack) Versus ϕ, θ = 90°, Phase Lag in Force Response Included in Theoretical Prediction.

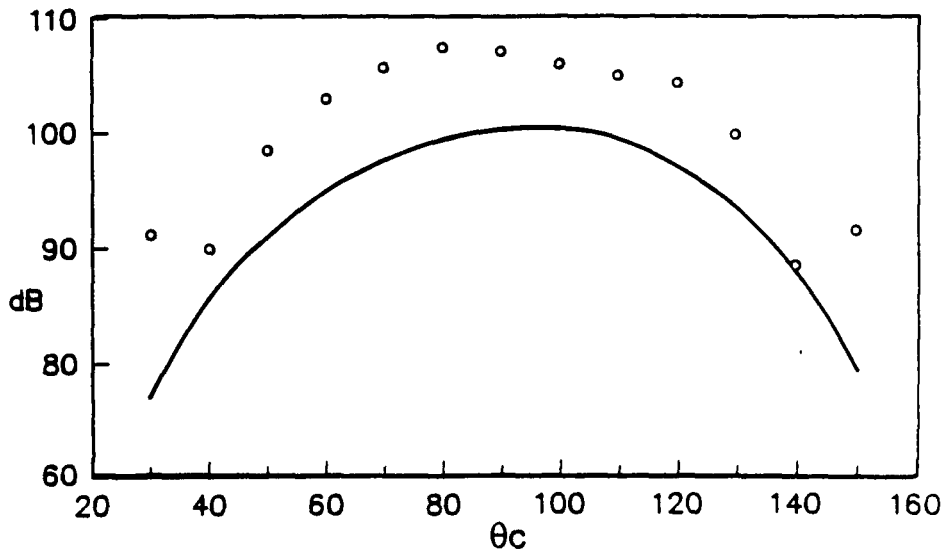

Figure 48. Four-Bladed SR-2, 745-fps Tip Speed, 100-fps Forward Flight Speed, Fundamental Blade Passing Frequency Noise. Acoustic Data Source is Reference 2.2.7, Symbols are Measured Data, and Full Line is Theoretical Prediction. Noise at Zero Angle-of-Attack Versus θ at 35-inch Radius from Center of Propeller.

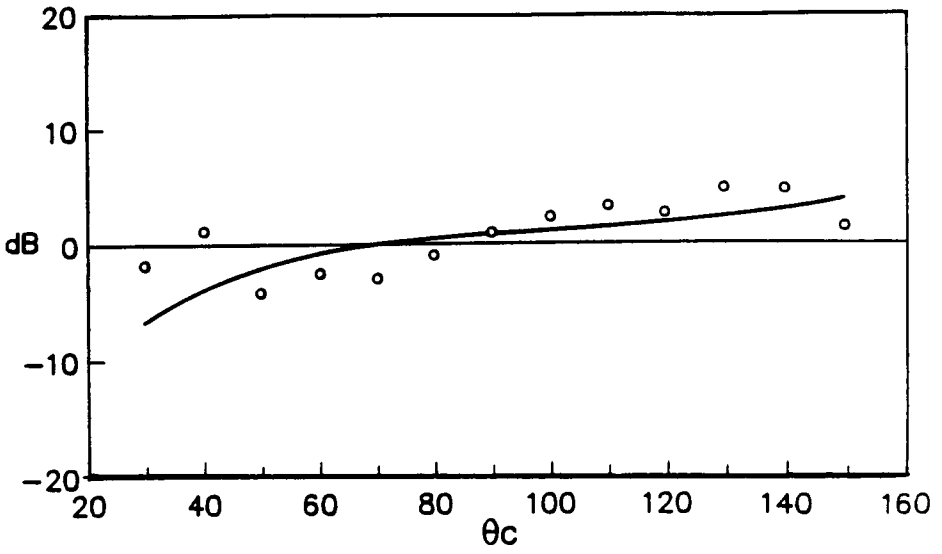

Figure 49. Four-Bladed SR-2, 745-fps Tip Speed, 100-fps Forward Flight Speed, Fundamental Blade Passing Frequency Noise. Acoustic Data Source is Reference 2.2.7, Symbols are Measured Data, and Full Line is Theoretical Prediction. Increase/Decrease of Noise Due to 9° Angle-of-Attack (Relative to Zero Angle-of-Attack) Versus θ. ϕ = 0°, Phase Lag in Force Response is Neglected in Theoretical Prediction.

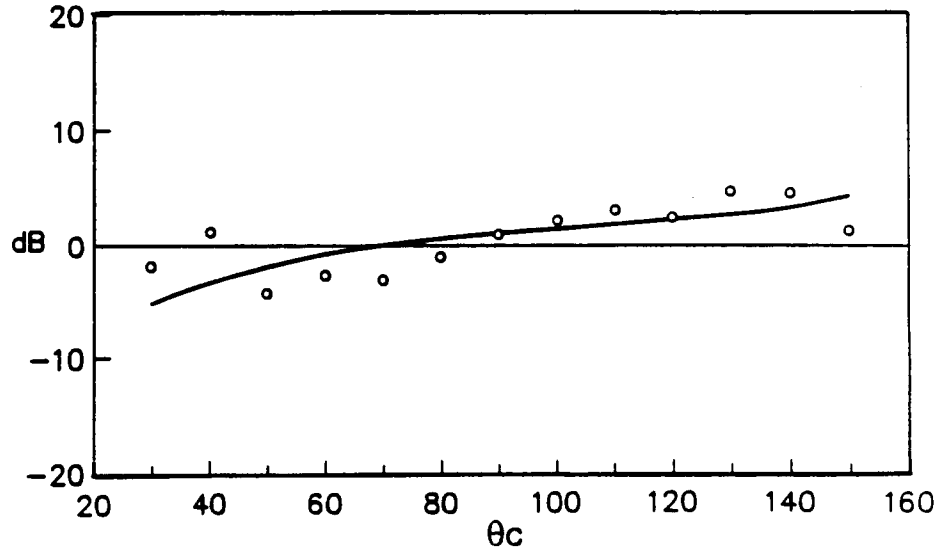

Figure 50. Four-Bladed SR-2, 745-fps Tip Speed, 100-fps Forward Flight Speed, Fundamental Blade Passing Frequency Noise. Acoustic Data Source is Reference 2.2.7, Symbols are Measured Data, and Full Line is Theoretical Prediction. Increase/Decrease of Noise Due to 9° Angle-of-Attack (Relative to Zero Angle-of-Attack) Versus θ. ϕ = 0°, Phase Lag in Force Response is Included in Theoretical Prediction.

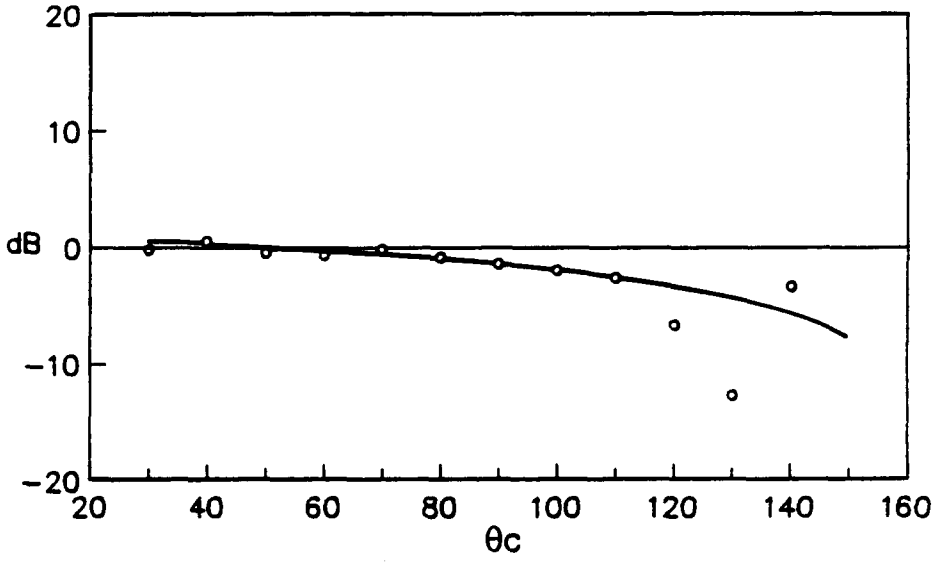

Figure 51. Four-Bladed SR-2, 745-fps Tip Speed, 100-fps Forward Flight Speed, Fundamental Blade Passing Frequency Noise. Acoustic Data Source is Reference 2.2.7, Symbols are Measured Data, and Full Line is Theoretical Prediction. Increase/Decrease of Noise Due to 9° Angle-of-Attack (Relative to Zero Angle-of-Attack) Versus θ. ϕ = 90°, Phase Lag in Force Response is Neglected in Theoretical Prediction.

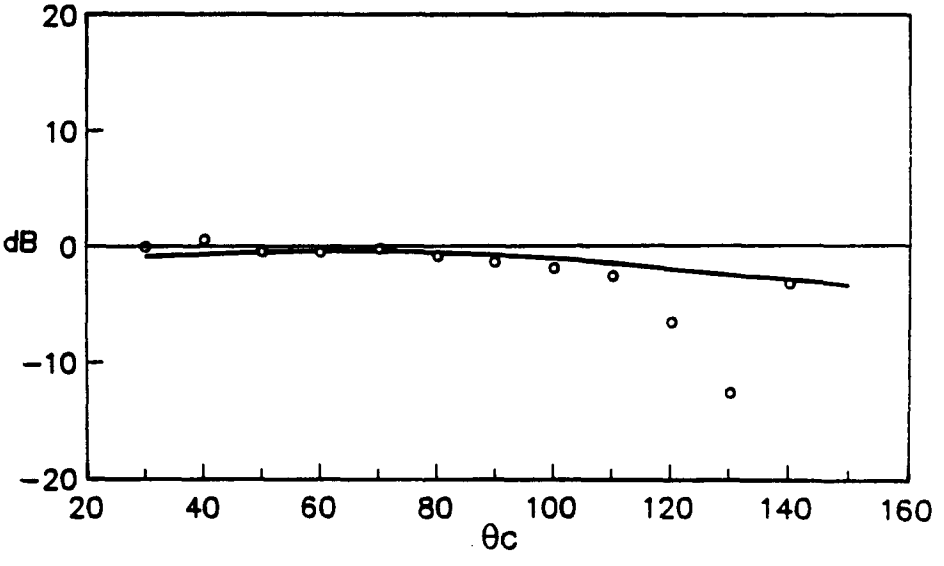

Figure 52. Four-Bladed SR-2, 745-fps Tip Speed, 100-fps Forward Flight Speed, Fundamental Blade Passing Frequency Noise. Acoustic Data Source is Reference 2.2.7, Symbols are Measured Data, and Full Line is Theoretical Prediction. Increase/Decrease of Noise Due to 9° Angle-of-Attack (Relative to Zero Angle-of-Attack) Versus θ. ϕ = 90°, Phase Lag in Force Response is Included in Theoretical Prediction.

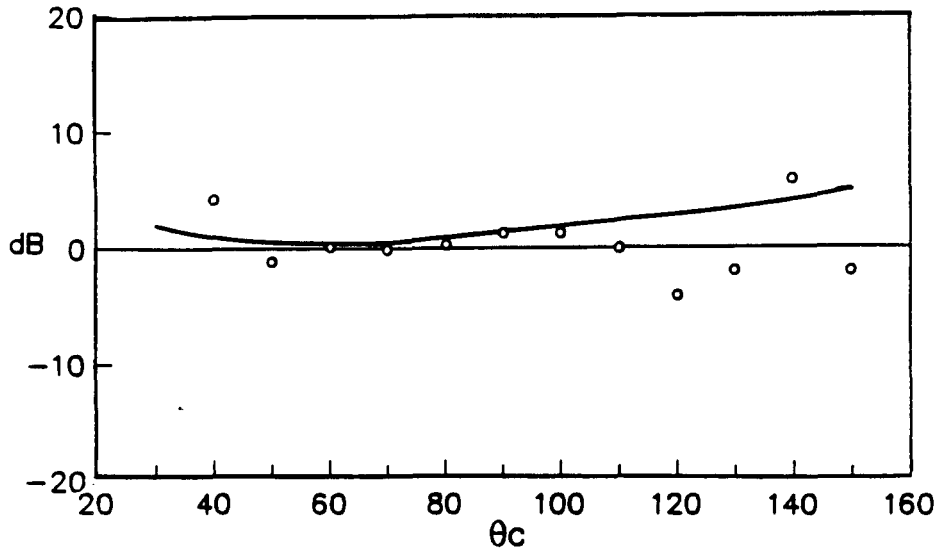

Figure 53. Four-Bladed SR-2, 745-fps Tip Speed, 100-fps Forward Flight Speed, Fundamental Blade Passing Frequency Noise. Acoustic Data Source is Reference 2.2.7, Symbols are Measured Data, and Full Line is Theoretical Prediction. Increase/Decrease of Noise Due to 9° Angle-of-Attack (Relative to Zero Angle-of-Attack) Versus θ. ϕ = 270°, Phase Lag in Force Response is Neglected in Theoretical Prediction.

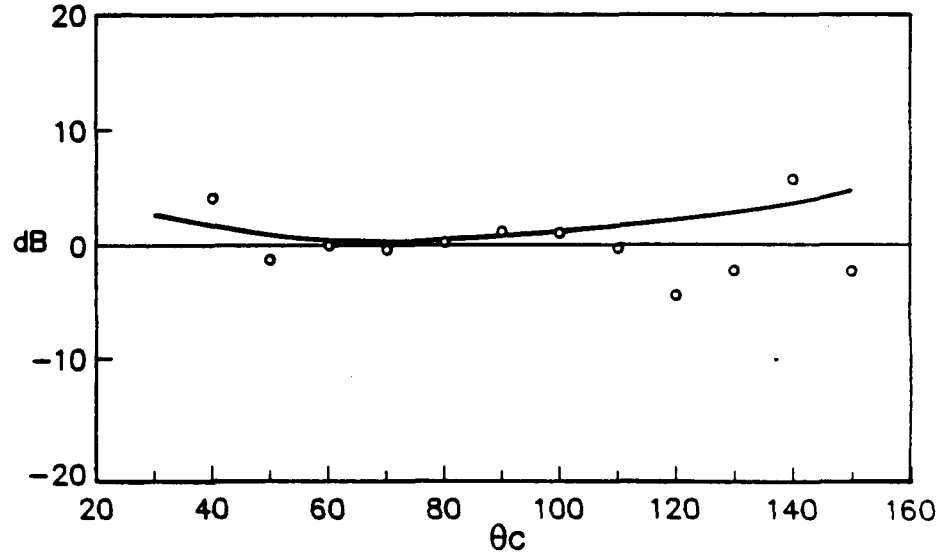

Figure 54. Four-Bladed SR-2, 745-fps Tip Speed, 100-fps Forward Flight Speed, Fundamental Blade Passing Frequency Noise. Acoustic Data Source is Reference 2.2.7, Symbols are Measured Data, and Full Line is Theoretical Prediction. Increase/Decrease of Noise Due to 9° Angle-of-Attack (Relative to Zero Angle-of-Attack) Versus θ. ϕ = 270°, Phase Lag in Force Response is Included in Theoretical Prediction.

C-2

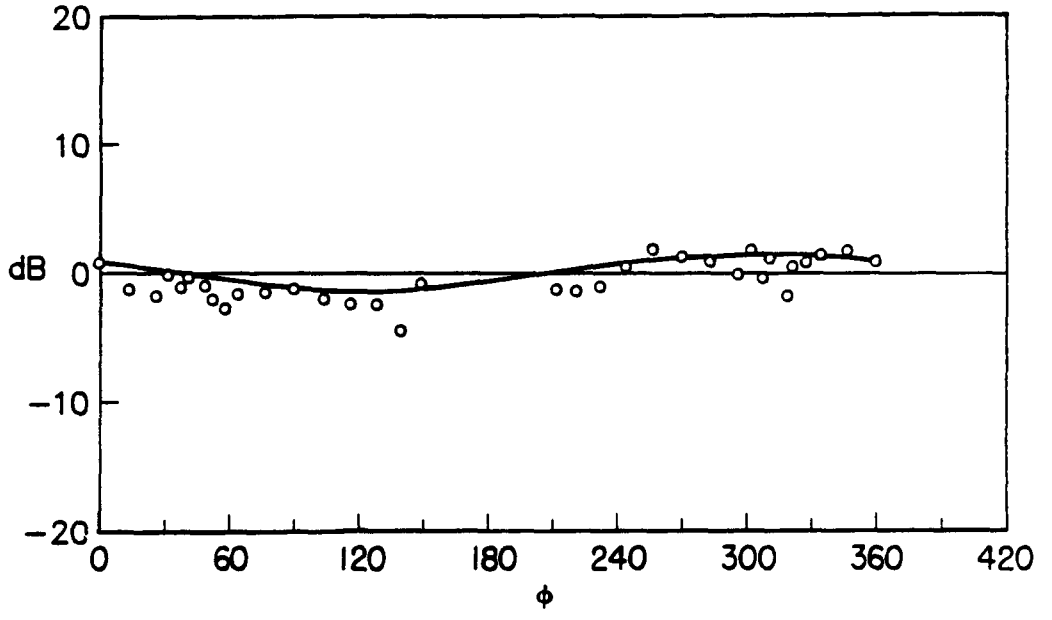

Figure 55. Four-Bladed SR-2, 745-fps Tip Speed, 100-fps Forward Flight Speed, Fundamental Blade Passing Frequency Noise. Acoustic Data Source is Reference 2.2.7, Symbols are Measured Data, and Full Line is Theoretical Prediction. Increase/Decrease of Noise Due to 9° Angle-of-Attack (Relative to Zero Angle-of-Attack) Versus ϕ, θ = 90°, Phase Lag in Force Response is Neglected in Theoretical Prediction.

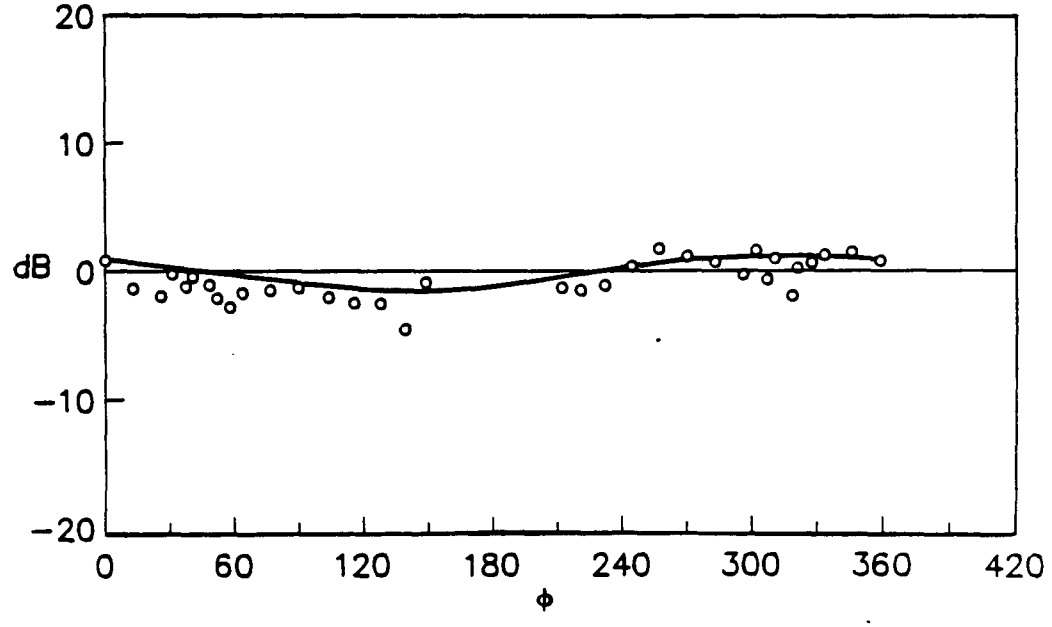

Figure 56. Four-Bladed SR-2, 745-fps Tip Speed, 100-fps Forward Flight Speed, Fundamental Blade Passing Frequency Noise. Acoustic Data Source is Reference 2.2.7, Symbols are Measured Data, and Full Line is Theoretical Prediction. Increase/Decrease of Noise Due to 9° Angle-of-Attack (Relative to Zero Angle-of-Attack) Versus ϕ, θ = 90°, Phase Lag in Force Response is Included in Theoretical Prediction.

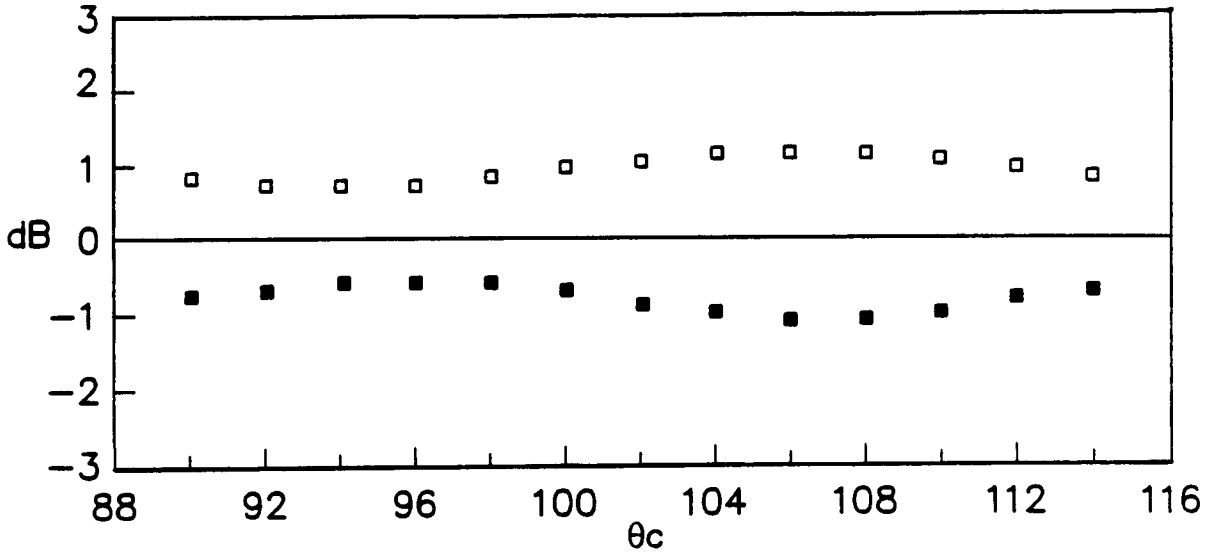

Figure 57. SR-3 Propeller, Forward Flight Mach Number = 0.8, Advance Ratio J = 3.06. Theoretical Predictions for Increase/Decrease of Noise Due to 4° Angle-of-Attack (Relative to Zero Angle-of-Attack) Shown by Symbols. Open Symbols are for ϕ = 0° (North Wall of Reference 2.2.8), and Closed Symbols are for ϕ = 180 ° (South Wall of Reference 2.2.8). Phase Lag in Force Response Neglected in Theoretical Prediction.

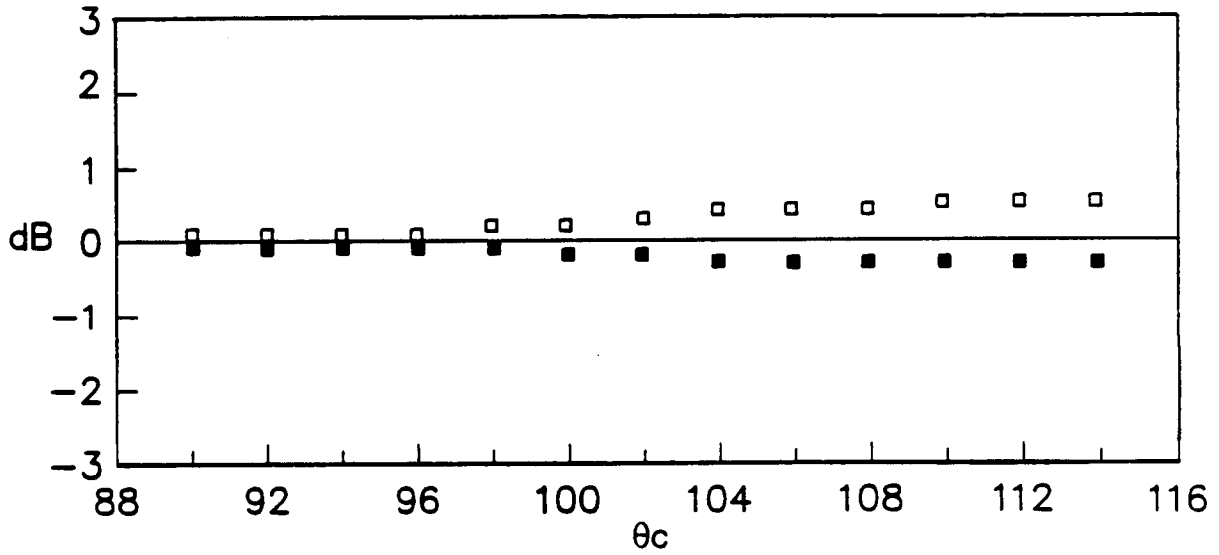

Figure 58. SR-3 Propeller, Forward Flight Mach Number = 0.8, Advance Ratio J = 3.06. Theoretical Predictions for Increase/Decrease of Noise Due to 4° Angle-of-Attack (Relative to Zero Angle-of-Attack) Shown by Symbols. Open Symbols are for ϕ = 0° (North Wall of Reference 2.2.8), and Closed Symbols are for ϕ = 180° (South Wall of Reference 2.2.8). Phase Lag in Force Response Neglected in Theoretical Prediction. Sweep of SR-3 Propeller Artifically Suppressed.

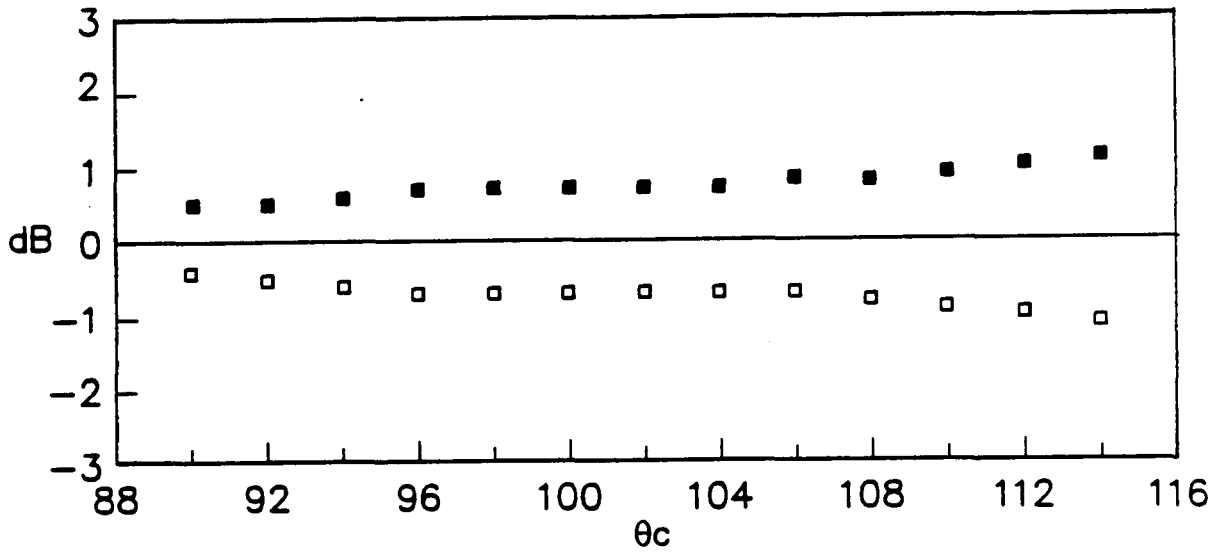

Figure 59. SR-3 Propeller, Forward Flight Mach Number = 0.8, Advance Ratio J = 3.06. Theoretical Predictions for Increase/Decrease of Noise Due to 4° Angle-of-Attack (Relative to Zero Angle-of-Attack) Shown by Symbols. Open Symbols are for ϕ = 0° (North Wall of Reference 2.2.8) and Closed Symbols are for ϕ = 180° (South Wall of Reference 2.2.8). Phase Lag in Force Response Included in Theoretical Prediction.

Reference 2.2.8; namely, that due to angle-of-attack, the north wall data consistently showed an increase in noise greater than that seen on the south wall (which sometimes showed a noise decrease).

It should be noted that the results presented in Figures 57 through 59 are plotted against "observer" rather than "emitted" angles. (The large forward flight Mach number of 0.8 leads to significant differences between current and retarded coordinates). Figure 58 shows that, if we artificially neglect the large sweep of the SR-3 propeller, the north-south wall asymmetry is predicted to disappear. A comment at the end of Reference 2.2.8 attributes the observed asymmetry in noise to such sweep, and the comparison of Figures 57 and 58 supports this view. Figure 59 shows that inclusion of a phase lag formula for convected two-dimensional gusts apparently gives an asymmetry exactly the reverse of that seen in Figure 57. This also is contrary to the data reported in Reference 2.2.8.

2.2.6 Concluding Remarks

The data/theory comparisons of Figures 39 through 56 are believed to constitute a somewhat stringent evaluation in that, essentially, differences in decibels due to angle-of-attack at specific microphone locations are being compared. These differences were obtained from measured, tabulated data which (in the case of Figures 39 through 56) were kindly supplied by the author of Reference 2.2.7. Less stringent tests would involve some smoothed version of the data, perhaps the examination of absolute levels in the form of contour plots, rather than specific differences due to angle-of-attack at precise microphone locations.

As illustrated (Figures 39 through 59), the areas of discrepancy are, by and large, confined to angles close to the propeller axis. Agreement between data and prediction improves significantly around the plane of rotation. Comparison between propeller noise prediction and data at angular locations close to the axis of rotation is always somewhat difficult, due to the low levels of noise present at such locations. The data shown in Figures 46 and 55 are of special interest, because there is some redundancy in the data shown here, and hence, some idea can be gained of the degree of data scatter. The results depicted in Figures 57 and 59 definitely support a conclusion that a phase lag formula deduced from two-dimensional, convected gust response theory for flat plate airfoils should not be used at this time.

It is recommended that the present analysis, without the above-mentioned phase lag term, be used to determine the installation effect on single rotation propeller noise. The result of such an exercise should be useful, particularly for angles around the plane of rotation.

2.3 Scattering of Propeller Noise by Aircraft Fuselage and Wings

2.3.1 Introduction

When free-field predictions of propeller noise are compared to measured flight and/or wind tunnel data, it is recognized that transducers installed on fuselage surfaces, or on wind tunnel walls do not record free-field acoustic radiation levels (see, for example, References 2.3.1 and 2.3.2). Several corrections become necessary in order to account for various forms

of acoustic scattering, such as reflection, refraction, and diffraction. Quantitative estimates of these effects are necessary, not only for comparison of predicted and measured propeller noise, but also for assessing the possible advantages in engine placement relative to fuselage and wing surfaces. Further, the nature of the sound field and its spatial distribution on and around the fuselage is of great relevance in the design of fuselage structures for minimizing sound transmission into the cabin.

The next subsection presents the nature of the problem, with respect to reflection, refraction, and diffraction. This is followed (in Section 2.3.2) by a detailed discussion of the analysis of propeller noise scattering by a cylindrical fuselage. The incident field is represented by pairs of helical waves emitted upstream and downstream of the propeller disk. The frequencies of the emitted field are determined by the harmonics of propeller blade passing frequency, and the associated spinning mode numbers are equal to the number of propeller blades multiplied by the relevant harmonic number. The radial dependence of the sound field is represented by cylindrical Hankel functions of order equal to the spinning mode number. Scattering calculations are made for the fundamental and two higher harmonics of the blade passing frequency. Results are presented to show the increase and decrease of the sound field on and around the fuselage surface relative to the incident field as a function of relevant parameters.

2.3.1.1 Nature of the Problem with Respect to Reflection, Refraction, and Diffraction

2.3.1.1.1 Reflection

a. **Rigid Flat Surface** - When a plane wave in an ambient homogeneous medium is incident upon a flat rigid surface of infinite extent, it will be reflected with a reflection coefficient of unity and in phase with the incident field. The combined field results in a pressure doubling; that is, a 6 dB increase relative to the incident field. This pressure doubling is independent of the angle of incidence, except at grazing incidence.

b. **Nonrigid Flat Surface** - Under the same conditions as a rigid flat surface (except that the surface is now being replaced by a locally reacting, nonrigid surface), the amplitude and phase of the reflection coefficient now become dependent, not only on the surface admittance, but also on the angle of incidence. The amplitude of the combined field (incident plus reflected) is no longer double that of the incident field; it is lower. The reduction relative to 6 dB depends on the amplitude and phase of the reflected field.

c. **Rigid Curved Surface** - Consider a condition similar to (a) above (except that the surface is no longer flat, but is rather curved in the form of a cylindrical fuselage). Acoustic focusing or defocusing may now be expected. If the surface is curved away from the side where the incident sound is coming from (that is, convex), defocusing produces a surface sound pressure increase of less than 6dB. Such a defocusing

effect was measured by Hubbard (Reference 2.3.3) and is recommended by the SAE for estimating reflection from a circular wall.

In addition to the defocusing effect, this configuration will also have an acoustic shadow region away from the side where the sound field is incident. In fact, sound can reach the shadow region as a result of diffraction. The actual level on the fuselage surface in the shadow region depends on the frequency, being lower for higher nondimensional frequencies based on the fuselage radius.

d. **Nonrigid Curved Surface** - Further changes of surface sound pressure levels are expected relative to case (c) where the surface was rigid.

The main purpose of this brief survey of reflection, or scattering, is to emphasize that the sound pressure level perceived on the surface is a function of the impedance perceived by the incident field. Quantitative estimates of the effects discussed in Items (c) and (d) above may be made using cylindrical scattering analysis. These will be discussed in more detail later and extended to include refraction effects.

2.3.1.1.2 Refraction

a. **Rigid Flat Surface with an Attached Boundary Layer** - In such a case, an incident sound field is refracted (there is a change in the direction of propagation relative to that of the incident field) in the boundary layer before being reflected by the rigid surface as illustrated in Figure 60. Below a certain angle of incidence (the so-called critical angle), the incident field may be so refracted that reflection takes place in the shear layer above the rigid surface.

In such an instance, the rigid surface is shielded from the incident field, and diffraction analysis must be used to estimate the sound field reaching the rigid surface.

Such an analysis has been carried out in 2D by Hanson (Reference 2.3.1), McAninch (Reference 2.3.4) and Mungur (Reference 2.3.5). Hanson studied the refraction effect for a flight configuration using a single and multiple shear layer over a rigid surface. McAninch analyzed the refraction in a wind tunnel configuration. Mungur studied both the flight and the wind tunnel configurations by numerically integrating a reduced form of the acoustic wave equation in the presence of a sheared flow and then matching the incident and reflected fields just outside the shear layer. This is equivalent to determining reflection from a surface at the edge of the shear layer whose admittance is equal to the numerically transferred admittance across the boundray layer of the rigid surface below the boundary layer.

Figures 61 and 62 summarize results of the 2D analysis, for both the flight and the wind tunnel configurations. That significant boundary layer shielding can occur for upstream incidence is the main conclusion reached by all three investigators (Hanson, McAninch, and Mungur).

SOUND FIELD EVALUATION INSIDE B-LAYER

- INCIDENT SOUND
- REFLECTED SOUND
- DIFFRACTED SOUND

} MODIFIED BY CONVECTION & REFRACTION

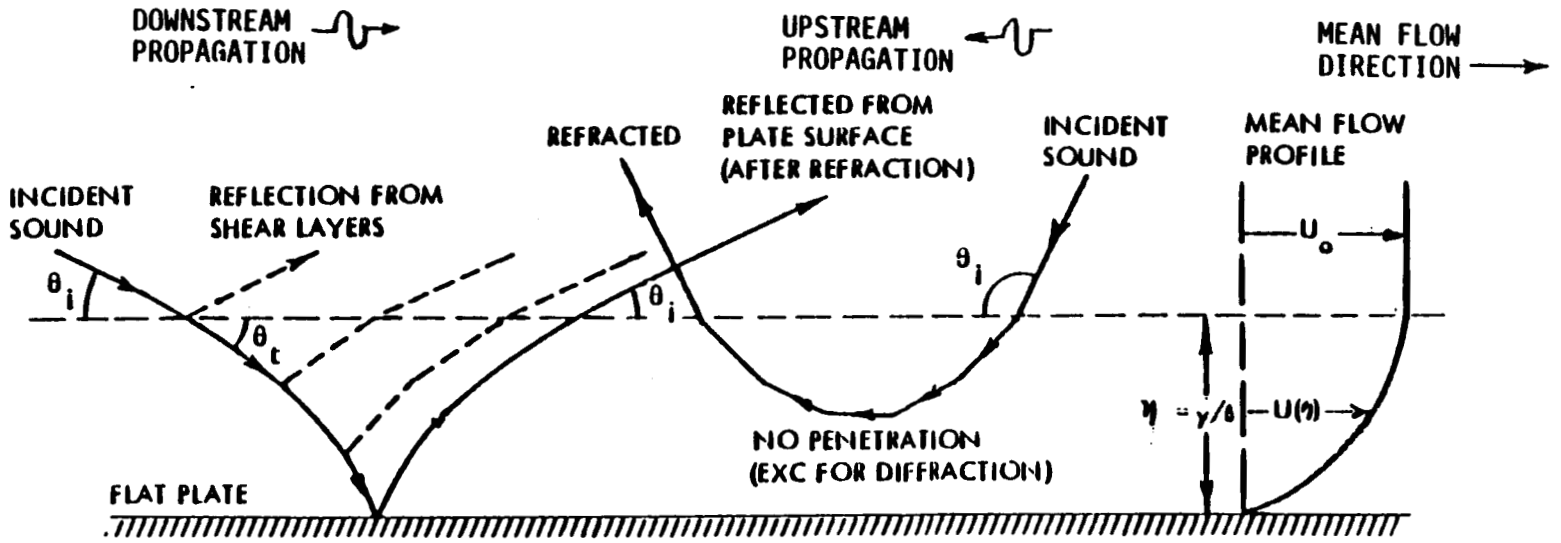

Figure 60. Convection and Refraction of Incident and Reflected Plane Sound Wave in the Boundary Layer of a Rigid Flat Plate in Wind Tunnel Configuration.

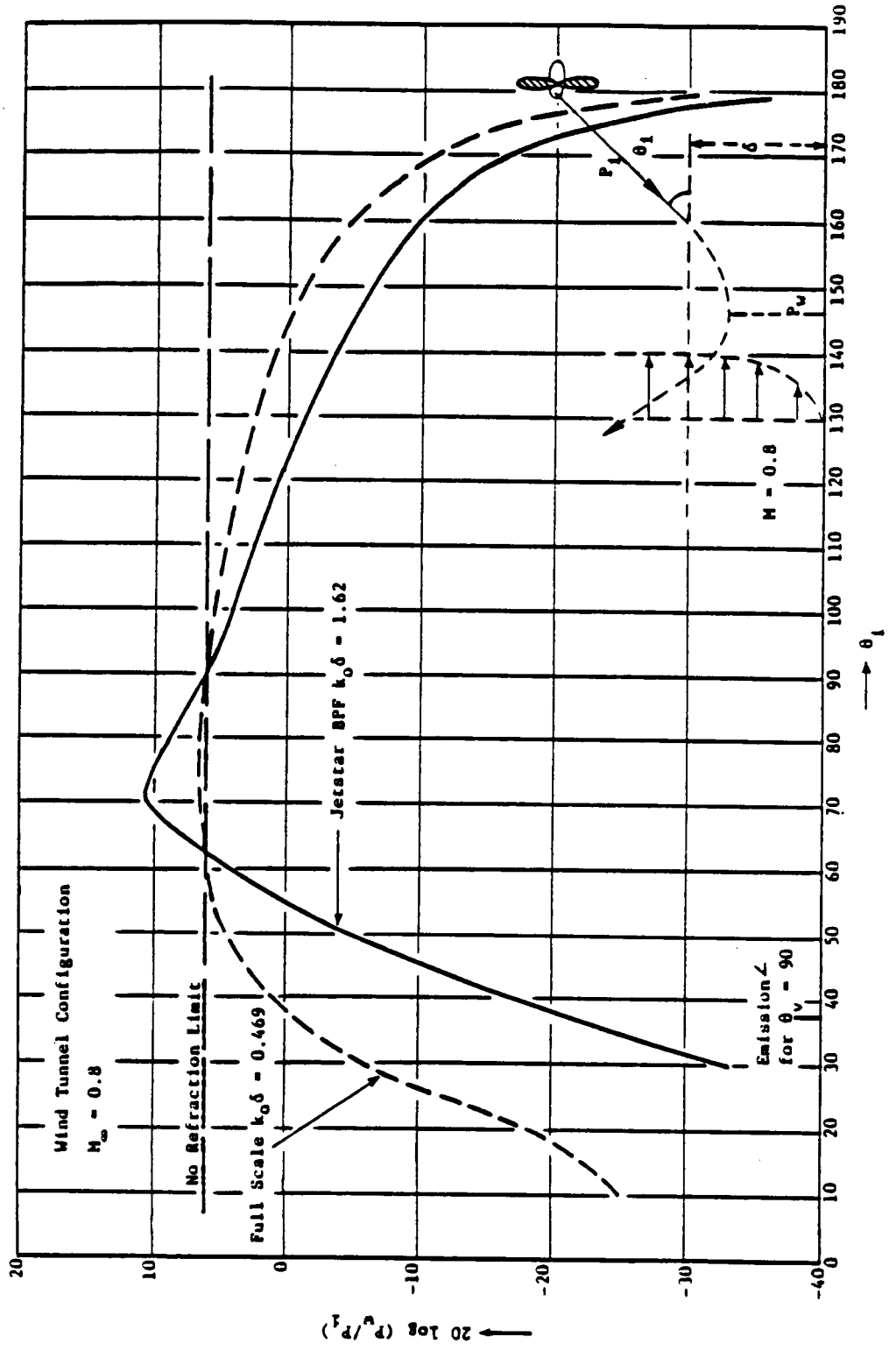

Figure 61. Variation of Wall SPL, 20 log (P_w/P_i), Relative to Incident SPL with Angle of Incidence for Mach Number of 0.8 and Frequency Parameter $k_o\delta$ = 1.62 (Jetstar Model Test) and $k_o\delta$ = 0.469 (Full Scale).

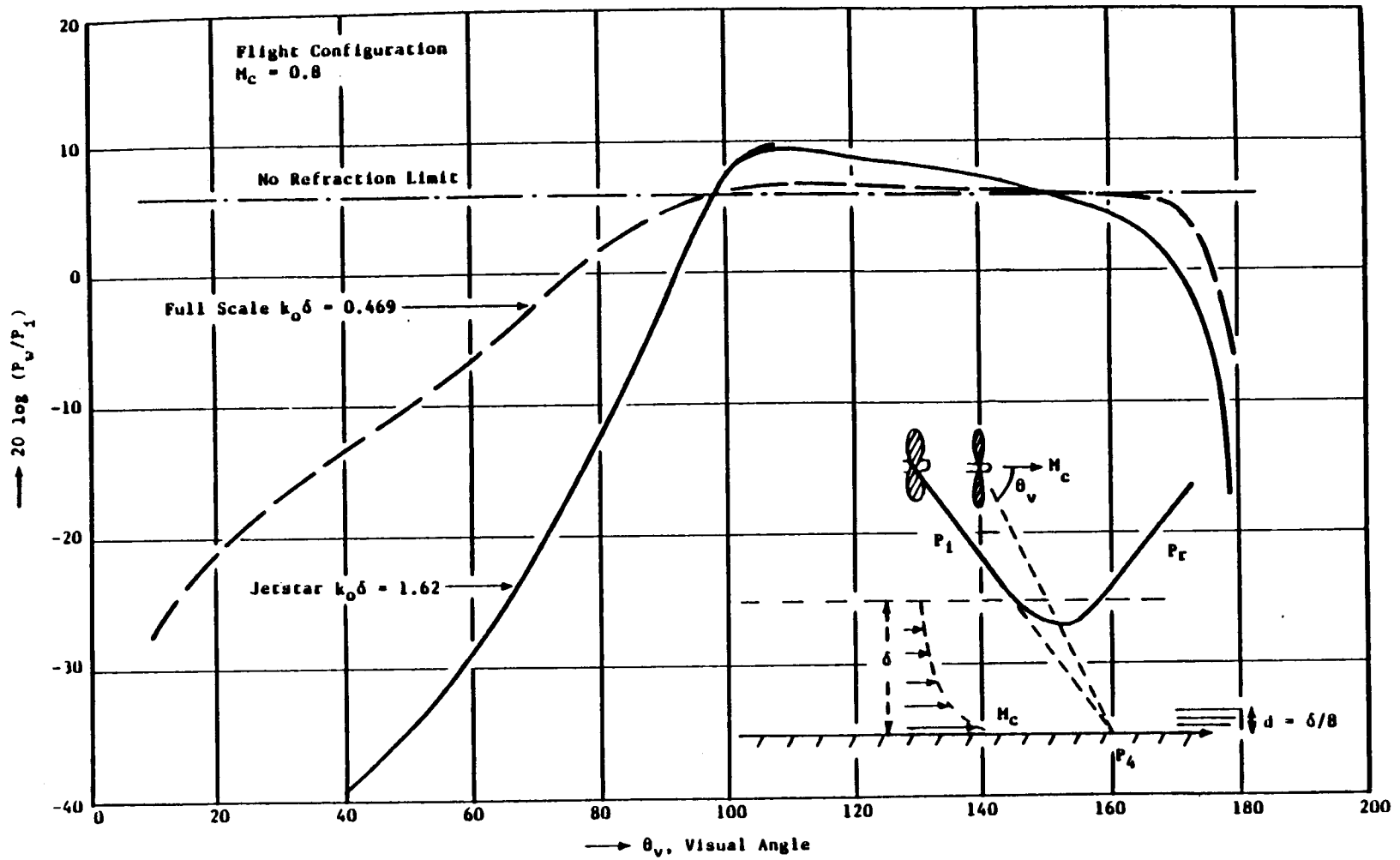

Figure 62. Variation of Wall SPL (Relative to Incident SPL) in Flight Configuration with Visual Angle (Propeller Location Relative to Fuselage Microphone) for $k_o\delta$ = 1.62 (Jetstar) and $k_o\delta$ = 0.469 (Full Scale).

Modeling that comes closer to the case of the scattering of propeller noise by a fuselage is a 3D scattering problem in the presence of flow and fuselage boundary layer. Hanson (Reference 2.3.6) has studied this case in some detail and shown some significant differences relative to the 2D model discussed earlier. This 3D scattering problem is the main subject of this work and is discussed in more detail in the next section.

2.3.2 Scattering of Propeller Noise by a Cylindrical Fuselage

Consider a propeller of radius R_p and center S (source) mounted on one side of a fuselage of radius R_f at a distance R_{cl} from the fuselage center as shown in Figures 63 and 64.

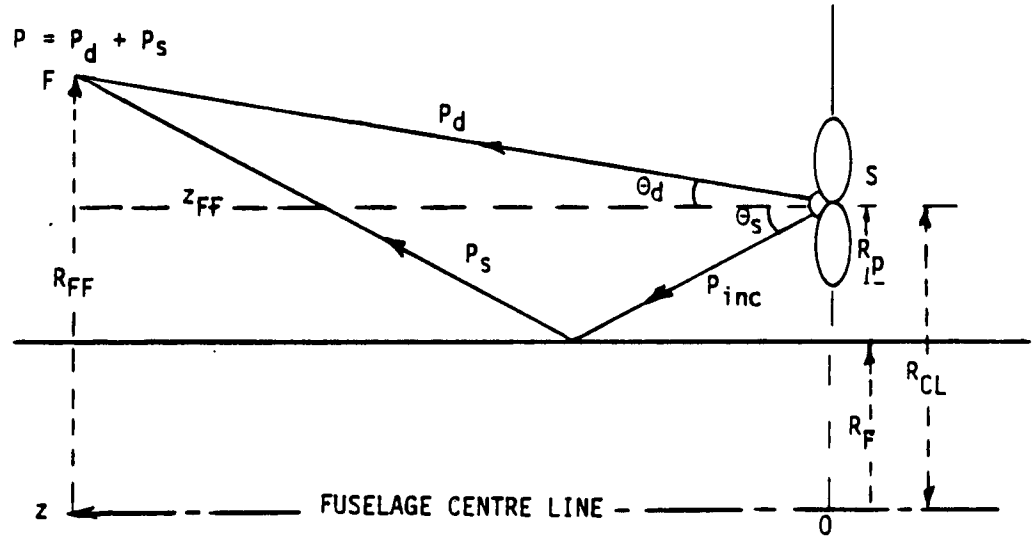

Figure 63. Fuselage Scattering of Propeller Noise.

At an arbitrary field point F, the sound field consists of the sum of a direct field P_d and a scattered field P_s. Both the direct and the scattered fields have characteristic directivities which are functions of the frequency and other parameters which are defined later.

Estimates of the amplitude, directivity, and phase of the scattered field relative to an incident field, P_{inc}, are made using acoustic diffraction analysis. Geometric ray theory is not adequate, due to the wavelength being of the order of the scattering dimension.

Of equal importance is the sound pressure level distribution on the surface of the fuselage, not only in the plane where the propeller is located, but also away from it and all around the fuselage, including shadow regions.

As indicated in Section 2.3.1, the combined sound pressure level depends not only on the amplitude of the incident and of the scattered fields, but also on their relative phase. This relative phase is a function of the fuselage surface impedance and the acoustic properties of the medium in which the sound is incident and scattered. For a rigid fuselage in a homogeneous,

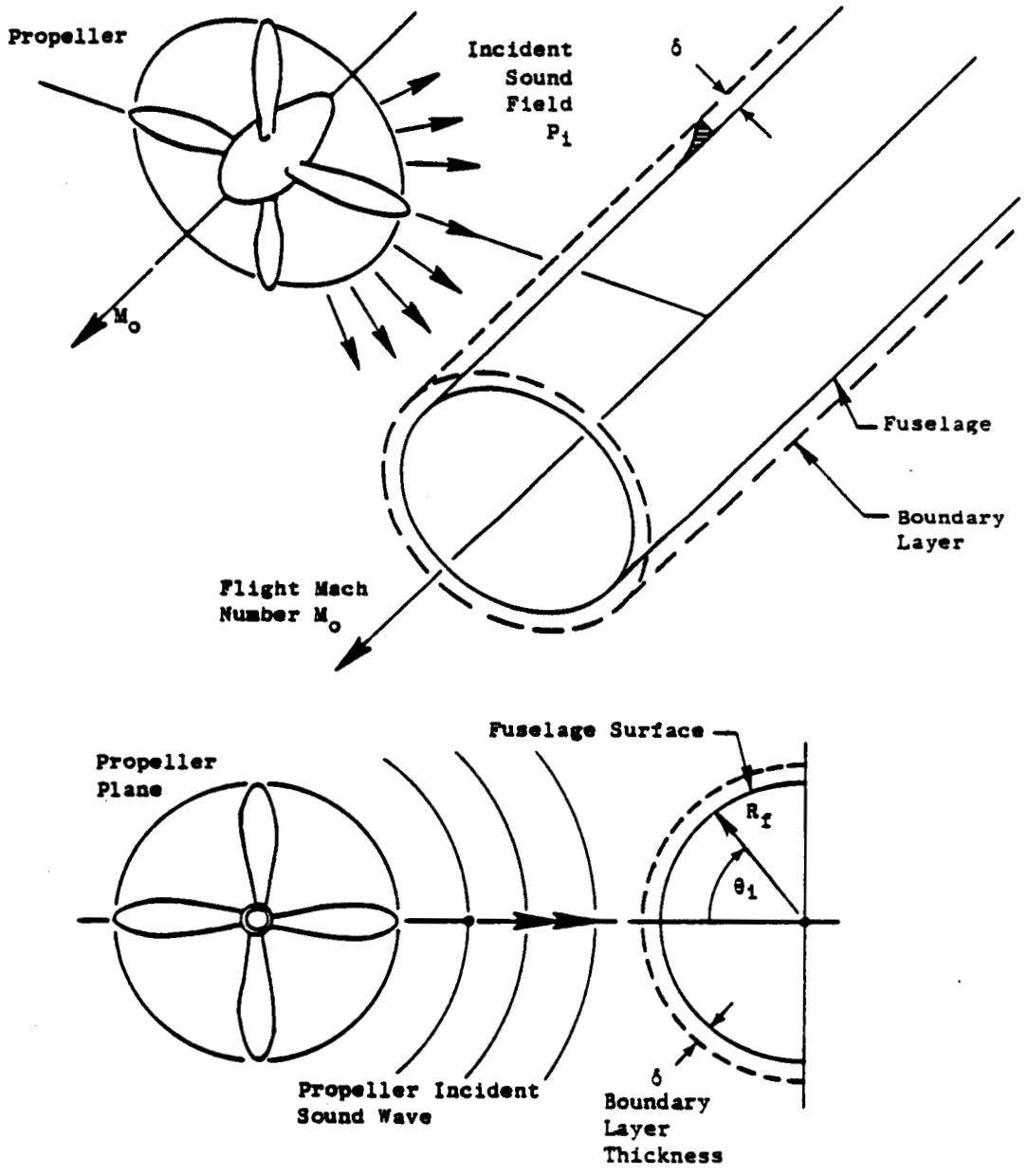

Figure 64. Illustration of Scattering of Propeller Emitted Sound Field by a Cylindrical Fuselage with Attached Boundary Layer in Forward Flight.

the scattered field on the source side of the fuselage is nearly in phase with the incident field, so that the combined field is increased in amplitude. Similarly, as may be expected, in the shadow region on the fuselage surface away from the source, the scattered field is nearly in antiphase with the incident field. Consequently, the combined field is lower than the incident field, thus, producing the so-called shadow region.

For a rigid fuselage with an attached boundary layer, both the amplitude and the phase of the scattered field relative to the incident field will be modified, resulting in a modified combined field, relative to the case with no attached boundary layer. In the analysis that follows, the boundary layer is treated as part of the fuselage, with a modified acoustic surface admittance; in other words, the fuselage surface would not appear rigid to the incident field. The estimation of this modified acoustic surface admittance would be part of the scattering analysis.

In this study, reflection, refraction, convection, and diffraction are all part of the scattering analysis used. The main objective is to estimate delta -dB (the increase or decrease of the pressure field on the surface of the fuselage relative to the free field, that is, the incident field that would have been there in the absence of the fuselage). As will be shown, several parameters influence the delta -dB.

2.3.2.1 The Governing Wave Equation

The sound field emitted from the propeller and incident on the fuselage, and the resulting scattered field, must satisfy an appropriate governing wave equation.

For a mean flow field that is not uniform, such as that in the boundary layer of a cylindrical fuselage in flight (Figure 65); the appropriate governing wave equation may be written in the form:

$$\nabla^2 P + 2\bar{\rho} \frac{\partial U}{\partial R} \frac{\partial v}{\partial z} - \frac{1}{c_o^2} \frac{D^2 P}{Dt^2} = 0 \qquad (2.3.1)$$

where

∇^2 = three-dimensional Laplacian in cylindrical coordinates,

$\frac{D}{Dt}$ = convected derivative = $\frac{\partial}{\partial t} + U \frac{\partial}{\partial z}$

U = axial component of the mean flow, which is a function of the radial coordinate R.

$\frac{\partial U}{\partial R}$ = Mean radial shear and is also a function of the radial coordinate.

v = radial component of the unsteady flow associated with the sound field.

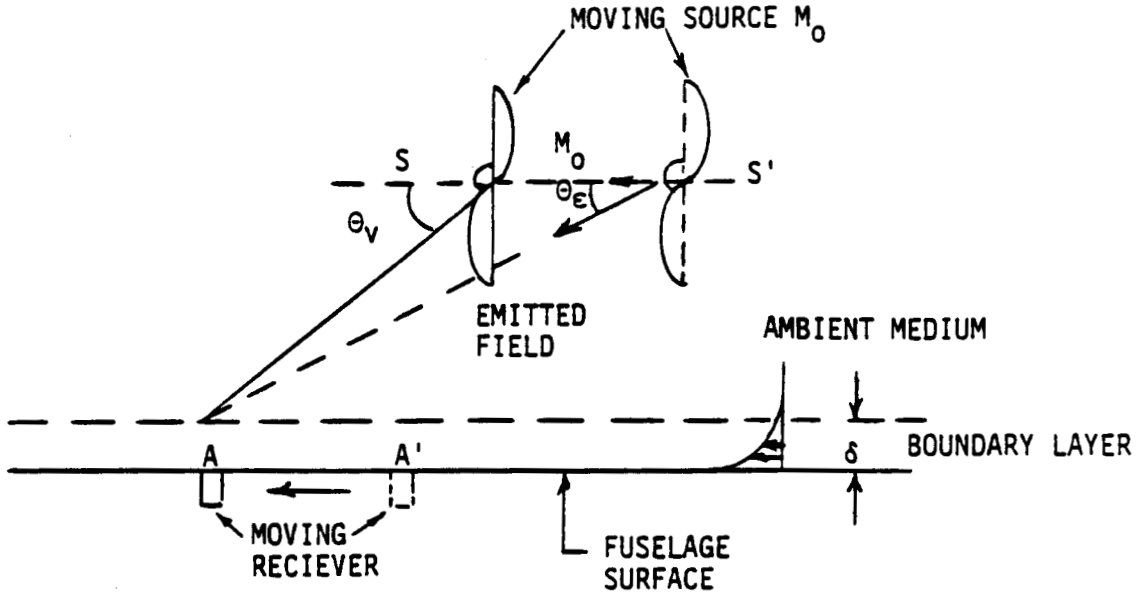

Figure 65. Flight Configuration.

A solution for Equation 2.3.1 may be expressed as:

$$P(R,\phi,z,\omega) = \sum_q A_q(\omega)\ F_q\ (R,k_z)\ e^{-jk_z\ z-jq\phi+j\omega t} \qquad (2.3.2)$$

where F_q (R, k_z) must satisfy a reduced form of Equation 2.3.1; namely,

$$\frac{d^2F}{dR^2} + \left\{ \frac{1}{R} + \frac{2K}{1-MK}\ \frac{dM}{dR} \right\}\ \frac{dF}{dR} + \left\{ k_o^{\,2}\ (1-MK)^2 - k_z^{\,2} - \frac{q^2}{R^2} \right\} F = 0 \qquad (2.3.3)$$

where:

$k_o = \omega/c_o$

$K = k_z/k_o$

$M = U/c_o$

and

q = an integer 0, ±1, ±2, . . .

Each term of Equation 2.3.2 represents a cylindrical wave spinning around the fuselage, propagating downstream or upstream (depending on the sign of the wave-vector k_z), and radiating radially away from the surface of the fuselage.

In flight, outside the boundary layer, the Mach number, M, becomes zero, and the shear term, dM/dR, vanishes as illustrated in Figure 65. In this case, outside the boundary layer, Equation 2.3.3 simplifies to a more familiar differential wave equation which may be satisfied by a Hankel function, so that $F_q(R,k_z)$ in Equation 2.3.2 may be replaced by:

$$F_q(R,k_z) = H_q(k_R R) \tag{2.3.4}$$

in which k_R and k_z are interrelated by the dispersion equation obtainable from Equation 2.3.3 in the form:

$$k_R^2 + k_z^2 = \underset{\sim}{k}^2 = k_o^2 (1-M_o K)^2 \tag{2.3.5}$$

By definition, the wave-vector, $\underset{\sim}{k}$, is associated with the direction of propagation of the wave-field. The axial and radial components of the wave-vector, $\underset{\sim}{k}$, are given by:

$$k_z = \underset{\sim}{k} \cos \theta \tag{2.3.6}$$

and

$$k_R = \underset{\sim}{k} \sin \theta. \tag{2.3.7}$$

where θ is the direction of radiation along which the wave-vector $\underset{\sim}{k}$ is aligned.

In flight, as shown in Figure 65, the acoustic medium outside the fuselage boundary layer is stationary. From Equation 2.3.5, with M_o set to zero,

$$|\underset{\sim}{k}| = |\underset{\sim}{k}_o| = (\omega/c_o)$$

However, because the source is moving with Mach number M_o, the frequency perceived by a fixed observer outside the fuselage boundary layer is Doppler shifted; thus,

$$\underset{\sim}{k} = \frac{\omega}{(1+M_o \cos \theta)\, c_o} \tag{2.3.8}$$

hence,

$$k_z = \underset{\sim}{k} \cos \theta = \frac{k_o}{(1+M_o \cos \theta)} \cos \theta$$

and

$$k_R = \underset{\sim}{k} \sin \theta = \frac{k_o}{(1+M_o \cos \theta)} \sin \theta$$

It should be noted that the angle θ is the angle of emission as shown in Figure 65. It is related to the geometric visual angle θ_v in the form,

$$\theta = \theta_v - \sin^{-1}(M_o \sin\theta_v) \tag{2.3.9}$$

2.3.2.2 Scattering Analysis

Having defined the governing wave-equation and the forms that the sound field may take outside the boundary layer, we may now refer to Figures 63 and 64 and write down some formal solutions.

The sound field at an arbitrary field point F at location (R,ϕ,z,ω), relative to a cylindrical coordinate coincident with the fuselage axis, may be written as:

$$P(R,\phi,z,\omega) = P_d(R,\phi,z,\omega) + P_s(R,\phi,z,\omega) \tag{2.3.10}$$

where P_d refers to the direct field emitted from the propeller source, and P_s refers to the field scattered by the fuselage surface as a result of an incident field P_{inc}. If the field point is on the fuselage surface, then the direct field and the incident field are coincident. The next objective is to evaluate the scattered field P_s in terms of the incident field P_{inc}. The analysis must be carried out in the frequency domain, because diffraction and scattering (including refraction) are frequency dependent phenomena.

2.3.2.2.1 The Scattered Field

Outside the boundary layer, as discussed in Section 2.3.2.1, the scattered field may be expressed in terms of cylindrical harmonics of yet undetermined amplitudes $A_q(\omega)$ in the form:

$$P_s(R,\phi,z,\omega) = \sum_{q=-\infty}^{\infty} A_q(\omega)\, H_q(k_R R)\, e^{-jk_z z - j\phi} \tag{2.3.11}$$

where

$H_q(k_R R)$ = cylindrical Hankel function of integral order and of the second kind (outgoing waves)

$k_R = |\underset{\sim}{k}| \sin\theta$

$k_z = |\underset{\sim}{k}| \cos\theta$

$\underset{\sim}{k}$ = propagation wave-vector = $k_o/(1+M_o\cos\theta)$

$k_o = (\omega/c_o)$

The amplitudes of A_q of the scattered field as expressed in Equation 2.3.11 must now be evaluated in terms of the incident field P_{inc} as shown in Figure 63. This incident field is that emitted from the propeller noise source S at angle θ_s and is a function of the propeller geometry and operating conditions.

2.3.2.2.2 The Incident Field

A spectral component of the sound emitted from a B-bladed propeller may be expressed in cylindrical harmonics of known or specifiable amplitudes in the form:

$$P_\varepsilon (r',\theta_\varepsilon',\phi',\omega_n) = D_n (\omega_n,\theta_\varepsilon') H_m (k_R R') e^{-jk_z z - jm\phi + j\omega_n t} \qquad (2.3.12)$$

where:

n = harmonic integer of the propeller blade passing frequency

$m = nB$

$\omega_n = c_o n B M_t / R_p$

c_o = adiabatic speed of sound

R_p = propeller radius

M_t = propeller tip circumferential Mach number

$k_R = |k| \sin \theta'_\varepsilon$

$k_z = |k| \cos \theta'_\varepsilon$

$|k| = |k_o|/(1 + M_o \cos \theta'_\varepsilon)$

$D_n(\omega_n,\theta'_\varepsilon)$ = spectral directivity of the emitted field

$H_m(\ )$ = cylindrical Hankel function of order m.

In the above expression for the emitted sound field (r', θ'_ε, ϕ') are spherical polar coordinates relative to an axis through the propeller center, and (R', ϕ', z') are cylindrical coordinates also relative to the propeller center, with $z' = r' \cos \theta'_\varepsilon$.

To express the scattered field of Equation 2.3.11 in terms of this incident field and boundary conditions on the surface of the fuselage (expressed in terms of a fuselage surface admittance), it is more convenient to express the incident field in coordinates coincident with the fuselage axis. It may be pointed out that the incident field is the same as the emitted field.

Each spectral component of the incident field, as expressed by each term of Equation 2.3.12, may be expanded in terms of the (R, z, ϕ) coordinates coincident with the fuselage and expressed in the following form (Reference 2.3.7):

$$P_{inc}\ (\omega_n, \ldots) = D_n\ (\omega_n, \theta_\varepsilon')\ e^{-jk_z z}\ H_m\ (k_R\ R')\ e^{-jm\phi}. \tag{2.3.13}$$

$$= D_n\ (\omega_n, \theta_\varepsilon')\ e^{-jk_z z} \sum_{\ell=-\infty}^{\infty} H_{m+\ell}\ (k_R\ R_{c1})\ J_\ell(k_R R)\ r^{-j\ell\phi}$$

where:

ℓ = an integer

R_{c1} = the distance between fuselage center line and propeller center

The relationship between (R, ϕ, z) and (R', ϕ', z') is shown in Figure 66.

Equation 2.3.13 expresses the propeller-emitted sound field in the form of multiple cylindrical waves converging onto the cylindrical fuselage. The axial wave number k_z of the incident wave is the same in either representation, with $k_z = \underset{\sim}{k} \cos \theta'$.

2.3.2.2.3 Boundary Condition at the Fuselage Surface in the Absence of a Boundary Layer

The scattered field P_s in Equations 2.3.10 or 2.3.11 associated with each spectral component of the incident field as expressed by Equation 2.3.13 may now be evaluated by subjecting the combined field (incident plus scattered) to pertinent boundary conditions at or near the fuselage surface. This may be specified as follows:

In the absence of a boundary layer and no mean flow:

at R = R_f, the fuselage radius,

$$\frac{\bar{\rho}\ c_o\ v_R}{P} = -A_F(R_F) \tag{2.3.14}$$

where:

P = P_{inc} + P_s of Equations 2.3.13 and 2.3.11,

ρ and c_o = mean density of the medium and adiabatic speed of sound, respectively,

v_R = radial component of velocity associated with combined sound field P,

and

$A_F(R_F)$ = fuselage surface acoustic admittance.

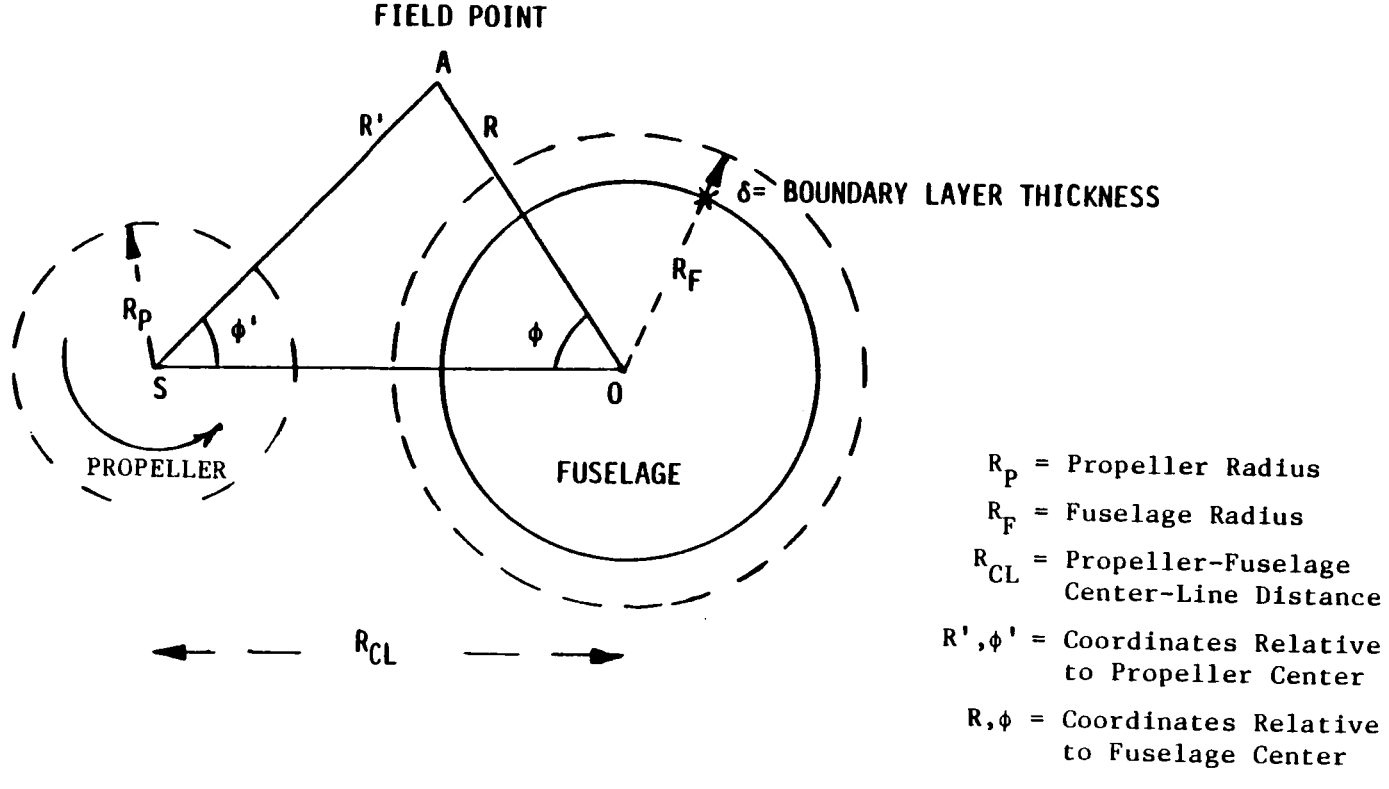

Figure 66. Cylindrical Coordinate Relative to Fuselage Axis (Forward Looking Aft).

The radial component of the velocity field, v_R, may be expressed in terms of the radial derivative of the combined pressure field, using the linearized momentum equation:

$$\bar{\rho}\, c_o v_R = -\frac{1}{jk_o}\frac{dP}{dR} \tag{2.3.15}$$

Substituting Equations 2.3.15, 2.3.11, and 2.3.13 into Equation 2.3.14, one may obtain the following:

$$\sum_q A_q H'_q(\,)\, e^{-jq\phi} + D_n(\omega_n) \sum_\ell H_{m+\ell}(\,) J'_\ell(\,) e^{-j\ell\phi} \tag{2.3.16}$$

$$= \sum_q A_F A_q H_q(\,) e^{-jq\phi} + D_n(\omega_n) \sum_\ell A_F H_{m+\ell}(\,) J_\ell(\,) e^{-j\ell\phi}$$

where:

$$H'_q(\,) = \frac{d}{dR}\{H_q(\,)\}$$

$$J'_\ell(\,) = \frac{d}{dR}\{J_\ell(\,)\}$$

and the argument in H'_q, J'_ℓ, H_q and J_ℓ is $k_R R_F$, and that in $H_{m+\ell}$ is $k_R R_{cl}$.

From the orthogonality of $e^{-jq\phi}$ and $e^{-j\ell\phi}$, Equation 2.3.16 may be simplified and rearranged in the form:

$$A_q H'_q(\,) = -\delta_{q\ell} D_n(\omega_n) H_{m+\ell}(\,) J'_\ell(\,) \gamma_{q\ell} \tag{2.3.17}$$

where

$$\gamma_{q\ell} = \frac{\{1 - A_F J_\ell(\,)/J'_\ell(\,)\}}{\{1 - A_F H_q(\,)/H'_q(\,)\}} \tag{2.3.18}$$

and

$\delta_{q\ell}$ = Kronecker delta

= 1 when $q = \ell$

= 0 when $q \neq \ell$.

Equation 2.3.17 allows the scattered amplitude, A_q, to be expressed in terms of the amplitude $D_n(\omega_n)$ of the spectral component of the incident field. It may be pointed out that if the fuselage surface is rigid, the fuselage surface admittance becomes zero, and $\gamma_{q\ell}$ in Equation 2.3.17 becomes unity.

In this case,

$$A_q = -D_n(\omega_n)\, H_{m+q}(\,)\, J'_q(\,)/H'_q(\,) \qquad (2.3.19)$$

If the fuselage surface is not rigid, then both the amplitude and phase of the scattered amplitude are modified relative to that of a rigid fuselage.

In evaluating the Bessel and Hankel functions, J_ℓ ( ) and H_q( ) and their derivatives, it may be recalled that the argument common to all is $k_R R_F$. In an ambient medium, this may be specified as $k_o R_F \sin\theta_i$, where θ_i is the angle the incident field makes with respect to the propeller axis.

Equation 2.3.17 will be used to reconstruct Equations 2.3.10 and 2.3.11 in terms of the incident field amplitude. This part of the analysis is deferred until after a discussion of the boundary layer effect.

2.3.2.2.4 Effect of the Presence of a Fuselage Boundary Layer on the Boundary Conditions

The boundary condition at the fuselage surface as expressed by Equation 2.3.14 is still valid. However, the pressure fields as expressed by Equations 2.3.11 and 2.3.12 are valid only outside the boundary layer and, therefore, cannot be applied at the fuselage surface.

To overcome this problem, the boundary condition is applied at the outer edge of the boundary layer, using an acoustic transferred admittance instead of the actual fuselage surface admittance. Such a transferred acoustic admittance is obtained by numerically integrating the applicable governing wave-equation; namely Equation 2.3.3, from the fuselage surface to the edge of the boundary layer. A fourth order Runge-Kutta integration scheme is used. Such a scheme requires subdividing the integration region (for our application, the boundary layer thickness) into several points, and evaluating the coefficients of the governing equation at and between each of these points. Details of such an application are given in Reference 2.3.8. In summary, the pressure field and its radial derivative at the outer edge of the boundary layer ($R_{f+\delta}$) may be expressed as:

$$\begin{Bmatrix} P \\ P' \end{Bmatrix}_{R_{f+\delta}} = [T] \begin{Bmatrix} P \\ P' \end{Bmatrix}_{R_f} \qquad (2.3.20)$$

where P and P′ are the pressure field and its radial derivative at the fuselage surface, respectively. [T] is a 2×2 transfer matrix obtained by the numerical integration of Equation 2.3.3 expressed in the form:

$$\begin{Bmatrix} F \\ F' \end{Bmatrix}' = \begin{bmatrix} 0 & 1 \\ -a & -b \end{bmatrix} \begin{Bmatrix} F \\ F' \end{Bmatrix} \qquad (2.3.20b)$$

where ' refers to the derivative with respect to R, and where a and b are the coefficients of F and dF/dR of Equation 2.3.3.

Evaluation of the transfer functions [T] requires evaluation of the coefficients of Equation 2.3.3 from point-to-point across the boundary layer. Consequently, the velocity profile; the Mach number, M_o; the spinning integer number, q (0, ±1, ±2, . . .); and (k_z/k_o), or the angle of incidence, must be specified. Thus, Equation 2.3.2 may be evaluated at each specified location on the fuselage relative to the propeller plane.

At the edge of the boundary layer, the following boundary condition is imposed:

$$\left(\frac{P'}{P}\right)_{R_f+\delta-\varepsilon} = \left(\frac{P'}{P}\right)_{R_f+\delta+\varepsilon} \qquad (2.3.21)$$

as

$$\varepsilon \to 0$$

In evaluating (P'/P) at $R_f + \delta-\varepsilon$, Equation 2.3.20 is used; and in evaluating (P'/P) at $R_f+\delta+\varepsilon$, Equations 2.3.11 and 2.3.13 are used. Thus, from Equation 2.3.20,

$$\left(\frac{P'}{P}\right)_{R_f+\delta-\varepsilon} = \frac{T_{21} + T_{22}\left(P'/P\right)_{R_f}}{T_{11} + T_{12}\left(P'/P\right)_{R_f}} \qquad (2.3.22)$$

and $(P'/P)_{Rf}$ is replaced by $-jk_o A_F(R_F)$ from Equations 2.3.15 and 2.3.15.

Equation 2.3.22 is a measure of the fuselage surface transferred admittance and may be denoted as $-A_t$.

Using Equation 2.3.2, expressions similar to Equations 2.3.16 and 2.3.17 are obtained with A_t replacing A_F.

The development in this section allows the use of classical scattering analysis to include boundary layer refraction effects.

2.3.2.2.5 Evaluation of the Sound Pressure Level on the Fuselage Surface

The sound pressure field on the fluid surface just outside the fuselage boundary layer is the sum of the incident and of the scattered fields. Using Equation 2.3.13 for the incident field

and Equation 2.3.11 (rearranged somewhat) for the scattered field, the sound pressure level at this surface $(R_f+\delta, \phi)$ may be written in the form,

$$P(R_f+\delta,\phi,k_z,\omega_n) = D_n(\omega_n,\theta_\varepsilon)\ e^{-jk_z z} \sum_{\ell} H_{m+L}(k_R R_{cl})\ J_\ell(a)\ e^{-jl\phi}$$

$$+ \sum_{q} A_q\ H'_q(a)\{H_q(a)/H'_q(a)\}\ e^{-jq\phi - jk_z z} \qquad (2.3.23)$$

where

$a = k_R(R_f + \delta)$,

and the summations on ℓ and q are theoretically from $-\infty$ to $+\infty$, but will be truncated due to the convergence of the series with increasing order.

Equation 2.3.17 allows the amplitude and phase of $A_q H'_q(a)$ to be expressed in terms of the incident amplitude $D_n(\omega_n,\theta_\varepsilon)$ and of the fuselage surface transferred admittance. If this is done, then Equation 2.3.23 becomes:

$$P(R_f+\delta,\phi,k_z,\omega_n) = D_n(\omega_n,\theta_\varepsilon)\ e^{-jk_z z}$$

$$* \left[\sum_{\ell} H_{m+\ell}(b)\ e^{-j\ell\phi} \left\{ J_\ell(a) - J'_\ell(a) \frac{H_\ell(a)}{H'_\ell(a)} \gamma_\ell \right\} \right] \qquad (2.3.24)$$

where

$b = k_R R_{cl}$

$a = k_R(R_f+\delta)$

$\gamma_\ell = \gamma_{q\ell}$ of Equation 2.3.18 with $q = \ell$.

and $k_R = \underset{\sim}{k} \sin\theta$ has been discussed previously and is defined in Equation 2.3.7 or 2.3.7a.

Equation 2.3.24 represents the principal result of the acoustic analysis accounting for the modification to an incident field (of the wave emitted from a propeller) by the scattering due to a cylindrical fuselage in the presence of convection, refraction, and diffraction.

Since the result is more conveniently expressed in terms of an increase or decrease relative to the incident field, the directivity term $D_n(\omega_n,\theta)$ does not need to be specified; it is canceled by the normalization process.

To obtain the acoustic pressure field on the surface of the fuselage, Equation 2.3.24 is used in conjunction with the pressure component of Equations 2.3.20 or 2.3.22 relating pressure fields at ($R_f + \delta$) and at R_f. Thus,

$$P(R_f+\delta,\ell) = \left\{ T_{11} + T_{12}\ (P'/P)_{Rf} \right\}\ P(R_f,\ell) \qquad (2.3.25)$$

Let $P(R_f)/P(R_f+\delta)$ be denoted by PWOBL(ℓ) for each of the spinning modes ℓ, where

$$PWOBL(\ell) = 1/\left\{ T_{11} + T_{12}(P'/P)_{R_f} \right\} \qquad (2.3.26)$$

and is evaluated numerically when integrating Equation 2.3.20b.

The pressure field on the fuselage surface may now be written as:

$$P(R_f) = \sum_{\ell} P(R_f,\ell) = \sum_{\ell} P(R_f+\delta,\ell)\ PWOBL(\ell) \qquad (2.3.27)$$

where $P(R_f+\delta\ ,\ \ell)$ is the expression in Equation 2.3.24 inside the sign corresponding to summation over ℓ.

2.3.3 Computed Results

A computer program has been developed to evaluate the sound pressure field on the fuselage surface and on the surface at the outer edge of the fuselage boundary layer, as expressed by Equations 2.3.26 and 2.3.27.

Numerical results have been computed to show the various effects of scattering by a fuselage and its attached boundary layer. As mentioned in Section 2.3.1.1, such scattering includes effects of reflection, refraction, and diffraction. These effects are functions of various geometric, aerodynamic, and operational parameters. Figures 66 and 67 will facilitate interpretation of some of the parameters used in presenting the results.

Unless indicated otherwise, most of the results have been evaluated for an 8-bladed propeller rotating at a rotor tip Mach number of 0.8, with a fuselage/propeller radius ratio of unity, and zero propeller tip clearance. The fuselage surface is assumed to be rigid. The mean velocity profile in the boundary layer corresponds to a Blasius profile on a flat plate.

2.3.3.1 Reflection and Diffraction in the Absence of Mean Flow

As a prelude to the presentation of results, Figure 68 has been chosen to show some salient features of reflection and diffraction. Two polar plots are presented demonstrating azimuthal distributions on and around the fuselage surface of the incident field and of the combined incident + scattered field, for sound emitted and incident at 90° to the propeller axis. The azimuthal angle is measured at the fuselage center relative to the line joining the propeller

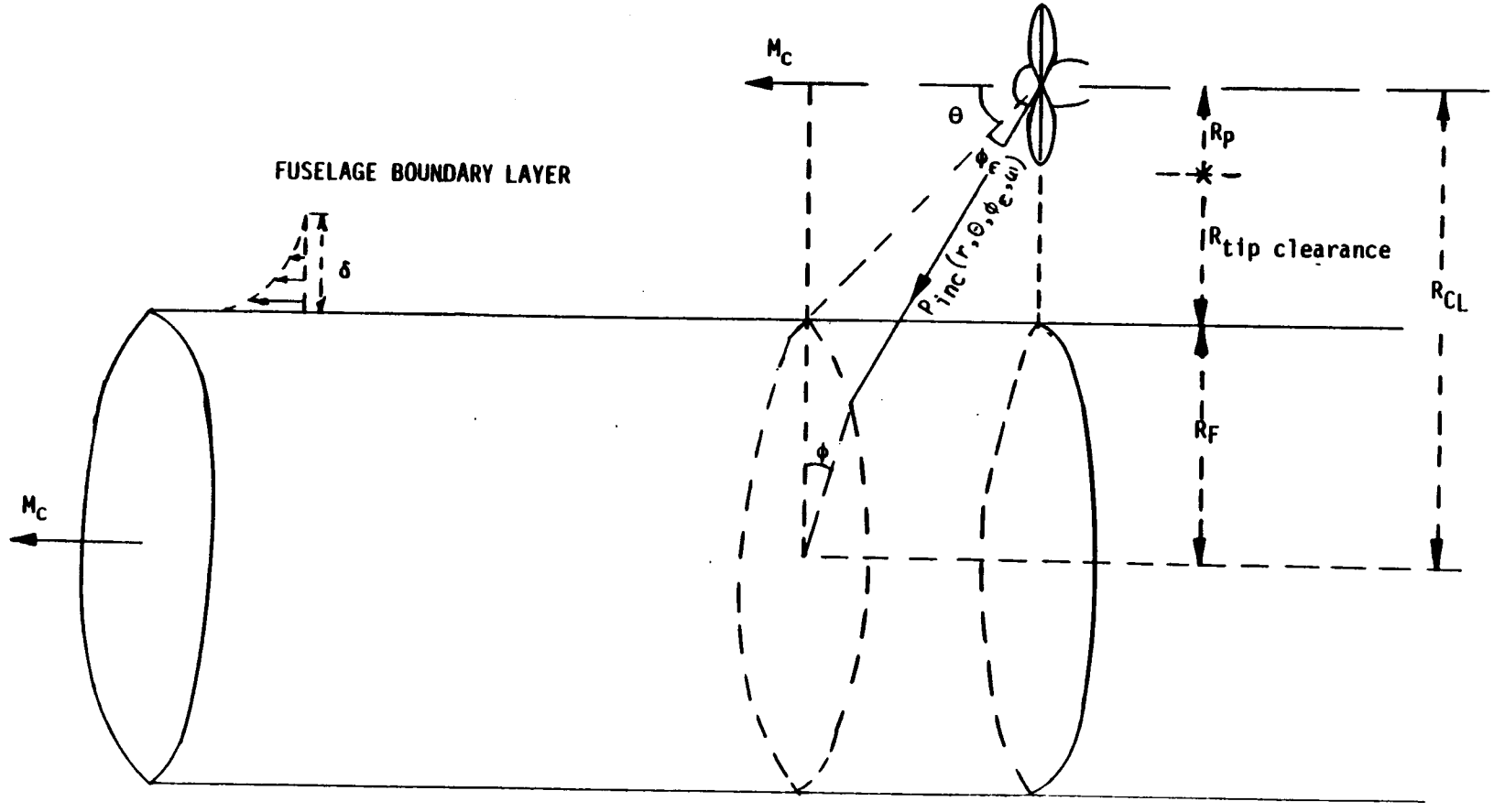

Figure 67. Relevant Parameters in the Scattering of Propeller Emitted Sound by a Fuselage.

center and the fuselage center as shown in the inset and in Figure 66. The incident field is normalized to that at $\phi = 0$, and is actually evaluated as $20 \log_{10} \{P_{inc}(R_f,\phi)/P_{inc}(R_f, 0)\}$. The deviation from 0 dB represents the decay of the emitted field from the propeller with distance and may differ from the inverse square law due to near field decay.

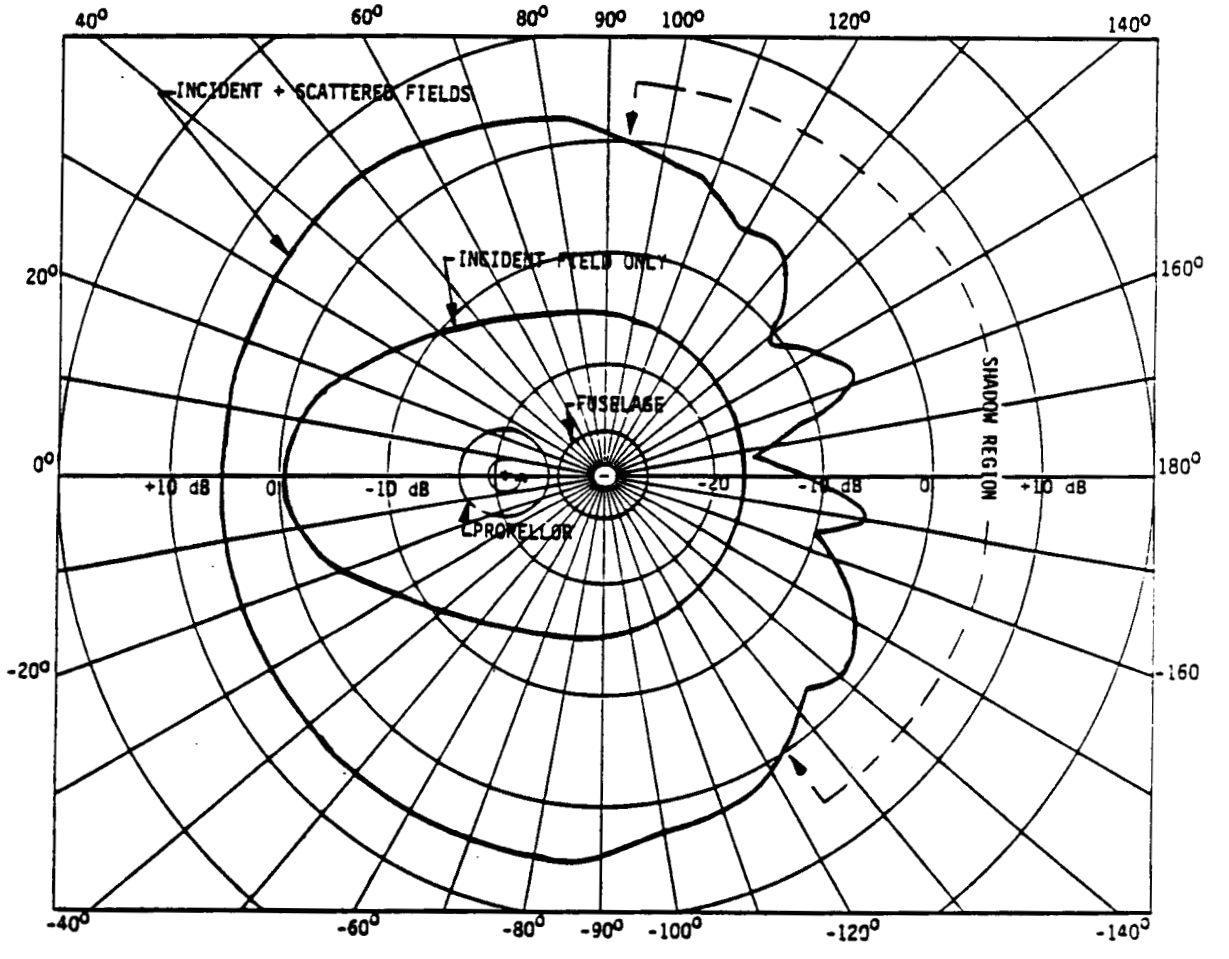

Figure 68. Relative Sound Pressure Level Distribution in dB on the Surface of a Rigid Fuselage Arising from the Scattering of an Incident Field Emitted from an 8-Bladed Propeller Operating at a Tip Mach No. of 0.7.

The other plot, denoted as incident + scattered fields, is the corresponding SPL distribution on the fuselage surface and is relative to the local incident field at the same location. The 0 dB circle is a reference level. Levels above 0 dB correspond to amplification, or in-phase reflection; levels below 0 dB correspond to attenuation or shadowing as a result of out-of-phase reflection (scattering).

Several features may be observed and commented on:

- There are two distinct regions on the fuselage surface where the SPL is above and below the 0 dB circle. In the region $93° > \phi > -123°$, the scattered field constructively interferes with the incident field to produce levels above 0 dB. In the region $93° < \phi < -123°$, a shadow zone is present where the scattered field interferes destructively with the incident field, producing relative levels below 0 dB.

  For this case of fuselage radius equal to propeller radius and zero propeller tip clearance, the geometric shadow should be $60° < \phi < -60°$. Within the shadow region, the SPL varies azimuthally producing "hard" and "soft" shadows which correspond to the well-known Fresnel diffraction.

  The depth of the shadow zone and the number of peaks and valleys within it are functions of the propeller frequency, blade number, and fuselage radius (not shown in the figure).

- A second important observation is that the fuselage SPL distribution is not symmetrical about the line joining the propeller and fuselage centers. The peak relative SPL for the case considered is around $\phi = -40$. This asymmetry is due to the fact that the incident field is that emitted from an 8-bladed propeller rotating in a counterclockwise direction. This asymmetric feature has also been observed by Hanson (Reference 2.3.6).

- The peak SPL on the fuselage surface at $\phi = 0$ is less than 6 dB, relative to the incident field, supporting the experimental results of Hubbard et al. (Reference 2.3.3) that reflection from curved surfaces does not produce pressure doubling. In fact, near pressure doubling (5.8 dB instead of 6 dB) occurs at $\phi = 320° = (-40°)$.

2.3.3.2 Influence of Fuselage Curvature

Figure 69 shows the azimuthal distribution of the combined incident and scattered fields (normalized by the local incident field) for two fuselage-to-propeller radius ratios, namely $(R_f/R_p) = 1$ and 2.

The other relevant parameters that are common to both distributions are:

- Blade number = 8
- Blade tip Mach number = 0.8
- No mean flow.

The main points of observation are:

- The relative SPL at $\phi = 0$ increases from 5.0 to 5.4 dB as (R_f/R_p) increases from 1 to 2

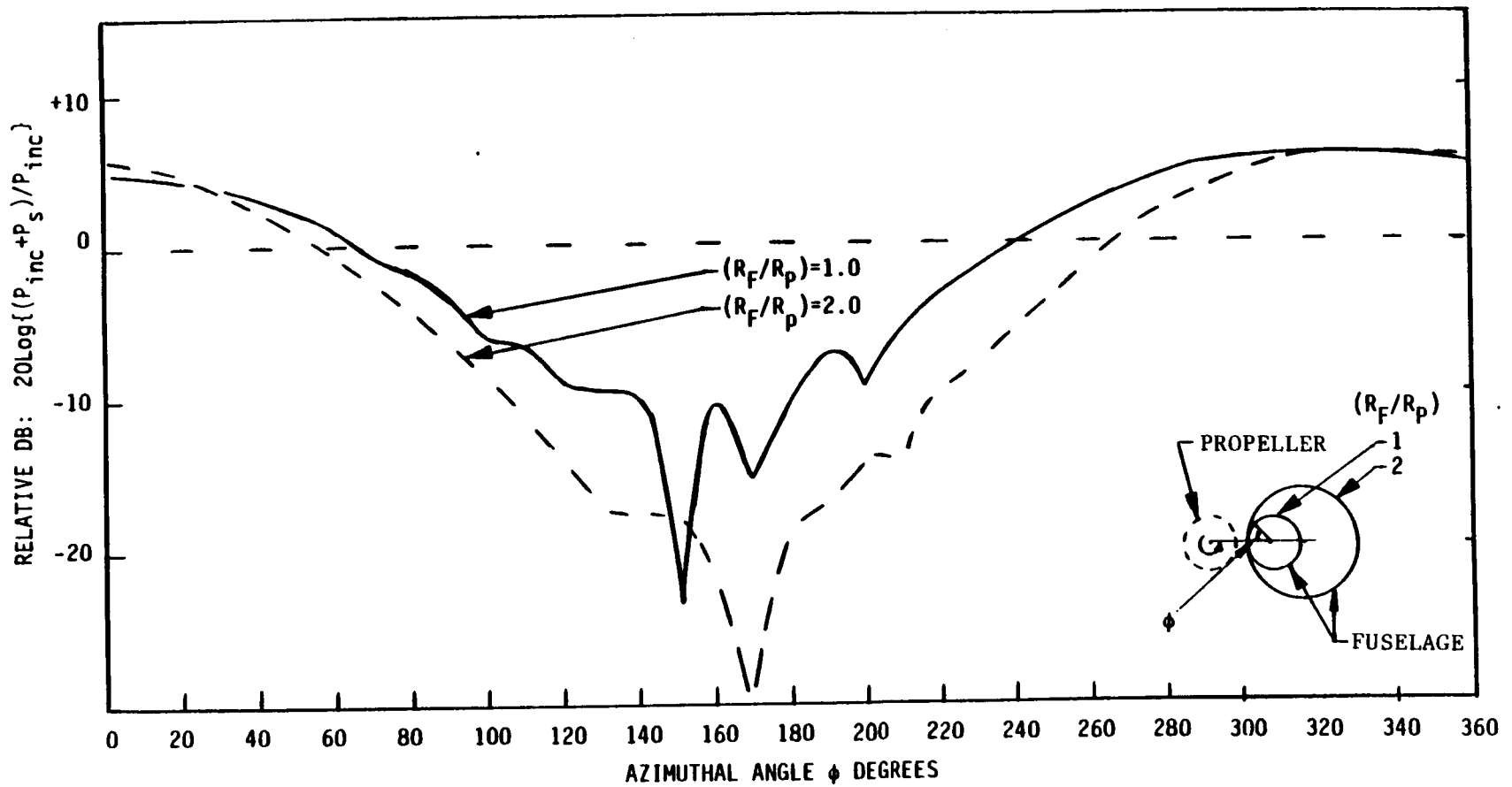

Figure 69. Influence of Fuselage/Propeller Radius Ratio on Combined (Incident and Scattered) Relative SPL Distribution on and Around Fuselage Surface for an 8-Bladed Propeller with Blade Tip Mach No. of 0.8.

- The peak relative SPL is 5.8 dB at $\phi = 335°$
- The shadow region is larger and deeper for the higher radius ratio.

2.3.3.3 Influence of Angle of Incidence on SPL Azimuthal Distribution

Figure 70 shows the no mean flow relative SPL distribution (incident + scattered fields normalized to incident field) on and around the fuselage surface for different angles of incidence.

Points of observation are:

- The azimuthal distribution is not symmetrical
- The shadow region reduces for lower angles of incidence
- For $\theta_i \leq 50°$, regions of amplification exceed 6 dB.

An amplification region (or regional focusing) prior to a shadow region is not uncommon in diffraction of wave fields such as that from a knife edge. Such a feature is apparent for $\theta_i = 50°$; however, the degree of amplification is unexpected. As will be shown later, the presence of flow and boundary layer modify these distributions.

2.3.3.4 Influence of Mean Flow and Boundary Layer

An example of the influence of mean flow and boundary layer on the azimuthal distribution of the combined incident + scattered fields (normalized by the incident field) is shown in Figure 71. It corresponds to a flight configuration of Mach No. 0.8 with angles of incidence of 50° and 130°. The boundary layer thickness is 0.01 of the fuselage radius. The blade number and the tip rotational Mach number are 8 and 0.8, respectively. The corresponding distribution for zero cruise Mach number is also shown.

All three curves correspond to azimuthal distributions around the fuselage at the outer edge of the boundary layer. The distribution at the fuselage surface is the same as that at the outer edge for the zero flight Mach number and for $M_c = 0.8$, with $\theta_i = 130°$. For $\theta_i = 50°$ and $M_c = 0.8$, the fuselage surface pressure at $R = R_f$ is 0.2 dB lower than that at $R = R_f + \delta$ (the outer edge of the fuselage boundary layer). This difference is larger for thicker boundary layers as is shown later.

The main points of observation are:

- Flight Mach number alters the symmetry of the combined pressure distribution relative to angle of incidence
- The flight Mach number reduces the relative SPL at $\phi = 0$ from 5.2 dB to 4.1 dB for $\theta_i = 50°$, and to 4.8 dB for $\theta_i = 130°$

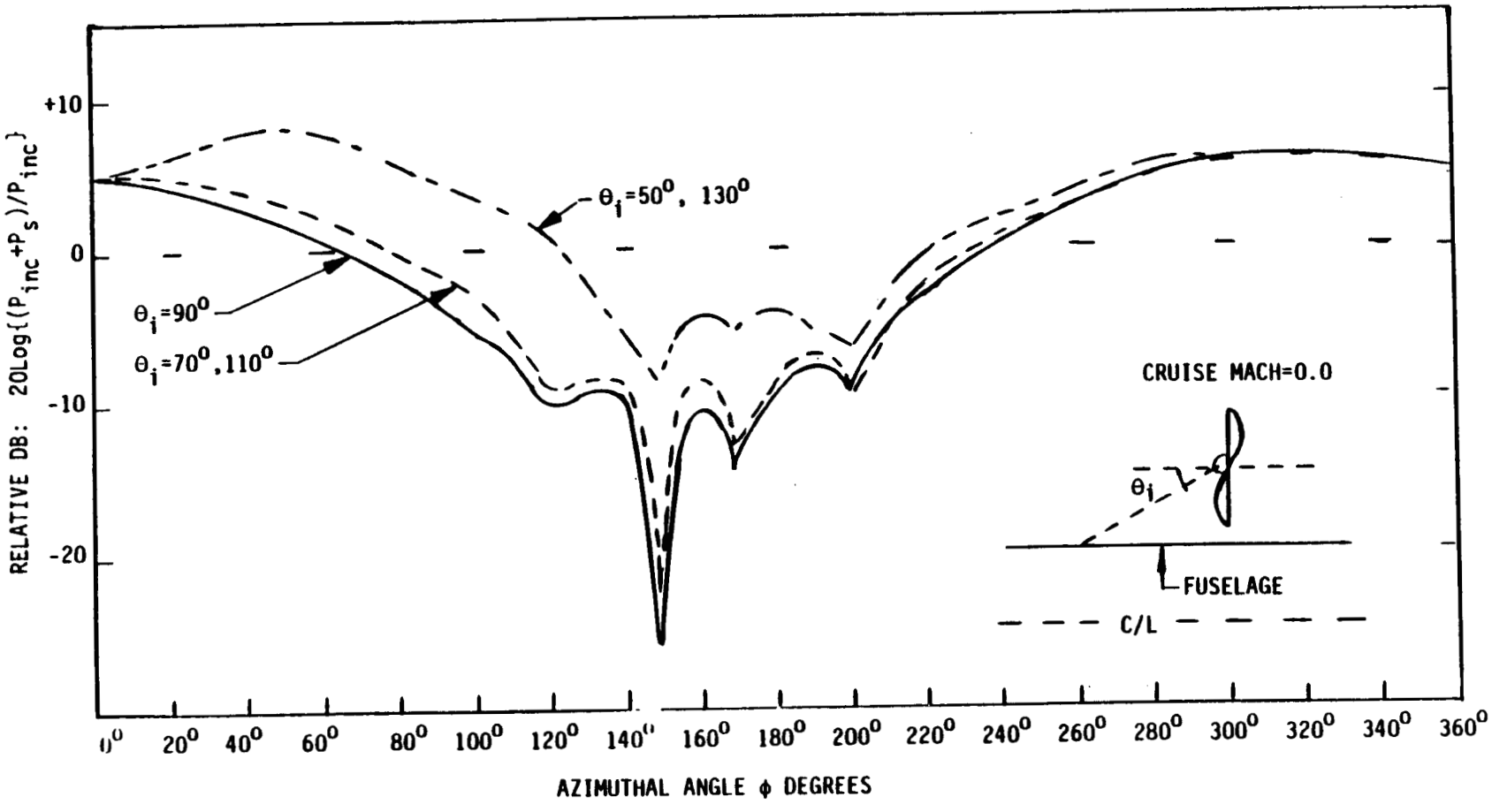

Figure 70. Effect of Angle-of-Incidence on the Relative Combined Incident and Scattered SPL Distribution on and Around the Fuselage Surface.

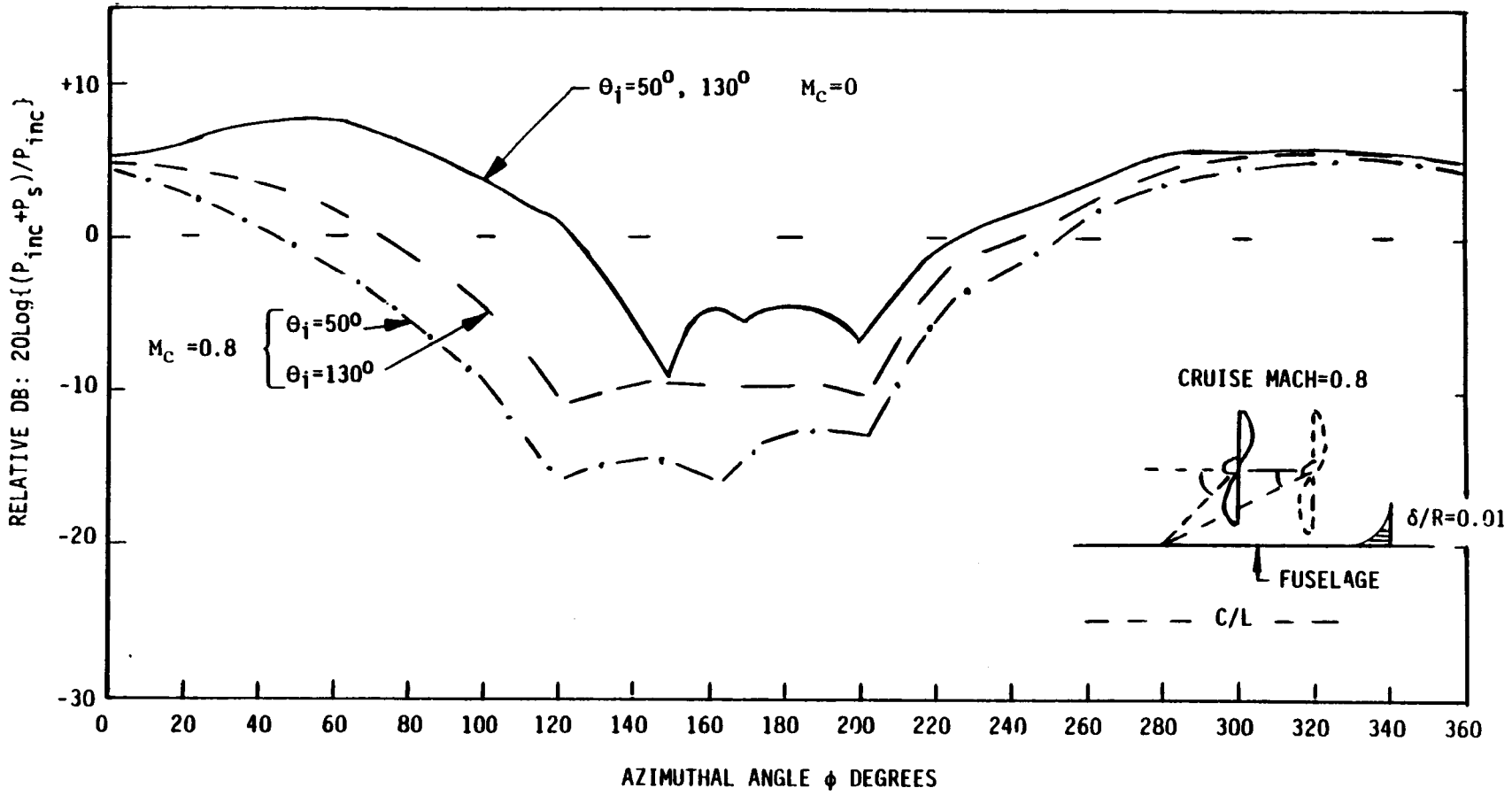

Figure 71. Influence of Cruise Mach Number on Relative SPL of Combined Incident and Scattered Fields for Angle-of-Incidence θ_i = 50° and 130°.

- Slight shadowing effect, -0.2 dB (not shown) for SPL below fuselage boundary layer.

2.3.3.5 Influence of Fuselage Boundary Layer Thickness and Cruise Mach Number

The influence of refraction due to the presence of a fuselage boundary layer is shown in Figure 72. The combined sound pressure level (incident + scattered fields normalized by the incident field) at the azimuthal angle $\phi = 0$ is shown as a function of visual angle of incidence. Two plots are shown, corresponding to levels above and below the fuselage boundary layer; namely at $R = R_f + \delta$ and $R = R_f$. The computations have been done for a flight Mach number of 0.8 and a boundary layer thickness ratio of $\delta/R_f = 0.10$. The actual profile across the boundary layer is that corresponding to a Blasius profile on a flat plate.

The main points of observation are:

- SPL relative to free field above the fuselage boundary layer and at $\phi = 0$ is higher than 0 dB (amplification) for all angles of incidence, ranging from 1.0 to 4.8 dB
- SPL relative to free field on the fuselage surface below the boundary layer is lower for upstream incidence than for downstream incidence and corresponds to boundary layer shielding
- Below the fuselage boundary layer, the range of angles of incidence where amplification (level above free field) exists is limited between $92° < \theta_i < 140°$.

Figure 73 shows the relative SPL distributions on the fuselage surface for three different boundary layer thickness ratios; namely $\delta/R_f = 0.01$, 0.05, and 0.1. The trend of increased refraction as (δ/R_f) increases is as expected.

Figure 74 illustrates the influence of cruise Mach number on the relative SPL distribution at $\phi = 0$ ad on the fuselage surface for $\delta/R_f = 0.1$. Again, the trend of increased fuselage boundary layer shielding is as expected.

The case of cruise Mach number equal to 0.8 compares favorably with Hanson's analytical results (Reference 2.3.6), allowing for possible differences in boundary layer profile and boundary layer thickness. It may be noted, however, that the other two cases (corresponding to cruise Mach numbers of 0.6 and 0.7) do not show the trends indicated by Hanson; namely, no refraction beyond 2-feet forward of the propeller plane. The present results show consistent trends of shielding similar to the case of Mach No. 0.8, but with less refraction.

2.3.3.6 Acoustic Shielding at Higher Harmonics of Blade Passing Frequency

All of the results presented thus far have been for the case of one times blade passing frequency. Figure 75 shows similar relative SPL distributions for three harmonics of the blade

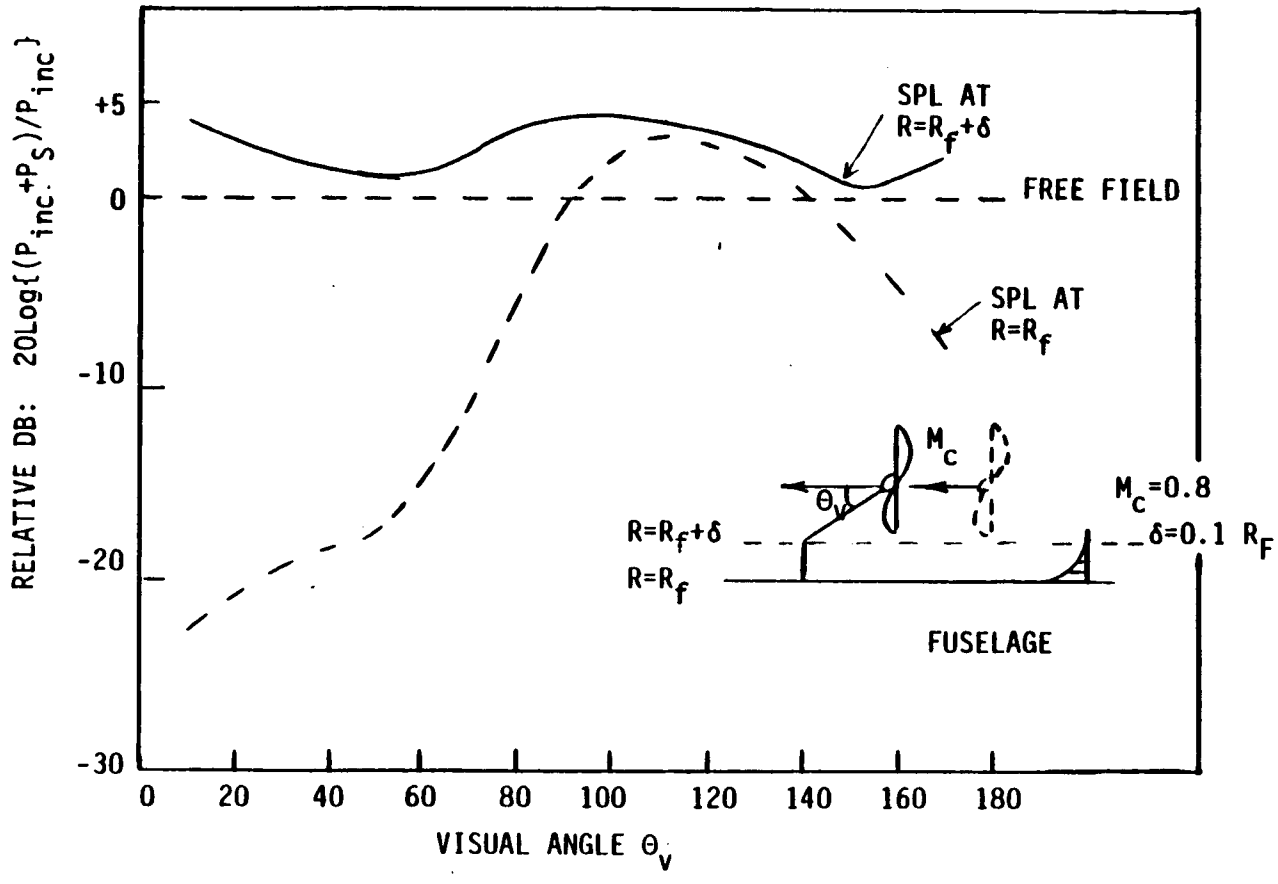

Figure 72. SPL Distribution (Incident and Scattered) Relative to Incident Field Below and Above Boundary Layer.

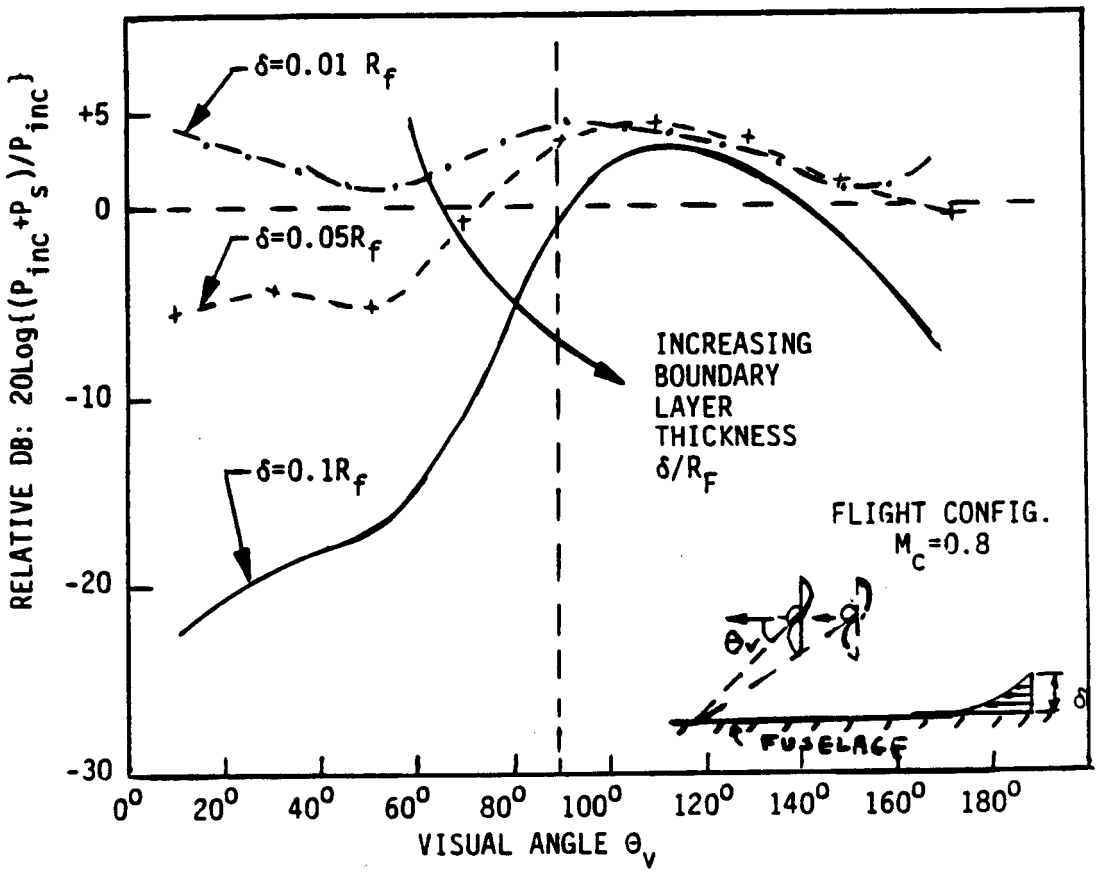

Figure 73. Influence of Boundary Layer Thickness on Relative SPL Distribution on Fuselage Surface at $\phi = 0$.

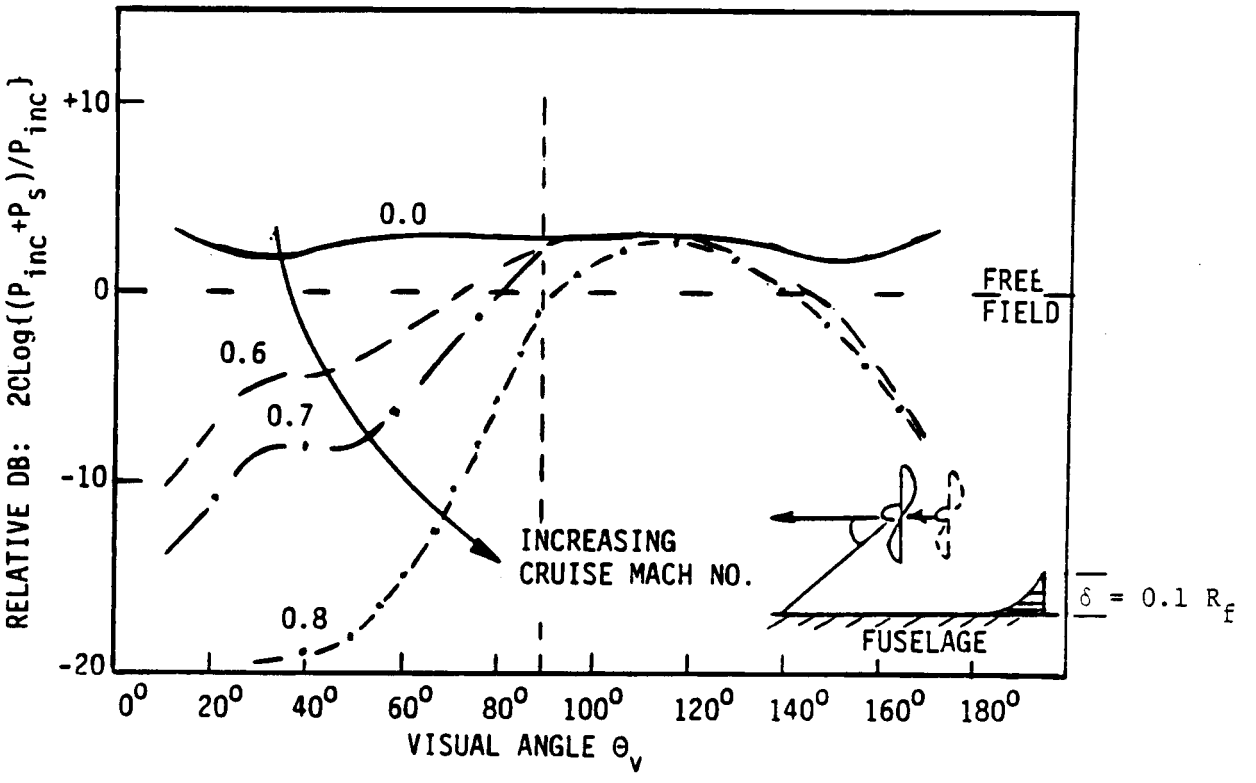

Figure 74. Influence of Cruise Mach Number on Relative SPL on Fuselage Surface at $\phi = 0$.

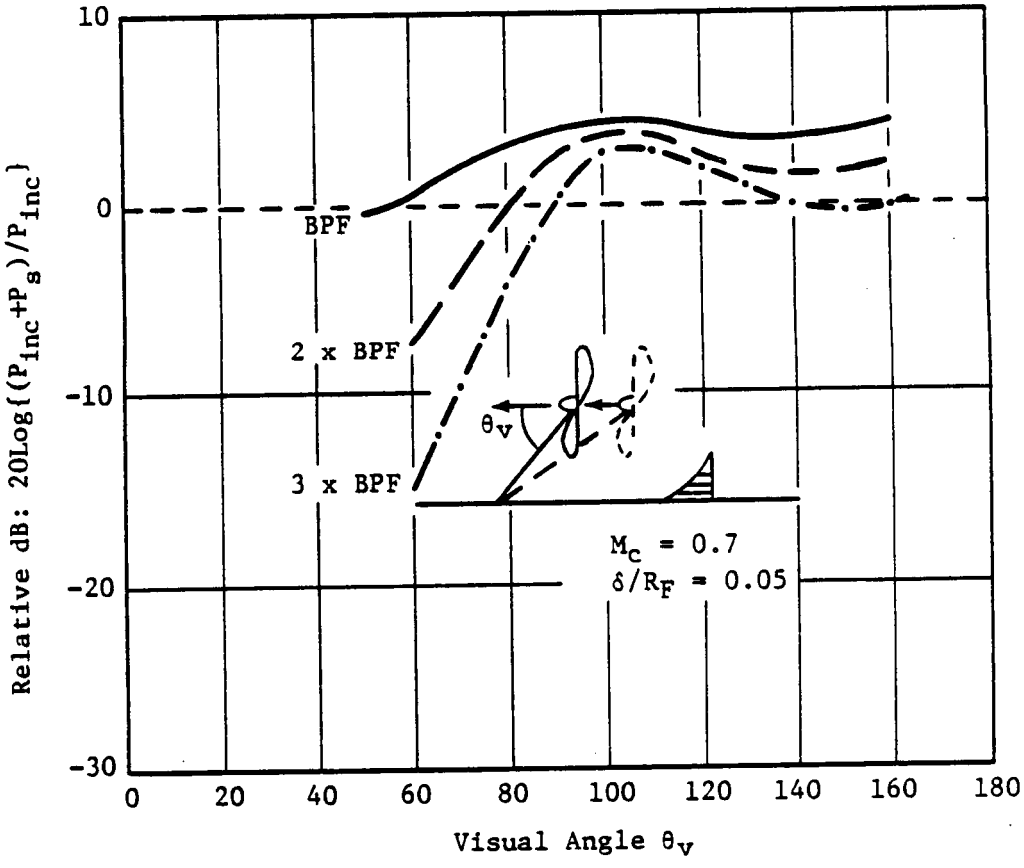

Figure 75. Combined Incident and Scattered Relative Sound Pressure Level Distribution on the Fuselage Surface at $\phi = 0$ for First Three Harmonics of BPF.

passing frequency. These distributions are the combined SPL (incident + scattered field normalized by the incident field) on the fuselage surface at $R = R_f$ and $\phi = 0$.

As expected, the combined fields at the higher harmonics undergo more refractive shielding. An interesting observation is that for angles of incidence $\theta_i > 90°$, the combined sound field at the blade passing frequency undergoes very little shielding; this is due to the thin boundary layer chosen for the illustration, namely $\delta/R_f = 0.01$. The corresponding fields at the higher harmonics undergo more shielding.

2.3.3.7 Comparison of 2D Plane Wave and 3D Cylindrical Wave Scattering by Boundary Layer

In Subsection 2.3.1.1.2, the refraction of a 2D plane wave by a rigid flat surface with an attached boundary layer was discussed. Figure 62 shows the boundary layer shielding effect for two frequencies.

To make a comparison with this 2D analysis, the cylindrical scattering analysis has been used to compute the SPL distribution for the following case:

Number of blades (B) = 8

Rotational tip Mach number (M_t) = 0.8

Cruise speed $M_c = M_z = 0.8$

Fuselage/propeller radius ratio (R_f/R_p) = 1

Boundary layer/fuselage radius ratio $\delta/R_f = 0.073$

The wave number:

$$k_o\delta = k_o R_p \frac{R_f}{R_p} \frac{\delta}{R_f}$$

$$= BM_t \times 1 \times 0.073$$

$$= 0.467$$

This wave number contrasts with that of 0.469 for the 2D analysis.

Figure 76 portrays the relative SPL distribution at $\phi = 0$ and $R = R_f$.

The 2D plane results are also presented; demonstrating remarkably similar trends. It appears that the 3D analysis yields lower amplification than the 2D case. In the shielding region, $\theta < 80$, the 3D analysis yields somewhat more shielding than the 2D analysis. It must be stressed that this comparison is for $\phi = 0$. As pointed out in Subsection 2.3.3.1, the

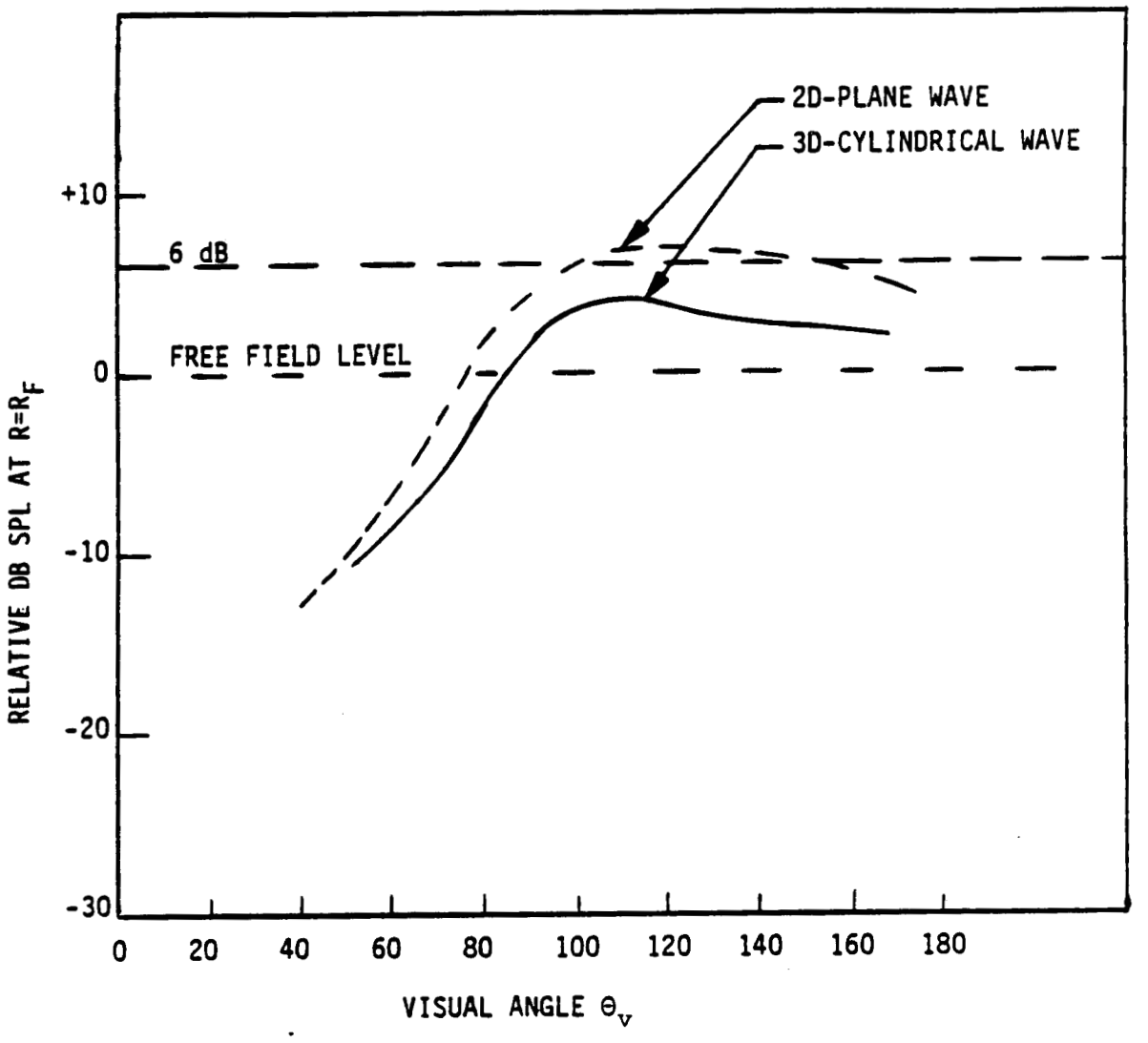

Figure 76. Comparison of Boundary Layer Refraction Effects Using 2D Plane and 3D Cylindrical Wave for $k_o\delta = 0.47$ and Flight Mach No. 0.8.

amplification is higher at some other value of ϕ. However, for $\phi \neq 0$, comparison with 2D plane wave refraction loses its meaning.

2.3.4 Concluding Remarks on Fuselage Scattering

An acoustic scattering analysis has been developed to make estimates of the acoustic shielding and amplification effects associated with sound incident upon a cylindrical fuselage supporting a mean flow boundary layer.

The estimate is evaluated in the form of a correction to be added to or subtracted from the incident free field. The incident field is chosen to be representative of acoustic emission from a propeller of specifiable blade number and rotating tip Mach number.

The main conclusions are as follows:

1. The combined sound pressure level distributions (incident + scattered) on the fuselage surface and at the outer edge of the boundary layer are not azimuthally symmetrical about the line joining the propeller and the fuselage center lines.

2. Regions of relative amplification and relative attenuation, corresponding to illuminated and shadow regions are functions of the fuselage-to-propeller radius ratio, the mean flow or cruise Mach number, the boundary layer thickness, and the harmonic of blade passing frequency under consideration.

3. On the fuselage surface, acoustic shielding occurs even in the illuminated region ($\phi = 0$), especially for angles of incidence $\theta_i < 90°$.

4. This refractive shielding becomes larger with increasing boundary layer thickness, mean flow or cruise Mach number, or frequency of the sound field.

3.0 INSTALLED TURBOPROP NOISE ANALYSIS

3.1 Configuration

3.1.1 Background

Under a separate NASA-sponsored effort, the PTA (Propfan Test Assessment) Program, acoustic data have been taken (under various flight conditions) from a large-scale propfan, mounted on the wing of a Gulfstream aircraft. Although data/theory comparisons were not required for the installed turboprop noise analysis portion of the current contract, it was felt that exercising the prediction models developed in the course of this work in order to predict the noise generated by a real (rather than a fictitious) propfan/airframe combination would be more meaningful. Consequently, it was decided that predictions should be made under conditions corresponding to those of three of the flights that were made during the test program, and that the predictions should be made at locations corresponding to those at which measurements had been taken on the aircraft. The three flight conditions selected represent the design point for the propfan (high altitude, high speed), together with two low altitude, low flight Mach number points at differing power and tip speed.

3.1.2 The PTA Airplane

The large-scale, 9-foot-diameter, SR-7L propfan was mounted on the left wing of a modified Gulfstream G-II business jet transport and was flight tested by the Georgia Division of the Lockheed Aeronautical Systems Company, under the NASA-sponsored Propfan Test Assessment Program (Reference 3.1.1). During this test, acoustic data were acquired with microphones located both on the fuselage of the airplane and on a boom situated further outboard than the propfan, and at the same sideline distance as the closest points on the fuselage. Figures 77 and 78 depict the PTA aircraft front view and plan view, respectively, while the various microphone locations on the fuselage surface and on the boom are shown in Figures 79 and 80. Tables 2 and 3 identify the microphone locations, in terms of the airplane coordinate system, as functions of: fuselage station (axial), water line (vertical), and butt line (horizontal). In addition, Table 4 shows the location of the center of the propfan disk in the same coordinates. It will be noted that Table 4 has three sets of coordinates, corresponding to three values of "nacelle tilt angle." This arises from the manner in which the propfan was mounted on the aircraft. One of the variables investigated during the flight test was the flow inflow angle in the vertical plane with regard to the propfan disk; thus, varying the tilt of the nacelle in the vertical plane permitted a greater range of inflow angle over the flight envelope than would have been possible otherwise.

The computer programs used to calculate the noise of the installed propfan require sideline distance and observer (or emission) angles relative to the center of the propfan disk as input, rather than airplane coordinates. Table 5 shows the locations of the microphones on the left side of the fuselage and on the boom in terms of sideline distances (DIST in Table 5) and observer angles (THETA) from the center of the disk at the two values of nacelle tilt angle for which the calculations were required. Also shown are tabulations of PHI, the azimuthal

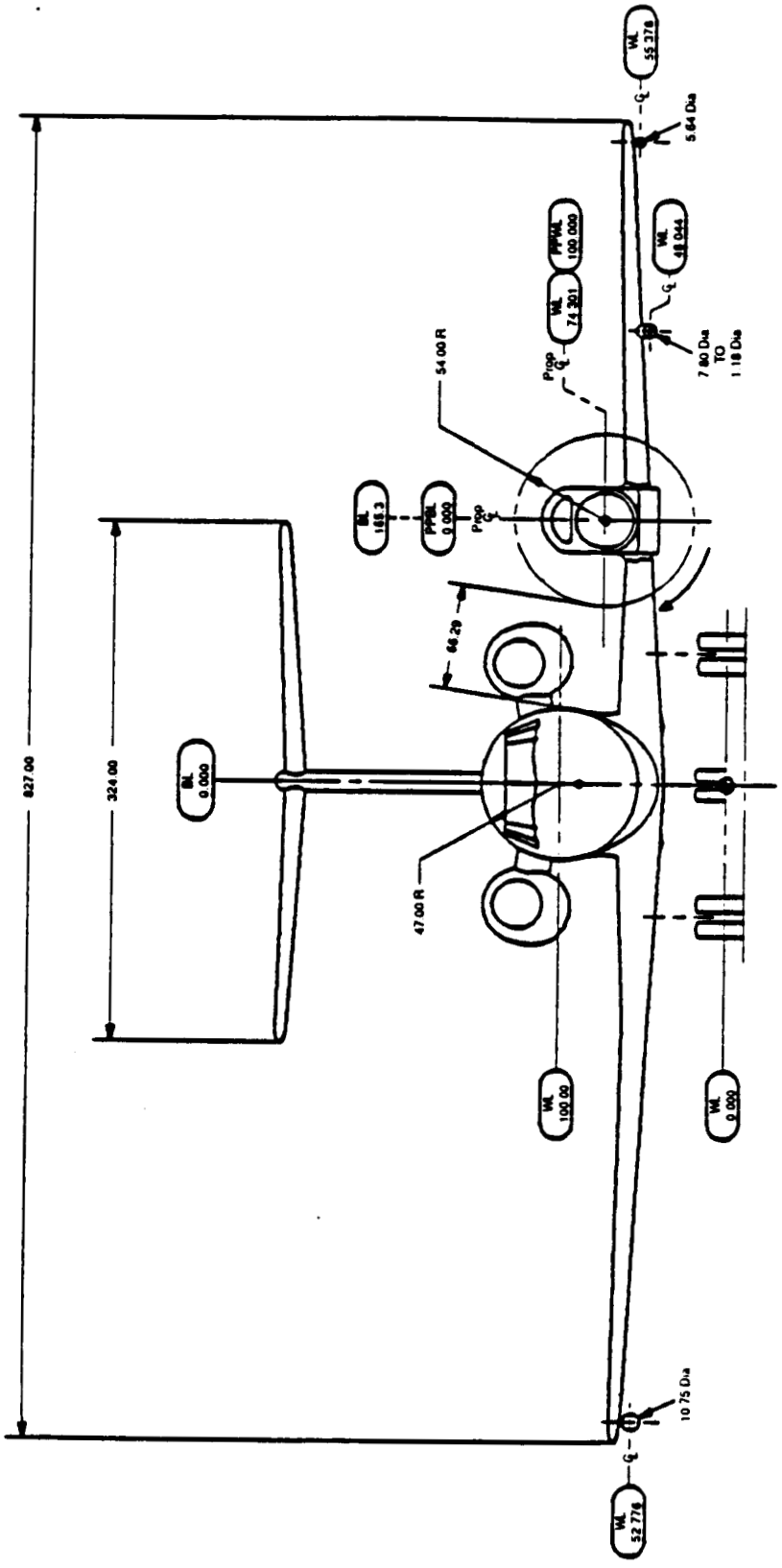

Figure 77. PTA Aircraft - Front View.

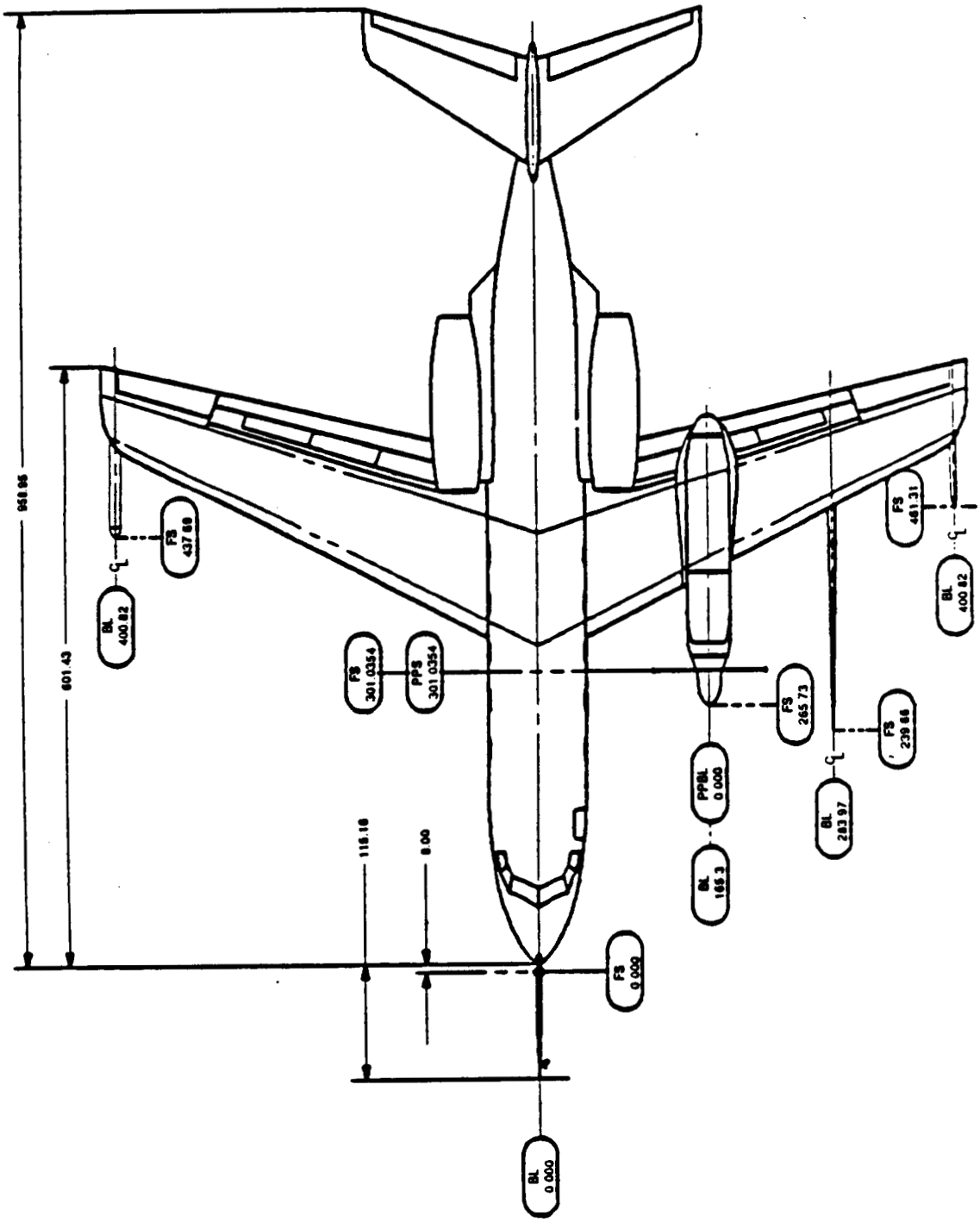

Figure 78. PTA Aircraft - Plan View.

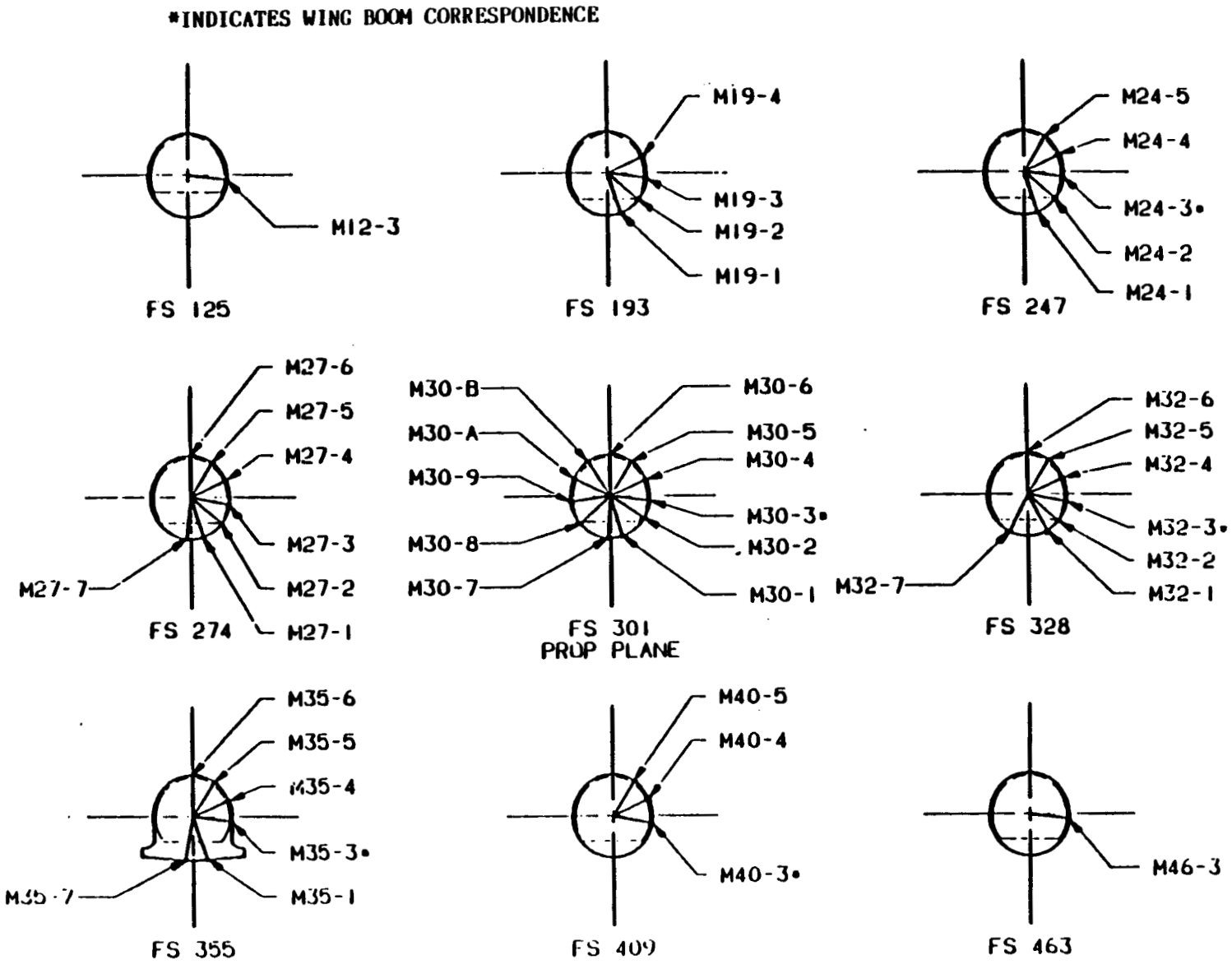

Figure 79. Fuselage External Microphone Locations, Looking Aft.

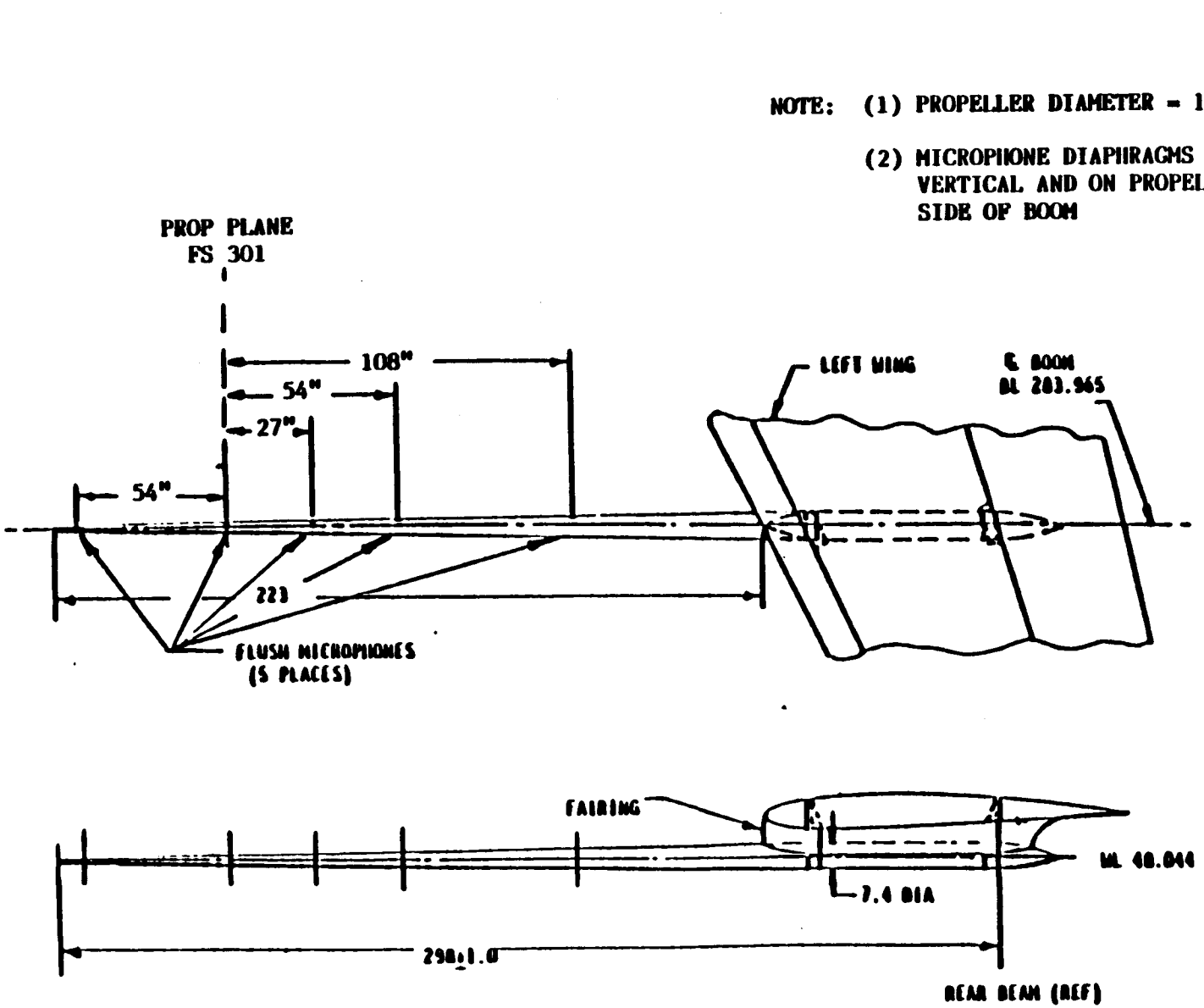

Figure 80. Acoustic Boom Installation and Microphone Locations.

Table 2. Fuselage Surface Locations for Prediction Purposes - 45 Locations.

FUSELAGE STATION (AXIAL)	125	195	247	274	301	328	355	409	463	
PROP DIAMETER (REF TO PP)	+1.63D	+0.98D	+0.5D	+0.25D	PROP PLANE	-0.25D	-0.5D	-1D	-1.5D	
WATER LINE										
147.00				0.00	0.00	0.00	0.00			BUTT LINE LOCATIONS FOR FUSELAGE LEFT SIDE (PROPELLER SIDE)
139.45			25.70	25.70	25.70	25.70	25.70			
118.92		43.03	43.03	43.03	43.03	43.03	43.03	43.03		
93.65	46.57	46.57	46.57		46.57		46.57		46.57	
91.71				46.27		46.27		46.27		
70.00		36.17	36.17	36.17	36.17	36.17				
55.85		16.17	16.17	16.17	16.17	16.17*	16.17*			
53.69				8.00R	8.00R	8.00R*	8.00R*			BUTT LINE LOCATIONS FOR FUSELAGE RIGHT SIDE
67.47					33.93R					
93.65					46.57R					
118.92					43.03R					
139.45					25.70R					

Table 3. Wing Boom Surface Locations for Prediction Purposes.

FUSELAGE STATION (AXIAL)	247	301	328	355	409	
PROP DIAMETER (REF TO PP)	+0.5D	PROP PLANE	-0.25D	-0.5D	-1.0D	
WATER LINE	283.965	283.965	283.965	283.965	283.965	BUTT LINE LOCATIONS FOR BOOM

Table 4. Propeller Disk Center Coordinates for the Three Nacelle Tilt Angles.

NACELLE TILT ANGLE	BUTT LINE BL	FUSELAGE STATION FS	WATER LINE WL
+2°	165.3L	300.235	77.718
-1°	↓	301.478	72.603
-3°	↓	302.454	69.233

Table 5. Microphone Locations in the Coordinates Required by the Computer Programs.

***** GULFSTREAM MICROPHONE LOCATIONS *****

FUSELAGE STATION		125.00	195.00	247.00	274.00	301.00	328.00	355.00	409.00	463.00		
DIST (FT)	PHI	**********	**********	**********	**********	THETA	**********	**********	**********	**********	PHI-FUSE	
1	14.94 157.26				81.67	90.24	98.81	106.99			97.68	
2	12.72 156.14			70.77	80.25	90.29	100.31	109.74			64.59	
3	10.75 161.38		50.80	67.58	78.51	90.34	102.14	113.00	130.13		31.41	Nacelle Tilt = +2° (Case 3)
4	9.98 172.36	34.36	48.70	66.04		90.37		114.57		143.65	-0.09	
5	9.99 173.30				77.65		103.04		132.22		-2.48	
6	10.78 183.42		50.87	67.63	78.54	90.34	102.11				-32.00	
7	12.56 188.34		55.08	70.55	80.13	90.29	100.44	109.97			-62.21	

BOOM STATION	247.00	301.00	328.00	355.00	409.00
DIST (FT)	**********	**********	THETA	**********	**********
10.19	66.48	90.36	102.79	114.12	131.64

FUSELAGE STATION		125.00	195.00	247.00	274.00	301.00	328.00	355.00	409.00	463.00		
DIST (FT)	PHI	**********	**********	**********	**********	THETA	**********	**********	**********	**********	PHI-FUSE	
1	15.11 155.77				81.38	89.85	98.32	106.45			99.41	
2	12.90 154.41			70.61	79.93	89.82	99.72	109.08			66.33	
3	10.90 159.25		50.84	67.38	78.13	89.79	101.47	112.26	129.43		33.15	Nacelle Tilt = -1° (Cases 1&2)
4	10.05 169.95	34.34	48.55	65.69		89.77		113.93		143.26	1.65	
5	10.05 170.88				77.16		102.41		131.73		-0.75	
6	10.76 181.15		50:50	67.13	77.99	89.79	101.60				-30.26	
7	12.51 186.41		54.64	70.05	79.62	89.82	100.02	109.63			-60.47	

BOOM STATION	247.00	301.00	328.00	355.00	409.00
DIST (FT)	**********	**********	THETA	**********	**********
10.10	65.79	89.77	102.35	113.83	131.58

angle, in the coordinate systems required by the installation effects and fuselage scattering computer codes.

3.2 Calculations

3.2.1 The Cases Analyzed

Tables 6 through 8 provide details of the propfan operating conditions for each case analyzed, and Table 9 defines the abbreviations utilized in these tables.

Case No. 1 (Table 6) corresponds to the design point for the SR-7L propfan; 35000-feet altitude, at a flight Mach number of 0.8, and a tip rotational Mach number also of 0.8. Cases 2 and 3 are low altitude flights; nominally 1000-feet altitude, and a flight Mach number of 0.3. Case 2 has a high tip rotational Mach number of 0.73, with a high power absorption of 5886 shp. On the other hand, Case 3 has a tip rotational Mach number of 0.62, with a correspondingly lower power; 4728 shp.

For each case, both uninstalled (free field, no unsteady loads included in the calculation) and installed (free field, with unsteady loads resulting from: angle-of-attack operation, the presence of the fuselage, and the effect of the wing lifting line) predictions were made. The uninstalled calculations were made for the microphones on the boom, as well as on the 93.65 and 91.71 water lines along the fuselage. The installed calculations were made for the microphones around the fuselage in the plane of the propfan (Fuselage Station 301) and at 0.25 propfan diameters upstream and downstream (Fuselage Stations 274 and 328). In addition, for Case 1 (the high flight Mach number case), fuselage scattering predictions were made for three fuselage boundary layer thicknesses.

3.2.2 Modifications to the Codes

The SRPFAN (Single Rotation PropFAn Noise) prediction code delivered under this contract requires the spanwise load distribution on the blades to be input as a swirl (or work) coefficient distribution, as described in Subsection 2.1.2.3 of this report. These distributions, along with the chordwise loading parameters, are input to the code by means of unique Loadfiles, obtained from an Euler flow solution of the particular operating conditions under consideration. For the particular cases reported here, NASA Lewis Research Center kindly supplied GE Aircraft Engines with Loadfiles generated from a Denton Euler code (Reference 3.2.1).

However, during the interim between the delivery of SRPFAN to NASA and the start of the present calculations, modifications had been made to the NASA version of the code, such that it now required spanwise loading to be input as a distribution of lift coefficient. Consequently the Loadfiles received contained lift (rather than swirl) coefficients. The GEAE code was modified to accept lift coefficient as input, while retaining the ability to scale the input distribution if necessary to match the required power input.

ORIGINAL PAGE IS
OF POOR QUALITY

Table 6. Prediction Case No. 1.

FLT 16, RUN 44 24-SEP-87

(1)	DATE	710.870		(64)	TQSD	2.14904	FT-LBF
(2)	FLT	16.0000		(65)	PSHP	3129.37	HP
(3)	RUN	0.000000E+00		(66)	SHPC	88888.0	%
(4)	STME	15:03:15.301	H/M/S	(67)	RPML	99.9078	%
(5)	ETME	15:03:59.801	H/M/S	(68)	RLMX	100.070	%
(6)	TAMB	0.000000E+00	DEGREE C	(69)	RLMN	99.4531	%
(7)	PAMB	0.000000E+00	PSI	(70)	RLSD	0.149800	%
(8)	RH	0.000000E+00	%	(71)	PMCP	0.000000E+00	%
(9)	WSMX	0.000000E+00	KNOTS	(72)	RPT	11489.4	RPM
(10)	WSMN	0.000000E+00	KNOTS	(73)	RPMN	97.3413	%
(11)	WSAG	0.000000E+00	KNOTS	(74)	RHMX	97.4414	%
(12)	WSD	0.000000E+00	DEGREE	(75)	RHMN	97.1328	%
(13)	PAMD	0.000000E+00	SLUGS/FT**3	(76)	RHSD	0.581600E-01	%
(14)	CG	1087.11	FPS	(77)	RPMC	13919.8	RPM
(15)	PMCG	0.000000E+00	LBF-SEC/FT**3	(78)	CP1	3638.31	HZ
(16)	ACGW	58105.6	LBF	(79)	TP1	13787.3	HZ
(17)	MTRU	0.800760		(80)	PRPM	1690.27	RPM
(18)	HAGL	0.000000E+00	FEET	(81)	VROT	796.519	FPS
(19)	HPT	34954.9	FEET	(82)	VPWD	791.472	FPS
(20)	HPMX	35015.4	FEET	(83)	VTH	1122.89	FPS
(21)	HPTN	34911.7	FEET	(84)	PTMR	0.806391	
(22)	HPSD	17.8101	FEET	(85)	MFWD	0.800760	
(23)	KTAS	468.604	KNOT	(86)	TMTH	1.13680	
(24)	KTMX	470.279	KNOT	(87)	BAPP	58.4036	DEGREE
(25)	KTMN	467.279	KNOT	(88)	BAMX	58.4375	DEGREE
(26)	KTSD	0.616170	KNOTS	(89)	BAMN	58.3789	DEGREE
(27)	VGO	791.472	FPS	(90)	BASD	0.882000E-02	DEGREE
(28)	KCAS	272.496	KNOT	(91)	IA	0.809540	DEGREE
(29)	TTMN	-18.6970	DEGREE C	(92)	SHPA	3072.53	HP
(30)	TTMX	-18.4688	DEGREE C	(93)	PSTQ	9547.14	FT-LBF
(31)	TTMN	-18.9316	DEGREE C	(94)	FNST	1583.16	LBF
(32)	TTSD	0.118700	DEGREE C	(95)	PBHP	384.066	HP
(33)	OATC	-47.6200	DEGREE C	(96)	PFBT	1193.39	FT-LBF
(34)	PA	499.025	PSF	(97)	PFBF	197.895	LBF
(35)	PTOT	761.262	PSF	(98)	PDPL	37.9324	HP/FT**2
(36)	COO	987.758	FPS	(99)	JP	3.12151	
(37)	SGMA	0.301300		(100)	CP	1.78716	
(38)	PMO	0.716630E-03	SLUGS/FT**3	(101)	CTP	0.424520	
(39)	PMOC	0.707857	LBF-SEC/FT**3	(102)	PFN	0.741480	%
(40)	QE	223.988	PSF	(103)	BPF1	225.369	HZ
(41)	ALPH	1.80954	DEGREE	~~(104)~~	~~RPM2~~	~~13767.4~~	~~%~~
(42)	ALMX	2.34890	DEGREE	~~(105)~~	~~R2MX~~	~~13767.0~~	~~%~~ DFR
(43)	ALMN	1.37940	DEGREE	~~(106)~~	~~R2MN~~	~~13767.0~~	~~%~~
(44)	ALSD	0.220840	DEGREE	~~(107)~~	~~R2SD~~	~~0.0000000E+00~~	~~%~~
(45)	SSNB	-.472310	DEGREE	(108)	RPM1	86.5348	%
(46)	SSMX	0.206100	DEGREE	(109)	R1MX	86.5508	%
(47)	SSMN	-.933600	DEGREE	(110)	R1MN	86.5000	%
(48)	SSSD	0.209750	DEGREE	(111)	R1SD	0.120800E-01	%
(49)	NTA	-1.00000	DEGREE	(112)	SPN1	2072.69	LBF
(50)	DHDT	-.139720	FPS	(113)	LSF1	0.916724E+08	HZ
(51)	PCAB	12.0050	PSI	(114)	LST1	0.362106E+09	HZ
(52)	PCMX	12.0049	PSI	~~(115)~~	~~RPM4~~	~~13767.4~~	~~%~~
(53)	PCMN	11.9961	PSI	~~(116)~~	~~R4MX~~	~~0.0000000E+00~~	~~%~~
(54)	PCSD	0.163000E-02	PSI	~~(117)~~	~~R4MN~~	~~0.0000000E+00~~	~~%~~ DFR
(55)	CDP	8.53955	PSI	~~(118)~~	~~R4SD~~	~~0.0000000E+00~~	~~%~~
(56)	TCAB	20.6730	DEGREE C	(119)	RPM2	92.8955	%
(57)	CC	1127.52	FPS	(120)	R2MX	92.9336	%
(58)	SIGC	0.000000E+00		(121)	R2MN	92.8633	%
(59)	PC	0.190524E-02	SLUGS/FT**3	(122)	R2SD	0.143300E-01	%
(60)	PMCC	2.14820	LBF-SEC/FT**3	(123)	SPN2	3063.23	LBF
(61)	TQE3	1430.52	FT-LBF	(124)	RSF1	0.916723E+08	HZ
(62)	TQMX	1435.50	FT-LBF	(125)	RST1	0.362106E+09	HZ
(63)	TQMN	1425.25	FT-LBF	(126)		0.000000E+00	0

Table 7. Prediction Case No. 2.

FLT 45, RUN 09R2 19-NOV-87

(1)	DATE	= 1009.87		(64)	TQSD	= 24.1798	FT-LBF
(2)	FLT	= 45.0000		(65)	PSHP	= 5953.11	HP
(3)	RUN	= 9.18000		(66)	SHPC	= 0.000000E+00	%
(4)	STME	= 08:31:17.801	H/M/S	(67)	RPML	= 100.256	%
(5)	ETME	= 08:32:00.801	H/M/S	(68)	RLMX	= 100.746	%
(6)	TAMB	= 8.60000	DEGREE C	(69)	RLMN	= 100.070	%
(7)	PAMB	= 14.9700	PSI	(70)	RLSD	= 0.116900	%
(8)	RH	= 69.0000	%	(71)	PMCP	= 0.000000E+00	%
(9)	WSMX	= 6.00000	KNOT	(72)	RPT	= 11529.4	RPM
(10)	WSMN	= 0.400000	KNOT	(73)	RPMN	= 96.3629	%
(11)	WSAG	= 4.30000	KNOT	(74)	RMMX	= 96.4570	%
(12)	WSD	= 355.000	DEGREE	(75)	RMMN	= 95.9648	%
(13)	PAMD	= 0.247765E-02	SLUGS/FT**3	(76)	RMSD	= 0.814200E-01	%
(14)	CG	= 1104.10	FPS	(77)	RPMC	= 13779.9	RPM
(15)	PMCG	= 2.73558	LBF-SEC/FT**3	(78)	CF1	= 4363.63	HZ
(16)	ACGW	= 61325.0	LBF	(79)	TF1	= 13835.3	HZ
(17)	MTRU	= 0.303400		(80)	PRPM	= 1696.16	RPM
(18)	HAGL	= 1030.00	FEET	(81)	VROT	= 799.295	FPS
(19)	HPT	= 587.548	FEET	(82)	VFWD	= 334.095	FPS
(20)	HPMX	= 879.624	FEET	(83)	VTH	= 866.309	FPS
(21)	HPTN	= 334.445	FEET	(84)	PTMR	= 0.726287	
(22)	HPSD	= 145.647	FEET	(85)	MFWD	= 0.303400	
(23)	KTAS	= 197.806	KNOT	(86)	TMTH	= 0.787181	
(24)	KTMX	= 200.866	KNOT	(87)	BAPP	= 36.8441	DEGREE
(25)	KTMN	= 192.790	KNOT	(88)	BAMX	= 37.1094	DEGREE
(26)	KTSD	= 2.20074	KNOT	(89)	BAMN	= 35.8086	DEGREE
(27)	VOO	= 334.095	FPS	(90)	BASD	= 0.284670	DEGREE
(28)	KCAS	= 198.614	KNOT	(91)	IA	= 3.70003	DEGREE
(29)	TTMB	= 11.9240	DEGREE C	(92)	SHPA	= 5886.03	HP
(30)	TTMX	= 12.1719	DEGREE C	(93)	PSTQ	= 18225.9	FT-LBF
(31)	TTMN	= 11.4922	DEGREE C	(94)	FNST	= 6612.03	LBF
(32)	TTSD	= 0.167190	DEGREE C	(95)	PSHP	= 735.754	HP
(33)	OATC	= 6.77646	DEGREE C	(96)	FFBT	= 2278.24	FT-LBF
(34)	PA	= 2071.69	PSF	(97)	FFBF	= 826.503	LBF
(35)	PTOT	= 2208.29	PSF	(98)	PDPL	= 72.6671	HP/FT**2
(36)	COO	= 1100.52	FPS	(99)	JP	= 1.31308	
(37)	SGMA	= 1.00776		(100)	CP	= 1.01303	
(38)	PMO	= 0.239663E-02	SLUGS/FT**3	(101)	CTP	= 0.526410	
(39)	PMOC	= 2.63755	LBF-SEC/FT**3	(102)	PFN	= 68.2328	%
(40)	QE	= 133.494	PSF	(103)	BFF1	= 226.154	HZ
(41)	ALPH	= 4.70003	DEGREE	(104)	RPM3	= 35.8340	%
(42)	ALMX	= 5.67040	DEGREE	(105)	R3MX	= 35.9219	%
(43)	ALMN	= 3.27620	DEGREE	(106)	R3MN	= 35.7461	%
(44)	ALSD	= 0.464830	DEGREE	(107)	R3SD	= 0.374000E-01	%
(45)	SSMB	= -2.35071	DEGREE	(108)	RPM1	= 64.5379	%
(46)	SSMX	= -1.47950	DEGREE	(109)	R1MX	= 64.5977	%
(47)	SSMN	= -4.76860	DEGREE	(110)	R1MN	= 64.4883	%
(48)	SSSD	= 0.778780	DEGREE	(111)	R1SD	= 0.274000E-01	%
(49)	NTA	= -1.00000	DEGREE	(112)	SFN1	= 253.452	LBF
(50)	DHDT	= 11.2407	FPS	(113)	LSF1	= 1002.52	HZ
(51)	PCAB	= 14.7940	PSI	(114)	LST1	= 3959.94	HZ
(52)	PCMX	= 14.8164	PSI	(115)	RPM4	= 32.4520	%
(53)	PCMN	= 14.7725	PSI	(116)	R4MX	= 32.5352	%
(54)	PCSD	= 0.810000E-02	PSI	(117)	R4MN	= 32.3516	%
(55)	CDP	= 0.407255	PSI	(118)	R4SD	= 0.474300E-01	%
(56)	TCAB	= 16.4770	DEGREE C	(119)	RPM2	= 60.2445	%
(57)	CC	= 1119.44	FPS	(120)	R2MX	= 60.3242	%
(58)	SIGC	= 1.00164		(121)	R2MN	= 60.1484	%
(59)	PC	= 0.238190E-02	SLUGS/FT**3	(122)	R2SD	= 0.424900E-01	%
(60)	PMCC	= 2.66638	LBF-SEC/FT**3	(123)	SFN2	= 158.243	LBF
(61)	TQE3	= 2711.89	FT-LBF	(124)	RSF1	= 907.899	HZ
(62)	TQMX	= 2724.25	FT-LBF	(125)	RST1	= 3586.20	HZ
(63)	TQMN	= 2592.00	FT-LBF	(126)	NZCG	= 1.00598	G

Table 8. Prediction Case No. 3.

FLT 41, RUN 13R 10-NOV-87

(1)DATE	=	909.869		(64)TQSD	=	4.29611	FT-LBF
(2)FLT	=	41.0000		(65)PSHP	=	4776.50	HP
(3)RUN	=	13.1800		(66)SHPC	=	88888.0	%
(4)STME	=	08:56:24.400	H/M/S	(67)RPML	=	87.8554	%
(5)ETME	=	08:57:16.801	H/M/S	(68)RLMX	=	88.1836	%
(6)TAMB	=	20.6000	DEGREE C	(69)RLMN	=	87.6914	%
(7)PAMB	=	14.8300	PSI	(70)RLSD	=	0.767200E-01	%
(8)RH	=	77.0000	%	(71)PMCP	=	83.5784	%
(9)WSMX	=	0.000000E+00	KNOTS	(72)RPT	=	10103.4	RPM
(10)WSMN	=	0.000000E+00	KNOTS	(73)RPMN	=	96.6103	%
(11)WSAG	=	0.000000E+00	KNOTS	(74)RHMX	=	96.6992	%
(12)WSD	=	0.000000E+00	DEGREE	(75)RHMN	=	96.4531	%
(13)PAMD	=	0.235416E-02	SLUGS/FT**3	(76)RHSD	=	0.394900E-01	%
(14)CG	=	1127.38	FPS	(77)RPMC	=	13815.3	RPM
(15)PMCG	=	2.65404	LBF-SEC/FT**3	(78)CF1	=	3199.40	HZ
(16)ACGW	=	60137.9	LBF	(79)TF1	=	12124.0	HZ
(17)MTRU	=	0.305290		(80)FRPM	=	1486.36	RPM
(18)HAGL	=	990.000	FEET	(81)VROT	=	700.431	FPS
(19)HPT	=	809.461	FEET	(82)VFWD	=	342.747	FPS
(20)HPMX	=	1034.25	FEET	(83)VTH	=	779.794	FPS
(21)HPTM	=	652.237	FEET	(84)FTMR	=	0.624233	
(22)HPSD	=	112.774	FEET	(85)MFWD	=	0.305290	
(23)KTAS	=	202.929	KNOT	(86)TMTH	=	0.694963	
(24)KTMX	=	204.932	KNOT	(87)BAPP	=	41.7865	DEGREE
(25)KTMN	=	200.167	KNOT	(88)BAMX	=	42.0508	DEGREE
(26)KTSD	=	1.17919	KNOTS	(89)BAMN	=	41.3984	DEGREE
(27)VOG	=	342.747	FPS	(90)BASD	=	0.149100	DEGREE
(28)KCAS	=	199.067	KNOT	(91)IA	=	5.94331	DEGREE
(29)TTMB	=	23.2630	DEGREE C	(92)SHPA	=	4728.73	HP
(30)TTMX	=	23.5488	DEGREE C	(93)PSTQ	=	16709.1	FT-LBF
(31)TTMN	=	22.7656	DEGREE C	(94)FNST	=	5191.58	LBF
(32)TTSD	=	0.245210	DEGREE C	(95)PSHP	=	591.091	HP
(33)OATC	=	17.8382	DEGREE C	(96)FFBT	=	2088.64	FT-LBF
(34)PA	=	2055.06	PSF	(97)FFBF	=	648.947	LBF
(35)PTOT	=	2192.29	PSF	(98)FDFL	=	58.3794	HP/FT**2
(36)COG	=	1122.07	FPS	(99)JP	=	1.53721	
(37)SGMA	=	0.961660		(100)CP	=	1.26730	
(38)FMG	=	0.228697E-02	SLUGS/FT**3	(101)CTP	=	0.564040	
(39)FMGC	=	2.56613	LBF-SEC/FT**3	(102)FFW	=	0.684169	%
(40)QE	=	134.072	PSF	(103)BPF1	=	198.182	HZ
(41)ALPH	=	3.94331	DEGREE	(104)RPM3	=	34.9100	%
(42)ALMX	=	5.24900	DEGREE	(105)R3MX	=	0.000000E+00	%
(43)ALMN	=	1.68070	DEGREE	(106)R3MN	=	0.000000E+00	%
(44)ALSD	=	0.516130	DEGREE	(107)R3SD	=	0.000000E+00	%
(45)SSNB	=	0.286000E-02	DEGREE	(108)RPM1	=	63.7793	%
(46)SSMX	=	0.626000	DEGREE	(109)R1MX	=	63.8672	%
(47)SSMN	=	-.556600	DEGREE	(110)R1MN	=	63.7266	%
(48)SSSD	=	0.264260	DEGREE	(111)R1SD	=	0.274000E-01	%
(49)NTA	=	2.00000	DEGREE	(112)SPN1	=	207.190	LBF
(50)DHDT	=	7.38108	FPS	(113)LSF1	=	97666.5	HZ
(51)PCAB	=	14.8030	PSI	(114)LST1	=	385783.	HZ
(52)PCMX	=	14.8271	PSI	(115)RPM4	=	31.2420	%
(53)PCMN	=	14.7832	PSI	(116)R4MX	=	31.3008	%
(54)PCSD	=	0.832000E-02	PSI	(117)R4MN	=	31.1680	%
(55)CDP	=	0.531780	PSI	(118)R4SD	=	0.212900E-01	%
(56)TCAB	=	22.1560	DEGREE C	(119)RPM2	=	58.9542	%
(57)CC	=	1130.36	FPS	(120)R2MX	=	59.2500	%
(58)SIGC	=	0.000000E+00		(121)R2MN	=	49.1094	%
(59)PC	=	0.233749E-02	SLUGS/FT**3	(122)R2SD	=	0.859650	%
(60)PMCC	=	2.64221	LBF-SEC/FT**3	(123)SPN2	=	113.625	LBF
(61)TQE3	=	2483.01	FT-LBF	(124)RSF1	=	87404.7	HZ
(62)TQMX	=	2492.00	FT-LBF	(125)RST1	=	345249.	HZ
(63)TQMN	=	2466.25	FT-LBF	(126)NZCG	=	1.01757	G

Table 9. Aircraft and Propeller Operating Conditions.

Definition of Abbreviations

Ground

1-DATE=TEST DATE
2-FLT =FLIGHT NUMBER
3-RUN =RUN NUMBER
4-STME=FROM TD4 FILE
5-ETME=FROM TD4 FILE
6-TAMB=GROUND AMBIENT TEMPERATURE
7-PAMB=GROUND AMBIENT PRESSURE
8-RH =GROUND RELATIVE HUMIDITY
9-WSMX=GROUND WIND SPEED MAX
10-WSMN=GROUND WIND SPEED MIN
11-WSAG=GROUND WIND SPEED AVERAGE
12-WSD =GROUND WIND SPEED DIRECTION
13-PAMD=GROUND AIR DENSITY
14-CG =GROUND SPEED OF SOUND
15-PMCG=GROUND CHAR. IMPEDANCE

Aircraft

16-ACGW=AIRCRAFT GROSS WEIGHT
17-MTRU=FREESTREAM MACH
18-HAGL=ALTITUDE ABOVE GROUND
19-HPT =ALTITUDE ABV SEA LEVEL MEAN
20-HPMX=ALTITUDE ABOVE SEA LEVEL-MAX
21-HPTM=ALTITUDE ABOVE SEA LEVEL-MN
22-HPSD=ALTITUDE ABOVE SEA LEVEL-SD
23-KTAS=TRUE AIR SPEED-MEAN
24-KTMX=TRUE AIR SPEED-MAX
25-KTMN=TRUE AIR SPEED-MIN
26-KTSD=TRUE AIR SPEED-SD
27-VOO =TRUE AIR SPEED
28-KCAS=CALIBRATED AIR SPEED
29-TTNB=FREESTREAM TOTAL TEMP-MEAN
30-TTMX=FREESTREAM TOTAL TEMP-MAX
31-TTMN=FREESTREAM TOTAL TEMP-MIN
32-TTSD=FREESTREAM TOTAL TEMP-SD
33-OATC=FREESTREAM STATIC TEMP
34-PA =FREESTREAM STATIC PRESSURE
35-PTOT=FREESTREAM TOTAL PRESSURE
36-COO =FREESTREAM SPEED OF SOUND
37-SGMA=DENSITY RATIO
38-PMO =FREESTREAM AIR DENSITY
39-PMOC=FREESTREAM CHAR. IMPEDANCE
40-QE =DYNAMIC PRESSURE
41-ALPM=ANGLE OF ATTACK-MEAN
42-ALMX=ANGLE OF ATTACK-MAX
43-ALMN=ANGLE OF ATTACK-MIN
44-ALSD=ANGLE OF ATTACK-SD
45-SSNB=SIDESLIP ANGLE-MEAN
46-SSMX=SIDESLIP ANGLE-MAX
47-SSMN=SIDESLIP ANGLE-MIN
48-SSSD=SIDESLIP ANGLE-SD
49-NTA =NACELLE TILT ANGLE
50-DHDT=CLIMB/DESCENT RATE

Cabin

51-PCAB=CABIN PRESSURE-MEAN
52-PCMX=CABIN PRESSURE-MAX
53-PCMN=CABIN PRESSURE-MIN
54-PCSD=CABIN PRESSURE-SD
55-CDP =CABIN DIFF PRESSURE
56-TCAB=CABIN TEMPERATURE
57-CC =CABIN SPEED OF SOUND
58-SIGC=CABIN DENSITY RATIO
59-PC =CABIN AIR DENSITY
60-PMCC=CABIN CHAR. IMPEDANCE

61-TQE1=POWER TURBINE TORQUE-MEAN
62-TQMX=DRIVE ENG PWR TURB TORQUE-MAX
63-TQMN=DRIVE ENG PWR TURB TORQUE-MIN
64-TQSD=DRIVE ENG PWR TURB TORQUE-SD
65-PSHP=POWER TURBINE SHP
66-SHPC=DRIVE ENG POWER TURBINE %MCP
67-RPML=POWER TURBINE % NP-MEAN
68-RLMX=DRIVE ENG PWR TURBINE % NP-MAX
69-RLMN=DRIVE ENG PWR TURBINE % NP-MIN
70-RLSD=DRIVE ENG PWR TURBINE % NP-SD
71-PMCP=PWR SECTION MAX CONTINUOUS PWR
72-RPT =DRIVE ENG PWR TURB ROT SPD-NP
73-RPMN=COMPRESSOR % NG-MEAN
74-RMMX=DRIVE ENG COMPRESSOR % NG-MAX
75-RMMN=DRIVE ENG COMPRESSOR %.NG-MIN
76-RMSD=DRIVE ENG COMPRESSOR % NG-SD
77-RPMC=DRIVE ENG COMP ROTATION SPD-NG
78-CF1 =DRIVE ENG COMP 1ST ROTOR FREQ
79-TF1 =DRIVE ENG TURB LAST ROTOR FREQ

PF Drive Engine

Prop Fan

80-PRPM=PROPFAN ROTATION SPEED
81-VROT=PROPFAN TIP ROTATION VEL
82-VFWD=PROPFN TIP FWD VEL=TRU AIR SPD
83-VTH =PROPFAN TIP HELICAL VEL
84-PTMR=PROPFAN TIP ROTATION MACH
85-MFWD=TIP FWD MACH=FREEST. MACH
86-TMTH=PROPFAN TIP HELICAL MACH
87-BAPP=BLADE ANGLE-B(3/4)-MEAN
88-BAMX=PROPFAN BLADE ANGLE-B(3/4)-MAX
89-BAMN=PROPFAN BLADE ANGLE-B(3/4)-MIN
90-BASD=PROPFAN BLADE ANGLE-B(3/4)-SD
91-IA =PROPFAN INFLOW ANGLE-UNINST
92-SHPA=SHAFT POWER
93-PSTQ=PROPFAN SHAFT TORQUE
94-FNST=SHAFT THRUST
95-PBHP=PROPFAN PWR PER BLADE
96-PFBT=PROPFAN TORQUE PER BLADE
97-PFBF=PROPFAN THRUST PER BLADE
98-PDPL=PROPFAN DSK PWR LDING
99-JP =ADVANCE RATIO
100-CP =PWR COEFFICIENT
101-CTP =THRUST COEFFICIENT
102-PFN =PROPFAN EFFICIENCY
103-BPF1=PROPFAN FUNDAMENTAL FREQ

LH Spey

104-RPM3=LP COMPRESSOR SPD-N1 %
105-R3MX=LPT SPEY ENG LP COMP SPEED-MAX
106-R3MN=LPT SPEY ENG LP COMP SPEED-MIN
107-R3SD=LPT SPEY ENG LP COMP SPEED-SD
108-RPM1=HP COMPRESSOR SPD-N2 %
109-R1MX=LPT SPEY ENG HP COMP SPEED-MAX
110-R1MN=LPT SPEY ENG HO COMP SPEED-MIN
111-R1SD=LPT SPEY ENG HP COMP SPEED-SD
112-SFN1=LPT SPEY ENG NET THRUST
113-LSF1=LPT SPEY ENG LPC:1ST ROTOR BPF
114-LST1=LPT SPEY ENG LPT:LAST ROT BPF

RH Spey

115-RPM4=LP COMPRESSOR SPD-N1 %
116-R4MX=RT SPEY ENG LP COMP SPEED-MAX
117-R4MN=RT SPEY ENG LP COMP SPEED-MIN
118-R4SD=RT SPEY ENG LP COMP SPEED-SD
119-RPM2=HP COMPRESSOR SPD-N2 %
120-R2MX=RT SPEY ENG HP COMP SPEED-MAX
121-R2MN=RT SPEY ENG HP COMP SPEED-MIN
122-R2SD=RT SPEY ENG HP COMP SPEED-SD
123-SFN2=RIGHT SPEY ENG NET THRUST
124-RSF1=RT SPEY ENG LPC:1ST ROT BPF
125-RST1=RT SPEY ENG LPT:LAST ROT BPF
126-=0

A minor modification was made to the SRPIE (Single Rotation Propfan Installation Effects) code to enable the calculation to be performed at specified values of ϕ (the azimuthal angle), rather than at predetermined 15° intervals.

No changes were made to the SRPFS (Single Rotation Propeller Fuselage Scattering) code.

3.3 Results

3.3.1 Case 1: Design Point

3.3.1.1 Uninstalled Predictions

Results calculated under free field conditions at the fuselage microphone locations along the 93.65 and 91.71 water lines and at the boom microphones are shown in Figures 81 and 82, respectively. The first three harmonics of BPF are shown in each figure.

It will be noted that, under these conditions, the predicted levels are the same at the fuselage surface (Figure 81) and at the boom (Figure 82). This is what would be expected from the prediction model, given that the boom and fuselage microphones were at virtually the same sideline distance (Table 5), and that the model predicts no azimuthal variations.

One feature depicted in Figure 81 (which is missing from Figure 82, due to the absence of a microphone at that location), is that all three harmonics of BPF are predicted to peak forward of the plane of rotation. In order to examine this feature, Figure 83 was plotted, showing the BPF tone predicted by the steady loading and thickness components of the acoustic model separately, together with the total already seen in Figure 81. It appears (from Figure 83) that the thickness noise prediction, combined with phasing effects, is causing the peak in the forward arc, with the relative phasing between the two components actually reducing the total level below the peak predicted by the steady loading model at Fuselage Station 355.

One final effect, seen in Figure 84, concerns the selection of the angle used to divide the lift on any blade section into its thrust and torque components. As described in Section 2.1, there is an option in the SRPFAN code allowing the use of either the helicoidal angle (β_Λ, in Figure 1) or the blade pitch angle (β_Π, in the same figure) in the evaluation of k_y in Equation 2.1.2. Figure 84 indicates the minor differences found between the two models. In general, use of the helicoidal surface option results in levels that are 1 to 2 dB higher than those obtained with the blade pitch angles. All of the results presented in this report (with the exception of Figures 84, 96, and 100), use the blade pitch angles to divide the section lift into its thrust and torque components.

3.3.1.2 Installation Effects

The effects of the installation environment (presence of a fuselage and wing lifting line, together with angle-of-attack operation) were calculated, again under free field conditions, at the microphones located on the left side of the fuselage in the plane of the propfan (Fuselage

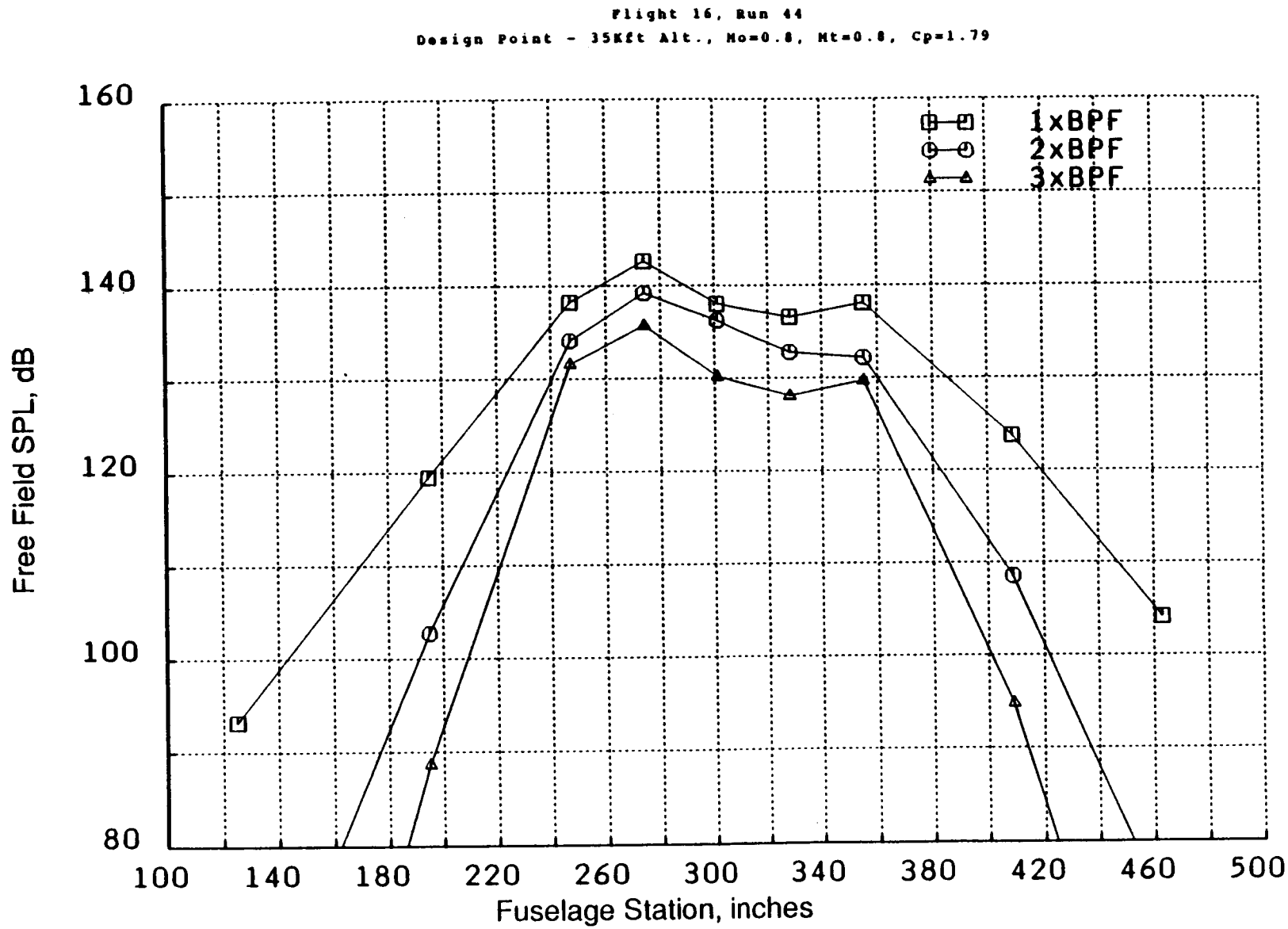

Figure 81. PTA Airplane Fuselage Predictions - Uninstalled (Prediction Case No. 1).

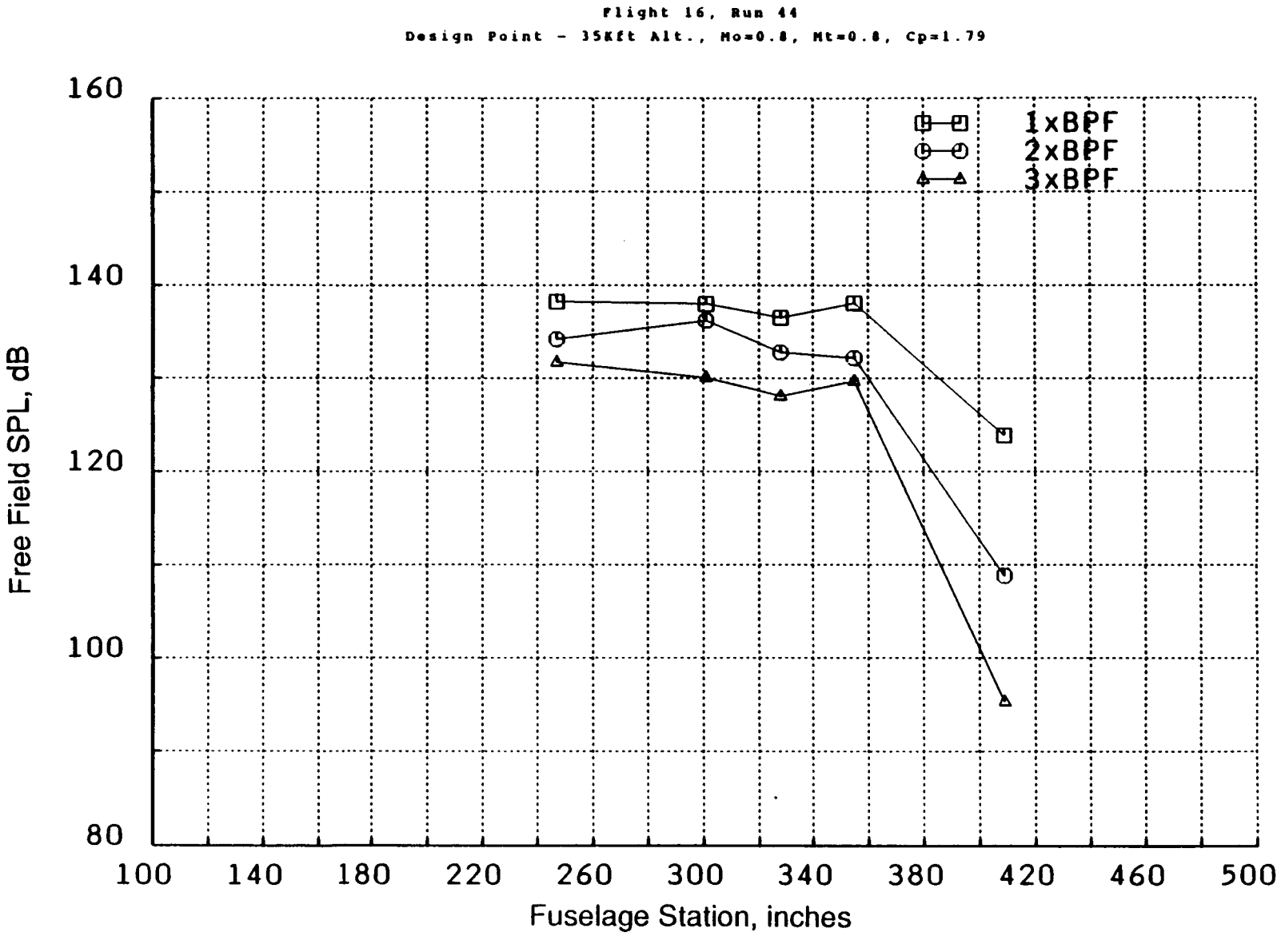

Figure 82. PTA Airplane Boom Predictions - Uninstalled (Prediction Case No. 1).

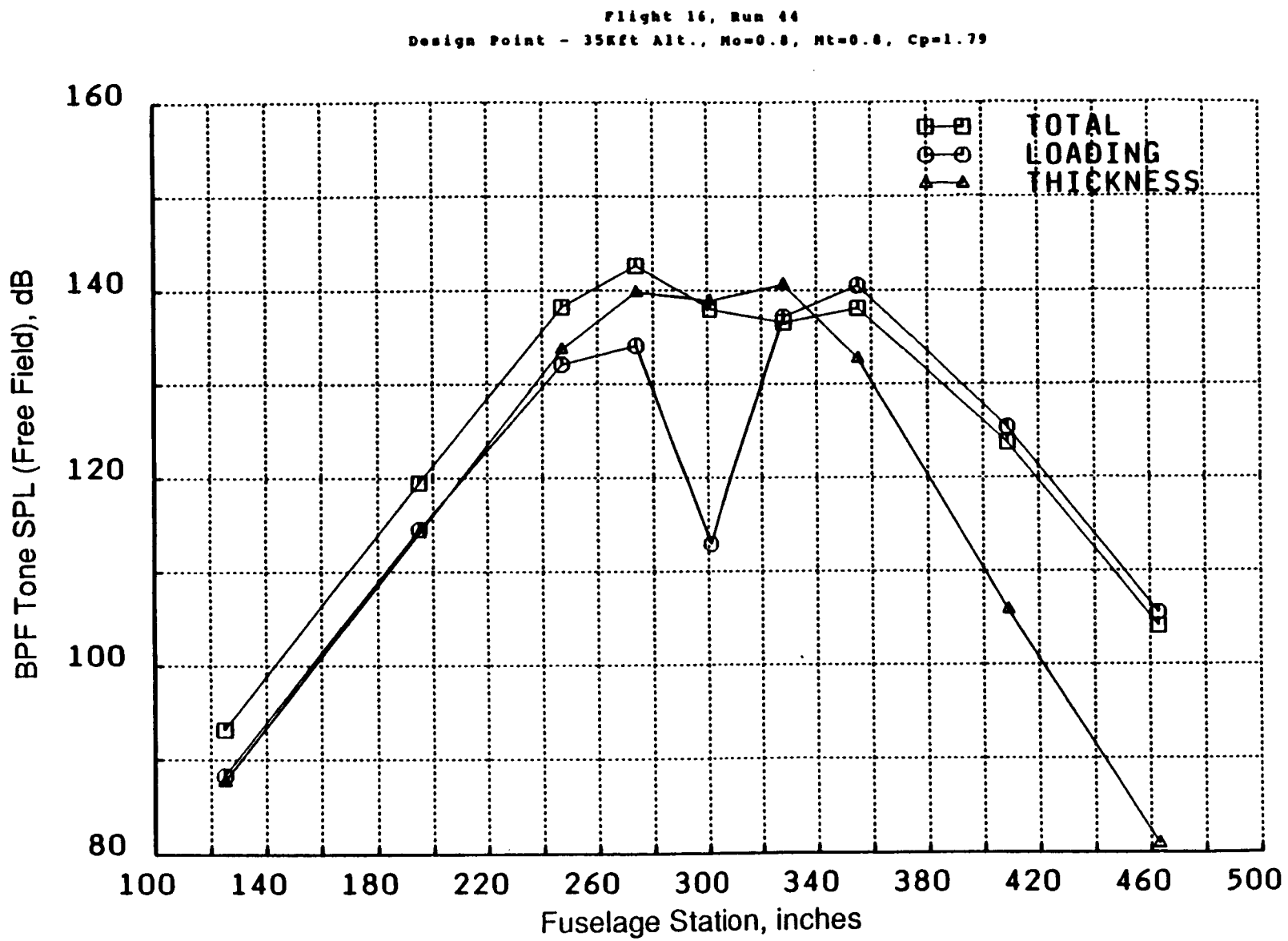

Figure 83. PTA Airplane Fuselage Predictions - Uninstalled (Prediction Case No. 1).

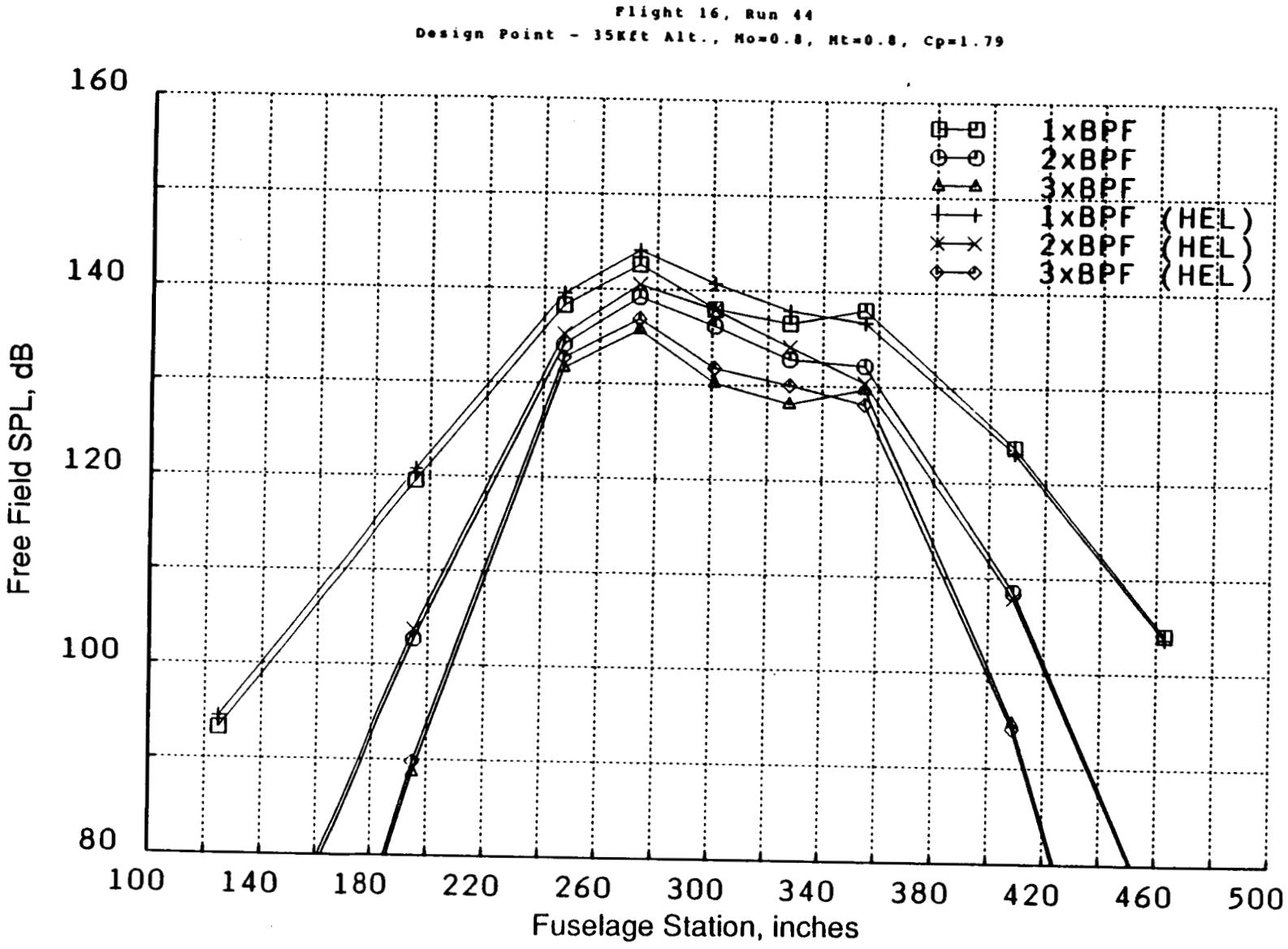

Figure 84. PTA Airplane Fuselage Predictions - Uninstalled (Prediction Case No. 1).

Station 301) and 0.25 propfan diameters upstream and downstream of this plane, at Fuselage Stations 274 and 328, respectively. Results are listed in Table 10 for the first and second harmonics of BPF, and the free field installed levels of the BPF tone are shown graphically in Figure 85. The effect of the installation is predicted to be small everywhere.

In order to make the prediction, it was assumed that the inflow angle to the propfan was given by the parameter "IA" (the combination of the airplane angle-of-attack and the nacelle tilt) in Table 6. For this case the value is low, namely 0.81°. Other inputs required are the wing lift coefficient and the location of the center of the propfan, relative to the wing lifting line. The lift coefficient was calculated from the aircraft gross weight and other relevant parameters given in Table 6, together with an estimate of the wing area scaled from Figure 78. In addition, the analytical model employed in the SRPIE code for the flowfield of a wing lifting line is restricted to rectangular (unswept) wings.

Consequently, it was assumed that the unswept wing lifting line passes through the midchord of the wing/fuselage installation. Finally, the blade section lift and drag coefficients versus angle-of-attack data required by the prediction code were obtained using the performance data given in Reference 3.3.1 for the SR-7A model propfan in the CLDSRP performance preprocessor.

3.3.1.3 Fuselage Scattering Effects

The final set of calculations performed for this high flight Mach number case were concerned with the effects of refraction and diffraction described in Section 2.3. These effects were shown to increase with increasing flight Mach No.; hence it was decided that, for this case only, an assessment would be made of their contribution.

Results were calculated for three values of fuselage boundary layer thickness: δ = 1 inch, δ = 3 inches (suggested by Lockheed), and δ = 6 inches. The predicted effects are shown in terms of "dBFW," which is defined as:

$$dBFW = 20\log_{10}(P(R_f,\phi)/P_i(R_f+\delta,\phi)$$

where $P(R,\phi) = P_i(R,\phi) + P_s(R,\phi)$, (incident + scattered fields.)

For pure reflection, dBFW = 6 dB.

Figure 86 presents the predicted effects of the three different boundary layer thicknesses on the fundamental BPF tone as a function of distance along the fuselage at a fuselage azimuthal angle, ϕ-fuse (Table 5), equal to zero. This approximately corresponds to the 93.65 and 91.71 water line locations used in the uninstalled predictions. The results are similar to those presented in Section 2.3, with the greatest decreases relative to the pure reflection 6 dB value occurring ahead of the plane of the propfan (Fuselage Station 301) as a function of boundary layer thickness, and the boundary layer being predicted to have negligible effect

Table 10. Predicted Installation Effects for Case 1 (Free Field).

CASE 1 (BPF)

FS WL	ISOLATED 274	ISOLATED 301	ISOLATED 328	DELTA 274	DELTA 301	DELTA 328	INSTALLED 274	INSTALLED 301	INSTALLED 328
147.00	138.5	134.5	133.6	-.7	-.5	-.4	137.8	134.0	133.2
139.45	140.2	135.9	134.7	-.7	-.5	-.4	139.5	135.4	134.3
118.92	141.9	137.3	135.9	-.7	-.5	-.3	141.2	136.8	135.6
93.65		138.0			-.3			137.7	
91.71	142.6		136.6	-.5		-.1	142.1		136.5
70.00	142.0	137.4	136.0	-.3	-.1	.1	141.7	137.3	136.1
55.85	140.6	136.1	134.9	-.2	-.1	.2	140.4	136.0	135.1

CASE 1 (2xBPF)

FS WL	ISOLATED 274	ISOLATED 301	ISOLATED 328	DELTA 274	DELTA 301	DELTA 328	INSTALLED 274	INSTALLED 301	INSTALLED 328
147.00	135.3	132.7	130.7	.0	-.3	-.2	135.3	132.4	130.5
139.45	131.7	134.0	131.7	.0	-.3	-.2	131.7	133.7	131.5
118.92	138.5	135.5	132.5	.0	-.3	-.1	138.5	135.2	132.4
93.65		136.2			-.2			136.0	
91.71	139.2		132.8	.0		.0	139.2		132.8
70.00	138.6	135.6	132.5	.1	-.2	.1	138.7	135.4	132.6
55.85	137.1	134.3	131.8	.1	-.1	.1	137.2	134.2	131.9

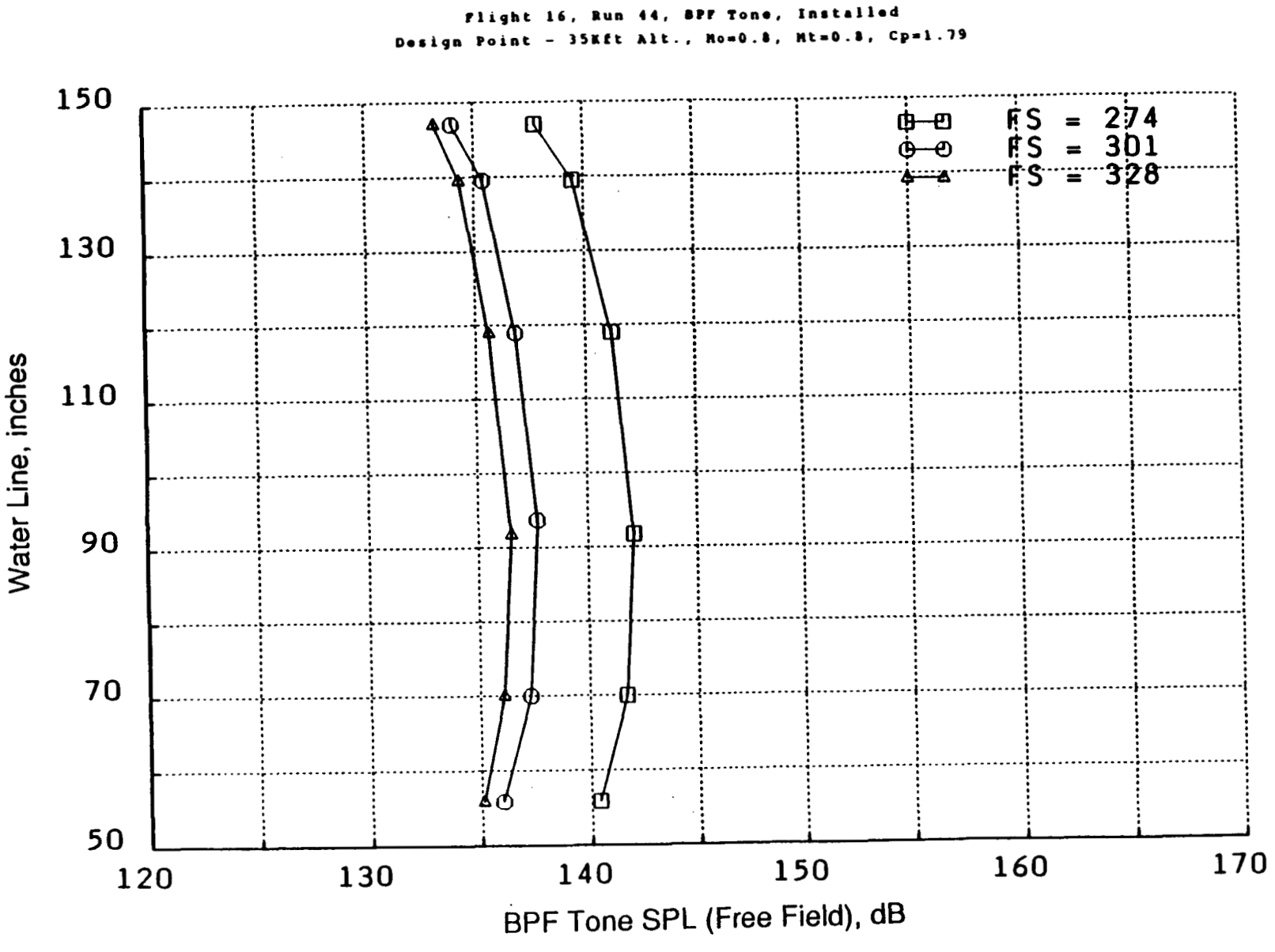

Figure 85. PTA Airplane Fuselage Prediction - With Installation Effect (Prediction Case No. 1).

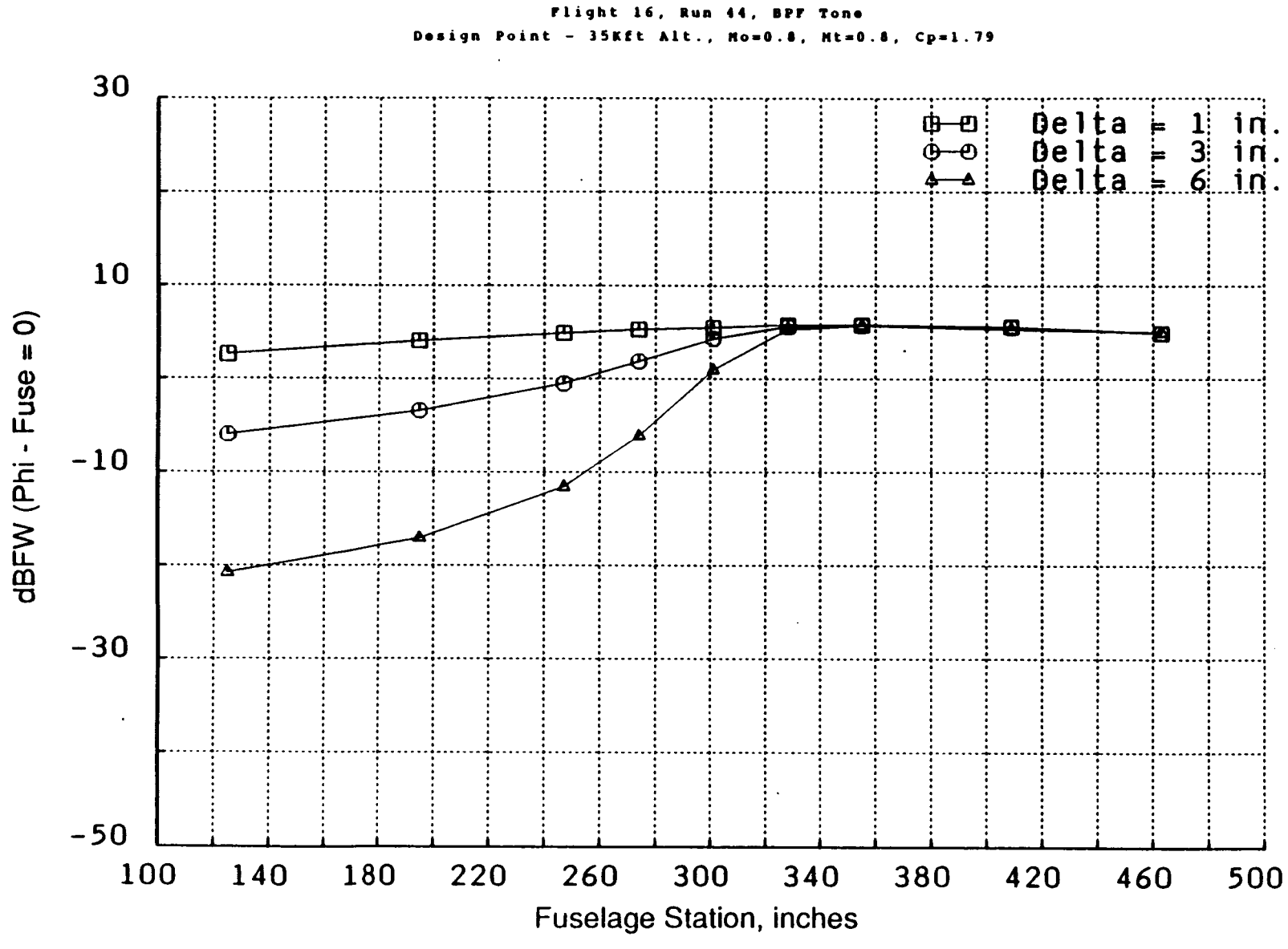

Figure 86. PTA Airplane Fuselage Scattering Prediction (Case No. 1).

downstream of approximately 0.25 propfan diameters aft of the plane of rotation (Fuselage Station 328).

Figure 87 shows the result of combining these effects with the BPF tone of Figure 81. It now appears that the location of the peak level is a function of fuselage boundary layer thickness, with the high level in the forward arc diminishing as the thickness is increased, while the levels aft of the propfan remain constant.

Figures 88 through 90 illustrate the effects predicted on the BPF tone at points around the left side of the fuselage, of the same three values of fuselage boundary layer thickness (1 inch, 3 inch, and 6 inch) as before, at Fuselage Stations 274, 301, and 328, respectively, in terms of dBFW. The "y-coordinate" is "ϕ-fuselage," where zero represents the position on the fuselage of a line connecting the midpoint of the propfan disk to the centerline of the fuselage.

Finally, Figures 91 through 93 represent the results of combining the fuselage scattering effects shown in Figures 88 through 90 with the installation effects of Table 10 and the isolated propfan steady loading and thickness prediction, to give predictions of the BPF tone levels that would be measured at the microphone locations around the fuselage in the plane of rotation of the propfan (Figure 92), and 0.25-diameters forward and aft of that plane (Figures 91 and 93, respectively).

These figures demonstrate the effects of the increase in fuselage boundary layer thickness, both along and around the fuselage surface. For example, in Figure 93 it can be seen that, whereas at the measurement locations at and below the 91.71 water line the predicted tone level is virtually independent of boundary layer thickness, above this point there is a relationship. It will be remembered (Figure 77) that the propfan rotates clockwise when viewed from forward looking aft. The blades are, thus, approaching the fuselage below the 91.71 water line, and retreating above it. Both the installation effects (other than angle-of-attack) and the fuselage scattering results are functions of the direction of rotation.

3.3.2 Case 2: Low Altitude, Full Power, and Tip Speed

3.3.2.1 Uninstalled Predictions

The input parameters used for these predictions are listed in Table 7, and the results predicted for the first three harmonics of BPF under free field conditions along the 91.71 and 93.65 water lines on the fuselage, and at the boom microphone locations, are shown in Figures 94 and 95. Comparison of these figures with Figures 81 and 82, which show equivalent predictions for the design point of the propfan, demonstrates the different character of the predicted tone noise from a propfan at supersonic helical Mach number (Case 1: $M_{HT} = 1.137$), and from the same propfan at a helical tip Mach No. of 0.787. At the lower Mach number, the directivity patterns for the three harmonics are smoother, with the predicted peak level occurring behind, or at, the plane of rotation. The peak predicted level is 10 to 12 dB lower at the lower tip helical Mach number, and the decrease in tone level with increase in harmonic order is more pronounced. The harmonic levels of Figure 81 are probably held up by the thickness

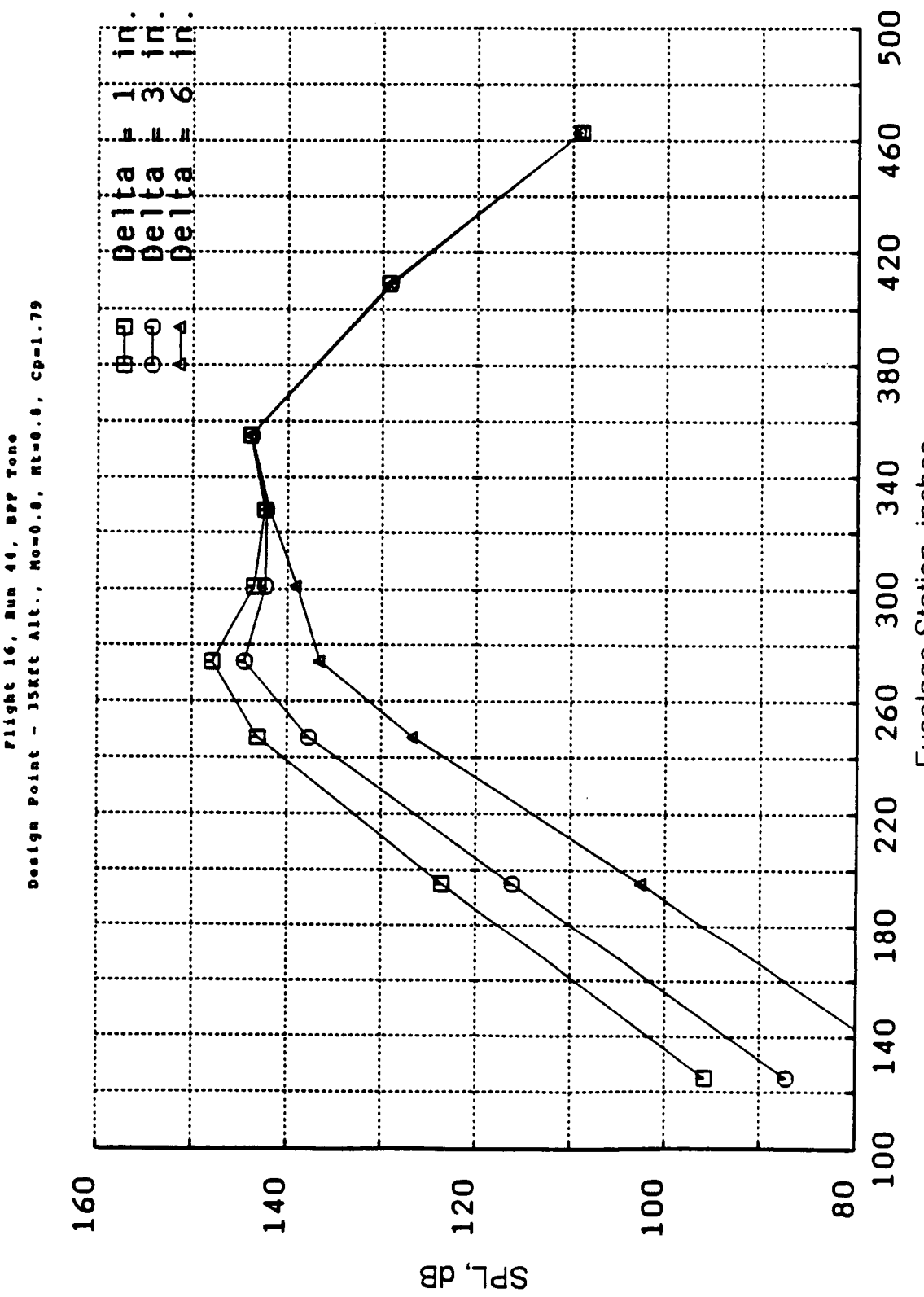

Figure 87. PTA Airplane Fuselage Prediction - With Fuselage Scattering (Prediction Case No. 1).

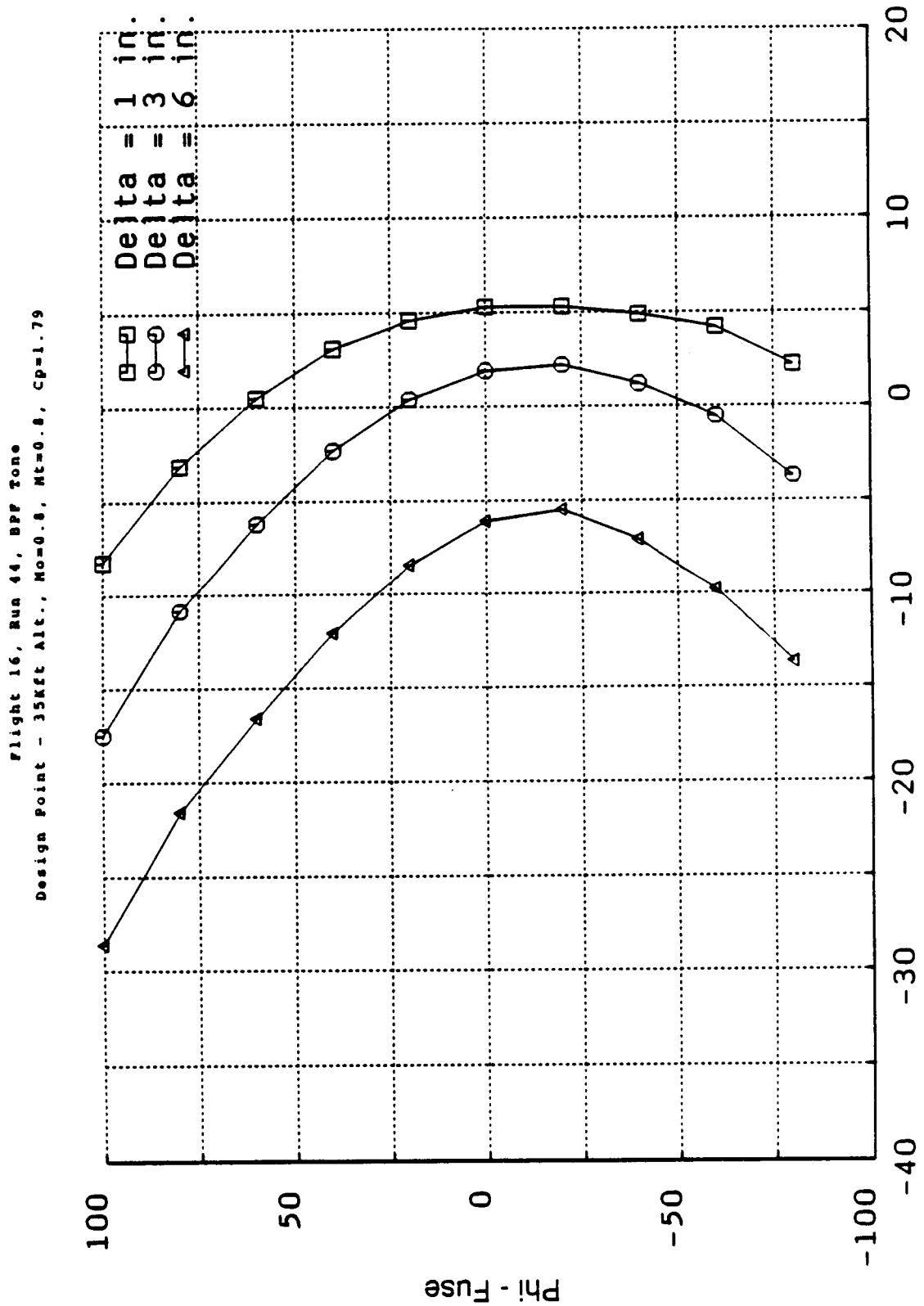

Figure 88. PTA Airplane Fuselage Scattering Prediction (Case No. 1).

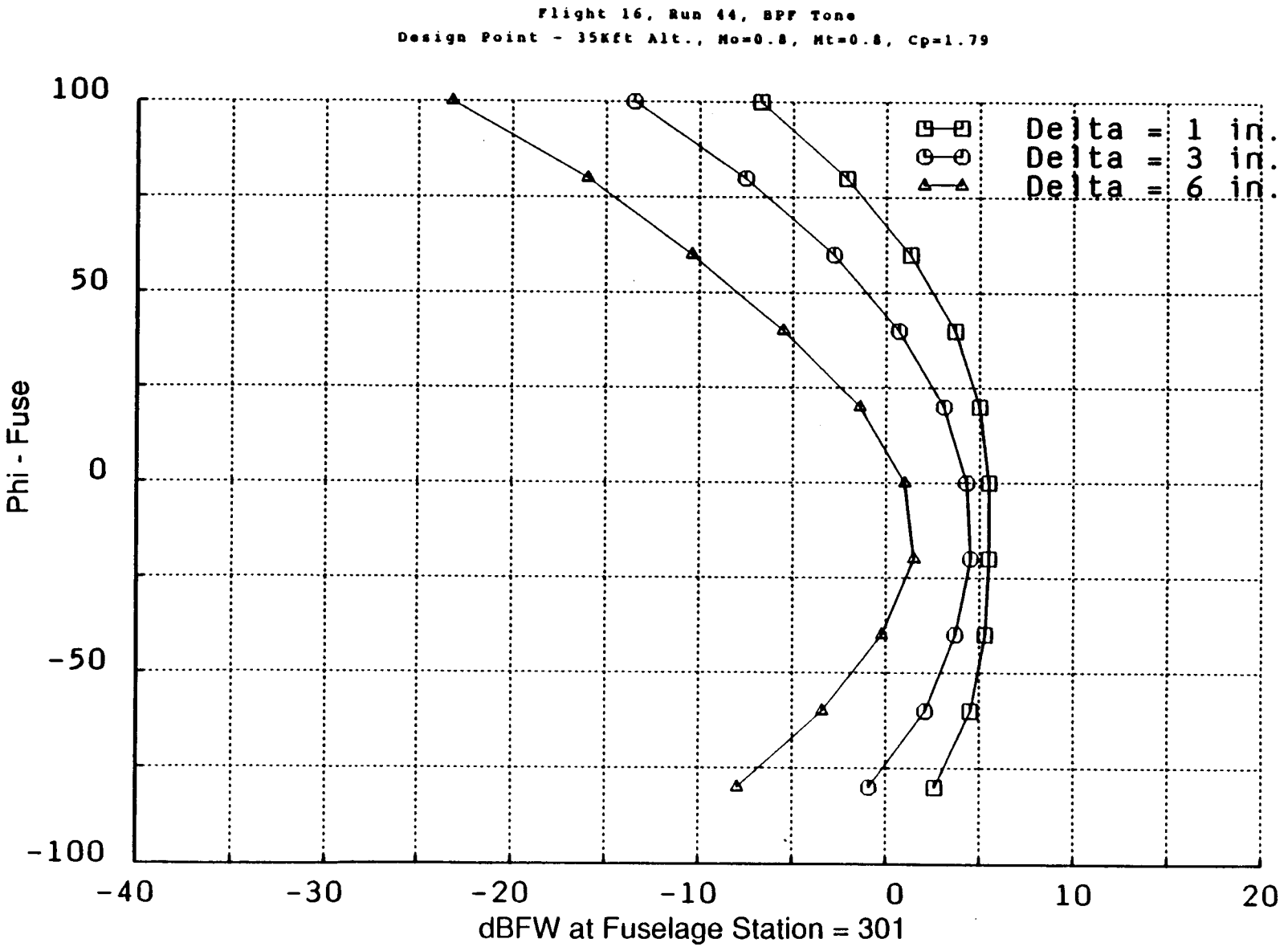

Figure 89. PTA Airplane Fuselage Scattering Prediction (Case No. 1).

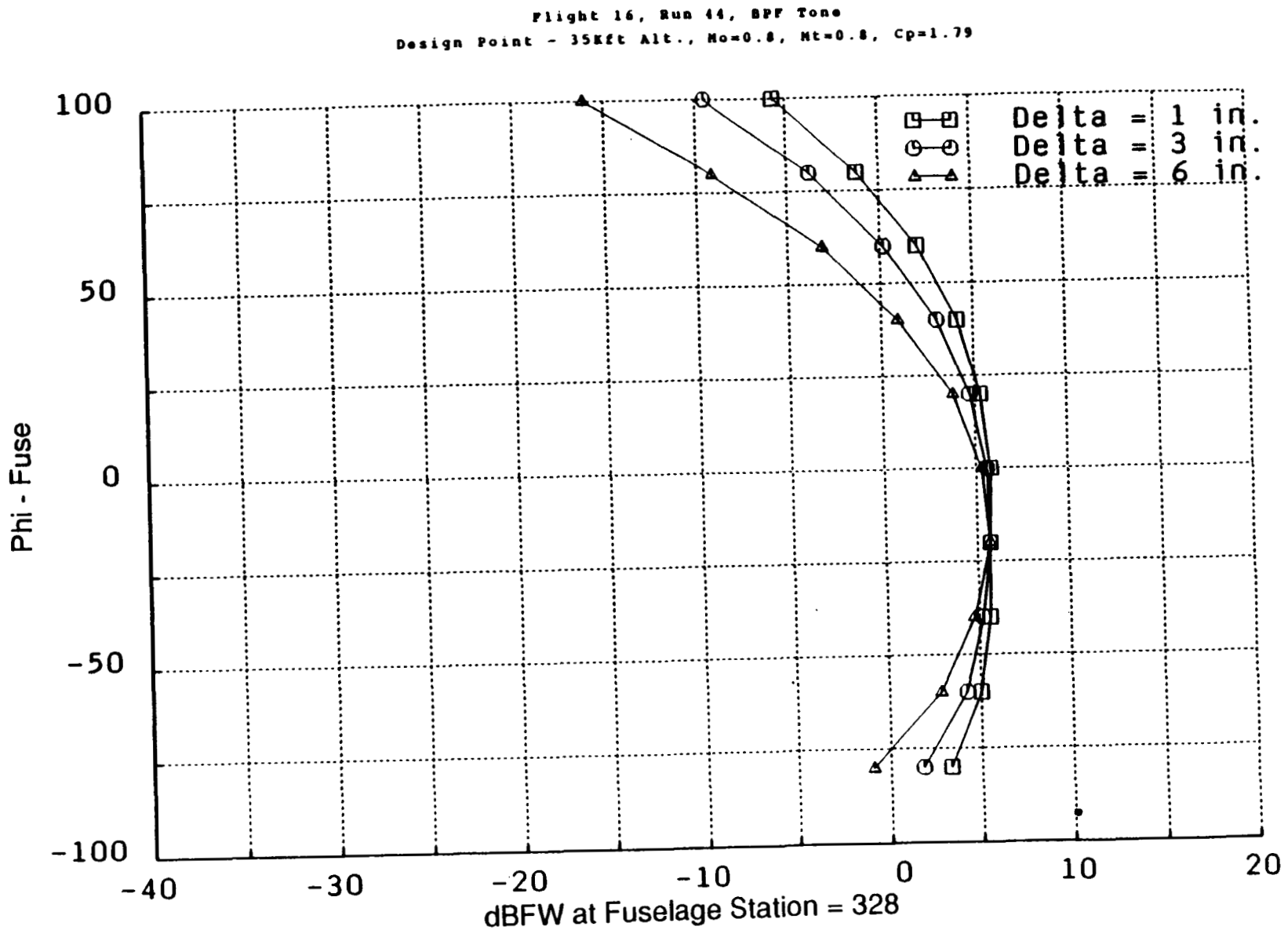

Figure 90. PTA Airplane Fuselage Scattering Prediction (Case No. 1).

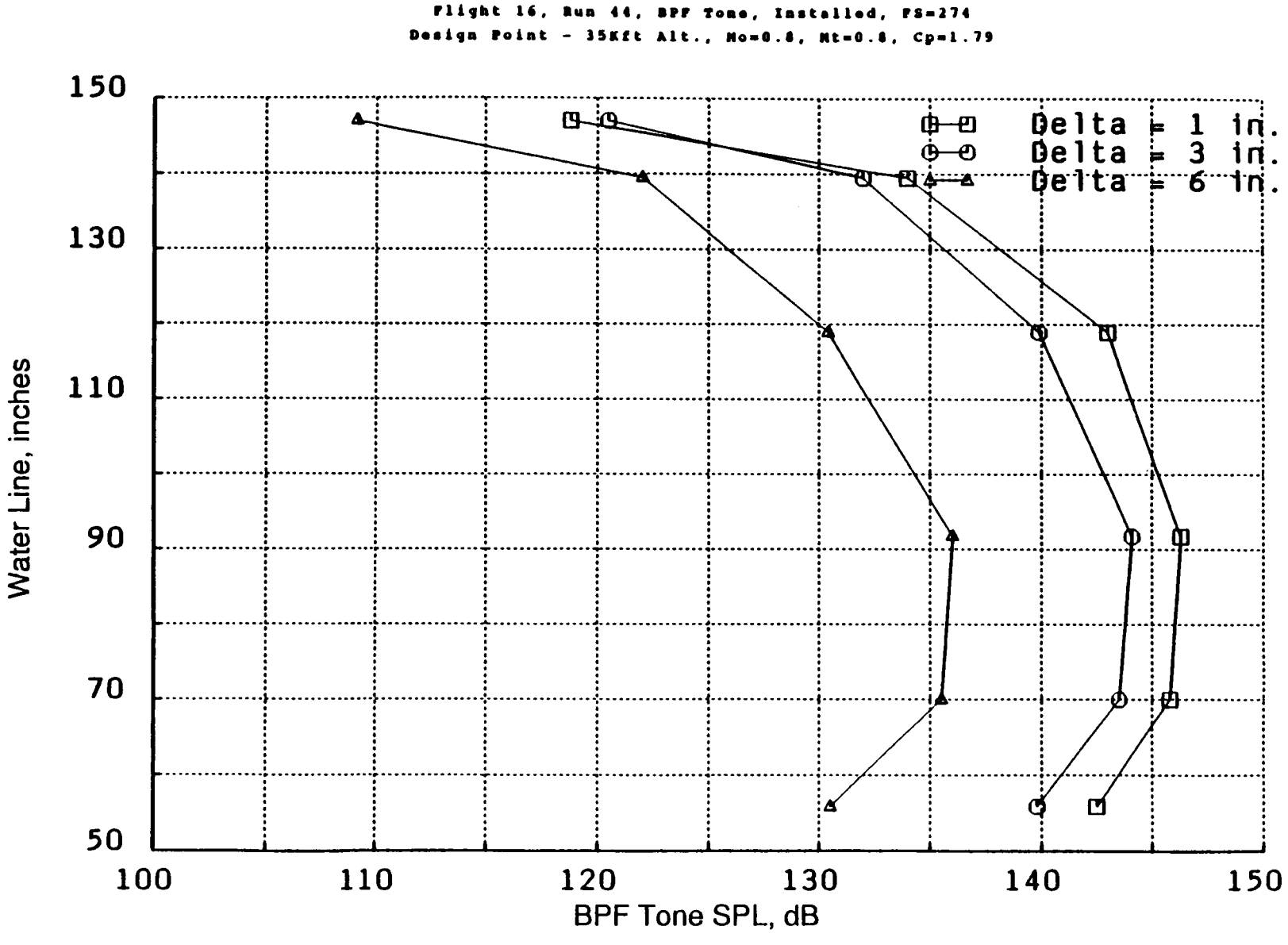

Figure 91. PTA Airplane Fuselage Prediction - with Fuselage Scattering (Prediction Case No. 1, Fuselage Station 274).

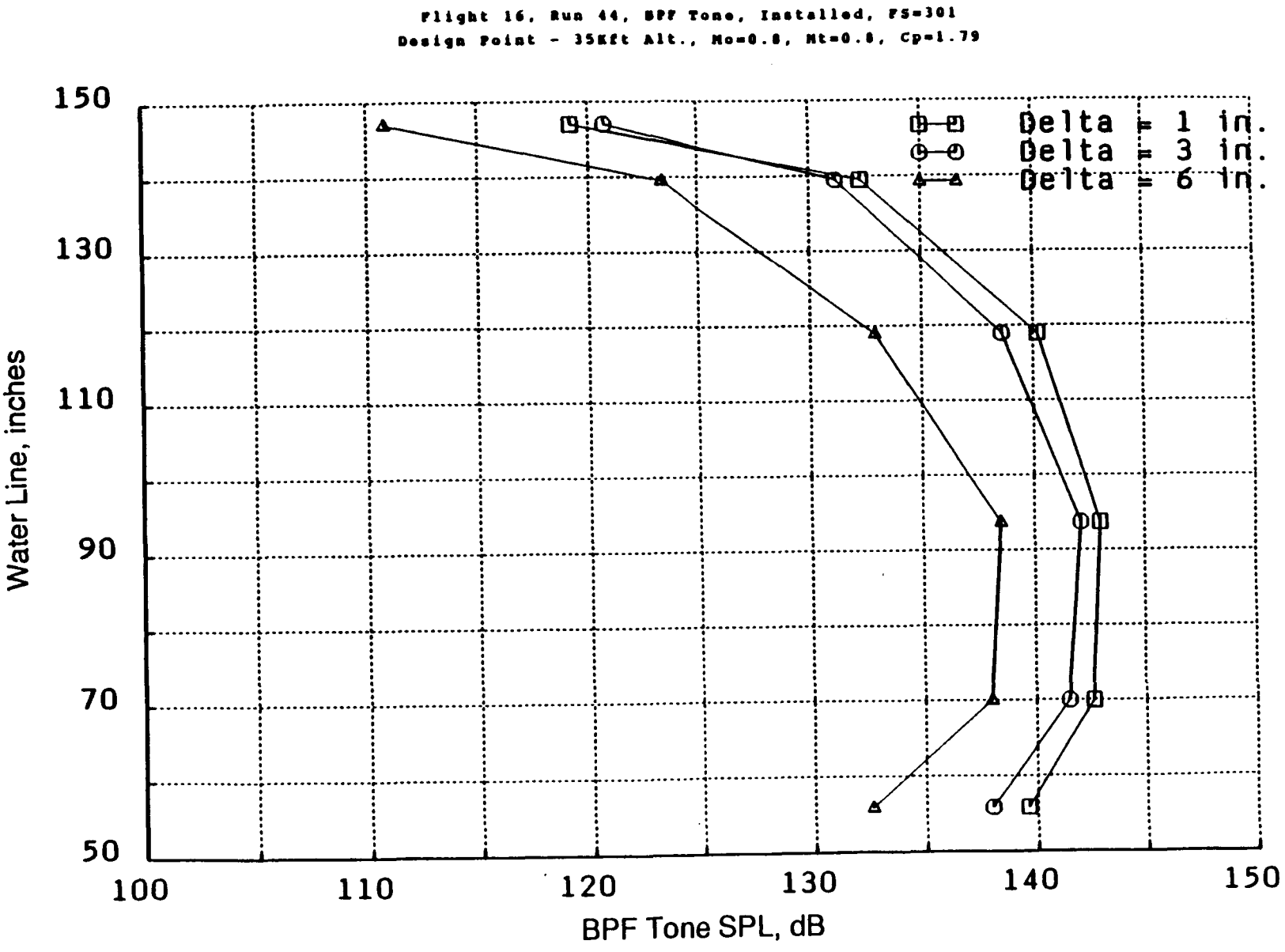

Figure 92. PTA Airplane Fuselage Prediction - With Fuselage Scattering (Prediction Case No. 1, Fuselage Station 301).

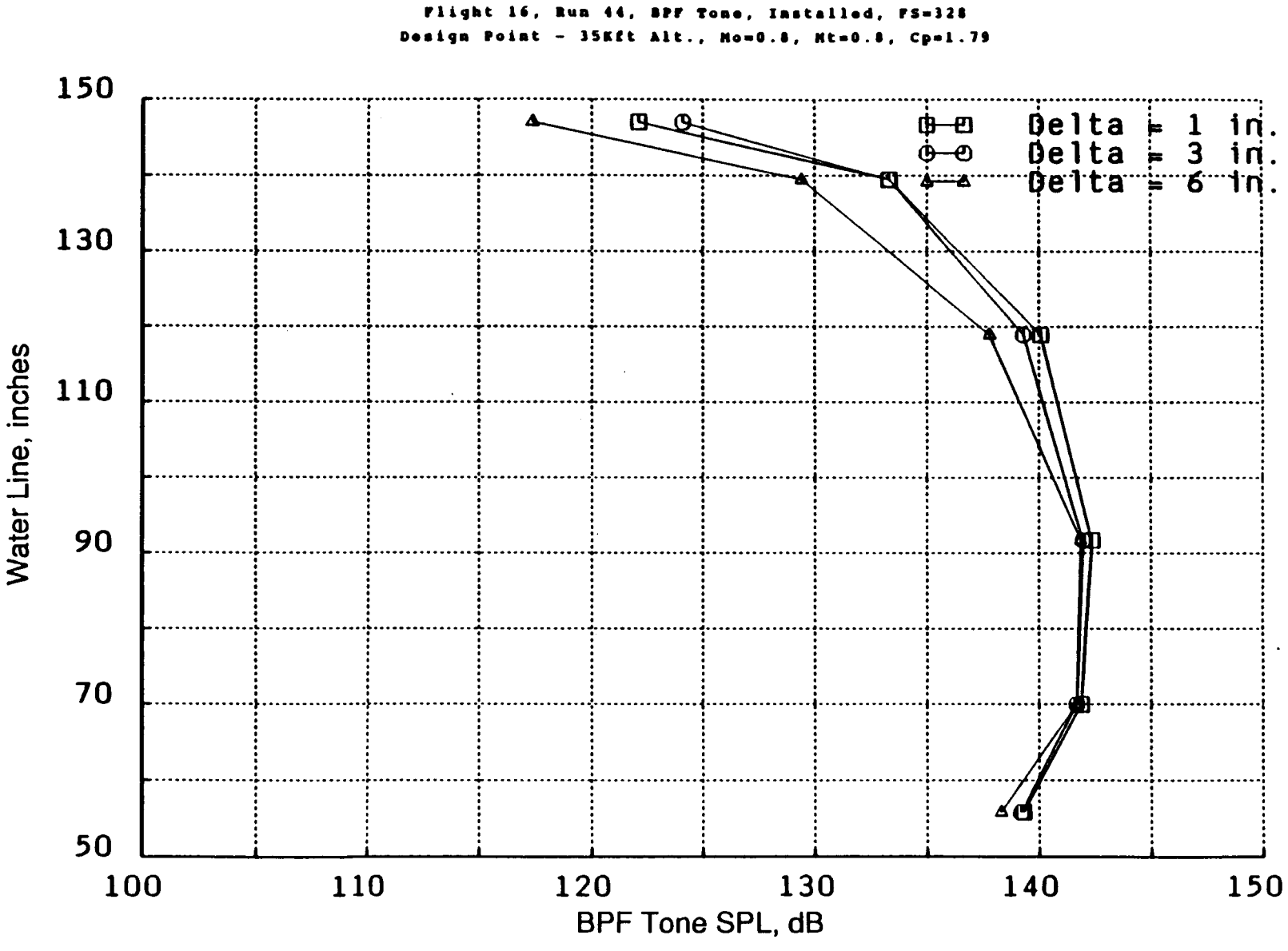

Figure 93. PTA Airplane Fuselage Prediction - With Fuselage Scattering (Prediction Case No. 1, Fuselage Station 328).

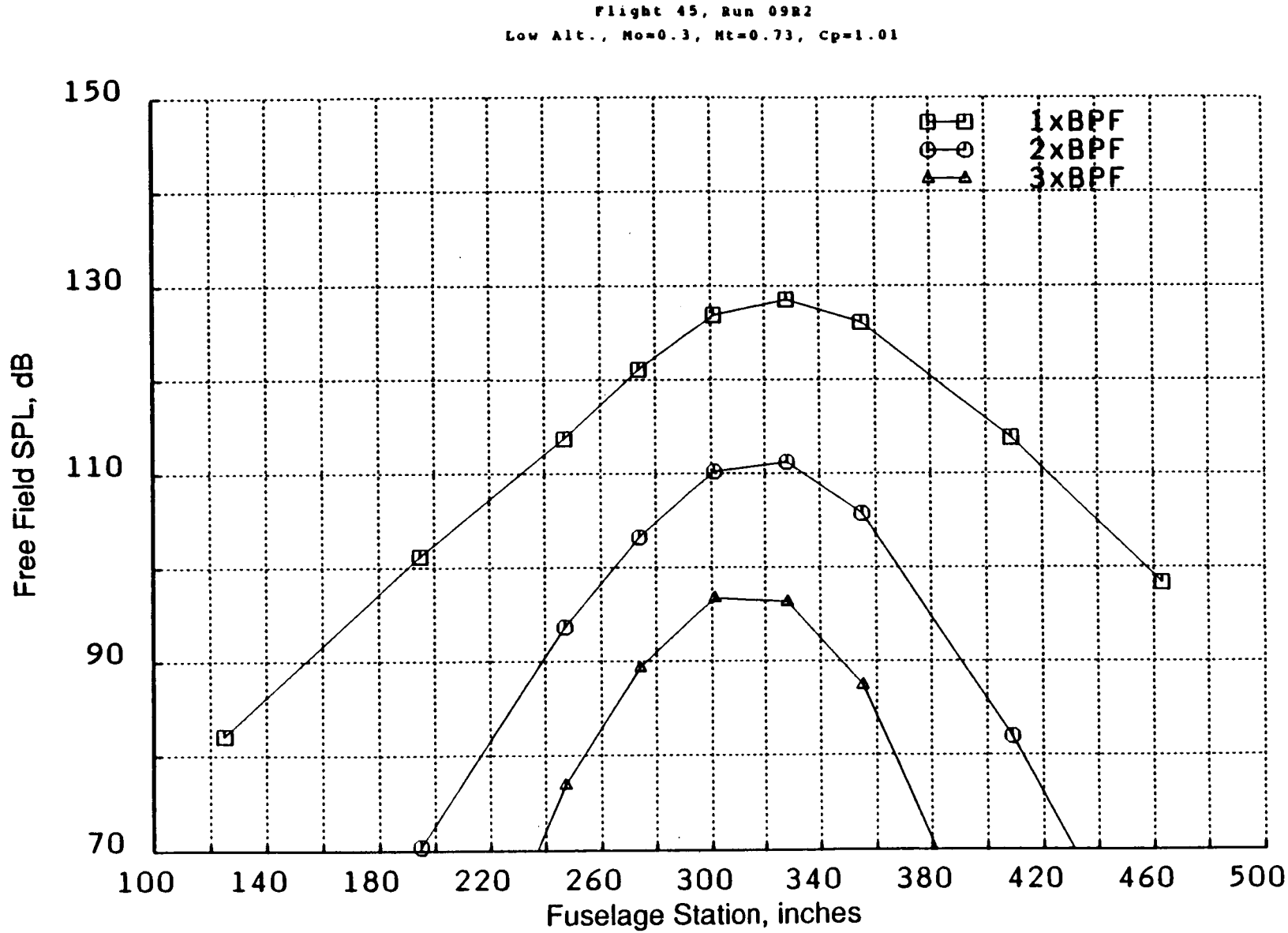

Figure 94. PTA Airplane Fuselage Predictions - Uninstalled (Prediction Case No. 2).

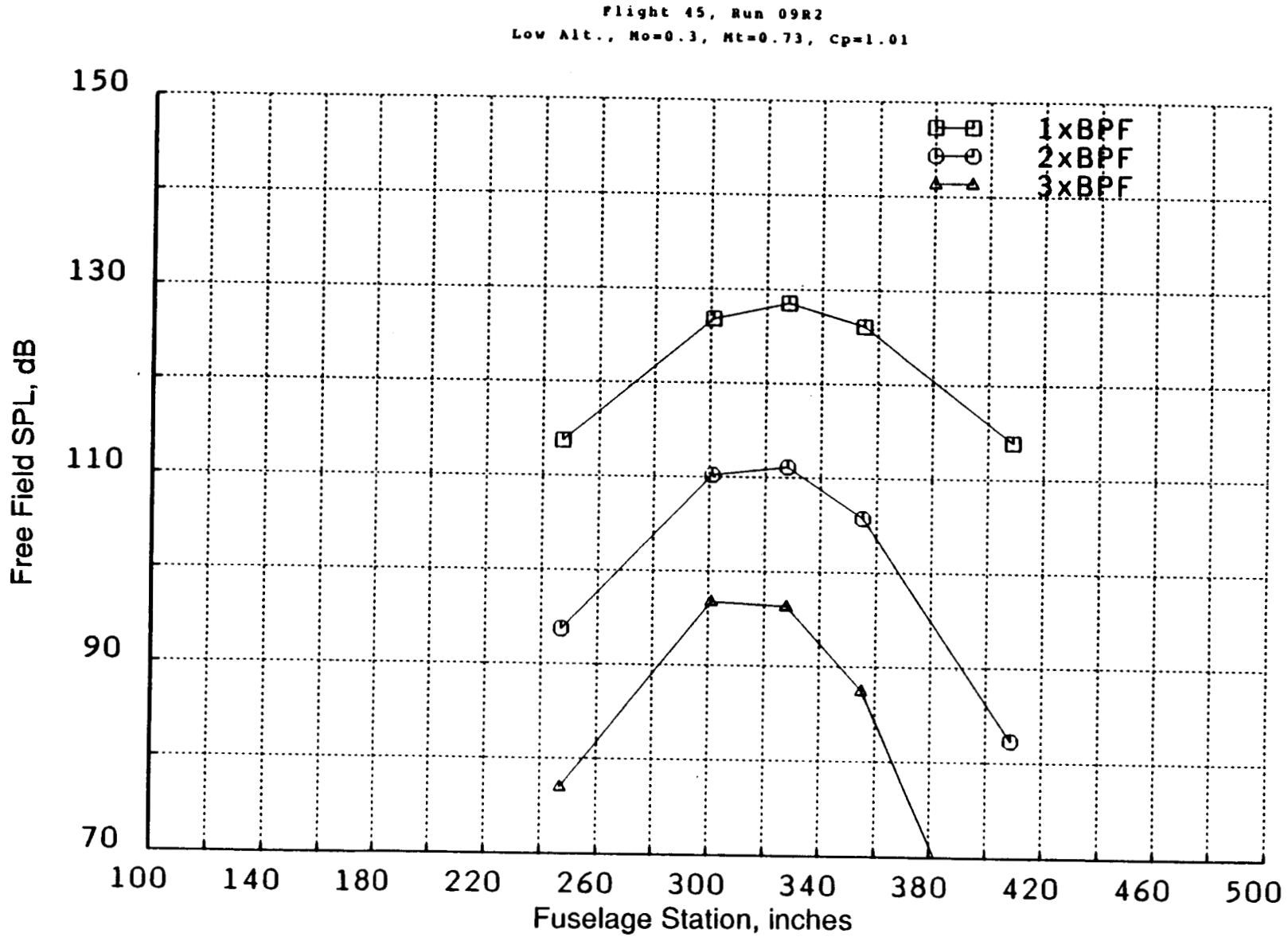

Figure 95. PTA Airplane Fuselage Predictions - Uninstalled (Prediction Case No. 2).

noise prediction which, as seen in Figure 83, is of equal or greater importance at the high helical tip Mach number point. In Figure 94, the decrease in level with increase in harmonic number is consistent with noise due to steady loading as the dominant source. As before, free field predictions at the boom microphone locations (Figure 95) are virtually identical to those illustrated in Figure 94.

As in the previous case, the two options for splitting the lift on the blade sections into their thrust and torque components were investigated. The results are shown in Figure 96. It is interesting to note, in comparing Figure 96 with Figure 84, that the two methods have "switched positions." For this low Mach number, off-design case, the predictions using the helicoidal surface in the acoustic prediction are consistently 1 to 2 dB lower in the peak region than those obtained with the blade pitch angles.

3.3.2.2 Installation Effects

Installation effects for this case were calculated using an angle-of-attack of 3.7°, obtained from Table 7. The wing lift coefficient was calculated from the aircraft gross weight and other relevant parameters from the same table. No low flight Mach number performance data was available for the SR-7 propfan design, so it was assumed that the C_L and C_D versus angle-of-attack characteristics of the blade sections were similar to those of the SR-3 model propfan.

Accordingly, data from the performance maps of Reference 3.3.2 were used as input to program CLDSRP. The results of the calculation are tabulated in Table 11 for the first and second harmonics of BPF, and Figure 97 shows the free field BPF tone levels predicted around the left side of the fuselage with installation effects included in the prediction.

Once again, the predicted installation effects are small, with the predicted decrease toward the top of the fuselage and increase toward the bottom of the fuselage in line with what would be anticipated with a positive angle-of-attack. No fuselage scattering predictions were made for this case.

3.3.3 Case 3: Low Altitude, Reduced Power, and Tip Speed

3.3.3.1 Uninstalled Predictions

Figures 98 through 100 are equivalent to Figures 94 through 96 for the full power and tip speed case described above. Examination of Tables 7 and 8 shows the predicted difference in the free field peak levels of Figures 94 and 98 to be a result that relates more to the difference in tip Mach number than to the difference in power absorbed in the two configurations.

The tip speed effect on steady loading noise from a point force can be written:

$$\Delta(\text{dB}) = 20*\text{Log}_{10}(V2/V1)\,\hat{}\,6$$

$$= 7.9 \text{ dB in this case;}$$

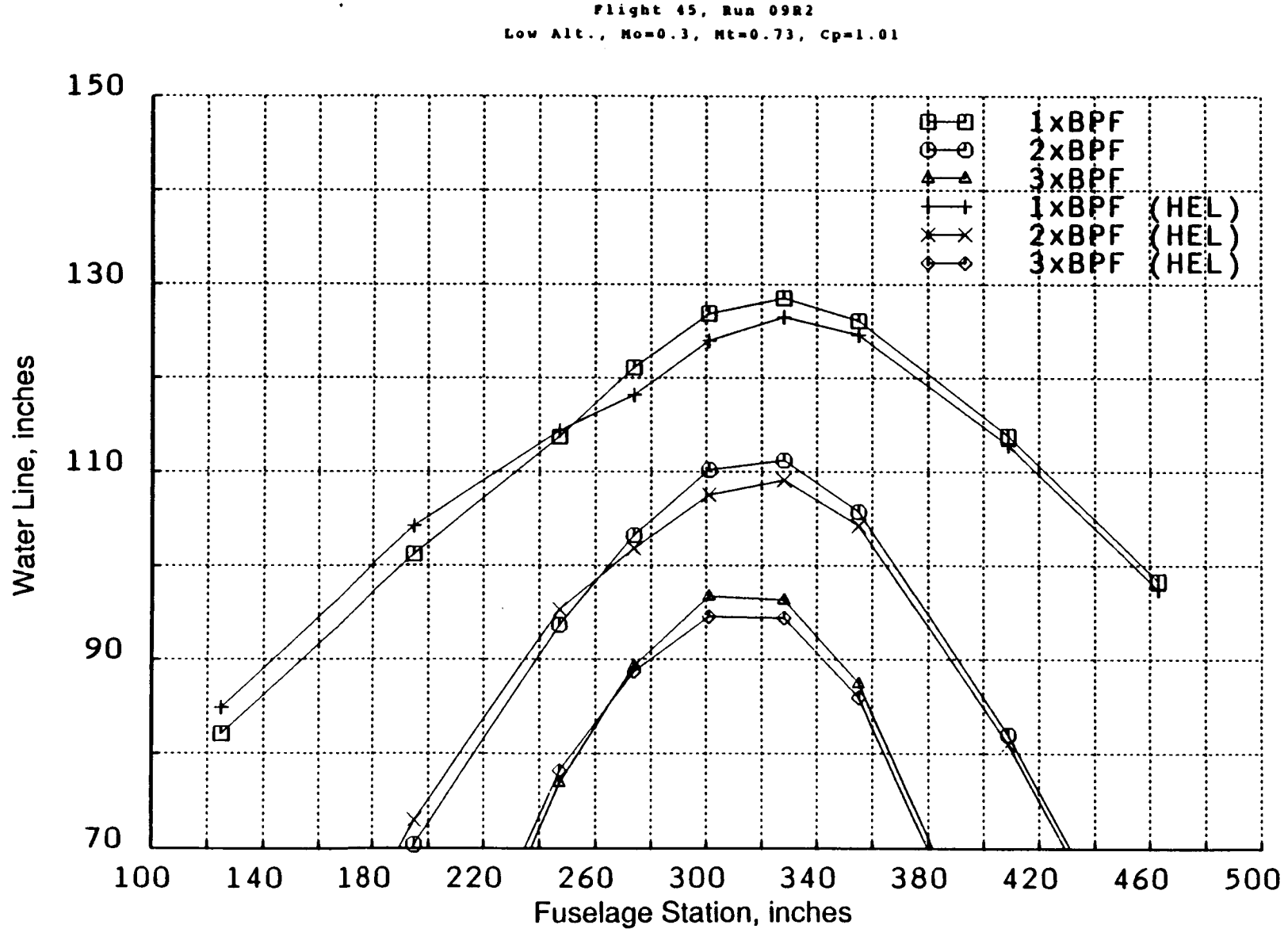

Figure 96. PTA Airplane Fuselage Predictions - Uninstalled (Prediction Case No. 2).

Table 11. Predicted Installation Effects for Case 2 (Free Field).

CASE 2 (BPF)

	ISOLATED			DELTA			INSTALLED		
FS	274	301	328	274	301	328	274	301	328
WL									
147.0	119.9	123.4	124.9	-.2	-.1	-.1	119.7	123.3	124.8
139.5	120.5	124.7	126.3	-.3	-.2	-.2	120.2	124.5	126.1
118.9	121.0	126.2	127.8	-.1	.0	.0	120.9	126.2	127.8
93.7		126.9			.5			127.4	
91.7	121.1		128.5	.2		.6	121.3		129.1
70.0	121.0	126.3	127.9	.6	.9	1.0	121.6	127.2	128.9
55.9	120.6	125.0	126.6	.8	1.1	1.2	121.4	126.1	127.8

CASE 2 (2xBPF)

	ISOLATED			DELTA			INSTALLED		
FS	274	301	328	274	301	328	274	301	328
WL									
147.0	102.6	106.7	108.1	.1	.2	.2	102.7	106.9	108.3
139.5	103.0	108.1	109.4	.0	.2	.1	103.0	108.3	109.5
118.9	103.2	109.5	110.6	.0	.3	.3	103.2	109.8	110.9
93.7		110.2			.6			110.8	
91.7	103.2		111.2	.1		.7	103.3		111.9
70.0	103.2	109.7	110.7	.4	.9	1.0	103.6	110.6	111.7
55.9	103.1	108.4	109.6	.6	1.0	1.2	103.7	109.4	110.8

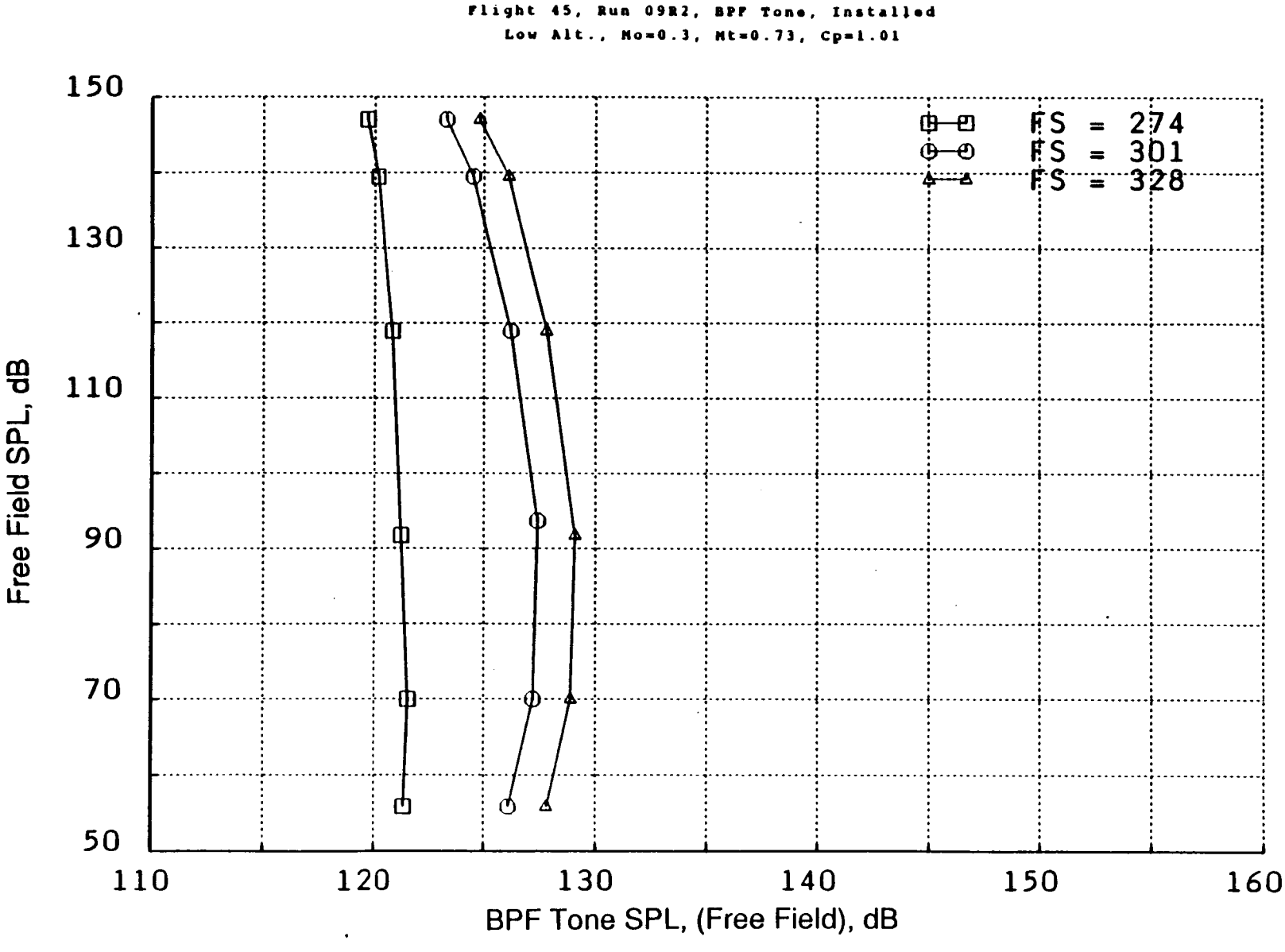

Figure 97. PTA Airplane Fuselage Prediction - With Installation Effects (Prediction Case No. 2).

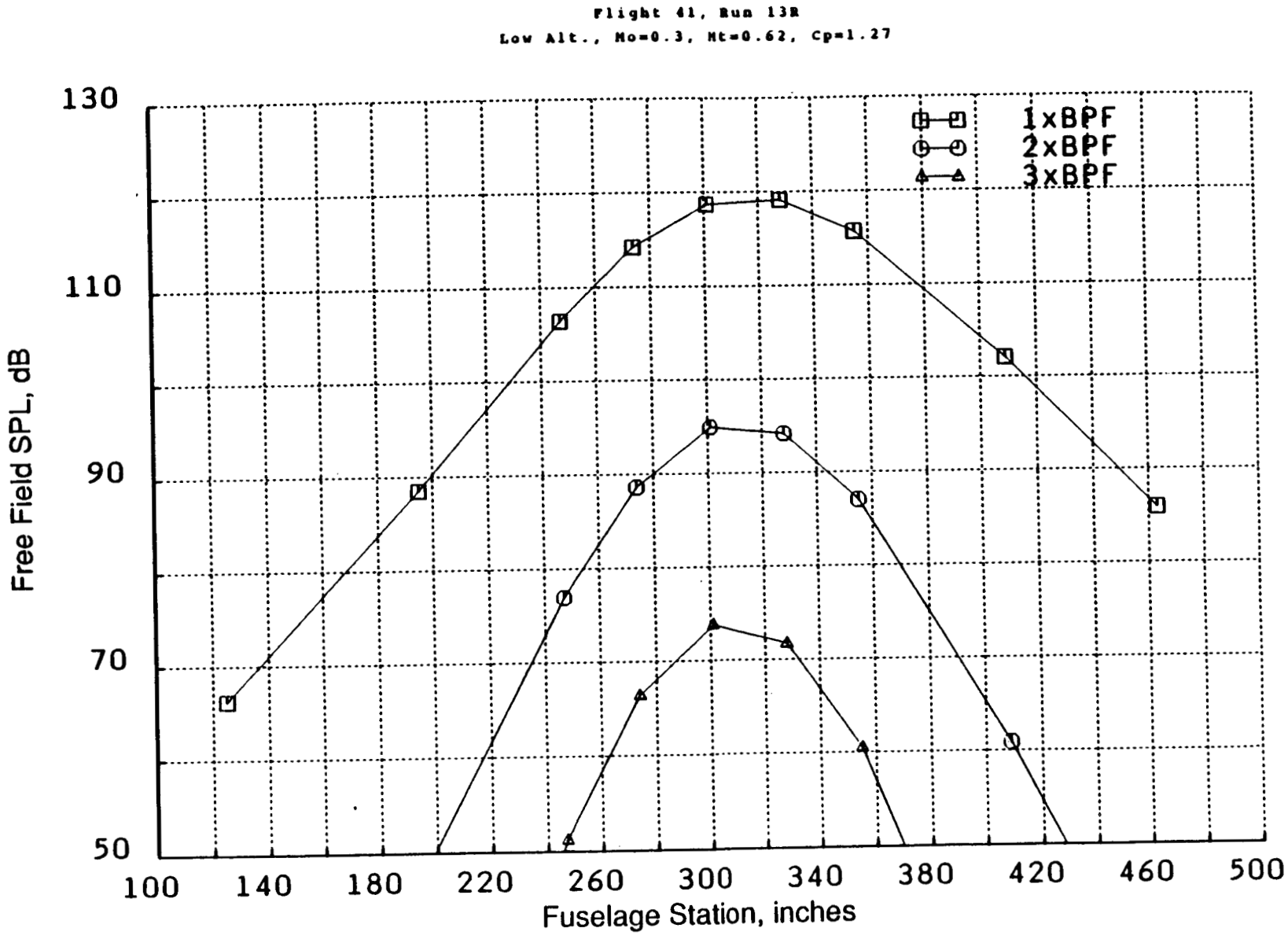

Figure 98. PTA Airplane Fuselage Predictions - Uninstalled (Prediction Case No. 3).

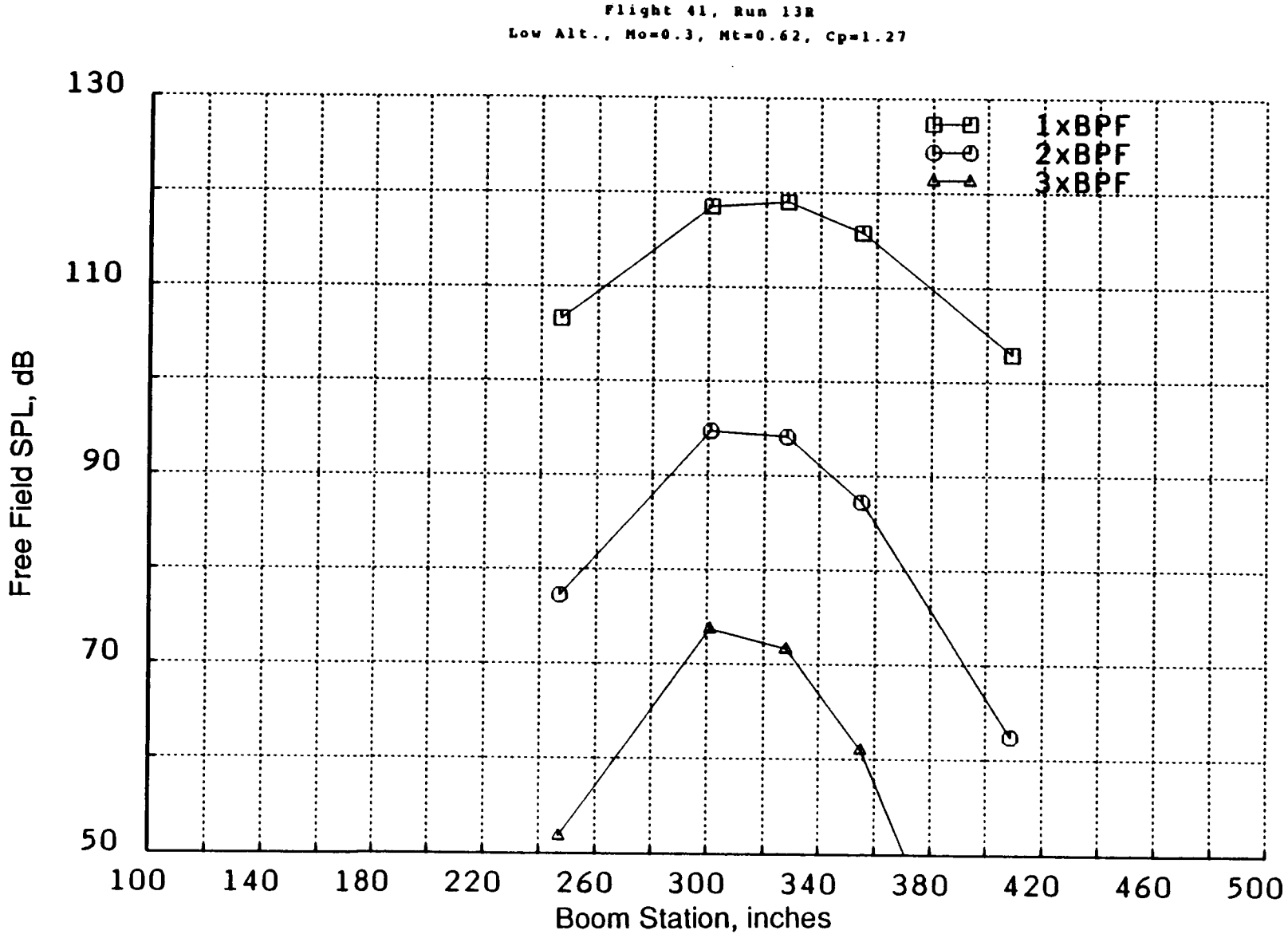

Figure 99. PTA Airplane Boom Predictions - Uninstalled (Prediction Case No. 3).

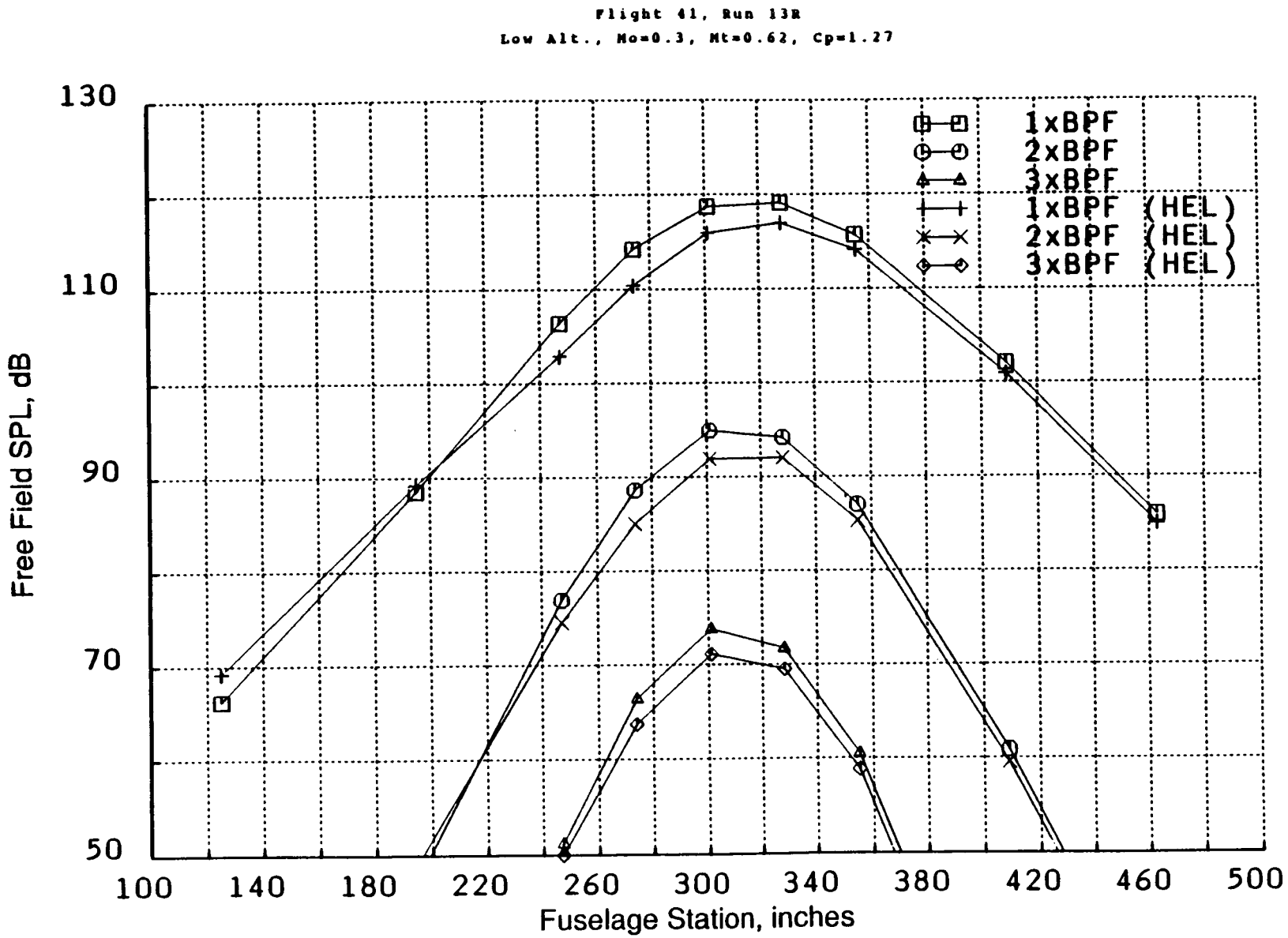

Figure 100. PTA Airplane Fuselage Predictions - Uninstalled (Prediction Case No. 3).

while, for the difference in power:

$$\Delta(dB) = 20*Log_{10}(shp2/shp1)$$

$$= 1.9\ dB.$$

The total of 9.8 dB is very close to the 9.4 dB predicted by the distributed source model, implying that, under these low speed conditions, the added complexity of the full model is not necessarily needed.

Once again, the boom results of Figure 99 are very similar to those calculated at the microphone locations on the fuselage (Figure 98). For this case, the nacelle tilt was +2°, leading to a slightly greater difference in sideline distance between the boom and the fuselage than was seen in the previous two cases (Table 5).

The differences between results calculated using the helicoidal surface angles to divide the lift into its components for the acoustic calculation and those obtained with the blade pitch angles are portrayed in Figure 100. As in Figure 96, the helicoidal surface results are approximately 2 dB lower than those obtained with the blade pitch angles.

3.3.3.2 Installation Effects

The nacelle tilt of +2° for this case resulted in an angle-of-attack of 5.94° (Table 8). The other installation inputs were calculated as before, from parameters also in Table 8.

The free field predicted results are shown in Table 12 and Figure 101. Although slightly larger than those predicted for Case 2, the predicted effects are again small, with the increase toward the bottom of the fuselage and the decrease toward the top in accordance with the expected angle-of-attack effect. Overall, the predicted free field levels around the fuselage (Figure 101) are lower than those shown for Case 2 (Figure 97) and exhibit less variation with fuselage station. Again, no fuselage scattering effects were calculated for this case.

3.4 Conclusions

The acoustic models developed under this contract as described in Section 2.0 of this report for the prediction of high speed turboprop noise resulting from steady loading and thickness sources on the blading together with installation effects arising from: angle-of-attack operation, the presence of a cylindrical fuselage, and the presence of a wing lifting line, have been exercised to predict the free field noise at various microphone locations on the aircraft for three flights of the Propfan Test Assessment airplane. In addition, for one flight representing the design point of the propfan, the fuselage scattering code which was also developed under this contract and described in Section 2.0 of this report was utilized to predict the levels that would be measured by microphones on the fuselage of the airplane, given any of three possible fuselage boundary layer thicknesses.

Table 12. Predicted Installation Effects for Case 3 (Free Field).

CASE 3 (BPF)

	ISOLATED			DELTA			INSTALLED		
FS	274	301	328	274	301	328	274	301	328
WL									
147.0	112.6	115.2	116.0	-.3	-.3	-.2	112.3	114.9	115.8
139.5	113.3	116.6	117.3	-.4	-.4	-.3	112.9	116.2	117.0
118.9	114.0	118.1	118.6	.0	.0	.1	114.0	118.1	118.7
93.7		118.7			.8			119.5	
91.7	114.2		119.1	.8		.9	115.0		120.0
70.0	114.0	118.0	118.6	1.4	1.4	1.5	115.4	119.4	120.1
55.9	113.4	116.7	117.4	1.6	1.7	1.8	115.0	118.4	119.2

CASE 3 (2xBPF)

	ISOLATED			DELTA			INSTALLED		
FS	274	301	328	274	301	328	274	301	328
WL									
147.0	87.8	91.3	91.7	.2	.1	.1	88.0	91.4	91.8
139.5	88.4	92.8	92.8	.2	.0	.0	88.6	92.8	92.8
118.9	88.6	94.2	93.8	.5	.3	.3	89.1	94.5	94.1
93.7		94.9			.9			95.8	
91.7	88.6		94.2	1.0		1.0	89.6		95.2
70.0	88.6	94.2	93.8	1.4	1.5	1.5	90.0	95.7	95.3
55.9	88.4	92.9	92.9	1.6	1.7	1.7	90.0	94.6	94.6

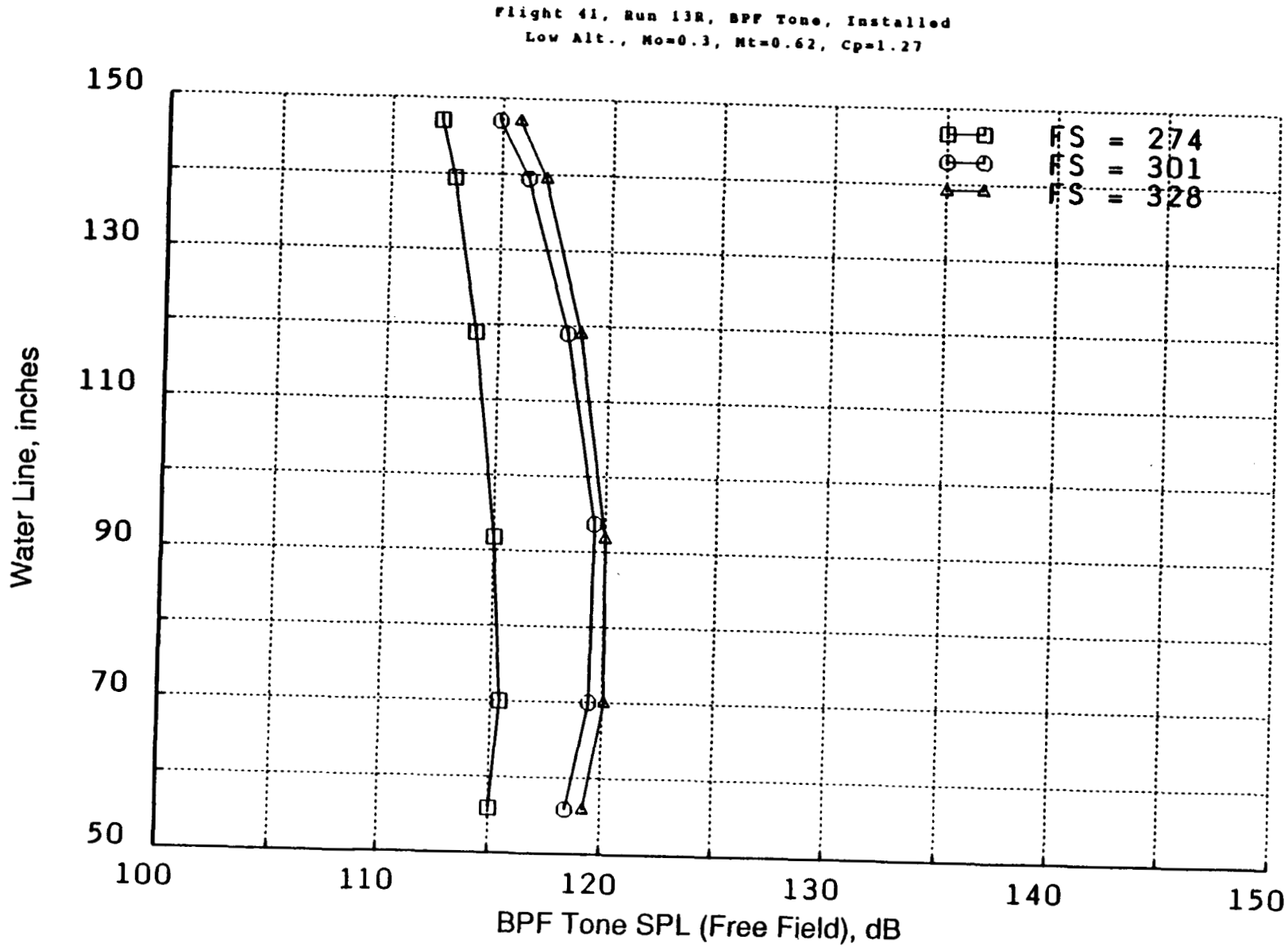

Figure 101. PTA Airplane Fuselage Prediction - With Installation Effect (Prediction Case No. 3).

The results show that at high helical tip Mach number (Case 1), the noise predicted due to the thickness (or volume) of the blades is comparable to, or even greater than, that predicted to result from the steady loading component alone. The slow dropping off of the peak levels with increase in harmonic number for this case has been ascribed to the thickness source.

The inclusion of fuselage scattering effects demonstrates that the location of the peak level on the fuselage at cruise can be a function of the thickness of the boundary layer on the fuselage. Under free field conditions, the maximum level is predicted to occur forward of the propfan plane. It has been shown that the presence of the boundary layer leads to a predicted reduction in the tone levels on the fuselage upstream of the propfan, while giving almost pure reflection in the aft region.

Installation effects at cruise are predicted to be less than 1 dB over the region in the vicinity of the propfan plane.

In the low flight Mach number regime (Cases 2 and 3) the predicted noise levels are dominated by steady loading effects. The predicted differences between Cases 2 and 3 ("full power and tip speed" versus "reduced power and tip speed") are shown to result more from the tip speed effect than from the reduction in power absorbed.

The predicted effects of the installation indicates levels increasing toward the bottom of the fuselage and decreasing toward the top in both cases (which is consistent with the angles-of-attack input), although the levels of the predicted effect are low everywhere.

An examination of the consequences of the use of the blade pitch angles rather than the helicoidal surface angles in dividing the blade section lift into its thrust and torque components for the acoustic calculation shows the difference between the two sets of results to be of the order of 1 to 2 dB. One interesting point noticed is that: whereas at cruise, results generated using the helicoidal surface are higher, in the low flight Mach number regime, the opposite is true. It is not known if this is a universal result, or a function of the particular geometry under consideration here.

4.0 OVERALL CONCLUSIONS

Acoustic models have been formulated and programmed under this contract to predict the tone noise generated by a high speed turboprop as a result of: the steady loading on the blades; the thickness (volume) of the blades; and the unsteady blade loads resulting from the installation environment. A model to predict modifications to the sound field emitted from the turboprop resulting from the curvature of an airplane fuselage and its attached boundary layer also has been formulated and programmed.

The steady loading and thickness model matches a frequency-domain, noncompact source, linear acoustic model with the solutions from a nonlinear, aerodynamic flow field analysis program that are used to obtain the blade loading distributions required as input by the acoustic code. The model was developed originally for the acoustic far field, and a semiempirical adjustment has been included to account for near field effects. An alternate method for predicting near field noise directly from the numerical flow field solution was tried and discarded as impractical at this time.

Results from the steady loading and thickness model have been compared with data from three model propfans (SR-2, SR-3, and SR-6) operating at high flight speed, both in a wind tunnel environment and in flight (mounted on the Jetstar aircraft). In general, the predictions show good agreement with the Jetstar boom data and moderate agreement with the data measured on the airplane fuselage and in the wind tunnel.

The installation effects model developed under this contract employs a quasi-steady formulation to predict the thrust and tangential forces on the blades resulting from the non-uniform flow environment in which the propfan operates when installed on an aircraft. The specific installation effects considered here are: angle-of-attack operation, the presence of a fuselage, and the presence of a wing lifting line. Calculation of the flow fields resulting from these effects has been included in this work.

The acoustic model is less sophisticated than that employed for the steady loading and thickness calculation, being compact in the chordwise direction, so the results obtained are presented as a delta, which can be applied to the outcome of a steady loading and thickness calculation.

Comparisons with SR-2 model data taken at a low wind tunnel Mach number show encouraging agreement.

The final model developed under this contract concerns the scattering of the sound field emitted by the propfan as a result of the presence of an airplane fuselage with its associated boundary layer. In the analysis, the emitted sound field is expressed in terms of multiple cylindrical waves converging onto the cylindrical fuselage. These waves are then scattered from the surface of the cylinder, or if a boundary layer is present, the effects of refraction through this layer are included. The results obtained with this model are in agreement with observed trends.

The three models developed under this contract have been exercised for three flights of the Propfan Test Assessment airplane. In this project, a 9-foot-diameter SR-7L propfan was mounted on the left wing of a modified Gulfstream II business jet. Microphones were installed along and around the fuselage, as well as on a wing-mounted boom. The predictions were made for flights whose operating conditions corresponded to the design point (high altitude cruise); a low altitude, high power and tip speed point; and a low altitude, reduced power and tip speed point. Data comparisons were not performed, but free field levels were predicted at various microphone locations for all three cases.

Results indicated the thickness component to be a strong contributor at cruise, with the location of the maximum level on the fuselage a function of the thickness of the fuselage boundary layer. In the low altitude, low flight Mach number regime, steady loading sources were the major contributors, with tip speed effects dominant. Installation effects were predicted to be fairly small in all three cases, with angle-of-attack effects appearing to dominate.

In conclusion therefore, three major computer programs have been delivered under this contract. They predict the noise generated by a high speed propfan as a result of its steady loading and thickness and its installation environment, together with corrections that should be applied to measurements taken on the surface of a fuselage.

These programs have been compared with data from a variety of sources, and on the whole, demonstrate reasonable agreement. In addition, two smaller programs have been delivered; one to convert the results of an aerodynamic flow solution to the input format required by the steady loading and thickness prediction code; the other to generate blade section C_L and C_D versus angle-of-attack data for input to the installation effects code. Possibilities for further work include the development of a rigorous near field model, and the effect (in the far field), of the presence of a fuselage in the near field.

REFERENCES

2.1.1 Ffowcs Williams, J.E. and Hawkings, D.L., "Sound Generation by Turbulence and Surfaces in Arbitrary Motion," Phil. Trans. Roy. Soc. (London), Ser. A, Vol. 264, May 8, 1969, pp 321-342.

2.1.2 Hawkings, D.L. and Lowson, M.V., "Theory of Open Supersonic Rotor Noise," J. Sound Vib., Vol. 36, No. 1, September 8, 1974, pp 1-20.

2.1.3 Ffowcs Williams, J.E. and Hawkings, D.L., "Theory Relating to the Noise of Rotating Machinery," J. Sound Vib., Vol. 10, No. 1, 1969, pp 10-21.

2.1.4 Whitfield, C.E. and Hawkings, D.L., "An Investigation of Rotor Noise Generation by Aerodynamic Disturbance," Inst. Mech. Engineers, Conference on Vibration and Noise in Pump, Fan and Compressor Installations, 1975.

2.1.5 Hawkings, D.L. and Lowson, M.V., "Noise of High Speed Rotors," AIAA Paper No. 75-450, March 1975.

2.1.6 Hubbard, H.H. and Lassiter, L.W., "Sound from a Two-Bladed Propeller at Supersonic Tip Speeds," NACA Report No. 1079, 1951.

2.1.7 Kurbjun, M.C., "Noise Survey of a Full-Scale Supersonic Turbine-Driven Propeller Under Static Conditions," NACA TN 4059, 1957.

2.1.8 Whitham, G.B., "On the Propagation of Weak Shock Waves," Journal of Fluid Mechanics, Vol. 1, 1956, pp 290-318.

2.1.9 Lighthill, M.J., "On Sound Generated Aerodynamically. I. General Theory," Proc. Roy. Soc. (London), Ser. A, Vol. 211, 1952, pp 564-587.

2.1.10 Goldstein, M.E., Aeroacoustics, McGraw-Hill, New York, 1976.

2.1.11 Hanson, D.B., "Helicoidal Surface Theory for Harmonic Noise of Propellers in the Far Field," AIAA Journal, Vol. 18, No. 10, October 1980, pp 1213-1220.

2.1.12 Denton, J.D., "A Time-Marching Method for Two- and Three-Dimensional Blade to Blade Flows," A.R.C. R. and M. 3775, 1975.

2.1.13 Ni, R.H., "A Multiple-Grid Scheme for Solving the Euler Equations," AIAA Journal, Vol. 20, No. 11, 1982, pp 1565-1571.

2.1.14 Jameson, A., Schmidt, W., and Turkel, E., "Numerical Solutions of the Euler Equations by Finite Volume Methods using Runge-Kutta Time-Stepping Schemes," AIAA Paper 81-1259, 1981.

2.1.15 Holmes, D.G. and Tong, S.S., "A Three-Dimensional Euler Solver for Turbomachinery Blade Rows," ASME Paper 84-GT-79, 1984.

2.1.16 Chaussee, D.S., "Computation of Three-Dimensional Flow Through Prop Fans," Nielson Engineering and Research Report NEAR-TR-199, Final Report for Contract No. NAS2-10025, June 1979.

2.1.17 Chaussee, D.S., and Kutler, P., "User's Manual for Three-Dimensional Analysis of Propellers Flow Fields", Flow Simulations Inc. Report FSI-80-04, December 1980. Prepared under NASA Contract NAS3-22375.

2.1.18 Sulc, J., Hofr, J., and Benda, L., "Exterior Noise on the Fuselage of Light Propeller Driven Aircraft in Flight," J. Sound Vib., Vol. 84, No. 1, 198, pp 105-120.

2.1.19 Rohrbach, E., Metzger, F.B., Black, D.M., and Ladden, R.M., "Evaluation of Wind Tunnel Performance Testings of an Advanced 45° Swept Eight-Bladed Propeller at Mach Numbers from 0.45 to 0.85," NASA CR-3505, March 1982.

2.1.20 Dittmar, J.H., Stefko, G.L., and Jeracki, R.J., "Noise of the 10-Bladed, 40° Swept SR-6 Propeller in a Wind Tunnel," NASA TM 82950, 1982.

2.1.21 "Jetstar Propeller Flight Test Program Acoustic Data Report," NASA Contract NAS4-2822, May 1983.

2.1.22 Brooks, B.M. and Mackall, K.G., "Measurement and Analysis of Acoustic Flight Test Data for Two Advanced Design High Speed Propeller Models," AIAA Paper AIAA-84-0250, 1984.

2.1.23 Dittmar, J.H., Jeracki, R.J., and Blaha, B.J., "Tone Noise of Three Supersonic Helical Tip Speed Propellers in a Wind Tunnel," NASA TM 79167, 1979.

2.1.24 Dittmar, J.H. and Jeracki, R.J., "Additional Noise Data on the SR-3 Propeller," NASA TM 81736, 1981.

2.1.25 Letter from NASA to P.R. Gliebe, 1984, "8 x 6 Foot Wind Tunnel Operating Conditions."

2.1.26 Mikkelson, D.C., Blaha, B.J., Mitchell, G.A., and Wikete, J.E., "Design and Performance of Energy Efficient Propellers for Mach 0.8 Cruise," NASA TM X-73612. Also, SAE Paper No. 770458, 1977.

2.1.27 Dittmar, J.H., Burns, R.J., and Leciejewski, D.J., "An Experimental Evaluation of the Effect of Boundary Layer Refraction on the Noise from a High-Speed Propeller," NASA TM 83764, September 1984.

2.1.28 Dittmar, J.H., "Further Comparison of Wind Tunnel and Airplane Acoustic Data for Advanced Design High Speed Propellers Models." NASA TM-86935, 1985.

2.1.29 Hawkings, D.L., "Noise Generation by Transonic Open Rotors," Mechanics of Sound Generation in Flows, Springer-Verlag, N.Y., 1979, pp 294-300.

2.2.1 Glauert, H., The Elements of Airfoil and Airscrew Theory (Second Edition), 1959.

2.2.2 Milne Thomson, L.M., Theoretical Hydrodynamics (Fourth Edition), 1960.

2.2.3 Article entitled "Airplane Propellers" by H. Glauert in Vol. IV of Aerodynamic Theory edited by W.F. Durand (Dover Edition, 1963).

2.2.4 Goldstein, M.E., Aeroacoustics, McGraw-Hill, New York, 1976.

2.2.5 Hawkings, D.L. and Lowson, M.V., "Theory of Open Supersonic Rotor Noise," J. Sound Vib., Vol. 36, No. 1, September 8, 1974, pp 1-20.

2.2.6 Hanson, D.B., "Noise of Counter Rotation Propellers," AIAA Paper 84-2305, 1984.

2.2.7 Block, P.J.W., "The Effects of Installation on Single and Counter Rotation Noise," AIAA Paper 84-2263, 1984.

2.2.8 Dittmar, J.H. and Jeracki, R.J., "Noise of the SR-3 Propeller Model at 2° and 4° Angle of Attack," NASA TM 82738, 1981.

2.2.9 Stefko, G.L. and Jeracki, R.J., "Wind Tunnel Results of Advanced High Speed Propellers in the Takeoff, Climb and Landing Operating Regimes," NASA TM 87054, 1985.

2.2.10 Rohrbach, E., Metzger, F.B., Black, D.M., and Ladden, R.M., "Evaluation of Wind Tunnel Performance Testings of an Advanced 45° Swept Eight-Bladed Propeller at Mach Numbers from 0.45 to 0.85," NASA CR-3505, 1982.

2.3.1 Hanson, D.B., "Shielding of Propfan Cabin Noise by Fuselage Boundary Layer," J. Sound Vib., 1982; also, Hamilton Standard Report HSER 8/65, 1981.

2.3.2 Dittmar, J.H. and Lasagna, P.L., "A Preliminary Comparison Between SR-3 Propeller Noise in Flight and in a Wind Tunnel." NASA TM 82805, 1982.

2.3.3 Hubbard, H.H. and Regier, A.A., "Free Space Oscillating Pressures Near Tips of Rotating Propellers," NACA Report 996.

2.3.4 McAninch, G.L., "A Note on Propagation Through a Realistic Boundary Layer," J. Sound Vib., Vol. 88 No. 2, 1983, pp 271-274.

2.3.5 Mungur, P. and Swift, G., "A Study of the Prediction of Cruise Noise and Laminar Flow Control Noise Criteria for Subsonic Air Transports," NASA CR-159104, 1979.

2.3.6 Hanson, D.B. and Magliozzi, B., "Propagation of Propeller Tone Noise Through a Fuselage Boundary Layer," AIAA Paper 84-0248, 1984.

2.3.7 Abramowitz, M. and Stegun, I., Handbook of Mathematical Functions, Dover Publications, N.Y., p 363.

2.3.8 Mungur, P. and Plumblee, H.E., "Propagation and Attenuation of Sound in a Soft Walled Annular Duct Containing a Sheared Flow," NASA SP-207, 1969, pp 305-327.

3.1.1 Various Authors, "NAS3-24339 Propfan Test Assessment Flight Test Results Review (DRD 235-03)," Charts presented at NASA Lewis Research Center, November 14, 1988.

3.2.1 Nallasamy, M., Clark, B.J., and Groeneweg, J.F., "Euler Analysis of the Three-Dimensional Flow Field of a High Speed Propeller: Boundary Condition Effects," Journal of Turbomachinery, Volume 109, No. 3, pp 332 through 339, July 1987.

3.3.1 Stefko, G.L., Rose, G.E., and Podboy, G.G., "Wind Tunnel Performance Results of an Aeroelastically Scaled 2/9 Model of the PTA Flight Test Propfan," AIAA Paper No. 87-1893, 1987.

3.4.2 Stefko, G.L., and Jeracki, R.J., "Wind Tunnel Results of Advanced High Speed Propellors at Takeoff, Climb, and Landing Mach Numbers," NASA Technical Memo, TM-87030, November 1985.